AN ABSTRACT OF THE DISSERTATION OF

Kasidit Chansawat for the degree of Doctor of Philosophy in Civil Engineering presented on April 28, 2003.
Title: Nonlinear Finite Element Analysis of Reinforced Concrete Structures Strengthened with FRP Laminates.

Abstract approved: Signature redacted for privacy.
Thomas H. Miller

Abstract approved: Signature redacted for privacy.
Solomon C.S. Yim

The Horsetail Creek (HC) bridge is an example of an Oregon bridge that was classified as structurally deficient and was not designed to withstand earthquake (EQ) excitations. A fiber-reinforced polymer (FRP) rehabilitation was performed on the HC bridge to increase flexural and shear capacities for traffic loads. However, a seismic retrofit has not yet been accomplished for this bridge.

Fully three-dimensional finite element (FE) models are developed to simulate and examine the structural behavior of both full-size reinforced concrete (RC) beams and the HC bridge using ANSYS. FE analyses are compared with tests of full-scale beams replicating the transverse beams of the HC bridge before and after FRP strengthening from linear and nonlinear ranges up to failure. The FE models can effectively predict the behavior of the beams, and analytical and experimental results correlate very well.

For the FE analyses of the HC bridge, soil-structure interface modeling is incorporated to replicate the actual bridge boundary conditions. Truck loadings are applied to the FE model at different locations, as in the actual bridge test. A sensitivity study is performed by varying uncertain bridge parameters to develop an FE bridge model best representing the actual bridge conditions. The optimal FE model obtained from the sensitivity study can accurately predict the magnitudes and trends in the strains.

After an optimal FE bridge model is established, a performance evaluation on the FRP strengthening of the HC bridge is conducted. Both unstrengthened and FRP-strengthened bridge models are subjected to two different types of loading; i.e., scaled gravity and scaled truck loads to failure. Comparisons of results show the improvement in structural performance due to FRP strengthening.

A seismic risk-related investigation of the HC bridge is also carried out. Nonlinear time-history analyses are performed using EQ acceleration-time histories applied to the HC bridge model. The ground motions are appropriate to the Pacific Northwest site and scaled so that the response spectrum, within natural periods of interest, matches the 1996 AASHTO design response spectrum. Based on the analytical results, column confinement is recommended to increase ductility and reduce potential for substructure collapse in future seismic events.

Nonlinear Finite Element Analysis of Reinforced Concrete Structures Strengthened with FRP Laminates

by
Kasidit Chansawat

A DISSERTATION

submitted to

Oregon State University

in partial fulfillment of
the requirements for the
degree of

Doctor of Philosophy

Presented April 28, 2003
Commencement June 2003

ACKNOWLEDGMENTS

At the outset, the completion of this dissertation is a dream come true to me. The dissertation is made possible due to the contributions and efforts of several people. For the first person, I would like to express my deepest gratitude and heartfelt appreciation to my major professor, Dr. Thomas H. Miller for his valuable advice and support throughout the dissertation. Besides those, his friendship and care are also highly appreciated. Next, I am really thankful to Dr. Solomon C.S. Yim for giving me his consistent guidance and assistance from the beginning and for serving as my co-major professor. Not only did these two people play a major role in the dissertation development, they also continuously offered me teaching assistantships, provided by the Department of Civil, Construction, and Environmental Engineering at Oregon State University (OSU) during my doctoral study. The investigation was financially supported in part by the Oregon Department of Transportation (ODOT). Sincere thanks also go to Dr. Damian I. Kachlakev for his contribution in the first part of the work and his participation as a committee member.

I also would like to thank Dr. Robert D. Layton for his interest and for serving as my minor professor; Dr. James R. Lundy for his academic and non-academic advice and support throughout the development and completion of this study and for serving as my committee member; and Dr. David D. Myrold for his

interest and for serving as a graduate council representative. In addition, I would like to thank Dr. John A. Gambatese for his encouragement and generous help for being a substitute committee member for Dr. Layton on my PhD final defense.

I am truly grateful to Sue M. Frey, a senior structural engineer at CH2M HILL, for the priceless opportunities she gave me to do the internship and to be a part of CH2M HILL. This is definitely a fundamental stepping stone toward my professional goal. Also, her professionalism has broadened my vision and helped me become a better structural engineer.

I am very thankful to Dr. Ted S. Vinson for his academic advice helping me solve problems in the project development; Dr. Stephen E. Dickenson for his valuable guidance in the earthquake modifications; Dr. Chistopher Higgins for his generous permission to let me use his powerful computer resources; and Tom Lieuallen and Paul Montagne for their computer system-based technical support and patience with my heavy uses of the engineering computer resources.

A special thanks is also given to the ANSYS gurus in the ANSYS forum for their useful comments and help on the program-related problems; David D. McCurry, Jr. for his clarification and comments; and Peter Seaders for his participation in the earthquake modifications.

For the next person, I would like to give sincere thanks and express my gratitude to Dr. Saksit Saengboon for his generous help and encouragement during my graduate degree pursuits or even before I came and continued my study in the United States. All four English skills he taught me not only have helped me

survive in the United States, but also have successfully helped me achieve a number of my professional and personal goals.

In addition, I wish to thank Cindy Loucks, Janet Mosley, Nancy and Andy Brickman, and others in the departmental office, including my Thai friends both at OSU and in Thailand, for their support which made my life a lot easier and happy during my stay in the United States.

Last but not least at all, I am forever grateful to my parents and my only sister for their immeasurable support and encouragement in every facet of my life. They are always there for me, no matter what. After having to be in the United States on my own, I just realized from them what truly unconditional love really meant. I know it is absolutely impossible to pay back what they have given me. What I can do for them in return is that I will always do at my best at everything to make them proud.

CONTRIBUTION OF AUTHORS

For Chapter 2, Dr. Damian I. Kachlakev directed the experimental portion of the work and participated in the first part of the FE development. Tanarat Potisuk was also involved with the FE development and writing of this chapter.

TABLE OF CONTENTS

TABLE OF CONTENTS (Continued)

Page

TABLE OF CONTENTS (Continued)

TABLE OF CONTENTS (Continued)

Page

TABLE OF CONTENTS (Continued)

TABLE OF CONTENTS (Continued)

LIST OF FIGURES

LIST OF FIGURES (Continued)

LIST OF FIGURES (Continued)

LIST OF FIGURES (Continued)

LIST OF FIGURES (Continued)

LIST OF TABLES

LIST OF APPENDIX FIGURES

LIST OF APPENDIX FIGURES (Continued)

NONLINEAR FINITE ELEMENT ANALYSIS OF REINFORCED CONCRETE STRUCTURES STRENGTHENED WITH FRP LAMINATES

CHAPTER 1: INTRODUCTION

1.1 OVERVIEW

Of 578,000 bridges in the US, more than 40% are classified either as structurally deficient or functionally obsolete by the Federal Highway Administration (FHWA). Three main factors causing the bridges to be in need of rehabilitation or replacement are deterioration of the bridges (corrosion), changes in use or increases in load requirements, and deficiencies in design and construction. The historic Horsetail Creek (HC) bridge in Oregon was classified as structurally deficient (Kachlakev 1998) for these reasons. The HC bridge was designed in 1913 and built in 1914. It is located on the Historic Columbia River Highway 100, 50 kilometers east of Portland, Oregon. The structure is a reinforced concrete (RC) deck girder bridge with spread footing foundations. The bridge having three 6.10-m. (20-ft.) spans is 18.28 m. (60 ft.) long and 7.32 m. (24 ft.) wide, built across the Horsetail Creek. The HC bridge is shown in Figure 1.1.

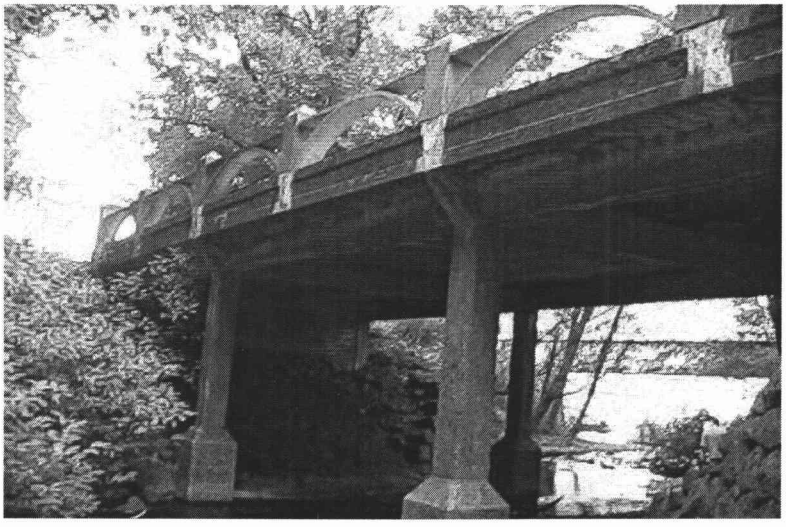

Figure 1.1. The Horsetail Creek Bridge before Strengthening

The plan and elevation of the bridge are shown in Appendix A along with reinforcement details.

During on-site inspections, some reinforcing steel bars were found to be exposed and corroded. The overall structural condition of the bridge was, however, generally good. Due to the age of the bridge, it was not designed to carry the heavier traffic volume and trucks that are common today. Moreover, the bridge beams were constructed without the presence of shear reinforcement required by current standards, a significant structural deficiency. Shear reinforcement is provided to ensure a more ductile flexural mode of failure rather than a shear failure giving no advance warning of distress.

Load rating of the HC bridge was performed by CH2M-Hill (1997). It was found that the bridge had only 6% of the required shear capacity for the transverse beams and only 34% for the longitudinal beams, due to the absence of shear reinforcement. Additionally, only approximately 50% of the required flexural capacity was present for the transverse beams.

Due to the fact that the HC bridge is an historical structure, rehabilitation was selected over replacement, and retrofit methods must maintain the historic character of the bridge.

1.2 IMPORTANCE OF FRP STRENGTHENING

One of the potential methods for bridge rehabilitation and strengthening is the use of fiber-reinforced polymer (FRP) composites. FRP composites consist of two discrete phases: continuous fibers and a resin matrix. The reinforcing fibers have high strength and stiffness, while the resin matrix binds the fibers together, which allows stress to be transferred from one fiber to another and produce a consolidated structure (Head 1992). FRP composites are generally classified into three types depending on the fiber used: glass-fiber-reinforced polymer (GFRP) composites; carbon-fiber-reinforced polymer (CFRP) composites; and aramid-fiber-reinforced polymer (AFRP) composites.

GFRP composites are the most commonly used FRP type, as they are economical to produce and have high tensile strength. They are, however, limited in high performance applications due to their relatively low stiffness and chemical degradation if exposed to severe hydrothermal conditions (Daniel and Ishai 1994). Glass fibers are inorganic, synthetic, multifilament materials. The two most commonly used types of fibers are E-glass and S-glass. S-glass fibers have higher strength and elastic modulus than E-glass.

CFRP composites are the predominant type used to achieve high stiffness and strength. Carbon fibers are produced from three types of polymer precursors: polyacrylonitrile (PAN) fibers, rayon fibers, and pitch (Kachlakev 1998). They can be divided into three categories: high strength (HS), high modulus (HM), and ultra high modulus (UHM).

Aramid fibers are tough, organic, synthetic fibers exhibiting excellent fatigue and creep behavior. Kevlar 29 and Kevlar 49 are the two most commonly used aramid fibers. AFRP composites fit well into a gap between GFRP composites having low modulus and tensile strength and CFRP composites having high modulus and tensile strength.

Two common methods of installing FRP composites are used in retrofitting RC structures. The first method is the wet lay-up method, which is the most commonly used (Teng et al. 2001). With the in-situ application of resin, an FRP sheet can be bonded to concrete surfaces or curved surfaces and can also be wrapped around corners. The other method is prefabrication of FRP composites in

various forms. They can be FRP pultruded plates for flexural strengthening or shells for column strengthening. The wet lay-up method is more flexible, while prefabrication provides better material quality control.

Compared with the traditional steel plate bonding technique for strengthening RC structures, FRP strengthening possesses several distinct advantages as follows:

1. FRP composites are noncorrosive and generally resistant to chemicals for durable performance (Teng et al. 2001).
2. FRP composites have a high strength-to-weight ratio. They can be 2 to 10 times as strong as steel plates, while their weight is only 20% that of steel (Darby 1999). This leads to relative simplicity in application in terms of site handling, a labor cost reduction, and reduced interruption to existing services.

Due to these properties, FRP strengthening was selected for the HC bridge. The Oregon Department of Transportation (ODOT) installed FRP sheets to the bridge, where the structural capacity was insufficient. The installation was complete in 1998. For the transverse beams, CFRP (to increase flexure capacity) and GFRP (to increase shear capacity) unidirectional laminates were attached at the bottom and on the sides of the beams, respectively, while only GFRP shear laminates were attached at the sides of the longitudinal beams. Figure 1.2 shows a GFRP sheet being applied on a cross beam. The FRP reinforcement details on both transverse and longitudinal beams are shown in Appendix A.

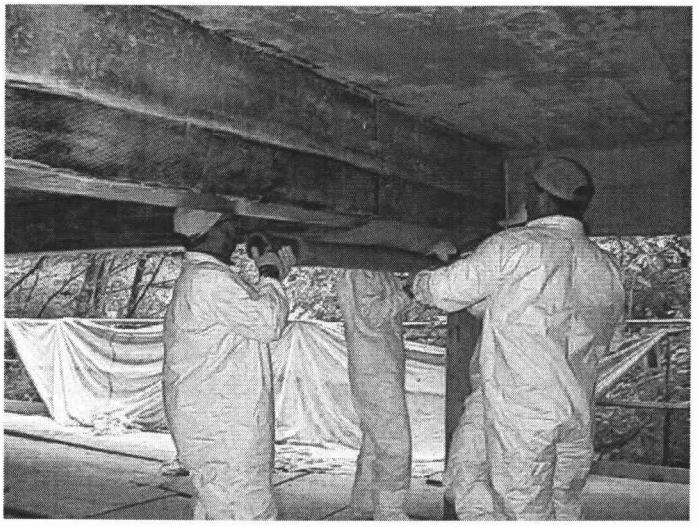

Figure 1.2. FRP Installation on the HC Bridge

1.3 SCOPE AND OBJECTIVES

The overall research program is split into three phases; i.e., Phase I: Experiments on the full-scale beams and the HC bridge; Phase II: Finite element (FE) analyses of the full-scale beams and the HC bridge; and Phase III: Structural predictions of the HC bridge both before and after FRP strengthening under static and dynamic loadings using FE models.

For Phase I, four full-scale RC beams with varying configurations of CFRP and GFRP were fabricated and tested at Oregon State University: 1) an unstrengthened (control) beam; 2) a flexure-strengthened beam; 3) a shear-strengthened beam; and 4) a flexure/shear-strengthened beam. All the beams were

constructed with the same geometry and steel placement. The control beam and the flexure/shear-strengthened beam replicate the transverse beams of the HC bridge before and after FRP retrofitting, respectively. For the flexure-strengthened beam, only the CFRP scheme was applied at the bottom of the beam, while only the GFRP scheme was applied on the sides of the shear-strengthened beam. However, the combination of the CFRP and GFRP schemes was applied on the flexure/shear-strengthened beam, as in the actual cross beams after FRP strengthening.

Conventional 60 mm. (2.36 in.) resistive strain gauges were placed throughout the beams; i.e., inside the beams on the steel rebars and on the concrete surface. Fiber optic gauges were installed on the FRP surface for the strengthened beams. Direct current displacement transducers (DCDTs) were used to collect deflection data. All beams were tested in third-point bending using a 2670 kN (600 kip) capacity (based on the internal frame testing capacity) Baldwin hydraulic testing machine. Based on investigations of the machine supporting structure, the total load that can be applied to the beams was, however, limited to 712 kN (160 kips). It should be noted that this limit was reached during the flexure/shear-strengthened beam test.

All the beams were subjected to a short-term monotonic loading to failure (except the flexure/shear-strengthened beam due to the limitation of the testing machine). Strain and deflection data were collected. Cracks were observed and mapped. These data were used later in the development of and in comparisons to

FE models (Phase II). For complete details of the full-scale beam experiments, refer to McCurry (2000) and Kachlakev and McCurry (2000).

For the HC bridge experiment in Phase I, fiber optic strain gauges were installed on one transverse beam and one longitudinal beam at various locations on both concrete and FRP surfaces to record strains during the tests. The locations of the gauges are shown in Appendix A. The experimental program performed by ODOT was truck load test with both empty and full truck loads statically applied on the middle of the bridge deck for seven locations, as shown in Appendix A. Strains for each loading scheme and location were collected, and calibrated before being used in comparisons to FE models in Phase II.

The truck load tests were conducted three times: in November 1999 (ODOT 1999), in November 2000 (ODOT 2000), and in February 2001 (ODOT 2001). The strain results from the last two tests (Nov. 2000 and Feb. 2001) correlated well with each other. The strain data from the Nov. 2000 test were selected and used in Phase II. The configuration and axle weights of the truck used in this test are shown in Appendix A. It should be noted that only the strain data from the bridge after FRP strengthening are available because the fiber optic strain gauges and FRP laminates were installed at the same time.

For Phase II, three-dimensional FE models were developed to simulate the structural behavior of both the full-size beams and the HC bridge. ANSYS, a general, multi-purpose FE program, was used. For the FE study of the full-scale beams, analytical results were compared with the experimental data from Phase I

from linear to nonlinear ranges up to failure in terms of load-strain and load-midspan deflection relationships, crack patterns, and ultimate loads.

For the analysis of the HC bridge, a sensitivity study on uncertain parameters that can significantly affect the structural behavior was performed in order to develop an optimal FE bridge model best representing the actual conditions. The parameters considered in the study are some aspects of bridge geometry, levels of existing damage, in-situ concrete strength, and stiffness of the soil foundation. Results from varying the parameters were compared with the field test data (from Phase I) in terms of strains on both the transverse and longitudinal beams versus various truck load locations on the bridge deck. The model providing the best estimates of the bridge response within reasonable conditions was selected as optimal and used later in Phase III. It was important to ascertain that the proposed bridge FE model can accurately simulate the service limit state response characteristics of the structure before it is used to predict static and dynamic bridge responses in the highly nonlinear state.

In Phase III, a performance evaluation of the HC bridge under static and dynamic loadings was conducted. For the static loading evaluation, both unstrengthened and strengthened FE bridge models were subjected to two different types of loading: i.e., mass-proportional and scaled truck loadings. The strengthened bridge FE model used in this phase was the optimal one from Phase II, and the bridge model before FRP strengthening was modified from this version. For each case, the load was gradually applied on the bridge models until failure.

Comparisons of results in terms of load-deflection relationships, crack patterns, yielding development in steel rebars, and load-carrying capacity were made.

Moreover, nonlinear dynamic FE analysis of the HC bridge was also performed to examine the effects of earthquakes (EQ). Deterministic EQ excitations were applied to the bridge models, and the bridge responses were analyzed using a nonlinear time-history analysis. The EQ acceleration time-histories used in the study were considered to be suitable for structures located in the Pacific Northwest. They were modified so that the mean response spectrum within natural periods of interest matched the 1996 AASHTO design response spectrum (AASHTO 1996) for the HC bridge.

The scope of this dissertation focuses on Phases II and III. Based on this scope, the purposes of the study are to:

1. Examine structural behaviors of the full-scale RC beams and the HC bridge, both before and after applying FRP laminates, using the FE method from linear to nonlinear analyses up to failure under static loads.
2. Assess the HC bridge's seismic risk and propose possible seismic retrofits of the bridge.
3. Develop a methodology for the general application of FE analysis to RC structures strengthened with FRP laminates and subjected to static and dynamic loadings.

1.4 FE MODELING METHODOLOGY

Modeling the complex behavior of RC structures using FE analysis is highly challenging. Once the structures crack, their behaviors become more nonlinear. The cracked structures are susceptible to numerical instability causing unconverged solutions. Therefore, loads must be applied gradually to the structures, and tolerance criteria must be properly adjusted to avoid convergence difficulties. The nonlinear analysis of RC structures is, then, time-consuming and takes a large amount of computer resources in terms of disk space and CPU time. Few researchers have used ANSYS to analyze RC structures, which impeded the early stages of the study. However, as the modeling and analysis techniques are better understood and become more familiar, progress can be made more easily, and analyses of more complex structures can be performed with confidence.

There are many differences and improvements in both modeling methodology and solutions between the developing work and the complete work that is presented in the following chapters. The major differences between the developing and complete work are pointed out as follows:

1.4.1 Modeling Methodology in the Developing Work

1. For the stress-strain relationship of concrete, the compressive strain-softening relationship was not implemented in the developing work. A perfectly plastic relationship was assumed instead.
2. Confinement effects due to FRP encasement, applied concentrated loads, steel stirrups in the columns were not included in the developing work.
3. For the FE study of the full-scale beams, an incremental direct force was applied to the models (force control). In addition, the nominal yield strength of the steel was used.
4. For the FE study of the HC bridge, existing damage was not taken into consideration. Soil-structure interface was not modeled. Additionally, a conservative concrete strength of 17.24 MPa (2500 psi) recommended by AASHTO (AASHTO 1989 and 1994) for bridges constructed before 1959 was used in the models.

During the development of the FE studies, work within Phase II was published in Kachlakev et al. (2001), Potisuk et al. (2001a and 2001b), and Chansawat et al. (2001a and 2001b).

1.4.2 Modeling Methodology in the Complete Work

1. The complete stress-strain relationship for the concrete was used in the complete work. Ascending and descending branches, including a cut-off point for the descending branch, were defined for concrete in compression.
2. Concrete confinement was taken into consideration. The confinement in the concrete is induced by FRP encasement, localized effects from an applied concentrated load, and steel ties in the columns. The confinement due to FRP encasement and effects from an applied concentrated load is discussed in Chapter 2, while the confinement due to FRP encasement and steel ties in the columns is covered in Chapters 3, 4 and 5.
3. For the FE study of the HC bridge, existing damage was included by introducing some cracks to the bridge models in the pre-loading step. This is presented in Chapter 3.
4. Soil-structure interface was modeled in the FE study of the HC bridge by replacing the bridge footings with translational and rotational spring elements to represent realistic boundary conditions of the bridge. Soil-structure interface modeling is explained in Chapters 3, 4, and 5.
5. A more realistic concrete strength for the HC bridge obtained from the sensitivity study (Chapter 3) and on-site pulse velocity measurements was used instead of the AASHTO recommended value and included in Chapters 3, 4, and 5

1.5 RESEARCH SIGNIFICANCE

The complex behavior of reinforced concrete beams and bridges strengthened with FRP composites is difficult to predict with current design and simplified analysis tools. In this study, fully three-dimensional finite element models are developed to examine the structural behavior of FRP-strengthened reinforced concrete beams and bridges. Complete stress-strain curves of concrete are defined in the FE models, as they are necessary to accurately predict structural behavior up to failure and post-failure. Moreover, concrete confinement in compression due to FRP encasement, localized effects from applied concentrated loads, and steel ties in the columns, is taken into account. In the FE analyses of the HC bridge, the soil-structure interface is modeled to realistically represent the foundation. Additionally, existing damage in the bridge is also considered.

The FE modeling methodology presented in this study can help to confirm theoretical calculations as well as provide a valuable supplement to laboratory investigations and field experiments of structural behavior of FRP-strengthened reinforced concrete beams and bridges. It can also be used to establish proper FE models to simulate behavior and estimate load-carrying capacity of reinforced concrete structures both with and without FRP strengthening without performing experimental testing.

REFERENCES

AASHTO Subcommittee on Bridges and Structures. (1989). *Guide Specifications for Strength Evaluation of Existing Steel and Concrete Bridges*. American Association of State and Highway Transportation Officials, Washington D.C.

AASHTO Subcommittee on Bridges and Structures. (1994). *Manual for Condition Evaluation of Bridges*. American Association of State and Highway Transportation Officials, Washington D.C.

AASHTO Subcommittee on Bridges and Structures. (1996). *Standard Specifications for Highway Bridges*. 16th ed., Including up to 1999 Interim Revisions. American Association of State and Highway Transportation Officials, Washington D.C.

CH2M Hill Consulting Engineers in conjunction with TAMS Consultants. (1997). "Evaluation and Resolution of Under Capacity State Bridges: Bridge #04543, Horsetail Creek Bridge." CH2M HILL, Inc., Corvallis, OR.

Chansawat, K., Kachlakev, D.I., Miller, T.H., and Yim, S.C.S. (2001a). "FEA of the Horsetail Creek Bridge Strengthened with FRP Laminates." 46th International SAMPE Symposium, 46(2), 1772-1783.

Chansawat, K., Kachlakev, D.I., Miller, T.H., and Yim, S.C.S. (2001b). "FE Modeling and Experimental Verification of an FRP Strengthened Bridge." SEM Annual Conference on Experimental and Applied Mechanics, 624-627.

Daniel, I.M., and Ishai, O. (1994). *Engineering Mechanics of Composite Materials*. Oxford University Press, NY.

Darby, J.J. (1999). "Role of Bonded Fibre-Reinforced Composites in Strengthening of Structures." *Strengthening of Reinforced Concrete Structures Using Externally-Bonded FRP Composites in Structural and Civil Engineering*, edited by L.L. Hollaway and M.B. Leeming, Woodhead Publishing, Cambridge, England.

Head, P.R. (1992). "Design Methods and Bridge Forms for the Cost Effective Use of Advanced Composites in Bridges." *Advanced Composite Materials in Bridges and Structures*, 15-30.

Kachlakev, D.I. (1998). "Strengthening Bridges Using Composite Materials." *SHWA-OR-RD-98-08, United States Department of Transportation Federal Highway Administration and the Oregon Department of Transportation*, Salem, OR.

Kachlakev, D.I., and McCurry, D.Jr. (2000). "Testing of Full-Size Reinforced Concrete Beams Strengthened with FRP Composites: Experimental Results and Design Methods Verification." *SPR387, United States Department of Transportation Federal Highway Administration and the Oregon Department of Transportation*, Salem, OR.

Kachlakev, D.I., Miller, T.H., Yim, S.C.S., Chansawat, K., and Potisuk, T. (2001). "Finite Element Modeling of Concrete Structures Strengthened with FRP Laminate." *SPR316, United States Department of Transportation Federal Highway Administration and the Oregon Department of Transportation*, Salem, OR.

McCurry, D., Jr. (2000). "Strengthening of Reinforced Concrete Beam Using FRP Composite Fabrics: Full-Scale Experimental Studies and Design Concept Verification." *MS Thesis*, Oregon State University, Corvallis, OR.

Oregon Department of Transportation (ODOT) Field Test Data. (1999). Private Correspondence, Salem, Oregon.

Oregon Department of Transportation (ODOT) Field Test Data. (2000). Private Correspondence, Salem, Oregon.

Oregon Department of Transportation (ODOT) Field Test Data. (2001). Private Correspondence, Salem, Oregon.

Potisuk, T., Kachlakev, D.I., Miller, T.H., and Yim, S.C.S. (2001a). "Effects of Shear Strengthening with GFRP on Reinforced Concrete Beams." 46th International SAMPE Symposium, 46(2), 1759-1771.

Potisuk, T., Kachlakev, D.I., Miller, T.H., and Yim, S.C.S. (2001b). "Experimental
Verification of FE Models of FRP Strengthened RC Beams." SEM Annual Conference on Experimental and Applied Mechanics, 620-623.

Teng, J.G., Chen, J.F., Smith, S.T., and Lam, L. (2001). *FRP Strengthened RC Structures*. John Wiley & Sons, Ltd, West Sussex, England.

CHAPTER 2: FE MODELS OF GFRP AND CFRP STRENGTHENING OF REINFORCED CONCRETE BEAMS

Kasidit Chansawat, Tanarat Potisuk, Thomas H. Miller, Solomon C.S. Yim, and Damian I. Kachlakev

ABSTRACT

Three-dimensional finite element (FE) models are developed to simulate the behavior of full-scale reinforced concrete beams strengthened with glass and carbon fiber-reinforced polymer laminates (an unstrengthened control beam, a flexural-strengthened beam, a shear-strengthened beam, and a beam with both shear and flexural strengthening). The FE models use eight-node, isoparametric elements with a smeared cracking approach for the concrete and three-dimensional layered elements to model the FRP composites. Analysis results are compared with data from full-scale beam tests through the linear and nonlinear ranges up to failure.

It was found that the FE models could effectively simulate the behavior of the full-scale beams. The analysis results agree very well with those from the experiments. The predicted crack patterns at failure strongly resemble the failure modes observed for the full-scale beam tests.

RESEARCH SIGNIFICANCE

The complex behavior of reinforced concrete beams strengthened with FRP composites is difficult to predict with current design and simplified analysis tools. The FE modeling methodology presented in this study can help in confirming these theoretical calculations as well as in providing a valuable supplement to laboratory investigations of structural behavior of FRP-strengthened reinforced concrete beams. Comparisons of experimental behavior and FE results are shown for the shear-critical beams tested.

2.1 INTRODUCTION

In the last decade, fiber reinforced polymer (FRP) composites have been used for strengthening structural members of reinforced concrete bridges which are structurally deficient or functionally obsolete due to changes in their use or consideration of increased loadings (Kachlakev 1998). Many researchers have found that FRP composites applied to such members provide reliable and cost effective rehabilitation (Kachlakev 1998 and Tedesco et al. 1996). Currently in the U.S., ACI Committee 440 is establishing design recommendations for FRP application to reinforced concrete (ACI 440 2002).

In many cases the currently available design and simplified analysis tools cannot provide complete and accurate predictions of behavior for reinforced concrete members strengthened with FRP composites, mainly due to the fact that these methods were developed originally for properties and behavior of conventional materials. To overcome these difficulties, the finite element method (FEM) is employed in this study to analyze the behavior of FRP-strengthened reinforced concrete beams. Modeling the complex behavior of reinforced concrete, which is nonhomogeneous, nonlinear, and anisotropic, is a difficult challenge in finite element analysis. Most early finite element (FE) models of reinforced concrete were based on a pre-defined crack pattern (Nilson 1968). With this approach, changes in the topology of the models were required as the load increased; therefore, the ease and speed of the analysis were limited. A smeared cracking approach was also introduced using isoparametric formulations to represent the cracked concrete as an orthotropic material. The smeared cracking approach overcomes these limitations and has been widely adopted for predicting the nonlinear behavior of concrete (Suidan and Schnobrich 1973).

The finite element analysis (FEA) and behavior are further complicated in FRP-strengthened reinforced concrete beams. FRP composites are orthotropic materials with two constituents, i.e. reinforcing and matrix phases. The reinforcing phase material is in the form of fibers, which are typically stiffer and stronger, whereas the matrix phase material is generally continuous, less stiff and weaker. Over the past few years, a number of researchers have studied the behavior and

modeling of reinforced concrete members strengthened with FRP composites. In these studies, the FE method was used with eight-node isoparametric elements and a smeared cracking approach for modeling the concrete; and two dimensional plate elements (Malek et al. 1998) or truss elements (Ross et al. 1999) for the FRP composites.

In this paper, ANSYS (ANSYS 1998) is used to simulate the behavior of four full-scale reinforced concrete beams, which replicated the transverse beams from the historic Horsetail Creek Bridge (HCB) (McCurry 2000), located along the Columbia River highway near Portland, Oregon. The FE model uses a smeared cracking approach for the concrete and three-dimensional layered elements to model FRP composites. In the model, perfect bond between the concrete and FRP material is assumed based on observed results (no debonding occurred in any of the experimental beams up to the point of failure).

2.2 EXPERIMENTS

In our experiment, four beams (McCurry 2000) were tested. These replicated the transverse beams of the Horsetail Creek Bridge, constructed in 1914 and still operational. The original transverse bridge beams were constructed without shear reinforcement. External reinforcement with FRP composites was

used to increase the strength of the beams due to the historic nature of the bridge, economics, and time constraints for the rehabilitation effort.

The four full-scale reinforced concrete beams were fabricated and tested at Oregon State University in order to compare their behaviors in the laboratory: 1) an unstrengthened (control) beam; 2) a flexural-strengthened beam; 3) a shear-strengthened beam; and 4) a beam with both shear and flexural strengthening. All beams were constructed with the same geometry and steel placement. The dimensions of the beams were 305 mm (12 in) wide, 770 mm (30 in) deep, and 6095 mm (120 in) long. Three main flexural steel rebars (#22) were placed close to the bottom face of the beams extending the full length. Two steel rebars (#19) were added near the bottom face at the midspan section and bent up to the top face at both ends. Two smaller steel rebars (#16) were also provided close to the compression face of the beams. Glass fiber reinforced polymer (GFRP) sheets were applied on the sides of the shear-strengthened beams (3 and 4) to mitigate the shear deficiency, and carbon fiber reinforced polymer (CFRP) sheets to the bottom of the flexural-strengthened beams (2 and 4) to increase the flexural strength. Fig. 2.1 shows the details of the four test beams. In particular, Fig. 2.1(a) shows the geometry and steel reinforcement details, while Figs. 2.1(b) to (d) show the FRP strengthening schemes for the flexural; shear; and flexural plus shear experimental beams, respectively. The experimental beams were simply supported and tested in third point bending (two support and two load points) as shown in Fig. 2.1(a).

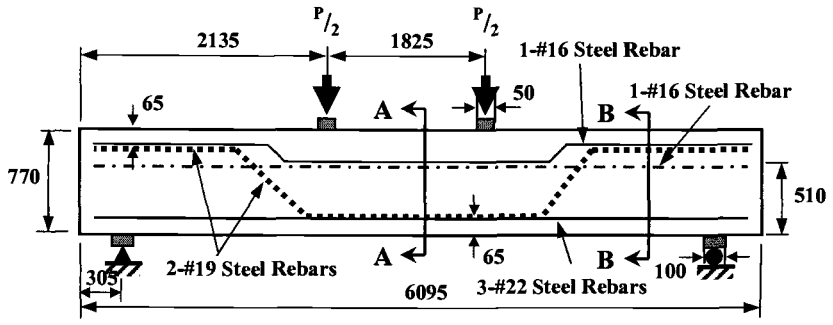

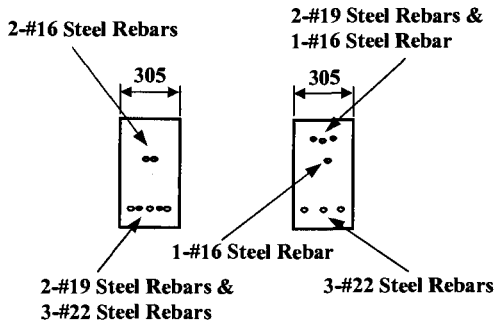

Section A-A Section B-B

(a)

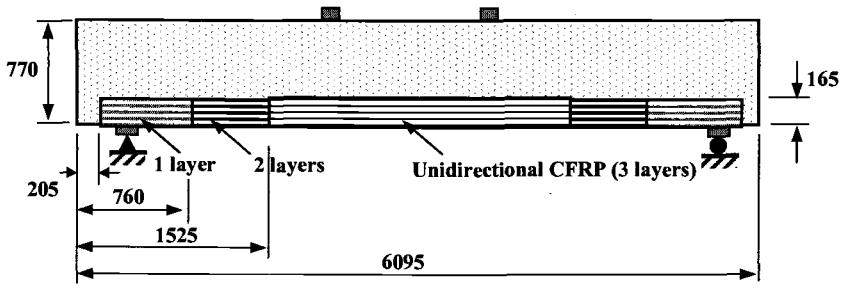

(b)

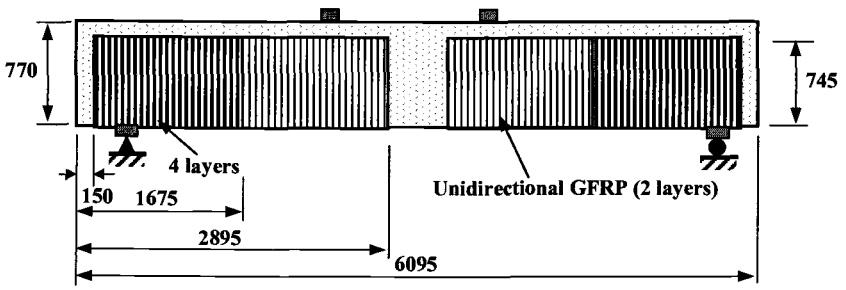

(c)

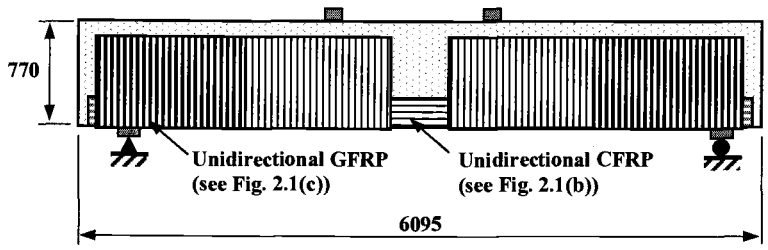

(d)

Figure 2.1. Experimental Beams (dimensions shown in mm): (a) Unstrengthened Beam; (b) Flexural-Strengthened Beam; (c) Shear-Strengthened Beam; (d) Flexural/Shear-Strengthened Beam (McCurry 2000)

2.3 FINITE ELEMENT MODELING

2.3.1 Element Types

In this study, three-dimensional, cracking reinforced concrete elements and layered solid elements are used to simulate the behavior of the FRP-strengthened reinforced concrete beams. Although ANSYS is employed here, the description of elements in this section is common to a number of commercial FE programs (e.g., ABAQUS and ADINA). For reinforced concrete, the 3D solid element (SOLID65 in ANSYS) with eight nodes and three degrees of freedom at each node, translations in the nodal x, y, and z directions, is used. This element is capable of plastic deformation, creep, crushing in concrete, and cracking in three orthogonal directions at each integration point. Time-dependent nonlinearities such as creep

and shrinkage are not modeled here. Moreover, to avoid premature failure in the FE simulation due to a significant local loss of stiffness from crushing, crushing capability is disabled in this study. A 3D truss (or spar) element (LINK8) with two nodes and three degrees of freedom at each node, translations in the nodal x, y, and z directions, models the discrete steel reinforcement. FRP composites are modeled with 3D layered structural solid elements (SOLID46) having eight nodes with three degrees of freedom at each node, translations in the nodal x, y, and z directions. The element allows for different material layers with different orientations and orthotropic material properties in each layer. The concrete 3-D solid elements (SOLID65) simulate the nonlinear material behavior with a smeared crack approach (William and Warnke 1975). When cracking occurs at an integration point, the material properties are adjusted to effectively model a "smeared band" of cracks, rather than discrete cracks. Specifically, when a principal stress at an integration point in a concrete element exceeds the tensile strength, the stiffness is reduced to zero in that principal direction perpendicular to the cracked plane. Each integration point is capable of cracking in three directions.

2.3.2 Material Properties

For the full-scale beam models, the elastic modulus for each concrete beam was estimated using a pulse velocity method (ASTM 1994). Responses of concrete

under loading without and with confinement are characterized by distinctly nonlinear behaviors, which can be modeled in the SOLID65 element. Complete stress-strain curves of concrete are needed to accurately predict structural behavior up to failure and post-failure. In compression, the stress-strain relationship can be divided into ascending and descending branches. For unconfined concrete, several numerical expressions have been developed for the complete curves (Wang et al. 1978 and Bangash 1989). For the ascending branch, those equations provide similar relationships. However, for the descending branch they are different. This is due to the fact that the stress-strain relationships are derived from experimental results where the slope of the descending branch depends on many factors; i.e., rate of loading, type of testing machine, size and location of the gauge length, and the presence or absence of ties or stirrups (Wang et al. 1978, Kent and Park 1971, Barnard 1964, and Balakrishnan and Murray 1988). In this study, the constitutive model from Desayi and Krishnan (1964) shown in Fig. 2.2(a) (regions AB and BC) is used to represent both ascending and descending branches of the stress-strain relationship for the unconfined concrete as follows:

$$\sigma = \frac{E_0 \epsilon}{1 + \left(\frac{\epsilon}{\epsilon_0'}\right)^2} \qquad [2.1]$$

in which

$$\epsilon_0' = 2\frac{f_c'}{E_0} \qquad [2.2]$$

and

$$E_0 = 4733\sqrt{f_c'} \qquad [2.3]$$

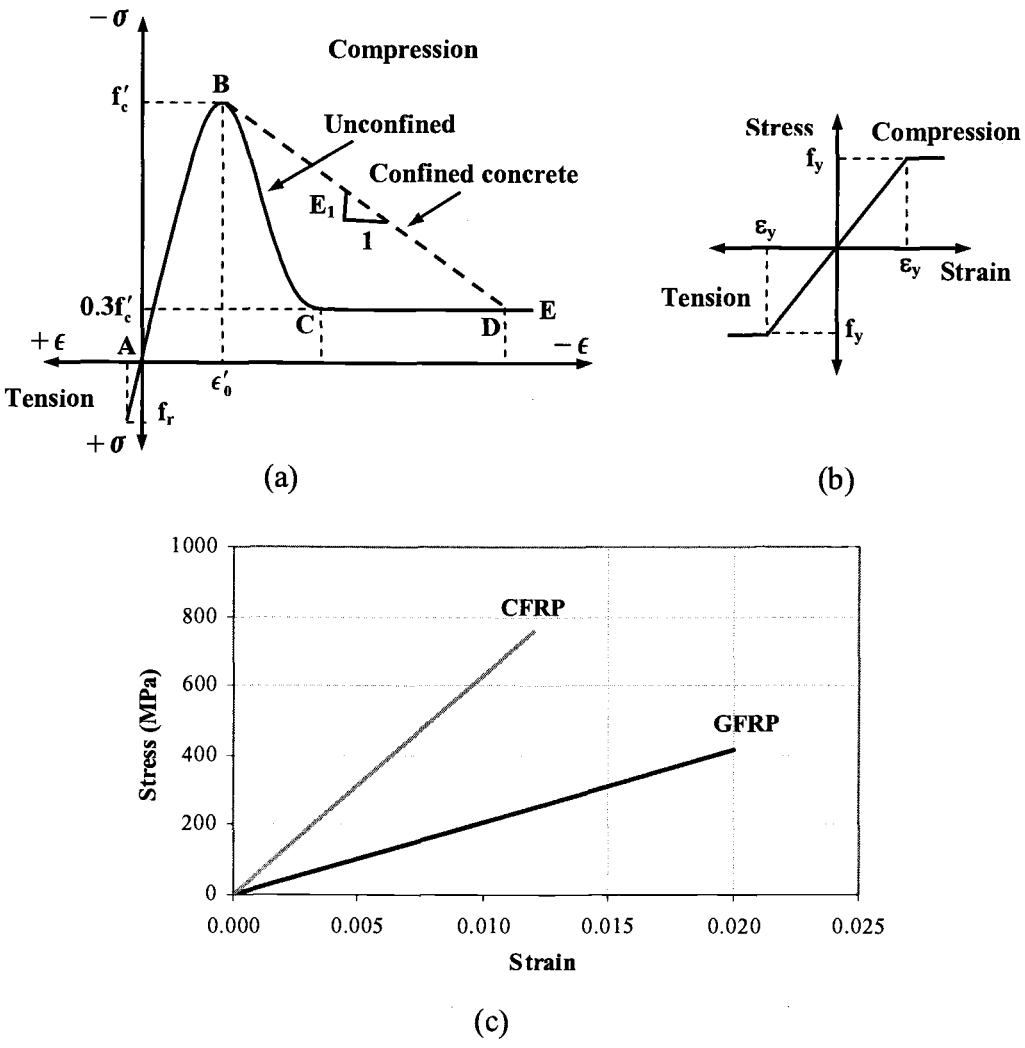

Figure 2.2. Uniaxial Stress-Strain Curve: (a) Concrete; (b) Steel Reinforcement; (c) FRP Composites in the Fiber Direction

Following the descending branch, concrete can undergo large strains (region CE from Fig. 2.2(a)) while still resisting about 20% - 30% of its maximum

load (Barnard 1964 and Stevens et al. 1991). In this study, it is assumed that the concrete can sustain a stress of $0.3f_c'$ after the descending branch.

Confinement in concrete occurs when compression causes lateral expansion due to Poisson's effect, increases in volume due to progressive internal cracking and then pressure outwards against the transverse reinforcement (Kent and Park 1971). The restraining reinforcement can be closely spaced steel stirrups or FRP encasement. Confinement can also be a localized effect from an applied concentrated load (Kemp 1998). Confinement enhances the strength and ductility of concrete in compression. In the HCB beams, there is no confinement due to steel stirrups. A number of researchers have developed stress-strain relationships for concrete confined by steel spirals or stirrups (Kent and Park 1971, Balakrishnan and Murray 1988, and Kemp 1998). However, no investigations of stress-strain relationships for FRP-confined concrete in flexural members were found. Studies have been focused on FRP confinement in columns, rather than in beams (Samaan et al. 1998 and Teng et al. 2001). For simplicity, it is assumed in this research that the behavior of FRP-confined concrete for flexural members is similar to that of stirrup-confined concrete. Thus, confinement has no effect on the slope of the ascending part of the stress-strain relationship, and it is the same as for unconfined concrete (Kent and Park 1971 and Bhatt and Kader 1998). In addition, the maximum compressive flexural stress for both unconfined and confined concrete is the same and equals the cylinder compressive strength, f_c'. For the descending branch, the slope for the FRP-confined concrete (region BD in Fig. 2.2(a)) is

assumed to be between that of the unconfined concrete and perfectly plastic behavior as follows (Balakrishnan and Murray 1988):

$$E_1 = -0.018E_0 \qquad [2.4]$$

As for the unconfined concrete, the confined concrete is also assumed to carry 30% of the maximum load at large strains (region DE in Fig. 2.2(a)).

For the concrete in tension, the stress-strain behavior is assumed to be linearly elastic with slope E_0 up to the tensile strength, f_r, calculated, based on ACI 318 (2002):

$$f_r = 0.623\sqrt{f_c'} \qquad [2.5]$$

Poisson's ratio for concrete in all beams is assumed to be 0.2. Another important material property is the shear transfer coefficient, which represents a shear strength reduction factor for those subsequent loads that induce sliding (shear) across the crack face (ANSYS 1998). The value of the shear transfer coefficient ranges from 0.0 to 1.0 with 0.0 representing a smooth crack (complete loss of shear transfer) and 1.0 representing a rough crack (no loss of shear transfer). For an open crack, the shear transfer coefficient varied between 0.05 and 0.50 in many studies of reinforced concrete structures (Isenburg 1993). Coefficient values selected (between 0 and 1) do not appear to be critical; however, a value greater than 0 is necessary to prevent numerical difficulties (Isenburg 1993). In this study, the open and closed crack shear transfer coefficients used are 0.2 and 1.0, respectively.

Material properties of the concrete used in the FE analyses for each beam are summarized in Table 2.1.

Table 2.1. Summary of Material Properties for Concrete

Beam	Concrete				
	E_c (GPa)*	f'_c (MPa)*	f_r (MPa)	ν	β_t
Unstrengthened beam	19.3	16.7	2.55	0.2	0.2
Flexural-strengthened beam	17.5	13.7	2.31	0.2	0.2
Shear-strengthened beam	18.2	14.7	2.39	0.2	0.2
Flexural/Shear-strengthened beam	17.1	13.0	2.25	0.2	0.2

*Based on pulse velocity method (McCurry 2000)

It should be noted that the elastic moduli were obtained from pulse velocity measurements to more accurately estimate the actual concrete stiffness of the beams. Elastic modulus estimates using tested cylinder strengths (using the relationship from eq. 2.3) were notably high, compared to those calculated from the design 28-day strengths and those obtained from the pulse velocity tests (McCurry 2000). That is, the average cylinder strength for each beam on the day of testing was 41.9 MPa (82 days), 30.5 MPa (125 days), 38.4 MPa (164 days), and 34.3 MPa (198 days) for the unstrengthened, flexure strengthened, shear strengthened, and flexure/shear strengthened beams, respectively. A design 28-day strength of 20.7 MPa was requested from the concrete supplier, and the concrete strengths based on

elastic moduli obtained from the pulse velocity tests (also using the relationship from eq. 2.3) are shown in Table 2.1. Due to more desirable casting and curing environments for the cylinders, the concrete cylinder strengths were much higher than the concrete strengths in the experimental beams although they were from the same mix and design batch. The cylinders were fully submerged in tap water and not removed from the water bath until the day of testing. On the other hand, due to the size of the beams, each beam was covered with regularly moistened burlap under plastic sheeting instead. Excess water was then always available for curing the cylinders, but not necessarily for the beams. The elastic moduli estimates from the pulse velocity method were, then, used instead of those based on cylinder tests.

The experimental and FE model beams included typical #16, #19 and #22 steel reinforcing bars (see Fig. 2.1(a)) with properties f_y = 455 MPa, E_s = 200 GPa, and ν = 0.3, reflecting the actual typical yield strength of steel obtained from the fabricator. The steel for the FE models is assumed to be elastic-perfectly plastic and identical in tension and compression as shown in Fig. 2.2(b).

In the FE models, each load is distributed over a small area as for the experimental beams. 25-mm thick steel plates (using 3D structural solid elements having 8 nodes with three degrees of freedom at each node, translations in the nodal x, y, and z directions) are added at the support locations in order to avoid stress concentration problems there. The steel plates are linear-elastic with an elastic modulus equal to 200 GPa and a Poisson's ratio of 0.3.

The FRP composites are assumed to be specially orthotropic and transversely isotropic materials; i.e., the mechanical properties are the same in any direction perpendicular to the fibers. GFRP is applied to the sides of the beams to increase the shear strength, due to its superior strain at failure. CFRP is applied to the bottom of the beams to provide added flexural strength, due to its high tensile strength. Linear elastic properties are assumed for the FRP as shown in Fig. 2.2(c) and summarized in Table 2.2. FRP material properties are based on design values supplied by the manufacturers.

Table 2.2. Summary of Material Properties for FRP Composites (McCurry 2000)

FRP composite	Elastic modulus (GPa)	Major Poisson's ratio	Limiting stress (MPa)	Limiting strain	Shear modulus (GPa)	Thickness of laminate (mm)
CFRP	$E_x = 62.0$ $E_y = 4.83$ $E_z = 4.83$	$\nu_{xy} = 0.22$ $\nu_{xz} = 0.22$ $\nu_{yz} = 0.30$	760	0.012	$G_{xy} = 3.27$ $G_{xz} = 3.27$ $G_{yz} = 1.86^*$	1.0
GFRP	$E_x = 20.7$ $E_y = 6.89$ $E_z = 6.89$	$\nu_{xy} = 0.26$ $\nu_{xz} = 0.26$ $\nu_{yz} = 0.30$	414	0.02	$G_{xy} = 1.52$ $G_{xz} = 1.52$ $G_{yz} = 2.65^*$	1.3

$^*G_{yz} = \frac{E_{y \text{ or } z}}{2(1+\nu_{yz})}$

2.3.3 Modeling Methodology

By taking advantage of the symmetry of the beams, a quarter of the full-size beam, with proper boundary conditions, is used for modeling. This approach reduces computational time and computer disk space requirements significantly. The steel reinforcement is simplified in the model by ignoring the inclined portions of the steel rebar present in the test beams. As no significant slip between concrete and steel reinforcement was observed in the testing, perfect bond between materials is assumed in this study.

A confined concrete constitutive model is used where the GFRP laminates or loading plate is present. Confinement from the CFRP plates at the bottom of the beams is considered negligible. The confinement near the applied loads (Stevens et al. 1991) also prevents severe element distortion and numerical instability. A number of analyses were performed to determine a proper size for this confined concrete region under the loads. The region was modeled as extending lengthwise a distance "d" from the left and right edges of the loading plate and a depth "d/8" from the bottom of the plate. The width of the confined concrete is equal to the width of the beam. These dimensions are shown in Fig. 2.3(a) and apply to the unstrengthened and flexural-strengthened beams. Confinement from the GFRP was assumed for all concrete elements in the shear and flexural/shear strengthened beam models.

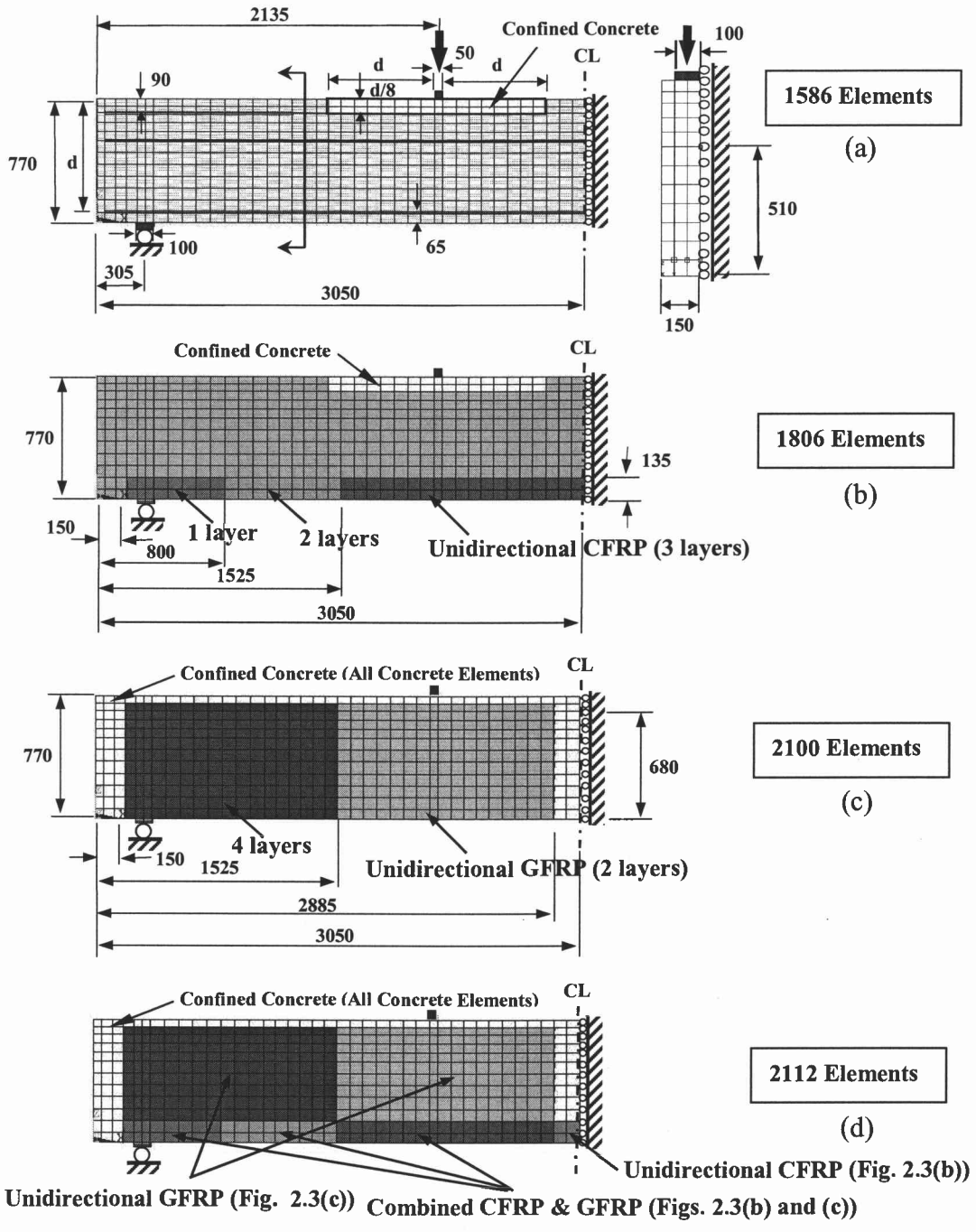

Figure 2.3. Finite Element Models (dimensions shown in mm): (a) Unstrengthened Beam; (b) Flexural- Strengthened Beam; (c) Shear-Strengthened Beam; (d) Flexural/Shear-Strengthened Beam

The various thicknesses from different numbers of layers of the FRP composites create discontinuities, which are not desirable for the FEA; therefore, a consistent thickness of FRP composites is used in the models to avoid discontinuities. The different thicknesses are accounted for by compensating with variations in the elastic and shear moduli in each layer. For example, if the thickness of FRP laminates in the models is doubled compared to the actual thickness on the test beams, the elastic and shear moduli are both reduced by 50%. Since no debonding of FRP laminates was observed in the test beams (except after crushing failure of the shear-strengthened beam), perfect bond between the concrete and FRP laminates is assumed. A convergence study was used to help determine an optimal FE model mesh density. However, element size for the smeared cracking model cannot be less than several times larger than the aggregate size (Bazant 1984); therefore, dimensions (width, length, and height) of concrete elements are approximately equal to 55 mm in this study. Minor modification of dimensions for the FRP reinforcing was made due to geometric constraints from the other elements in the models, i.e. meshing of concrete elements, steel rebar locations and required output locations. Fig. 2.3 shows the FE models for the four beams.

2.3.4 Nonlinear Analysis Approach

Newton-Raphson equilibrium iteration, a series of successive linear approximations with corrections, is used to solve for the nonlinear behaviors of the full-scale beams. Incremental displacement is gradually applied to the beam (displacement-control). Both force and displacement convergence tolerances are properly specified, 0.5% and 1%, respectively. The maximum number of iterations per loading increment is 60.

2.4 COMPARISON OF RESULTS

The experimental beams were tested to the maximum possible load. For the unstrengthened, flexural-strengthened, and shear-strengthened beams, this was the respective beam capacity. However, for the flexural/shear-strengthened beam, the loading was limited by the available testing machine (McCurry 2000).

2.4.1 Load-Strain Plots

Conventional 60 mm resistive strain gauges were placed throughout the experimental beams; i.e., inside the beams on the steel rebar, on the concrete

surface, and on the FRP surface. Comparisons of the load-tensile strain plots from the FE analyses and the experimental data for the #22 steel rebar at midspan are shown in Fig. 2.4.

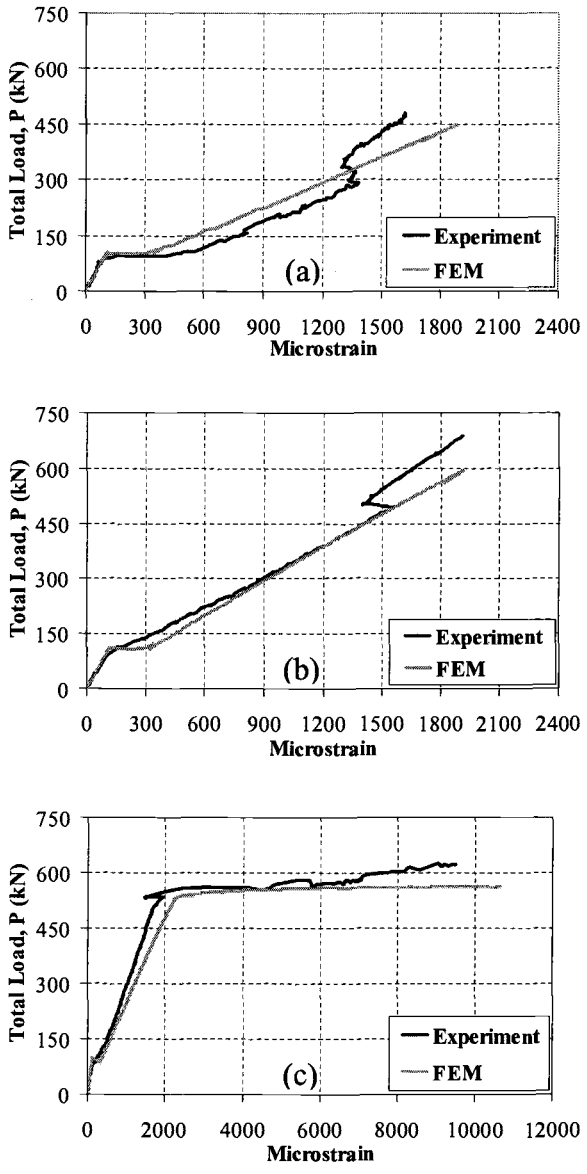

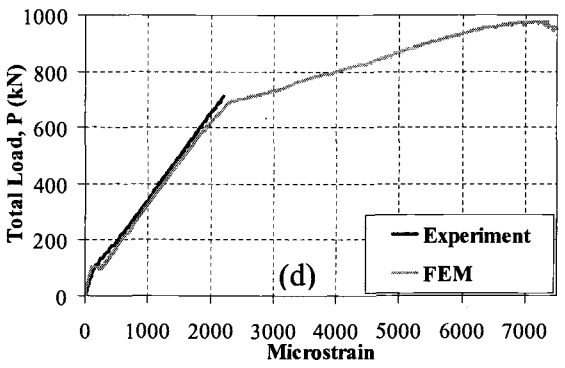

Figure 2.4. Load-Tensile Strain Plots for Main Steel Rebar: (a) Unstrengthened Beam; (b) Flexural-Strengthened Beam; (c) Shear-Strengthened Beam; (d) Flexural/Shear-Strengthened Beam (Experimental beam did not fail)

In both the linear (prior to concrete cracking) and nonlinear ranges, the strains from the FEA correlate very well with those from the experiments. The reversing strain in the control (Fig. 2.4(a)) and flexural-strengthened (Fig. 2.4(b)) experimental beams is most likely a local effect caused by the major cracks close to the midspan. This behavior does not occur in the FE models with smeared cracking.

Comparisons of the load-tensile strain plots for the FRP composites are shown in Fig. 2.5.

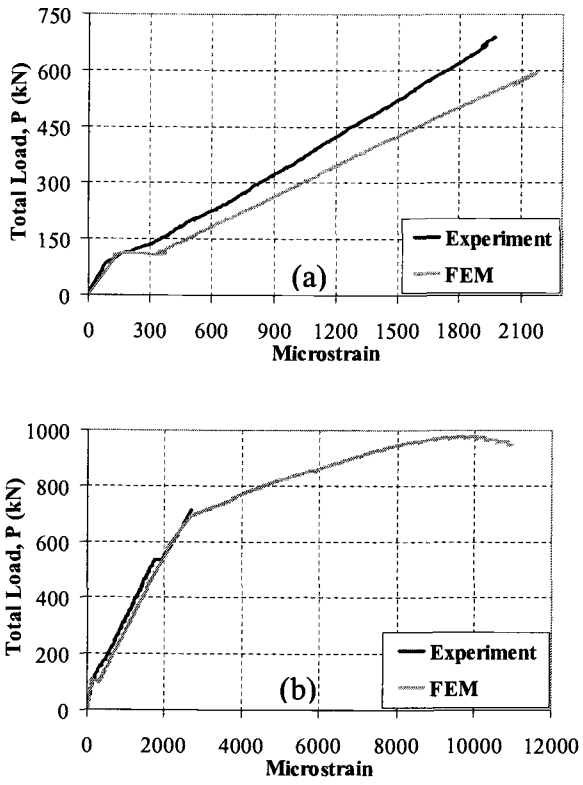

Figure 2.5. Load-Tensile Strain Plots for FRP composites: (a) Flexural-Strengthened Beam; (b) Flexural/Shear- Strengthened Beam (Experimental beam did not fail)

For the flexural-strengthened beam (Fig. 2.5(a)) and the flexural/shear-strengthened beam (Fig. 2.5(b)), experimental strain data were collected at midspan and center of the bottom of the beams on the surface of the CFRP. The load-tensile strain plots show reasonable agreement for the strains from the FEA and the experimental results. Specifically, the measured and predicted CFRP tensile strains at failure of the beam are 1970 and 2180 microstrain, respectively, and the

calculated corresponding stresses equal to 120 and 140 MPa, respectively, for the flexural-strengthened beam. For the flexural/shear-strengthened beam, the maximum predicted strain at the peak load in the CFRP from the FEA is 11000 microstrain. These strains are less than the limiting strain of the CFRP shown in Table 2.2; therefore, the CFRP still behaves linearly. For the experimental flexural-strengthened beam, Figs. 2.4(b) and 2.5(a) show that slip between the concrete and CFRP is not significant. The experimental strain in the CFRP at failure is only 3% higher than the tensile strain in the main steel rebar.

Fig. 2.6 presents a comparison between the load-compressive strain (in concrete) plots collected at midspan at the center of the top face from the experimental beams and the results from the FEA.

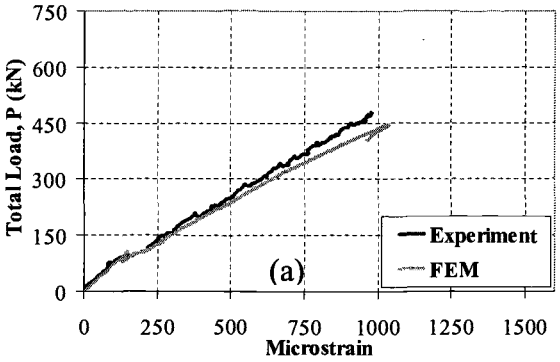

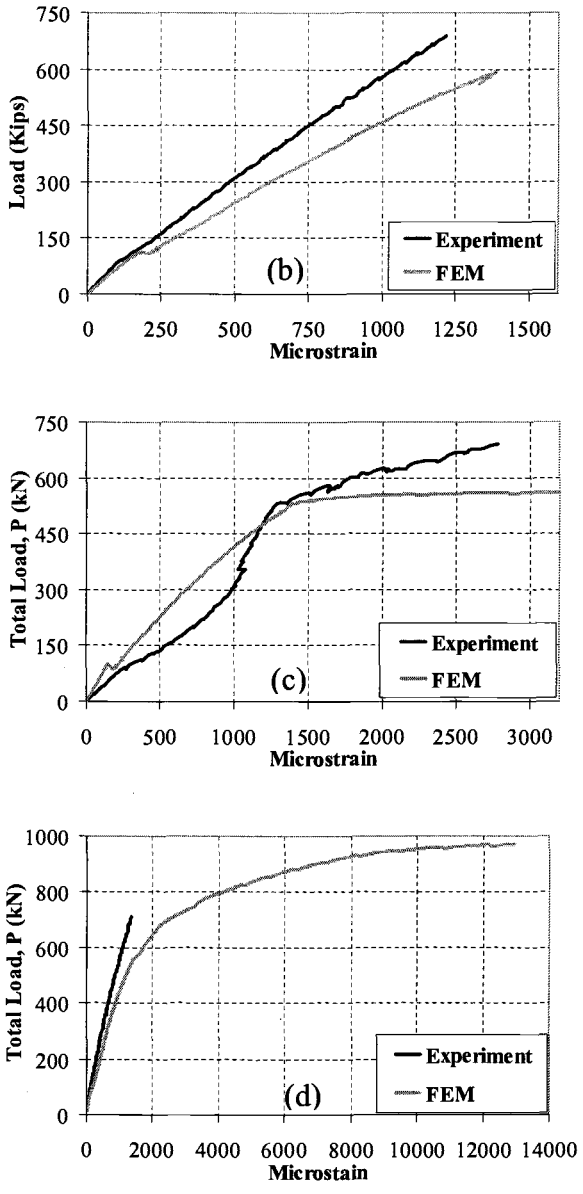

Figure 2.6. Load-Compressive Strain Plots for Concrete: (a) Unstrengthened Beam; (b) Flexural-Strengthened Beam; (c) Shear-Strengthened Beam; (d) Flexural/Shear-Strengthened Beam (Experimental beam did not fail)

For the unstrengthened beam (Fig. 2.6(a)), the load-compressive strain plots from the FEA and the experimental data show good agreement. For the shear-strengthened beam (Fig. 2.6(c)), the load-strain plots from the FE and experimental results are generally comparable. The experimental beam, however, shows unexpected nonlinear behavior for applied loads from 0 to 470 kN, presumably a result of local material imperfections. Cracks occurring at the interfaces between the cement and aggregate due to their differences in elastic modulus, thermal coefficient, and response to changes in moisture content when the concrete is hardened may be the source of the local material imperfections. At about 535 kN, large strains occur in both the FE model and the experimental beam. This load is very close to the yield load of the steel as shown in Fig. 2.4(c). After the yielding of the steel, large concrete strains occur in both the experimental beam and the FE model; however, the slope of the load-compressive strain plot from the experimental data is greater than that from the FEA. The assumption of elastic-perfectly plastic steel in the model causes this difference. Strain hardening occurs in the actual steel bar. For the flexural and flexural/shear strengthened beams, the trends of the FE and the experimental results are generally similar.

2.4.2 Load-Deflection Plots

Direct current differential transducers (DCDTs) were used to collect the deflections at midspan at the center of the bottom face of the experimental beams. Comparisons between load-deflection plots from the experimental results and the FE analyses at the same locations are shown in Fig. 2.7.

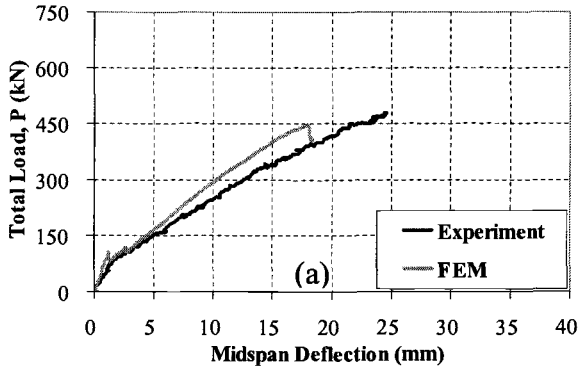

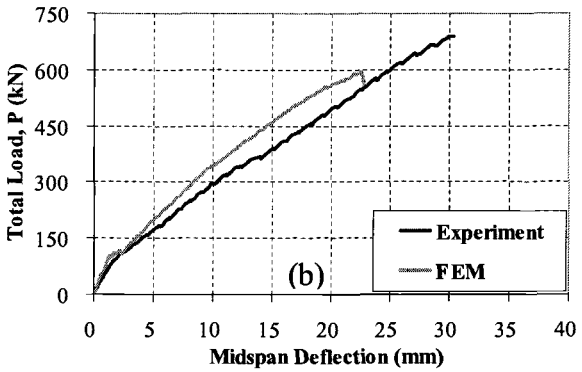

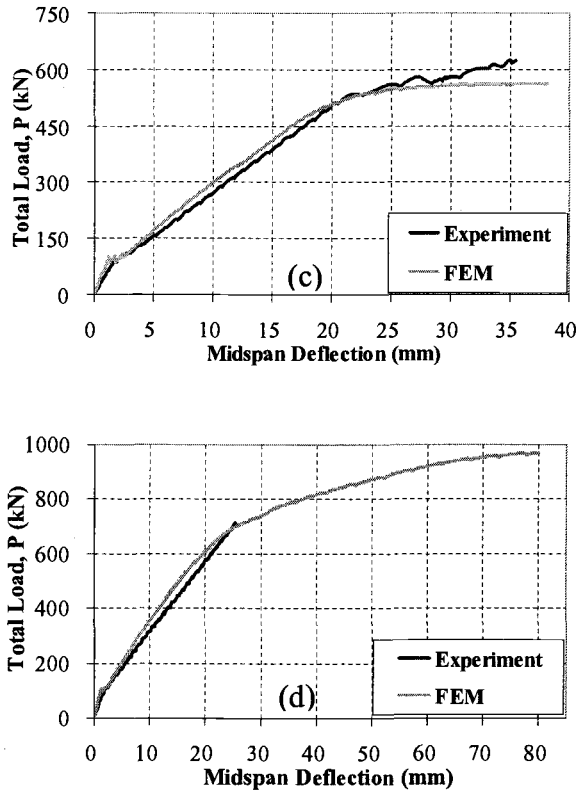

Figure 2.7. Load-Deflection Plots: (a) Unstrengthened Beam; (b) Flexural-Strengthened Beam; (c) Shear-Strengthened Beam; (d) Flexural/Shear-Strengthened Beam (Experimental beam did not fail)

In general, the load-deflection plots for the beams from the FE analyses agree quite well with the experimental data. The FE load-deflection plots in the linear range are somewhat stiffer than the experimental plots. After first cracking, the stiffnesses of the FE models are again higher than those of the experimental beams. There are several effects that may cause the higher stiffnesses in the FE models. First, microcracks are present in the concrete of the experimental beams

prior to loading, and could be produced by drying shrinkage in the concrete and/or handling of the beams. On the other hand, the FE models do not account for the microcracks that reduce the stiffness of the experimental beams. Next, perfect bond between the concrete and steel reinforcing is assumed in the FE analyses, but some slip takes place for the experimental beams. As bond slip occurs, the composite action between the concrete and steel reinforcing is reduced. Thus, the overall stiffness of the experimental beams is expected to be lower than for the FE models (which also generally impose additional constraints on behavior).

2.4.3 Crack Patterns

In the experiment, the failure modes for the beams were as predicted, as shown in Fig. 2.8. Table 2.3 shows comparisons between experimental and predicted ultimate loads

(a)

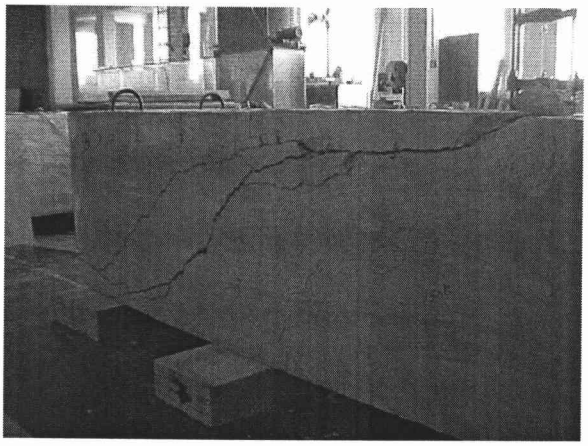

(b)

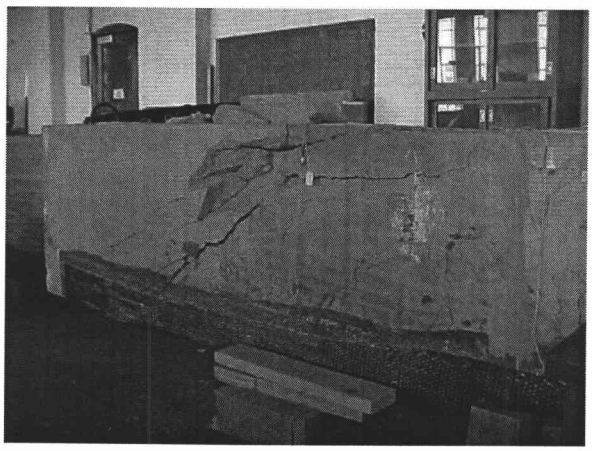

(c)

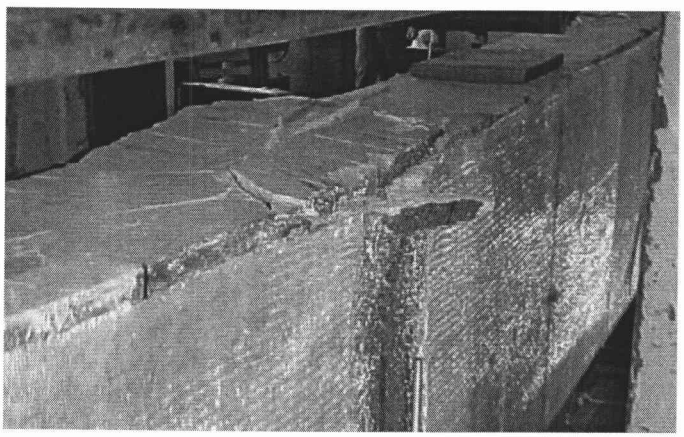

Figure 2.8. Experimental Beams at Failure: (a) Unstrengthened Beam; (b) Flexural-Strengthened Beam; (c) Shear-Strengthened Beam

Table 2.3. Comparisons between Experimental and Predicted Ultimate Loads

Beam	Ultimate load (kN) from experiment, Failure mode (McCurry 2000)	Ultimate load (kN) from FEA	% Difference	Ultimate Load (kN) from hand calculation, Failure mode
Unstrengthened beam	475, Shear	447	-6	292, Shear
Flexural-strengthened beam	690, Shear	594	-14	265, Shear
Shear-strengthened beam	690, Flexure	568	-18	514, Flexure
Flexural/Shear-strengthened beam	N/A	971	N/A	708, Flexure

The unstrengthened and flexural-strengthened beams both failed in shear (Figs. 2.8(a) and (b)), but the flexural-strengthened beam failed at a higher load as shown in Table 2.3. Fig. 2.8(c) shows the shear-strengthened beam that failed in flexure at midspan, with yielding of the steel reinforcing followed by a compression failure at the top of the beam. The flexural/shear-strengthened beam was not loaded to failure due to testing machine capacity limitations. Fig. 2.9 shows evolutions of crack patterns developing in each beam from the FEA results.

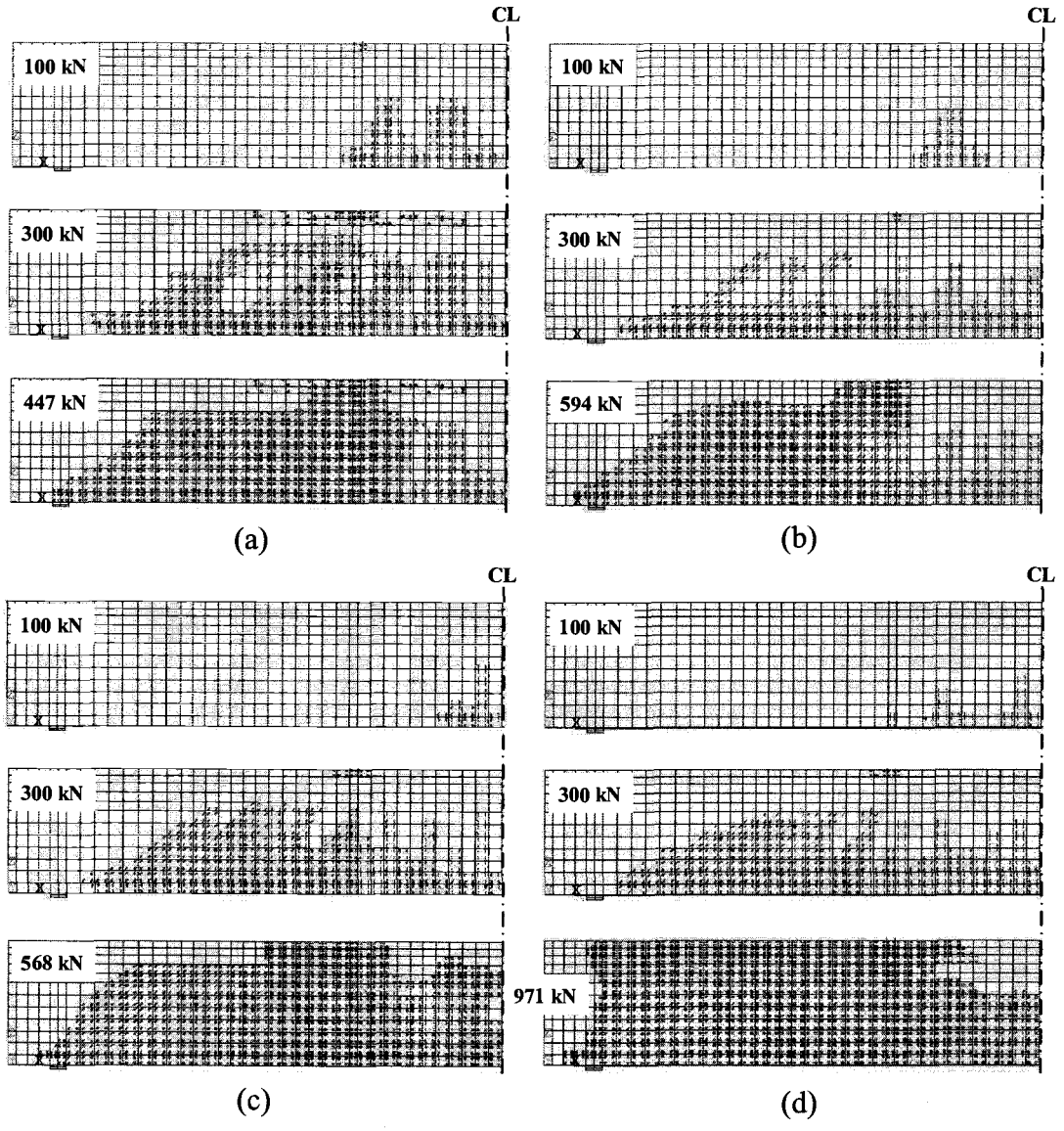

Figure 2.9. Evolution of Crack Patterns: (a) Unstrengthened Beam; (b) Flexural-Strengthened Beam; (c) Shear-Strengthened Beam; (d) Flexural/Shear-Strengthened Beam

The appearance of the cracks reflects the failure modes for the beam models. Crack patterns obtained from the FE analyses at the peak load (Fig. 2.9) and the failure modes of the experimental beams (Fig. 2.8) agree very well. For the FE models of the unstrengthened (Fig. 2.9(a)) and flexural-strengthened beams (Fig. 2.9(b)), smeared cracks spread over the high shear stress region and occur mostly at the ends of the beam from the support extending toward the loading area. FEA accurately predicts that both these beams fail in shear. For the shear-strengthened beam model (Fig. 2.9(c)), numerous cracks occur at midspan and the crack pattern and steel yielding (Fig. 2.4(c)) at the midspan support the experimental results that the beam fails in flexure. Calculations suggested that the experimental flexural/shear-strengthened beam would be limited by the crushing strength of the concrete and fail in flexure (McCurry 2000). The crack pattern at failure predicted by FEA is shown in Fig. 2.9(d). Numerous cracks occur at the top of the beam, and many flexural cracks are observed at the midspan as well. Moreover, the steel at midspan in the model yields as shown in Fig. 2.4(d). These observations support the conclusion that the beam fails in flexure.

2.4.4 Loads at Failure

Table 2.3 shows comparisons between the ultimate loads of the experimental beams and the final loads from the FEA. For the experimental beams,

the ultimate loads were defined where the beams rapidly lost load carrying capacity, and the resulting displacements and strains far exceeded the corresponding range of the instrumentation. The use of displacement control in the FEA allows for the descending portion of the load-deflection relationship to be defined (Figs. 2.7(a) and (b)), to clearly show the capacity of the beams. Models previously analyzed with incremental loading (force control) have an un-converged solution defining failure. It is noteworthy that the descending branch was obtained for shear failure-controlled beams only. For the beams failing in flexure (e.g. shear and flexure/shear strengthened beams), the more ductile beams exceed the displacement criteria tolerance before the descending branch can be traced (Figs. 2.7(c) and (d)).

It is observed that the FE models underestimate the strengths of the beams as anticipated for the following reasons. First, the inclined portions of the steel reinforcement are excluded from the FE models, resulting in a lower load carrying capacity than the actual experimental beams. Additionally, strain hardening in steel is not included in the FE models. This reduction in load carrying capacity is expected, and shown in Fig. 2.7(c). Second, toughening mechanisms at the crack faces; i.e., the grain bridging process, interlocking between the cracked faces, crack tips blunted by voids, and the crack branching process, may also slightly delay the failures of the experimental beams before complete collapse. The FE models do not have these mechanisms. Finally, the assumptions of perfect bond between steel and concrete, and between FRP and concrete increase the stiffness of the beams,

however, they may actually lower the ultimate load-carrying capacity. Stresses occurring at the same load at the same location in the perfect bond models are generally higher than if some slip between materials is included, and may produce premature local failures.

In Table 2.3, the ultimate load for each beam including its failure mode from hand calculations is also included. The hand calculations included beam capacity based on flexure and that based on shear. Lower capacity controls and is defined as the ultimate load. For flexure-based capacity, a simple, direct, and general analytical procedure derived from equilibrium and strain compatibility is employed. Classical flexural failure modes are considered; i.e., compression failure (crushing of the concrete in compression occurs before yielding of the reinforcing steel); tension failure (yielding of the reinforcing steel in tension is followed by concrete crushing); and FRP rupture (yielding of the reinforcing steel in tension is followed by FRP rupture). Basic assumptions in flexure theory are made. For the shear and flexure/shear strengthened beams, GFRP contribution to flexural capacity is not taken into account. For shear-based capacity, the simplified shear strength from ACI 318 (2002) is used. For the unstrengthened and flexure strengthened beams, only the concrete contribution to shear capacity is considered. For the shear and flexure/shear strengthened beams, a modified method (Kachlakev 1998) based on a conservative strain limit is used. It is also assumed that there is no CFRP contribution to shear capacity in the flexure/shear strengthened beam.

2.5 CONCLUSIONS

The general behaviors of the FE models show very good agreement with observations and data from the full-scale beam tests. The load-strain plots showing local behavior at selected locations from the FEA in general show good agreement to the experimental data. The load-deflection plots at midspan from the FE models have similar trends with those from the experimental beams, but the FE models are slightly stiffer than the experimental beams both in the linear and nonlinear ranges. The effects of bond slip (between the concrete and steel reinforcing) and microcracks occurring in the actual beams were excluded in the FE models and resulted in the higher stiffnesses of the FE models. The crack patterns at the final loads from the FE models correspond well with the failure modes of the experimental beams. The final loads from the FE analyses are lower than the experimental ultimate loads by 6%-18%. The three-dimensional cracking FE models presented in this study demonstrate the behaviors of the full-scale beams and provide additional large-scale test results and a better understanding of the FRP-strengthened concrete beams. Knowledge gained from this paper can be used to conservatively estimate load-carrying capacity of FRP-reinforced concrete beams using FE models. The FEM models can be used in further studies to develop design rules for strengthening reinforced concrete members using FRP.

ACKNOWLEDGMENTS

This research was supported by the Oregon Department of Transportation (ODOT), Salem, OR and the Department of Civil, Construction, and Environmental Engineering, Oregon State University, Corvallis, OR.

REFERENCES

ACI 318-02, American Concrete Institute. (2002). *Building Code Requirements for Reinforced Concrete*. American Concrete Institute, Farmington Hills, Michigan.

ACI 440, American Concrete Institute. (2002). *Guide for the Design and Construction of Externally Bonded FRP Systems for Strengthening Concrete Structures*. American Concrete Institute, Farmington Hills, Michigan.

American Society for Testing and Materials (ASTM) Subcommittee C09.70. (1994). *Standard Test Method for Static Modulus of Elasticity and Poisson's Ratio of Concrete in Compression*, Designation C 469-94, ASTM, West Conshohocken, Pennsylvania.

ANSYS. (1998). *ANSYS User's Manual Revision 5.5*. ANSYS, Inc., Canonsburg, Pennsylvania.

Balakrishnan, S., and Murray, D.W. (1988). "Concrete Constitutive Model for NLFE Analysis of Structures." *Journal Struct. Engrg.*, ASCE, 114(7), 1449-1466.

Bangash, M.Y.H. (1989). *Concrete and Concrete Structures: Numerical Modeling and Applications*. Elsevier Science Publishers, LTD., Essex, England.

Barnard, P.R. (1964). "Researches into the Complete Stress-Strain Curve for Concrete." *Magazine of Concrete Research*, 16(49), 203-210.

Bazant, Z. P. (1984). "Mechanics of Fracture and Progressive Cracking in Concrete Structures." *Fracture Mechanics of Concrete*, edited by Sih, G. C. and Tommase, A. D., Martinus Nijhoff, Dordrecht.

Bhatt, P., and Kader, M.A. (1998). "Prediction of Shear Strength of Reinforced Concrete Beams by Nonlinear Finite Element Analysis." *Computers and Struct.*, 68, 139-155.

Desayi, P. and Krishnan, S. (1964). "Equation for the Stress-Strain Curve of Concrete." *Journal of the American Concrete Inst.*, 61, 345-350.

Isenburg, J. (1993). *Finite Element Analysis of Reinforced Concrete Structures II.* ASCE, New York, New York.

Kachlakev, D. I. (1998). "Strengthening Bridges Using Composite Materials." *FHWA Report No. OR-RD-98-08*, Salem, Oregon.

Kemp, A.R. (1998). "The Achievement of Ductility in Reinforced Concrete Beams." *Magazine of Concrete Research*, 50(2), 123-132.

Kent, D.C., and Park, R. (1971). "Flexural Members with Confined Concrete." *Journal Struct. Div.*, ASCE, 97(7), 1969-1990.

Malek, A. M., Saadatmanesh, H., and Ehsani M. R. (1998). "Prediction of Failure Load of R/C Beams Strengthened with FRP Plate Due to Stress Concentration at the Plate End." *ACI Structural Journal*, 95(1), 142-152.

McCurry, D., Jr. (2000). "Strengthening of Reinforced Concrete Beam Using FRP Composite Fabrics: Full-Scale Experimental Studies and Design Concept Verification." *MS Thesis*, Oregon State University, Corvallis, Oregon.

Nilson, A. H. (1968). "Nonlinear Analysis of Reinforced Concrete by the Finite Element Method." *Journal of the American Concrete Inst.*, 65(9), 757-766.

Ross, C. A., Jerome D. M., Tedesco J. W., and Hughes M. L. (1999). "Strengthening of Reinforced Concrete Beams with Externally Bonded Composite Laminates." *ACI Structural Journal*, 96(2), 212-220.

Samaan, M., Mirmiran, A., and Shahawy, M. (1998). "Model of Concrete Confined by Fiber Composites." *Journal Struct. Engrg.*, ASCE, 124(9), 1025-1031.

Stevens, N.J., Uzumeri, S.M., Collins, M.P., and Will, T.G. (1991). "Constitutive Model for Reinforced Concrete Finite Element Analysis." *ACI Structural Journal*, 88(1), 49-59.

Suidan, M. and Schnobrich, W. C. (1973). "Finite Element Analysis of Reinforced Concrete." *Journal of the Structural Division*, ASCE, ST10, 2109-2122.

Tedesco, J. W., Stallings J. M., El-Mihilmy, M., and McCauley, M. (1996). "Rehabilitation of Concrete Bridges Using FRP Laminates." 4th Materials Conference, "Materials for the New Millennium," editor K. Chong, American Society of Civil Engineers, Washington, D. C.

Teng, J.G., Chen, J.F., Smith, S.T., and Lam, L. (2001). *FRP Strengthened RC Structures*. John Wiley & Sons, Ltd, West Sussex, England.

Wang, P.T., Shah, S.P., and Naaman, A.E. (1978). "Stress-Strain Curves of Normal and Lightweight Concrete in Compression." *Journal of ACI*, 75(11), 603-611.

William, K. J. and Warnke, E. P. (1975). "Constitutive Model for the Triaxial Behavior of Concrete." *Proceedings, International Association for Bridge and Structural Engineering*, Vol. 19, ISMES, Bergamo, Italy, 174-190.

NOTATION

CL	=	centerline of the beams
E_0	=	initial modulus of elasticity of concrete (MPa)
E_1	=	slope of descending branch of FRP-confined concrete (MPa)
E_s	=	elastic modulus of steel reinforcement (MPa)
E_x, E_y, E_z	=	elastic moduli of FRP composites in the x (fiber direction), y, and z directions (MPa)
f_r	=	ultimate tensile strength (modulus of rupture) of concrete (MPa)
f_y	=	yield stress of steel reinforcement (MPa)
f'_c	=	ultimate compressive strength of concrete (MPa)
G_{xy}, G_{xz}, G_{yz}	=	shear modulus of FRP composites for the xy, xz, and yz planes (MPa)
P	=	total applied load (kN)
β_t	=	shear transfer coefficient
ε	=	strain in concrete
ε_y	=	yield strain of steel reinforcement
ε'_0	=	compressive strain at ultimate compressive strength of concrete
σ	=	stress in concrete (MPa)
υ	=	Poisson's ratio
υ_{xy}, υ_{xz}, υ_{yz}	=	major Poisson's ratios of FRP composites for the xy, xz, and yz planes

CHAPTER 3: NLFE ANALYSIS OF AN FRP-STRENGTHENED REINFORCED CONCRETE BRIDGE. I: MODELING AND EXPERIMENTAL CALIBRATION

by Kasidit Chansawat, Solomon C.S. Yim, Member, ASCE,
and Thomas H. Miller, Member, ASCE

ABSTRACT

Three-dimensional finite element models are developed to examine the structural behavior of the Horsetail Creek Bridge strengthened by fiber-reinforced polymers (FRP). Nonlinear finite element (NLFE) analysis is performed using ANSYS, a general-purpose finite element program. SOLID65, LINK8, SOLID46, MATRIX27 and SHELL143 elements represent concrete, discrete reinforcing steel bars, FRP laminates, and soil-structure interaction, respectively. Nonlinear material properties are defined for the first two types of elements. Truck loadings are applied to the FE bridge model at different locations, as in an actual bridge test. A sensitivity study is performed varying bridge geometry, pre-cracking load, strength of concrete, and stiffness of the soil foundation. Comparisons between ANSYS predictions and field data are made in terms of strains in the beams for various truck load locations. The effects of varying the parameters are discussed. It is found that all the parameters can potentially influence the bridge response and are needed for selection of an FE model that best represents the actual bridge

conditions. The proposed FE bridge model predicts the magnitudes and trends in the strains accurately.

3.1 INTRODUCTION

3.1.1 Overview

Many bridges in the US are in need of strengthening, because of an increase in loading, a change in use, or corrosion. The Horsetail Creek (HC) bridge in Oregon is an example of a bridge that was classified as structurally deficient, and was not designed to carry the traffic loads that are common today. The bridge was rated and found to have only 6% of the required shear capacity for the transverse beams and only 34% for the longitudinal beams, due to the absence of shear stirrups. Moreover, the transverse beam had only approximately 50% of the required flexural capacity (CH2M 1997). Some exposed, corroded reinforcing steel was also found during on-site inspection. However, the overall condition of the structure was generally good.

The strengthening approach used was to increase the load-carrying capacity of the bridge with fiber-reinforced polymer (FRP) materials. FRP sheets were laminated to both transverse and longitudinal beams to address deficiencies in shear and flexural capacities. In the case of the transverse beams, both shear and flexural strengthening were required, while only shear strengthening was needed for the

longitudinal beams. Specifically, CFRP (Carbon-FRP) flexural and GFRP (Glass-FRP) shear laminates were attached at the bottom and at the sides of the transverse beams, respectively, while only GFRP laminates were attached at the sides of the longitudinal beams. In general, these FRP materials were relatively easy to install, and a cost-effective upgrade for the bridge.

3.1.2 The Horsetail Creek Bridge

The Horsetail Creek Bridge was built in 1914. It is located in the Columbia Gorge on the Columbia River Highway, 50 kilometers east of Portland, Oregon. The bridge, with spread footing foundations, is 18.28 m. (60 ft.) long and 7.32 m. (24 ft.) wide. It has three 6.10-m. (20-foot) spans across the Horsetail Creek. The FRP rehabilitation to correct the structural deficiencies was completed in 1998.

3.1.3 Strength of In-Situ Concrete

The actual strength of in-situ concrete is an important parameter to be defined in FE models of RC structures to obtain accurate solutions. Core sample testing can be performed to examine the actual concrete strength. However, it was not available for the historic structure. Pulse-velocity tests were, then, conducted

instead to provide estimates of the material properties of the in-situ concrete. A PUNDIT6 test instrument was used with the direct transmission method (Malhotra and Carino 1991), and performed on various structural and non-structural portions of the bridge. The range of measured in-situ concrete strength based on the pulse velocity measurements is between 25.9 MPa (3750 psi) and 32.1 MPa (4650 psi). It should be noted that to conservatively evaluate the strength of the HC bridge before and after the FRP retrofitting, a 17.2 MPa (2500 psi) compressive strength of concrete was first assumed, which complies with AASHTO bridge rating recommendations for all bridges built prior to 1959 (AASHTO 1994). The actual compressive strength of the concrete (and modulus of elasticity) is most likely substantially higher than the value used in the initial FE model, due to strength gains over time and the conservative nature of these estimates.

The sensitivity study performed here will strongly suggest that the actual concrete strength be within the range of 25.9 MPa to 32.1 MPa based on the pulse velocity measurements, and higher than that recommended by AASHTO, as expected.

3.1.4 Foundation Modeling

Foundation rigidity can make a large difference in the distribution of forces throughout a bridge structure. Continuous structures (e.g. the HC bridge) can be

very effective at redistributing forces, but they are also very sensitive to support conditions and foundation stiffnesses (Hambly 1991). In addition, differential settlement of supports can induce significant bending in continuous structures. As a result, realistic soil-structure interface modeling is needed.

Due to a lack of specific geotechnical data for the bridge and locations nearby, geologic maps of the area were examined. The HC bridge is topographically located between 122° 02' 30" – 122° 05' 00" longitude and 45° 35' – 45° 36' latitude. This area is a transition zone of Grande Ronde basalt bedrock and lacustrine and fluvial sedimentary rocks (Walker and MacLeod 1991). The topographic location and geological properties of soil foundation of the bridge are shown in Appendix B. From Phillips (1987), it is a transition zone of Grande Ronde basalt and talus deposits (rubble deposits on steep slopes and below rockfalls; consists of Columbia River basalt clasts forming talus cones below cliffs). Both maps show the bridge location in a zone of basalt bedrock. It was also observed in the field that the Horsetail Creek's bed, on which the bridge footings are standing, is covered primarily by basalt.

Basalt is an igneous rock formed when hot molten silicate material from within the earth's crust solidifies. E_{basalt} can range between 20 GPa (2.8×10^6 psi) and 110 GPa (16×10^6 psi), and Poisson's ratio ranges between 0.14 and 0.25 (Jumikis 1983).

3.2 MODELING METHODOLOGY AND NONLINEAR ANALYSIS APPROACH

In this paper, fully three-dimensional finite element bridge models are developed for the HC bridge strengthened with FRP laminates. Modeling methodology and nonlinear analysis approach in ANSYS are presented. To calibrate the FE models to best represent the actual bridge conditions, bridge experiments were conducted, and a sensitivity study performed. The details of the experiments will be presented later. The results from the FE bridge model are compared with the field test data in terms of strains on both the transverse and the longitudinal beams versus various truck load locations on the bridge deck. In addition, influences of the parameters on structural behaviors are discussed.

3.2.1 Concrete

The SOLID65, 3-D reinforced concrete solid element, is used to represent concrete in the models. The element, using a $2 \times 2 \times 2$ Gaussian set of integration points, is defined by eight nodes having three degrees of freedom at each node: translations in the nodal x, y, and z directions. This element is capable of cracking in tension and crushing in compression. Cracking is treated as a "smeared band" of cracks in ANSYS, rather than discrete cracks, and can occur on up to three different

planes at an integration point of the element once stresses in the concrete exceed the tensile strength of the material. For the modeling of crushing, the material is assumed to crush if all principal stresses are in compression, when the material at an integration point fails in uniaxial, biaxial, or triaxial compression (ANSYS 1998). At this point, the material can no longer contribute to the stiffness/strength of the structure. Consequently, when crushing occurs, the local stiffness significantly reduces, which, in turn, may lead to a "rapid collapse" in the FE simulation. In order to avoid such an undesired (numerical, but non-physical) behavior, the crushing capability of the SOLID65 element is not employed in this study. This element can also model concrete with or without reinforcing bars. If the rebar capability is used, the bars will be smeared throughout the element. Nevertheless, in this study a discrete bar element is used instead of the smeared reinforcing approach.

The most important aspect of the SOLID65 element here is the treatment of nonlinear material properties. The responses of concrete under loading (with and without confinement due to lateral ties in the columns and FRP jackets on the beams) are characterized by distinctly nonlinear behaviors. Complete stress-strain curves for both unconfined and confined concrete are needed to accurately predict failure and post-failure behavior. However, in this research a service loading was applied in the bridge test. The concrete compressive stress was still low and within the ascending branch of the stress-strain curves for both unconfined and confined concrete. As a result, only the equations for the ascending branch are discussed

here. Part II of this paper presents a performance evaluation of the bridge (Chansawat et al. 2002b) and will discuss the complete curves, as they are important to predict the strength of the RC structures. Moreover, a finite element study of full-scale beams replicating the transverse members of the bridge before and after FRP repair was performed. Chansawat et al. (2002a) also discusses the complete relationships and examines effects of confinement of concrete in beams.

3.2.1.1 Unconfined Concrete

Wang et al. (1978) and Bangash (1989) have developed expressions for stress-strain relationships of unconfined concrete.

In this study the constitutive model for unconfined concrete in compression follows Desayi and Krishnan's model (Bangash 1989):

$$\sigma = \frac{E_0 \epsilon}{1 + \left(\frac{\epsilon}{\epsilon'_0}\right)^2} \qquad [3.1]$$

in which

$$\epsilon'_0 = 2\frac{f'_c}{E_0} \qquad [3.2]$$

and

$$E_0 = 4733\sqrt{f'_c}\ \text{[MPa]} = 57000\sqrt{f'_c}\ \text{[psi]}\ \text{(ACI 2002)} \qquad [3.3]$$

3.2.1.2 Confined Concrete

Concrete confinement occurs when concrete under compression experiences lateral dilation due to Poisson's effect, increases in volume due to progressive internal cracking, and bears against the transverse reinforcement (e.g., rectangular ties or FRP jacket), which, then, applies a confining reaction to the concrete (Kent and Park 1971). In this study, confined concrete can be divided into two types as follows:

Rectangular ties-confined concrete: In general, the degree of confinement in columns with steel ties depends on the amount and spacing of steel, yield strength of steel, tie configuration, area of concrete core, concrete compressive strength, and longitudinal reinforcement. Many analytical models for the compressive stress-strain behavior of concrete confined by rectangular ties have been developed to express the increase in strength and ductility (Park et al. 1982 and Mander et al. 1988).

In this study, a model (Park et al. 1982) is used as follows:

$$f_c = Kf'_c\left[\frac{2\varepsilon_c}{0.002K} - \left(\frac{\varepsilon_c}{0.002K}\right)^2\right] \qquad [3.4]$$

in which

$$K = 1 + \frac{\rho_s f_{yt}}{f'_c} \qquad [3.5]$$

The maximum stress is assumed to be Kf'_c at a strain of $\varepsilon_0 = 0.002K$. This is a modified form of the model of Kent and Park (1971). It improves the original Kent and Park model by taking the enhancement in the concrete strength due to

confinement into account, and was especially developed for rectangular columns with rectangular hoop steel. The columns of the HC bridge are of this type of configuration.

FRP-confined concrete: Similar to confinement in columns, concrete in beams which is restrained (due to closely spaced steel stirrups, FRP encasement, or even a localized effect of an applied concentrated load) in the direction normal to the applied stress may be considered as confined concrete. This confinement enhances strength and ductility. A number of researchers have developed stress-strain relationships for concrete confined by steel stirrups in beams (Balakrishnan and Murray 1988 and Kemp 1998). However, we found no evidence of investigations of stress-strain relationships for FRP-confined concrete in flexural members. Researchers have focused on FRP confinement in columns (Teng et al. 2001). Thus, for simplicity and sufficient accuracy, as presented in Chansawat et al. (2002a), it is assumed that in beams the behavior of FRP-confined concrete is similar to that of stirrup-confined concrete. The approaches of Kent and Park (1971) and Bhatt and Kader (1998) are used. This approach assumes that the confinement has no effect on the slope of the ascending part of the stress-strain curve and the maximum flexural stress achieved by both unconfined and confined concrete is the same and equal to f'_c. Based on this approach, the confinement for beams affects only the descending branch of the stress-strain curve to show more ductility.

The concrete is assumed to behave linearly in compression up to 30 percent of the compressive strength. In the constitutive model for concrete under uniaxial tension, the material is assumed to be linearly elastic with modulus E_0 up to the tensile strength, f_r, which can be calculated, based on ACI (2002):

$$f_r = 0.623\sqrt{f_c'}\ (\text{MPa}) \ = 7.5\sqrt{f_c'}\ (\text{psi}) \qquad [3.6]$$

Typical stress-strain curves for both unconfined and confined concrete are shown in Fig. 3.1(a).

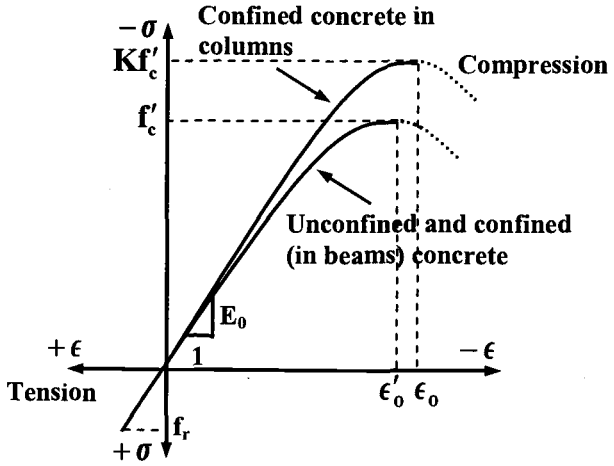

Concrete parameter	Concrete Strength, f'_c (MPa)					
	17.24	22.06	27.58	31.03	32.41	37.23
K	1.109	1.085	1.068	1.061	1.058	1.051
f_r (MPa)	2.59	2.93	3.27	3.47	3.55	3.80
E_0 (GPa)	19.65	22.23	24.86	26.36	26.94	28.88
ε'_0	0.0018	0.002	0.0022	0.0024	0.0024	0.0026
ε_0	0.0022	0.0022	0.0021	0.0021	0.0021	0.00210

(a)

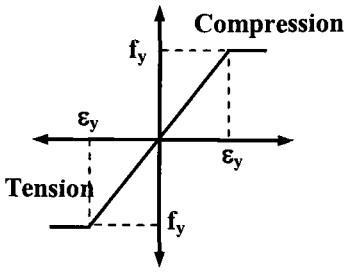

(b)

Figure 3.1. Typical Stress-Strain Curves: (a) Concrete and Parameter Values; (b) Reinforcing Steel

3.2.2 Reinforcing Steel

The LINK8, 3-D spar element, is used to represent the reinforcing steel. It is a uniaxial tension-compression element that can also include nonlinear material properties. The element has two nodes with three degrees of freedom at each node.

For monotonic uniaxial loading, four methods can be used to represent the stress-strain relationship for the steel bar; i.e., elastic-perfectly plastic, elastic strain hardening, tri-linear stress-strain, and a complete stress-strain curve. Of the four methods, the elastic-perfectly plastic representation is most often selected (Isenberg 1993) and is used in this study (Fig. 3.1(b)).

3.2.3 FRP

The SOLID46, 3-D layered structural solid element, is used to represent the FRP materials. The element has eight nodes with three degrees of freedom at each node. Layer thickness, layer material direction angles, and orthotropic material properties also need to be defined. No slippage is assumed between the element layers (perfect interlaminate bond).

FRP laminates are considered brittle materials, and the stress-strain relationship is roughly linear up to failure. In addition, for the service loading applied in the bridge test, tensile stresses in the FRP elements are far lower than

their ultimate strengths. Consequently, in this study it is assumed that the stress-strain relationships for the FRP laminates are linearly elastic.

3.2.4 Soil-Structure Interface Modeling

Two types of ANSYS elements are used for modeling the soil-structure interaction: MATRIX27 and SHELL143. MATRIX27 is an arbitrary element whose stiffness is specified in this study. The element is defined by two nodes having six degrees of freedom at each node: translations in the nodal x, y, and z directions and rotations about the nodal x, y, and z axes. The element, with a defined stiffness for each degree of freedom, can serve as a multi-directional spring-like element, which is used to represent the foundation. SHELL143, a 4-node, plastic, small strain shell element, is used to model the "base plate" under the columns and the end abutments. This "base plate" connects the bridge structure model and the MATRIX27 elements together. The element has four nodes having six degrees of freedom at each node. Having the same degrees of freedom at each node enables connections to MATRIX27 elements. The stiffness of the "base plate" must be large enough to reduce the stress concentration effect at the MATRIX27 element placed at the center bottom of the column to represent the bridge footing on the supporting soil.

The shallow footing foundations on basalt bedrock are considered as linear-elastic springs (Jumikis 1983). These stiffnesses are derived based on the theory of an elastic half-space found in Poulos and Davis (1973), Whiteman and Richart (1967), and Hambly (1991). Stiffnesses used in this study from Whiteman and Richart (1967) are as follows:

$$K_z = \frac{G_s}{1-\nu_s}\beta_z\sqrt{bd} \qquad [3.7]$$

$$K_x = 2(1+\nu_s)G_s\beta_x\sqrt{bd} \qquad [3.8]$$

$$K_y = 2(1+\nu_s)G_s\beta_y\sqrt{bd} \qquad [3.9]$$

$$K_{mx} = \left(\frac{G_s}{1-\nu_s}\right)\beta_{mx}bd^2 \qquad [3.10]$$

$$K_{my} = \left(\frac{G_s}{1-\nu_s}\right)\beta_{my}bd^2 \qquad [3.11]$$

in which

$$G_s = \frac{E_{soil}}{2(1+\nu_s)} \qquad [3.12]$$

The coefficients β_z, β_x, β_y, β_{mx}, and β_{my} can be found in that reference. Stiffnesses will be defined for the MATRIX27 element at each degree of freedom. Torsional stiffness (rotational stiffness about vertical axis) is not defined, as no unbalanced horizontal forces are applied in the bridge test. Unlike the shear modulus, G_s, or Young's modulus, E_s, Poisson's ratio, ν_s, insignificantly affects the spring constants for the rigid base resting on an elastic half-space (Whiteman and Richart 1967). Soil-structure interface models, including the length and width of the footings (b and d), are shown in Fig. 3.2.

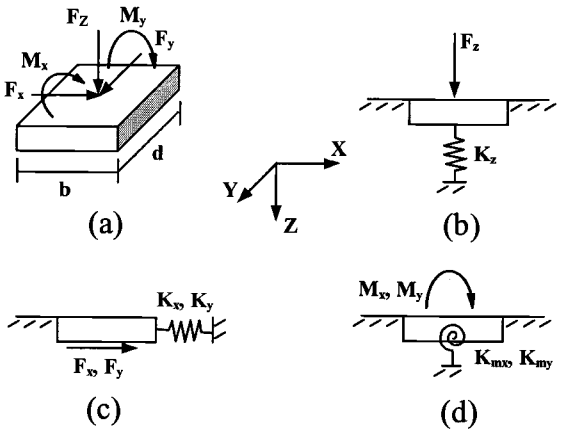

Footing location	Footing Dimensions (m)	
	Length (b)	Width (d)
Middle columns	1.52	1.52
East and west columns	1.52	1.37
West wall	5.79	0.30

Figure 3.2. Soil-Structure Interface Modeling (Hambly 1991): (a) Foundation Geometry; (b) Vertical Stiffness; (c) Horizontal Stiffness; (d) Rotational Stiffness

A summary of the material properties used for each component in the FE bridge model is shown in Table 3.1.

Table 3.1. Material Properties

Type of material	Material Properties				
	ν	E MPa (psi)	G MPa (psi)	Strength MPa (psi)	Thickness mm (in)
(1)	(2)	(3)	(4)	(5)	(6)
Concrete	0.2	19700 - 28900 (2.85E+06 - 4.19E+06)	- -	17.2 - 37.2 (2500 - 5400)	- -
Reinforcing steel	0.3	200000 (29000000)	- -	f_y = 276* (40000*)	- -
CFRP laminate	ν_{12} = 0.216 ν_{13} = 0.216 ν_{23} = 0.3*	E_{11} = 62100 (9000000) E_{22} = 4830* (700000) E_{33} = 4830* (700000)	G_{12} = 3270* (473700) G_{13} = 3270* (473700) G_{23} = 1860** (270000)	$\sigma_{ult(ten.)}$ = 958* (139000)	1.1* (0.042)
GFRP laminate	ν_{12} = 0.216 ν_{13} = 0.216 ν_{23} = 0.3*	E_{11} = 20700 (3000000) E_{22} = 6900* (1000000) E_{33} = 6900* (1000000)	G_{12} = 1520* (220000) G_{13} = 1520* (220000) G_{23} = 2650** (385000)	$\sigma_{ult(ten.)}$ = 600* (87000)	1.3* (0.052)
Soil	0.25***	100 - 19600***	- -	- -	- -
Base plate	0.3	2.07E+11	- -	- -	25.4 (1.0)

Notes: * Kachlakev and McCurry (2000)

** $G_{23} = \frac{E_2}{2(1+\upsilon_{23})}$

***Jumikis (1983) and Hambly (1991)

3.2.5 Nonlinear Analysis Approach

The nonlinear behavior of the structures under loading is caused not only by the transition of concrete from an uncracked to cracked state, but also by the nonlinear material properties of concrete in compression and steel as it yields.

Newton-Raphson equilibrium iteration, a series of successive linear approximations with corrections, is used to solve the nonlinear problem.

For the nonlinear analysis, the load must be increased gradually to avoid non-convergence. Tolerances in both force and displacement criteria may have to be gradually increased along the loading history to avoid a diverged solution. In this study, the maximum force and displacement convergence tolerances are 0.5% and 1%, respectively. The maximum number of iterations per loading increment is 50.

3.2.6 Analysis Assumptions

The following are the general analysis assumptions made for the HC bridge models in this study to provide reasonably good simulations for the complex behavior:

a) The bonds between each element/material type are assumed perfect; that is, there is no slippage between concrete and reinforcing steel bars, between concrete and FRP laminates, and between different FRP layers. Unless the failure mode of a structure involves a bond failure, the perfect bond assumption used in the structural modeling will not cause a significant error in the predicted load-deflection response (Isenberg 1993).

b) Poisson's ratio is assumed to be constant throughout the loading history.

c) The shear transfer coefficients for closed and open cracks in the SOLID65 element are assumed to be 1.0 and 0.2, respectively. The coefficients defined for the concrete element represent shear strength reduction factors when cracks occur. Values range from 0.0 to 1.0. A value of 0.0 refers to a smooth crack, while 1.0 refers to a rough crack. These factors are used to determine how much shear force can be transferred across open or closed cracks. For closed cracks, β is always assumed to equal 1.0. However, for an open crack, β varies from 0.05 to 0.5 (Bangash 1989). A value of 0.0 for β must be avoided to prevent numerical difficulties. In this study, a β-value of 0.2 for open cracks is used. This value is selected based on results in Chansawat et al. (2002a).

d) The concrete is assumed to be isotropic prior to cracking and orthotropic after cracking (ANSYS 1998 and Isenberg 1993). The steel is assumed to be isotropic. The FRP material is assumed to be specially orthotropic-transversely isotropic. That is, the material properties in the two directions that are both perpendicular to the fiber direction are identical.

e) No failure occurs at the soil foundation.

f) Time-dependent nonlinearities such as creep, shrinkage, and temperature change are not included in this study.

3.3 HC BRIDGE EXPERIMENT AND FE MODELING

3.3.1 Loading Conditions and Field Data

Field test data for the bridge were provided by the Oregon Department of Transportation (ODOT). The tests involved two different truck loading levels applied along the centerline of the bridge deck; i.e., empty and full truck loads. Strain data were collected for seven locations of the truck for both load levels. Fiber optic sensors were attached on both the concrete and FRP laminates on the bottom and on the sides of the beams to measure strains occurring from the truck load tests. They were located on one transverse beam and one longitudinal beam of the bridge. The field test data were collected after FRP strengthening.

In this paper, based on the full truck load, only the strain at the center bottom fiber of the concrete for the transverse beam at midspan (TC) (T–transverse beam and C–at center), and the strains at the center bottom fiber of the concrete for the longitudinal beam at various locations (LE, LC, and LW) (L–longitudinal beam; and E, C, and W–at east, center, and west sides, respectively) are examined. The positions of the truck defined by the distance of the front axle of the truck from the east end of the bridge are shown in Fig. 3.3(a). Note that the truck is shown only at positions 1 and 7. The locations of both the transverse and the longitudinal beams, on which the fiber optic sensors are attached, are shown in Figs. 3.3(a) and (b) (shaded area). The configuration of the dump truck used in the selected test, including the axle weights, is shown in Fig. 3.3(c).

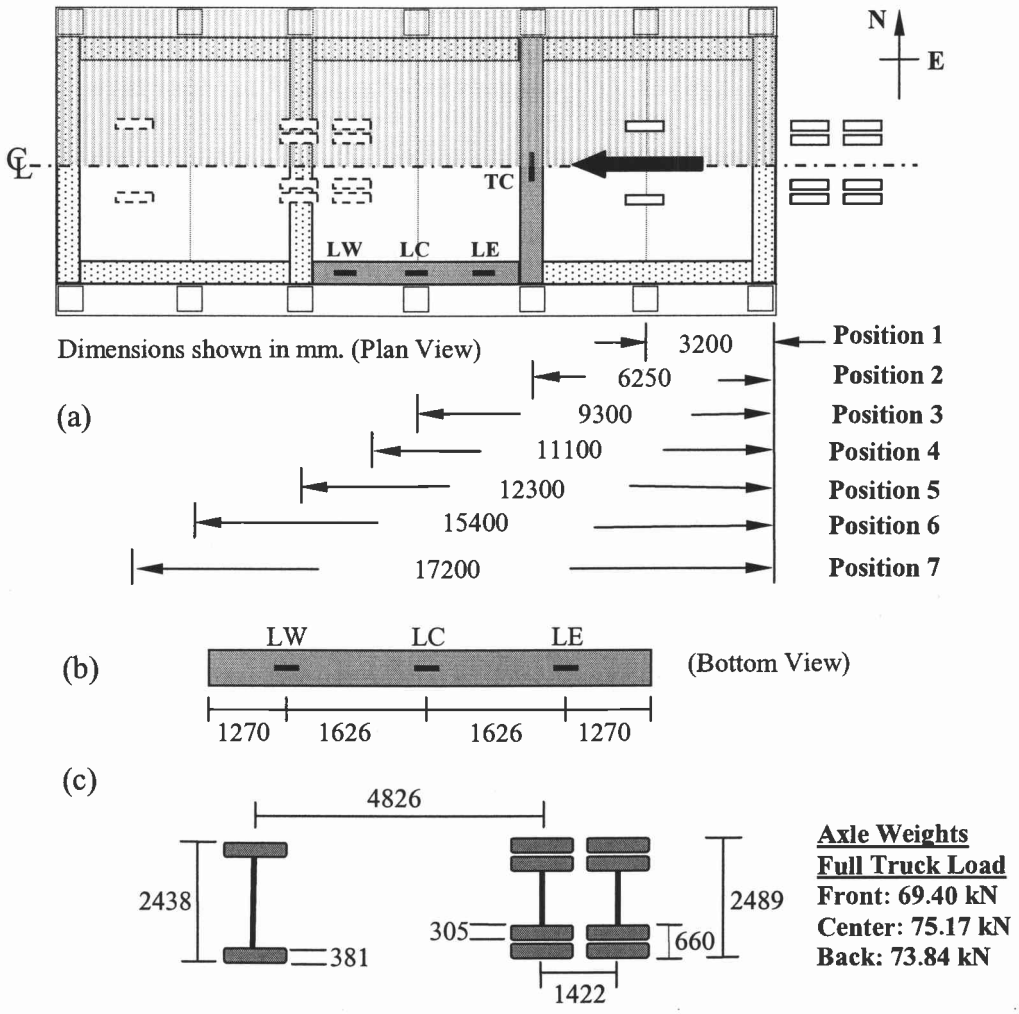

Figure 3.3. Loading Conditions: (a) Locations of Truck and Monitored Beams; (b) Sensors on Longitudinal Beam; (c) Truck Configuration

3.3.2 FE Modeling and Loading Procedures

3.3.2.1 Bridge Modeling

The constitutive models, ANSYS elements, material properties, and assumptions previously discussed are used in the bridge analysis. Unconfined concrete is used for the bridge deck, the cover of the columns, and the curb of the bridge. Taking advantage of symmetry, only a longitudinal half of the bridge is modeled, as shown in the lighter area on Fig. 3.3(a). For the final model, used to best represent the actual bridge conditions, the total number of elements is 16791: 10504 elements for concrete (SOLID65), 4954 elements for steel bars (LINK8), 1168 elements for FRP (SOLID46), 160 SHELL143 elements, and 5 MATRIX27 elements.

A good FE model does not necessarily need to have all of the details as in the actual structure, but it should have all of the details that affect the behaviors of interest. To make the FE models more efficient when analyzed in ANSYS and to reduce the model complexity, run-time, and memory requirements, modeling modifications were made for the bridge as follows:

Equivalent thickness of FRP laminates: The HC bridge is retrofitted with several different combinations of both CFRP and GFRP laminates in order to resist the expected bending moments and shear forces, respectively. This of course induces non-uniformity in the thickness, which leads to a modeling difficulty. With the special layer modeling capacity in the SOLID46 (FRP) element, a portion

of the structure consisting of different materials and fiber orientations is represented using one SOLID46 element. Moreover, the thickness of the FRP laminates, which varies along the actual bridge, can be kept constant using equivalent thickness modeling. For example, when the original laminate thickness is reduced by half, the modulus of elasticity and shear modulus in all three directions are doubled, and vise versa. Poisson's ratios are independent of the thickness of laminate; therefore, they are kept the same throughout.

"Lumping" of reinforcing steel bar areas: To be able to limit the number of elements effectively in both transverse and longitudinal beams, when there are many reinforcing steel bars at the same level, they are lumped, equally distributed, and arranged in such a way that they can fit the pre-defined FE mesh at that level.

The FE bridge model is shown in Fig. 3.4 with typical FRP reinforcement (Fig. 3.4(a)), steel reinforcement in beams, columns, and deck (Figs. 3.4(a) - (c)), and soil-structure interface modeling (Fig. 3.4(d)).

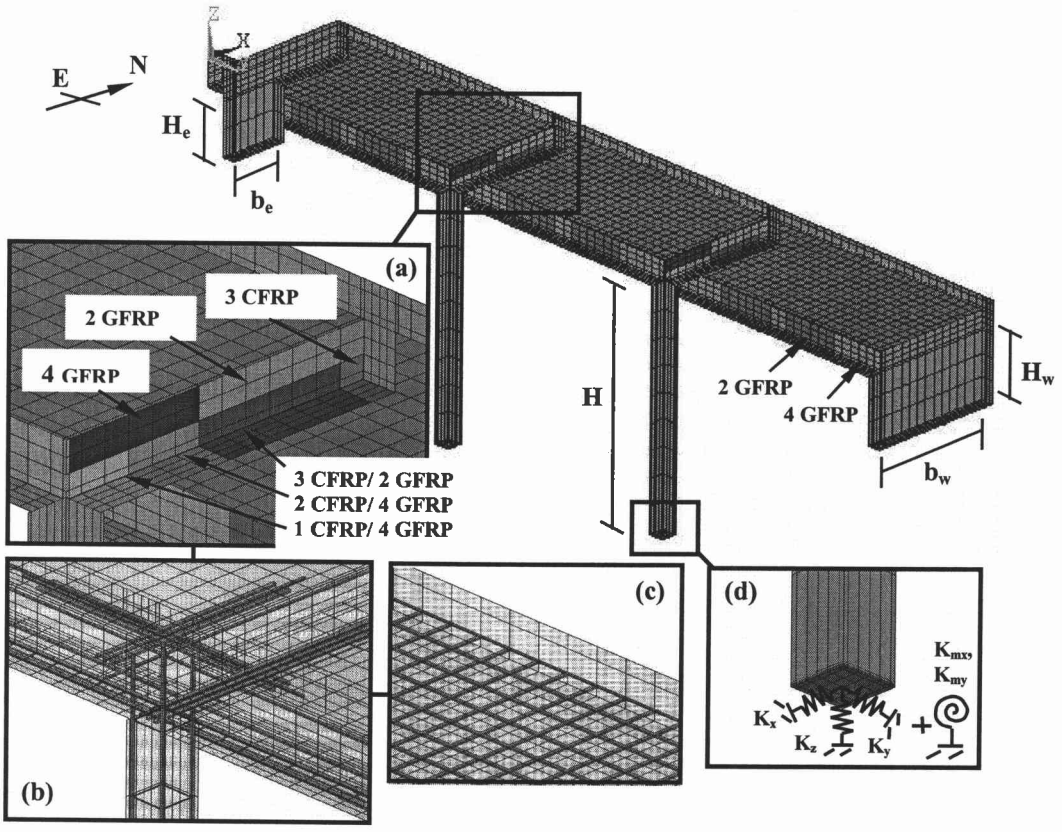

Figure 3.4. FE Bridge Modeling: (a) Typical FRP Reinforcement; (b) Typical Steel Reinforcement in Beams and Columns; (c) Typical Steel Reinforcement in Bridge Deck; (d) Typical Soil-Structure Interface Modeling

Note: 4 GFRP represents four layers of GFRP laminates, while 1 CFRP/4 GFRP, for example, represents a combination of one layer of CFRP laminate and four layers of GFRP laminates.

3.3.2.2 Loading Procedure

Two main loadings are applied in the analysis; i.e., a pre-cracking loading (if performed) and truck load steps. The pre-cracking loading is applied using a uniformly distributed load on the bridge deck and, then, gradually increasing it until the bridge starts cracking. After the cracks are introduced to the bridge model, the load is gradually removed. Following that, the truck load is gradually applied on the bridge deck at each location for the various analyses. Self-weight of the bridge is not included, as not seen in the strains from the truck loading. Truck load simplification is explained in Appendix B.

3.4 CALIBRATION OF FEM PREDICTIONS WITH FIELD TEST MEASUREMENTS

3.4.1 Comparison Procedure

Two parameters which can significantly affect the bridge structural behavior; i.e., the strength of the in-situ concrete and soil stiffness, E_{soil}, are unknown. However, from the pulse velocity measurements and the geological evidence, reasonable ranges for these unknown properties are obtained. Besides these parameters, some geometrical properties of the bridge are also unknown; i.e., the actual depths of the footings. In addition, existing crack patterns on the bridge

were not mapped before FRP strengthening. Sensitivity study is, therefore, required to investigate these unknown parameters and develop a model to best simulate actual bridge conditions.

Sum of squares (SS) is used as a criterion in the sensitivity study to objectively select the best model, supplementing visual comparison of the strain plots between FE predictions and field data. SS is calculated based on four strain locations (TC, LE, LC, and LW) for seven full truck locations as follows:

$$SS = \sum_{i=1}^{4} \sum_{j=1}^{7} (\varepsilon_{FEM_j} - \varepsilon_{EXP_j})_i^2 \qquad [3.13]$$

The minimum SS implies the best model, which most closely predicts the strain results from the bridge test. After 42 sensitivity cases are performed varying the strength of the concrete, E_{soil} for each foundation location, bridge geometry, and damage level of the bridge, the bridge model with reasonable material properties and the minimum SS is selected; i.e., model NL3-12. It should be noted that 27 cases are shown here. The summary of sensitivity study cases varying these unknown parameters is shown in Table 3.2. The SS for each case is plotted in Fig. 3.5. In addition, strain calculating approach for FE models is discussed in Appendix B.

Table 3.2. Summary of Sensitivity Study

Case	Pre-cracking load (kN)	MATERIAL PROPERTIES					Geometrical Properties					
		f'_c	E_{soil} (MPa)			$E_{base\ plate}$	W_w	b_w	H_w	H	H_e	b_e
		(MPa)	Under cols.	East end	West end	(GPa)	(m)	(m)	(m)	(m)	(m)	(m)
(1)	(2)	(3)	(4)	(5)	(6)	(7)	(8)	(9)	(10)	(11)	(12)	(13)
(a) No Pre-Cracking Load												
L1-1	- -	17.24	"Fixed"	"Fixed"	"Fixed"	2.07E+08	0.914	0	0	4.877	0	0
L1-2	- -	22.06	"Fixed"	"Fixed"	"Fixed"	2.07E+04	0.305	0	0	4.877	0	0
L1-3	- -	27.58	"Fixed"	"Fixed"	"Fixed"	2.07E+08	0.914	0	0	4.877	0	0
L1-4	- -	27.58	19600	19600	19600	2.07E+08	0.914	0	0	4.877	0	0
L1-5	- -	27.58	19600	100	100	2.07E+08	0.914	0	0	4.877	0	0
L2-1	- -	17.24	"Fixed"	"Fixed"	"Fixed"	2.07E+08	0.914	2.896	1.524	5.486	1.219	1.067
L2-2	- -	17.24	100	100	100	2.07E+08	0.305	2.896	1.524	5.486	1.219	1.067
L3	- -	17.24	"Fixed"	"Fixed"	"Fixed"	2.07E+08	0.914	2.896	1.524	6.096	1.829	0
(b) Moderate Pre-Cracking Load												
NL2-1	1680	27.58	19600	19600	19600	2.07E+08	0.305	2.896	1.524	5.486	1.219	1.067
NL2-2	1680	32.41	19600	19600	19600	2.07E+08	0.305	2.896	1.524	5.486	1.219	1.067
NL2-3	1680	37.23	19600	19600	19600	2.07E+08	0.305	2.896	1.524	5.486	1.219	1.067
(c) Initial Pre-Cracking Load												
NL2-4	1399	27.58	19600	19600	19600	2.07E+08	0.305	2.896	1.524	5.486	1.219	1.067
NL2-5	1479	31.03	19600	19600	19600	2.07E+08	0.305	2.896	1.524	5.486	1.219	1.067
NL3-1	1319	27.58	19600	19600	19600	2.07E+08	0.305	2.896	1.524	6.096	1.829	0
NL3-2	1311	27.58	490	980	200	2.07E+08	0.305	2.896	1.524	6.096	1.829	0
NL3-3	1311	27.58	980	490	200	2.07E+08	0.305	2.896	1.524	6.096	1.829	0
NL3-4	1315	27.58	490	490	200	2.07E+08	0.305	2.896	1.524	6.096	1.829	0
NL3-5	1319	27.58	490	2450	345	2.07E+08	0.305	2.896	1.524	6.096	1.829	0
NL3-6	1315	27.58	490	490	345	2.07E+08	0.305	2.896	1.524	6.096	1.829	0
NL3-7	1315	27.58	655	655	200	2.07E+08	0.305	2.896	1.524	6.096	1.829	0
NL3-8	1315	27.58	483	483	483	2.07E+08	0.305	2.896	1.524	6.096	1.829	0
NL3-9	1315	27.58	655	655	655	2.07E+08	0.305	2.896	1.524	6.096	1.829	0
NL3-10	1315	27.58	827	827	827	2.07E+08	0.305	2.896	1.524	6.096	1.829	0
NL3-11	1315	27.58	1000	1000	1000	2.07E+08	0.305	2.896	1.524	6.096	1.829	0
NL3-12	1315	27.58	1172	1172	1172	2.07E+08	0.305	2.896	1.524	6.096	1.829	0
NL3-13	1315	27.58	1345	1345	1345	2.07E+08	0.305	2.896	1.524	6.096	1.829	0
NL3-14	1315	27.58	1517	1517	1517	2.07E+08	0.305	2.896	1.524	6.096	1.829	0

Notes: 1. "Fixed" means a sufficiently high E_{soil} is used to provide a fixed boundary condition.
2. L–No pre-cracking load (essentially linear analysis), NL–With pre-cracking load (nonlinear analysis)

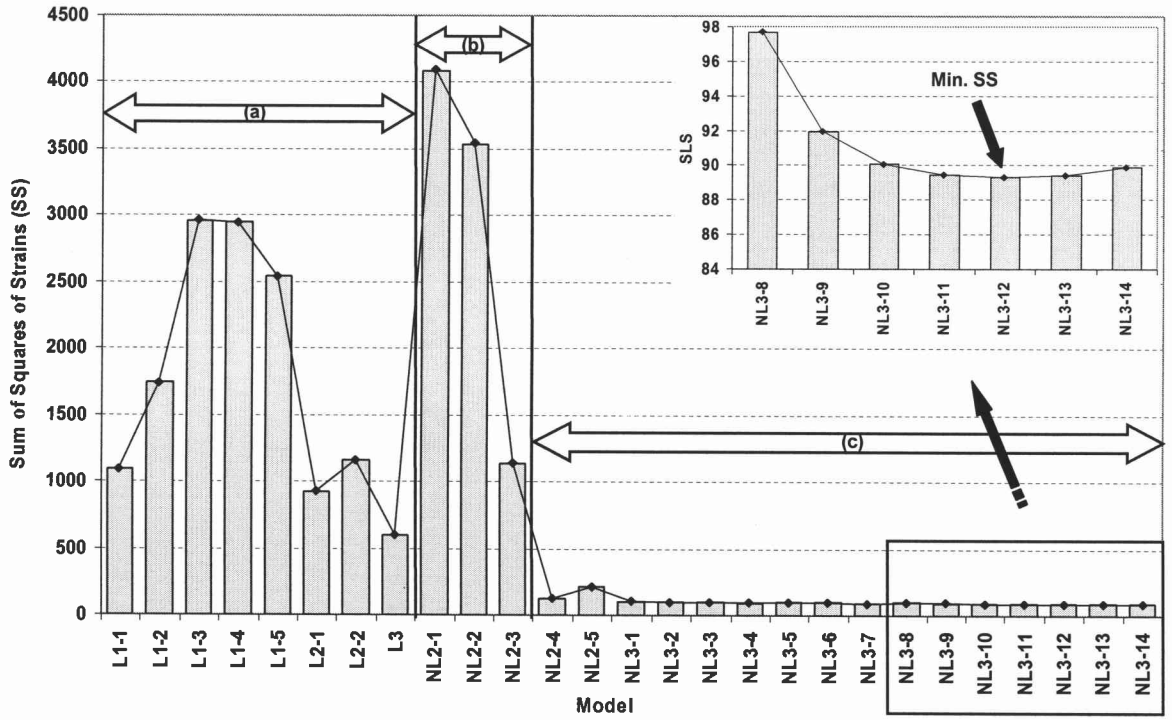

Figure 3.5. Plots of Sum of Squares of Strains for All Study Cases: (a) No Pre-Cracking Load; (b) Moderate Pre-Cracking Load; (c) Initial Pre-Cracking

To represent the effects of the moving truck on the structural behavior of the bridge, the strains are plotted versus the distances of the single front axle of the truck from the east end of the bridge. Basically, these plots are similar to "influence lines," but for a truck instead of a unit load. Comparisons of the strains between FE analysis based on the best model (NL3-12) and field data are shown in Figs. 3.6(a) – (d).

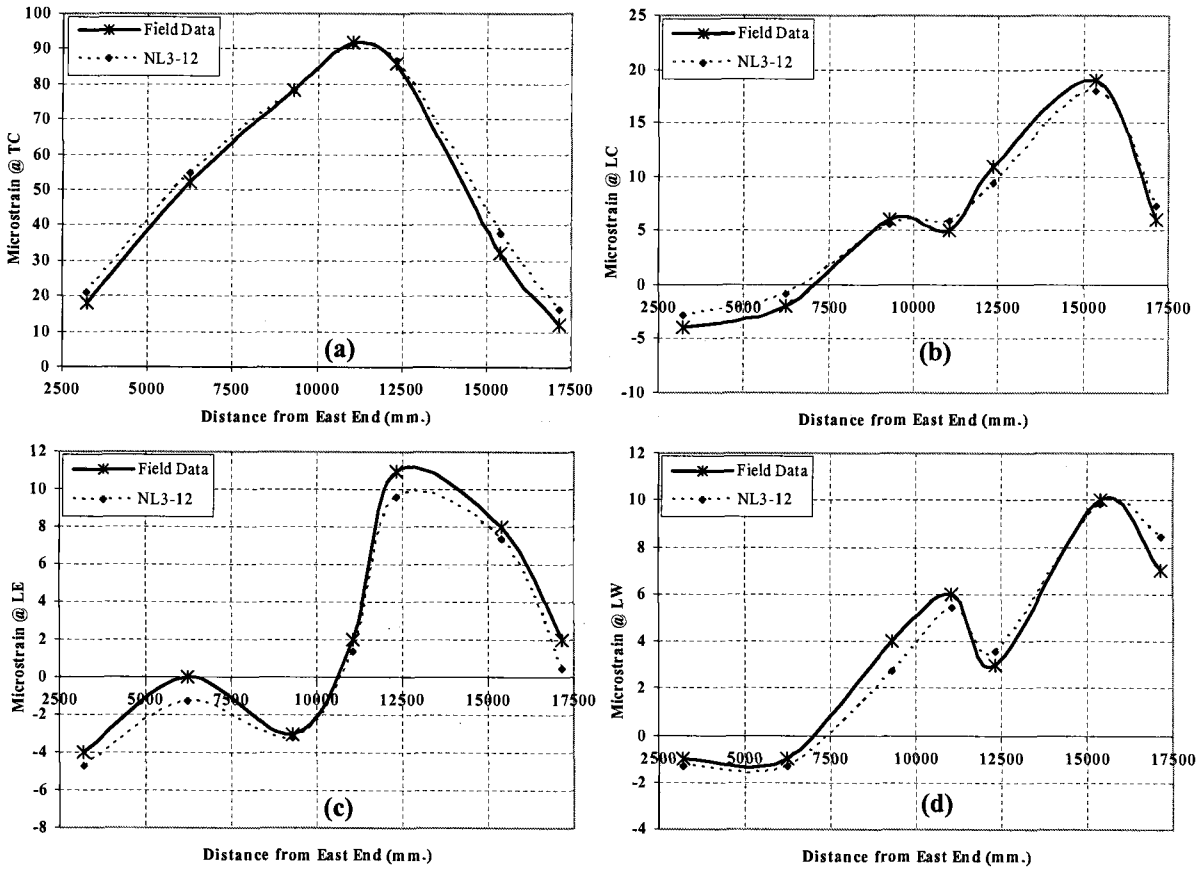

Figure 3.6. Comparisons of Strain vs. Truck Distance between Field Data and FE Prediction from NL3-12 for each Sensor

Note: Data points are shown for each truck location along the bridge deck.

As seen in the figures, the proposed model predicts very well both magnitudes and trends in the strains for the various truck load locations. From Fig. 3.6(a), the maximum strain for TC is obtained if the single axle of the truck is at 11100 mm from the end of the bridge deck (Position 4 from Fig. 3.3(a)) because at this location the loads from the middle tandem axles are right above the transverse beam, to which the fiber optic sensors are attached (Fig. 3.3(a)). The maximum value for LC (Fig. 3.6(b)) occurs when the single axle of the truck is at 15400 mm from the end of the bridge deck (Position 6). This is due to the fact that at Position 6 the loads from the tandem axles most significantly affect the middle span of the longitudinal beam, to which the fiber optic sensors are attached. For LE (Fig. 3.6(c)), the maximum strain occurs when the truck is at Position 5 because the tandem axles are closest to the sensor. Large strains for LW (Fig. 3.6(d)) are obtained when the truck is at 11100 mm and 15400 mm from the end (Positions 4 and 6), as the single and tandem axles are closest to the sensor. However, the maximum occurs for Position 6 because the loads from the tandem axles are much higher than from the single axle.

3.4.2 Sensitivity Study

The sensitivity study provides useful understanding about how each parameter influences the bridge behavior (i.e., the strain-truck load location relationship).

3.4.2.1 Influence of Geometry of the HC Bridge

The main models from cases L1-1, L2-1, and L3 will be investigated. The differences among these three models are the middle column height (H), heights of the east and west columns (H_e, H_w) and widths of the east and west walls (b_e, b_w). For case L1-1, no east and west walls and columns are modeled, and the middle columns are shortest. For case L2-1, all columns and walls are modeled, while case L3's model has the longest middle and east columns without the east wall. Other parameters are fixed for all models to be able to examine only the influence of bridge geometry.

Comparisons of TC and LE strains for the various truck locations in each analysis are plotted against the field data in Figs. 3.7(a) and (b).

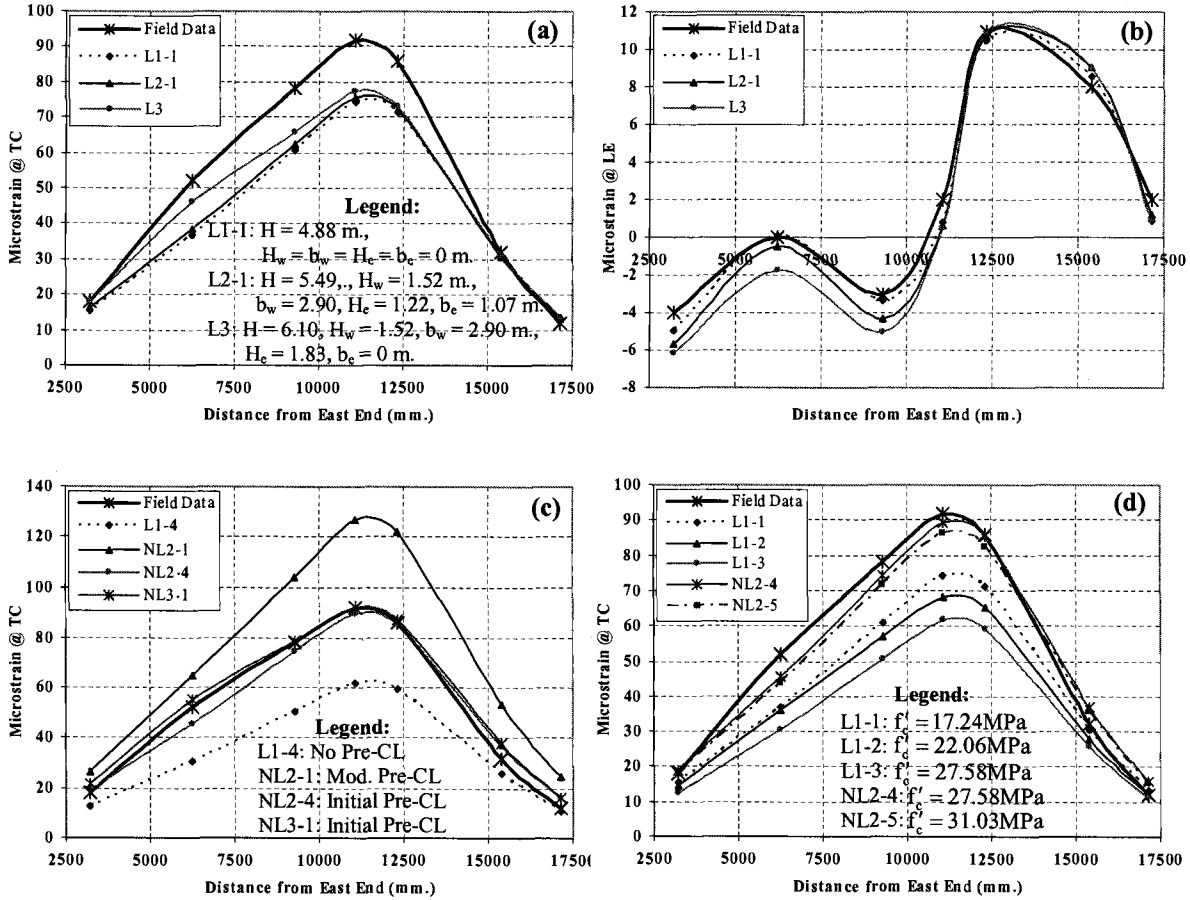

Figure 3.7. Influences of Bridge Parameters: (a) and (b) Bridge Geometry; (c) Pre-Cracking Load; (d) Strength of Concrete; (e) to (h) Soil Stiffness

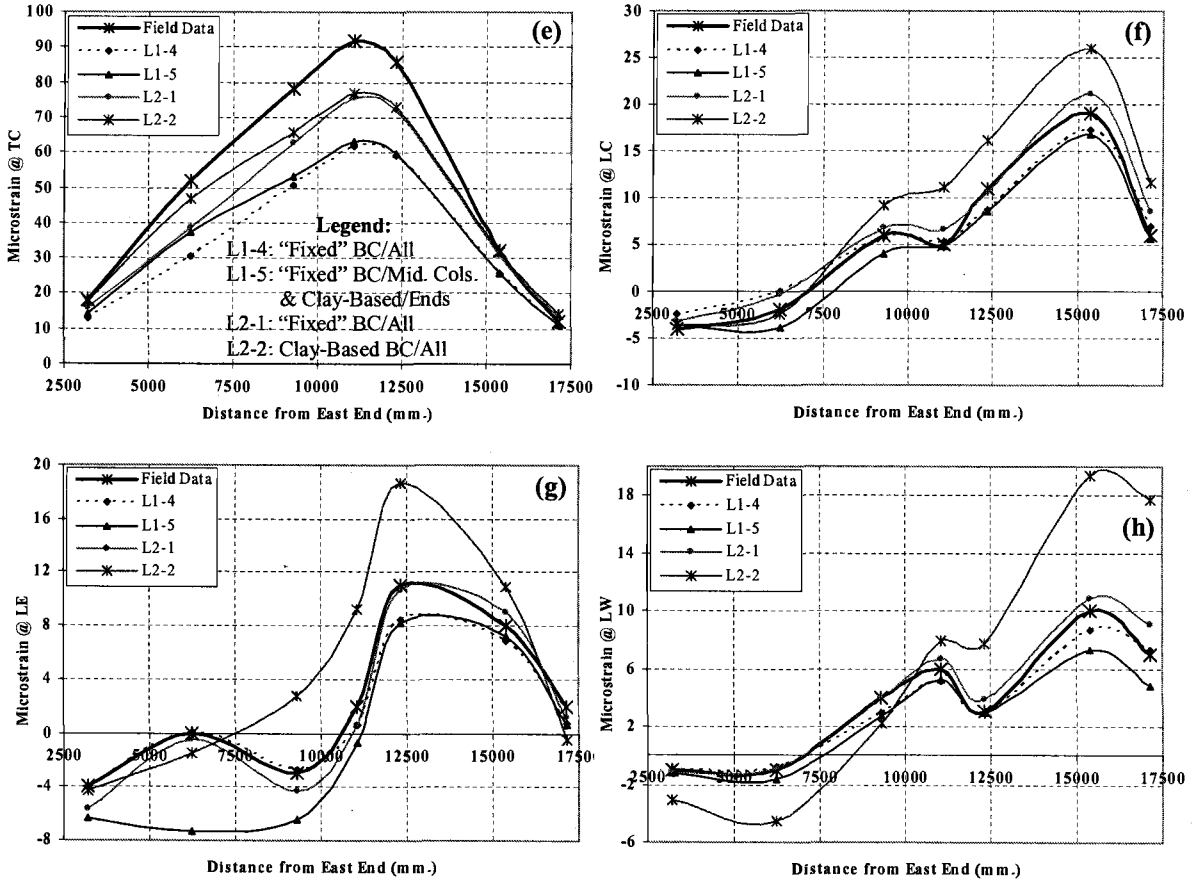

Figure 3.7 (Cont'd). Influences of Bridge Parameters: (a) and (b) Bridge Geometry; (c) Pre-Cracking Load; (d) Strength of Concrete; (e) to (h) Soil Stiffness

Notes: 1. For Fig. 3.7(c), Mod. = Moderate; CL = Cracking Load
2. For Fig. 3.7(e), BC = Boundary Condition; All = All Footings; Mid. Cols. = Middle Columns; Ends = Footings at Bridge Ends. f'_c = 27.58 MPa for Cases L1-4 and L1-5, and f'_c = 17.24 MPa for Cases L2-1 and L2-2.

For TC (Fig. 3.7(a)), it can be seen that the first portion of the L3 curve increases, as the truck is at Positions 1 to 4. Higher strains are observed for the model with longer middle and east columns and without the east wall, which makes the bridge more flexible. However, when the truck moves from Positions 5 to 7, the decreasing trends in the strain for all the cases are similar, as the loads are sufficiently far from the sensor. For LE (Fig. 3.7(b)), higher strains for the various truck locations are obtained from the models with the longer middle columns. The geometrical changes insignificantly affect the strain responses at LC and LW (not shown here). When the west wall footing width (W_w) is decreased from 0.914 m to 0.305 m in the model, the trends in the strains for all the cases (not shown here) stay about the same.

Among these three primary models, Fig. 3.5 shows that SS for Model 3 (L3) is a minimum. The geometry of this model will be used most often when the influence of soil foundation stiffness is examined, as it most accurately predicts the strain values.

3.4.2.2 Influence of Pre-Cracking Load

The bridge is cracked under a uniformly distributed pre-cracking load before the truck load is applied, to represent existing damage to the bridge. The level of damage is controlled by the magnitude of the pre-cracking load: no pre-cracking, initial, and moderate pre-cracking loads. Case L1-4 as the no pre-cracking load case; NL2-1 as the moderate pre-cracking load case; and NL2-4 and NL3-1 as the initial pre-cracking load cases will be discussed. See Table 3.2 for load levels associated with these cases. The bridge does not crack under the applied full truck load alone. Therefore, the uncracked bridge structure behaves linearly.

For the pre-cracking load cases, as the distributed load is applied on the bridge deck, cracks are introduced to the transverse beams. The cracked bridge behaves nonlinearly. Structural stiffness is updated at the end of each load sub-step to reflect the material nonlinearities and changes in status of concrete material. The moderate pre-cracking load induces more cracks than the initial pre-cracking load, which is the lowest load first cracking the bridge. The comparison of TC strain results for each case is plotted in Fig. 3.7(c). It is obvious that the model without introduced cracks (L1-4) is too stiff. For a better match using the uncracked model, the strength of the concrete must be unreasonably low (lower than 17.2 MPa (2500 psi)). On the other hand, if too many cracks are introduced to the bridge (in moderate pre-cracking load case (NL2-1)) the bridge becomes too flexible.

Conversely, the strength of the concrete must be unrealistically raised to provide a better prediction. However, when the initial pre-cracking load (NL2-4 and NL3-1) is used, the strain predictions are dramatically improved. They are best for NL3-1 having the same bridge geometry as case L3. The significant improvement after applying the initial pre-cracking load can even more clearly be observed in terms of SS (Fig. 3.5). As a result, the initial pre-cracking using a uniformly distributed load will be used in the model to replicate the existing cracks in the actual bridge. For LE, LC, and LW, no significant variations among these cases were observed.

3.4.2.3 Influence of Strength of In-Situ Concrete

Cases L1-1, L1-2, L1-3, NL2-4, and NL2-5 will now be examined. For the case with no pre-cracking, the concrete strength varied from 17.24 MPa, 22.06 MPa to 27.58 MPa for L1-1, L1-2, and L1-3, respectively. For the initial pre-cracking load case, the concrete strength is 27.58 MPa and 31.03 MPa for NL2-4 and NL2-5, respectively. Comparison of TC strain results is shown in Fig. 3.7(d). The same trend can be obtained both with and without pre-cracking loads. That is, as f_c' increases, the bridge structure is stiffer, which, in turn, lowers the strains for the various truck locations for each case. The results also show that when an f_c' of 27.58 MPa is used under the initial pre-cracking load (NL2-4), the strain predictions are closest to the field data. Moreover, the concrete strength falls

within a reasonable range obtained from the pulse velocity measurements. As a result, an f_c' of 27.58 MPa is assumed for the strength of the in-situ concrete. Again, no significant changes can be noticed for LE, LC, and LW due to the f_c' variation.

3.4.2.4 Influence of Soil Stiffness

It can be concluded from the previous discussion on the influences of bridge geometry, pre-cracking load, and strength of concrete that varying these parameters significantly affects only the TC strain. It can also be concluded that the bridge geometry from case L3, with an initial pre-cracking load, and an f_c' of 27.58 MPa should be used as a base model for the next adjustment in the sensitivity study; i.e., influence of soil stiffness. It is observed that soil stiffness mainly affects the shape of the "influence line" for LE, LC, and LW strains. It also moves the curves up and down within a narrow band about the field results. Fine-tuning these strain curves by varying E_{soil} at the various locations is needed in order to obtain the FE model that can best represent the actual bridge conditions.

It is found that even when the lowest value for E_{basalt} (19.6 GPa) is used, the response is still almost the same as that of the bridge having "fixed" boundary conditions (L1-3 and L1-4) (not shown in the strain plots included), as seen from

the same SS value (Fig. 3.5). The soil stiffness should be sufficiently lowered to cause the bridge model to be affected by the soil conditions. It is, consequently, assumed that there are softer soil materials than basalt between the bridge foundation and basalt bedrock and that the combined soils still behave linearly. For the extreme case, it is assumed that the footings are on very stiff clay (E_{clay} = 100 MPa from Hambly (1991)). E_{soil} will be varied between E_{basalt} and E_{clay}.

To clearly present the influence of soil stiffness, the study cases causing the most dramatic changes in strain results will be discussed first; i.e., cases L1-4, L1-5, L2-1, and L2-2. For case L1-4, it is assumed that all the footings are on basalt, while for case L1-5, the foundations at the bridge ends are on stiff clay. With a different bridge geometry (longer columns with east and west walls) and lower f_c', all the footings are assumed to be on basalt ("fixed" boundary conditions yield the same results as basalt-based boundary conditions) for case L2-1, while all are assumed to be on stiff clay for case L2-2. The comparisons of the strain results are shown in Figs. 3.7(e) to (h). Like the influence of extending the column height, larger strains can be observed for TC (Fig. 3.7(e)) when the soil stiffness is reduced either at all foundation locations or only at foundations at the bridge ends. For LE (Fig. 3.7(g)) when the truck is at Position 2, if basalt is replaced by clay at the bridge end foundations (L1-5), a relatively high negative strain can be observed. For the more flexible ends, the tandem axles, which are still on the east span, tend to deflect the monitored longitudinal beam upwards. Unlike the other cases, for case L2-2, in which basalt is replaced by clay at all locations, when the truck moves

to Position 3, the effect from the single axle is sufficient to cancel that from the tandem axles on the other span, which induces a positive strain at LE. For the other strains (Figs. 3.7(f) and (h)), using the softer soil material causes a more flexible structure, which increases deflections (and strains) under loading.

With the base model, E_{soil} is varied to fine-tune the LE, LC, and LW strain curves from cases NL3-1 to NL3-14. The strain results are not plotted here, as they are very close to one another. However, the SS for each case is plotted in Fig. 3.5 to show how the changes in E_{soil} improve the strain predictions. From cases NL3-8 to NL3-14, it is assumed that the footings are on the same type of foundation, and the soil stiffness is increased by an increment of 172 MPa. Fig. 3.5 shows that the SS is lower (as E_{soil} is higher) and reaches a minimum for case NL3-12. As a result, the FE model from case NL3-12 is selected to be that which can best represent the actual bridge conditions. Again, the comparisons of the strains between the FE model from case NL3-12 and the field data are shown in Figs. 3.6(a)-(d).

3.5 CONCLUSIONS

In this study, the soil-structure interface is incorporated into the FE models, and a sensitivity study on the influences of bridge geometry, pre-cracking load (damage level), and strength of concrete is performed. In the sensitivity study,

comparisons of the strain results between ANSYS predictions and the experimental data show that the proposed FE model (from case NL3-12) is a realistic representation for the HC bridge in terms of the number of elements, structural details, reasonable concrete and soil properties, and, especially, accurate predictions.

The bridge model has to be pre-cracked with an initial load before the service truck load is applied to take the existing damage in the actual bridge into consideration. The actual concrete strength is much higher than the value suggested by AASHTO, and is estimated using pulse-velocity measurements and verified in the sensitivity study. That is, the estimated concrete strength from this study is 27.6 MPa (compared with the AASHTO recommended f_c' of 17.3 MPa) and is within the f_c' range of 25.9 MPa to 32.1 MPa obtained from the pulse-velocity measurements. Soil-structure interaction modeling is important to fine-tune the FE model. This is done by replacing the foundation with translational and rotational spring elements. From the study, it is indicated that varying the soil stiffness mainly affects the strains on the monitored longitudinal beam. Besides visual inspection of the strain plots for FE predictions and field data, the SS of the strains is used as a tool to objectively select the most representative FE model from a large number of study cases.

The FE analysis shows that when the single axle of the full truck is positioned at 11.05 m and 15.39 m from the east end of the bridge deck (Positions 4 and 6), the maximum strain values are developed in the monitored transverse and

longitudinal beams, respectively, except that the maximum LE strain occurs when the load is positioned at 12.34 m (Position 5). This is because the loads from both the single and tandem axles strongly influence the beams when positioned at those locations.

ACKNOWLEDGMENTS

This project was supported by the Oregon Department of Transportation (ODOT), Salem, OR, and the Department of Civil, Construction, and Environmental Engineering, Oregon State University, Corvallis, OR.

REFERENCES

AASHTO Subcommittee on Bridges and Structures. (1994). *Manual for Condition Evaluation of Bridges*. American Association of State and Highway Transportation Officials, Washington D.C.

ACI Committee 318. (2002). *Building Code Requirements for Structural Concrete (ACI 318-02) and Commentary (ACI 318R-02)*. ACI, Farmington Hills, MI.

ANSYS User's Manual, Vol. I-IV; Revision 5.5. (1998). Swanson Analysis System, Inc., Houston, PA.

Balakrishnan, S., and Murray, D.W. (1988). "Concrete Constitutive Model for NLFE Analysis of Structures." *J. Struct. Engrg.*, ASCE, 114(7), 1449-1466.

Bangash, M.Y.H. (1989). *Concrete and Concrete Structures: Numerical Modeling and Applications*. Elsevier Science Publishers, LTD., Essex, England.

Bhatt, P., and Kader, M.A. (1998). "Prediction of Shear Strength of Reinforced Concrete Beams by Nonlinear Finite Element Analysis." *Computers and Struct.*, 68, 139-155.

Chansawat, K., Potisuk, T., Miller, T.H., Yim, S.C.S., and Kachlakev, D.I. (2002a). "FE Models of GFRP and CFRP Strengthening of Reinforced Concrete Beams." Submitted to *ACI Struct. J.*

Chansawat, K., Miller, T.H., and Yim, S.C.S. (2002b). "NLFE Analysis of an FRP-Strengthened Reinforced Concrete Bridge. II: Performance Evaluation." Submitted to *J. of Bridge Engrg.*, ASCE.

CH2M Hill Consulting Engineers in conjunction with TAMS Consultants. (1997). "Evaluation and Resolution of Under Capacity State Bridges: Bridge #04543, Horsetail Creek Bridge." CH2M HILL, Inc., Corvallis, OR.

Hambly, H.C. (1991). *Bridge Deck Behavior*. 2nd ed. Clays Ltd, St Ives plc, England. Isenberg, J. (1993). *Finite Element Analysis of Reinforced Concrete Structures II*. ASCE, New York, NY.

Jumikis, A.R. (1983). *Rock Mechanics*. Gulf Publishing Co., Houston, TX.

Kachlakev, D.I., and McCurry, D.Jr. (2000). "Testing of Full-Size Reinforced Concrete Beams Strengthened with FRP Composites: Experimental Results and Design Methods Verification." *SPR387, United States Department of Transportation Federal Highway Administration and the Oregon Department of Transportation*, Salem, OR.

Kemp, A.R. (1998). "The Achievement of Ductility in Reinforced Concrete Beams." *Magazine of Concrete Research*, 50(2), 123-132.

Kent, D.C., and Park, R. (1971). "Flexural Members with Confined Concrete." *J. Struct. Div.*, ASCE, 97(7), 1969-1990.

Malhotra, V.M., and Carino, N.J. (1991). *CRC Handbook on Nondestructive Testing of Concrete.* CRC Press Inc., Boca Raton, FL.

Mander, J.B., Priestley, M.J.N., and Park, R. (1988). "Theoretical Stress-Strain Model for Confined Concrete." *J. Struct. Engrg.*, ASCE, 114(8), 1804-1826.

Park, R., Priestley, M.J.N., and Gill, W.D. (1982). "Ductility of Square-Confined Concrete Columns." *J. Struct. Div.*, ASCE, 108(4), 929-950.

Phillips, W.M. (1987). *Geologic Map of the Vancouver Quadrangle, Washington and Oregon.* Washington State Department of Natural Resources, Olympia, WA.

Poulos, H.G., and Davis, E.H. (1973). *Elastic Solutions for Soil and Rock Mechanics.* John Wiley & Sons, Inc., NY.

Teng, J.G., Chen, J.F., Smith, S.T., and Lam, L. (2001). *FRP Strengthened RC Structures.* John Wiley & Sons, Ltd, West Sussex, England.

Walker, G.W., and MacLeod, N.S. (1991). *Geologic Map of Oregon: Scale 1:500000.* U.S. Geological Survey, Denver, CO.

Wang, P.T., Shah, S.P., and Naaman, A.E. (1978). "Stress-Strain Curves of Normal and Lightweight Concrete in Compression." *J. of ACI*, 75(11), 603-611.

Whiteman, R.V., and Richart, F.E. (1967). "Design Procedures for Dynamically Loaded Foundations." *J. of the Soil Mech. and Foundations Div.*, ASCE, 93(6), 169-193.

NOTATION

b = length of footing;

b_e = east wall width;

b_w = west wall width;

d = width of footing;

E_{basalt}, E_{clay} = moduli of elasticity of basalt and clay;

$E_{base\ plate}$ = modulus of elasticity of base plate;

E_{soil} = modulus of elasticity of soil;

E_0 = initial modulus of elasticity of concrete in beams;

E_{11}, E_{22}, E_{33} = moduli of elasticity of FRP in fiber direction and in the axes perpendicular to the fiber direction;

F_z, F_x, F_y = unit vertical and horizontal forces in x and y directions;

f_c = compressive stress in confined concrete in columns;

f_c' = uniaxial compressive strength of concrete;

f_r = uniaxial tensile strength (modulus of rupture) of concrete;

f_y = yield strength in reinforcing steel bars;

f_{yt} = yield strength of steel ties;

G = shear modulus of FRP;

G_s = shear modulus of soil;

G_{12}, G_{13}, G_{23} = shear moduli of FRP in the 1-2, 1-3, and 2-3 planes. The 1-2 and 1-3 planes are the planes perpendicular to the fiber direction;

H = middle column height;

H_e = east end column height;

H_w = west end column height;

K = modification factor for confined concrete strength;

K_z, K_x, K_y = vertical and horizontal (x and y directions) spring stiffnesses;

K_{mx}, K_{my} = rotational spring stiffnesses about x and y axes;

M_x, M_y = unit moments about x or y axes;

SLS = sum of the least square;

W_w = west wall footing width;

β = shear transfer coefficient;

β_z, β_x, β_y = vertical and horizontal (x and y directions) stiffness coefficients;

β_{mx}, β_{my} = rotational stiffness coefficients about x and y axes;

ε = compressive strain in concrete;

ε_c = compressive strain in confined concrete in columns;

ε_{FEM}, ε_{EXP} = analytical and experimental strains;

ε_y = yield strain in reinforcing steel bars;

ϵ_0 = compressive strain at ultimate confined compressive stress in concrete in columns;

ϵ_0' = compressive strain at ultimate unconfined and confined compressive stress in concrete in beams;

ρ_s = ratio of volume of rectangular steel ties to volume of concrete core measured to outside of the peripheral tie;

σ = compressive stress in concrete;

$\sigma_{ult(ten.)}$ = ultimate tensile strength of FRP in the fiber direction;

ν = Poisson's ratio;

ν_s = Poisson's ratio of soil;

ν_{12}, ν_{13}, ν_{23} = Poisson's ratios in the 1-2, 1-3, and 2-3 planes. The 1-2 and 1-3 planes are the planes perpendicular to the fiber direction.

CHAPTER 4: NLFE ANALYSIS OF AN FRP-STRENGTHENED REINFORCED CONCRETE BRIDGE. II: PERFORMANCE EVALUATION

by Kasidit Chansawat, Thomas H. Miller, Member, ASCE,
and Solomon C.S. Yim, Member, ASCE

ABSTRACT

A nonlinear finite-element (NLFE) analysis is performed using ANSYS, a general-purpose FE program, to provide estimates of the structural response of the Horsetail Creek Bridge before and after fiber-reinforced polymer (FRP) strengthening. Fully three-dimensional cracked FE bridge models are developed using a sensitivity study to best represent the actual bridge conditions. Multi-directional springs are placed at the bridge supports to simulate realistic boundary conditions. Mass-proportional and scaled truck loadings are gradually applied until failure occurs. Load-deflection relationships, crack patterns, and yielding of reinforcing steel are compared for strengthened and unstrengthened bridge models to evaluate the FRP retrofit. The proposed FE bridge models show a significant improvement in structural performance due to the FRP retrofit. The capacities of the bridge are increased by 37% and 28% based on scaled gravity and scaled truck loadings, respectively. Failure modes are also revealed for each model; i.e., shear

and flexural failures in the transverse beams of the unstrengthened and FRP-strengthened bridges, respectively.

4.1 INTRODUCTION

Structural behavior in terms of inelastic response, load distribution characteristics, and ultimate strength of reinforced concrete (RC) bridges strengthened with FRP composites cannot be completely assessed with the simplified procedures currently used in design and evaluation. Extensive experiments testing a number of specimens with different design parameters are often not time and cost effective. Moreover, destructive testing can only be performed on bridges subject to replacement or on smaller component members.

Comprehensive analytical techniques are necessary to provide reliable estimates of response in the linear and nonlinear ranges for these bridge structures. Nonlinear finite-element (NLFE) analysis can be used in evaluating the existing strength of bridge structures and for estimating the actual capacity of strengthened bridges. The Horsetail Creek (HC) bridge in Oregon is an example of an RC bridge strengthened with FRP laminates to correct structural deficiencies.

This study is focused on implementing NLFE analysis for determining the HC bridge's structural responses in both the linear and nonlinear ranges before and after FRP strengthening.

The main objective of this study is to evaluate the improved performance of the Horsetail Creek Bridge offered by the FRP laminates. Three-dimensional finite element models are developed for both the unstrengthened and FRP-strengthened HC bridge. Scaled gravity and scaled truck loadings are applied to failure. Analyses of both full-scale beams replicating the transverse beams of the HC bridge and the overall bridge were conducted. The analysis of the full-scale beams will be presented later, and the analysis of the HC bridge under service loading has been presented in Part I (Chansawat et al. 2002b)

4.2 MODELING METHODOLOGY

4.2.1 Constitutive Models

The five ANSYS elements described in Part I (Chansawat et al. 2002b) are, again, used in this study; i.e., SOLID65 (concrete), LINK8 (reinforcing steel), SOLID46 (FRP), MATRIX27 (soil stiffness), and SHELL143 ("base plate"). In Part I, only the equations for the ascending branch of the stress-strain curves for both unconfined and confined concrete have been presented, as they are sufficient to analyze bridge response under service loading. However, when the strength of the bridge is of interest, the complete stress-strain curves are required.

As discussed in Part I, a 3-D reinforced concrete solid element (SOLID65) is used in ANSYS for the concrete modeling. Numerous researchers have

developed stress-strain models to represent concrete behavior under various conditions. In compression, the complete stress-strain relationships for both unconfined and confined concrete are required in the FE simulations to obtain accurate predictions of structural behaviors to failure. Confinement in concrete can significantly affect the shape of the stress-strain curve for the descending branch. Besides the degree of confinement, the slope of the descending branch is also dependent on the rate of loading, type of testing machine, size and location of strain gauge, and the presence or absence of ties or stirrups (Wang et al. 1978, Kent and Park 1971, Barnard 1964, and Balakrishnan and Murray 1988). Moreover, the descending portion is critical as a portion of the concrete compression zone is usually in this range of strains at ultimate (Wang et al. 1978).

The following are the constitutive models used in the study for both unconfined and confined concrete:

Unconfined Concrete – The expressions from Desayi and Krishnan's model (Bangash 1989) are implemented for both ascending and descending parts (region ABD in Fig. 4.1) as follows:

$$\sigma = \frac{E_0 \varepsilon}{1 + \left(\frac{\varepsilon}{\varepsilon_0'}\right)^2} \qquad [4.1]$$

where $\epsilon_0 = 2f_c'/E_0$ and $E_0 = 4733\sqrt{f_c'}$ [MPa] (ACI 2002).

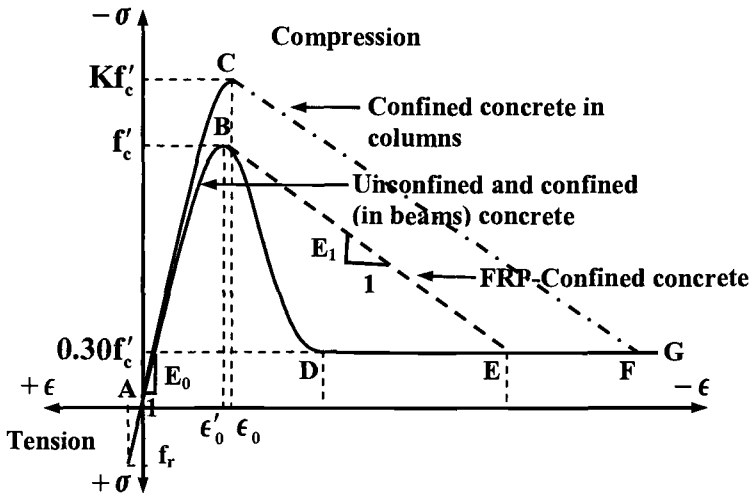

Concrete parameter	Value
K	1.068
f'_c	27.58 MPa
f_r	3.27 MPa
E_0	24.86 GPa
E_1	0.45 GPa
ε'_0	0.00222
ε_0	0.00214

Figure 4.1. Typical Stress-Strain Curves and Parameter Values Used for Concrete

Confined Concrete – The effect of concrete confinement is taken into account in the study to avoid underestimation of the failure load (Balakrishnan et al. 1988). In this study, a modified form of Kent and Park's model (Park et al. 1982) is used for concrete confined by rectangular ties in columns as follows:

For ascending branch (region AC): $f_c = Kf'_c\left[\frac{2\epsilon_c}{0.002K} - \left(\frac{\epsilon_c}{0.002K}\right)^2\right]$ [4.2]

where $K = 1 + \rho_s f_{yt}/f'_c$, and the maximum stress is assumed to be Kf'_c at a strain of $\varepsilon_0 = 0.002K$.

For descending branch (region CF): $f_c = Kf'_c[1 - Z_m(\epsilon_c - 0.002K)]$ [4.3]

where $Z_m = \dfrac{0.5}{\dfrac{3 + 0.29f'_c}{145f'_c - 1000} + \dfrac{3}{4}\rho_s\sqrt{\dfrac{h''}{s_t}} - 0.002K}$

For concrete confinement in beams as discussed in Part I, several researchers (Balakrishnan and Murray 1998 and Kemp 1998) have developed stress-strain relationships for concrete confined by steel stirrups, but none for confinement by FRP sheets. Accordingly, for simplicity it is assumed that for flexural members the behavior of FRP-confined concrete is similar to stirrup-confined concrete. In the study of the full-scale beams (Chansawat et al. 2002a), it was shown that FE models using this assumption can reasonably predict behaviors of the structural members. Thus, the assumptions of Kent and Park (1971) and Bhatt and Kader (1998) that the slope of the ascending part is independent of the confinement, and the maximum flexural stress achieved by both unconfined and confine concrete is the same and equal to f_c' (region AB) are applied. For the descending branch (region BE), the slope of the FRP-confined concrete from Balakrishnan and Murray (1988) and Balakrishnan et al. (1998) is as follows:

$$E_1 = -0.018E_0 \qquad [4.4]$$

For the stress-strain relationships discussed above, a cut-off point for the descending branch is assumed to be at $0.3\,f_c'$. Beyond this point, the concrete can still sustain stress at indefinitely large strain (regions DG, EG, or FG) (Barnard 1964 and Stevens et al. 1991). In the FE simulations, failure of members will occur before the concrete strain becomes excessive (Kent and Park 1971).

For the concrete in tension, the material is assumed to be linearly elastic with modulus E_0 up to the tensile strength, f_r, which can be calculated, based on ACI (2002):

$$f_r = 0.623\sqrt{f_c'} \text{ (MPa)} \quad [4.5]$$

Typical stress-strain curves and parameter values used in the study for the concrete are shown in Fig. 4.1.

Poisson's ratio is assumed to be constant throughout the loading history and equal to 0.2. Shear transfer coefficients (β) representing shear strength reduction factors when cracks occur are defined for the concrete element. Again, β values for closed and open cracks are assumed to be 1.0 and 0.2, respectively, as in Part I.

For the FE study of the full-scale beams, a typical yield strength for reinforcing steel provided by the fabricator is used (f_y = 455MPa), while the nominal yield strength is used in the FE models of the bridge (f_y = 276 MPa).

A summary of the material properties used in the FE models of the bridge is shown in Table 4. Material properties for concrete, soil, and "base plate" are obtained from the sensitivity study in Part I.

Table 4. Material Properties (Kachlakev and McCurry 2000)

Type of material	Material Properties				
	ν	E (MPa)	G (MPa)	Limiting value (Stress or Strain)	Thickness (mm)
(1)	(2)	(3)	(4)	(5)	(6)
Concrete	0.2*	24900*	--	--	--
Reinforcing steel	0.3*	199900*	--	$f_y = 276$*	--
CFRP laminate	$\nu_{12} = 0.216$ $\nu_{13} = 0.216$ $\nu_{23} = 0.3$	$E_{11} = 62100$ $E_{22} = 4830$ $E_{33} = 4830$	$G_{12} = 3270$ $G_{13} = 3270$ $G_{23} = 1860$**	$\varepsilon_{FRP} = 0.012$	1.1
GFRP laminate	$\nu_{12} = 0.216$ $\nu_{13} = 0.216$ $\nu_{23} = 0.3$	$E_{11} = 20700$ $E_{22} = 6900$ $E_{33} = 6900$	$G_{12} = 1520$ $G_{13} = 1520$ $G_{23} = 2650$**	$\varepsilon_{FRP} = 0.02$	1.3
Soil	0.25*	1170*	--	--	--
Base plate	0.3*	2.07×10^{11}*	--	--	25.4*

Notes: * From Part I. Other parameter values for concrete, see Fig. 4.1.

$$^{**}G_{23} = \frac{E_2}{2(1+\upsilon_{23})}$$

4.2.2 Modeling Approach

Taking advantage of symmetry, only a longitudinal half of the bridge is modeled to effectively reduce CPU time and disk space. Perfect bonding between concrete and steel is assumed, and should be acceptable unless a bond failure occurs (Isenberg 1993). Moreover, no slip was observed in testing of the full-scale beams.

The FRP-confined concrete model is used in both transverse and longitudinal beams of the FRP-strengthened bridge as CFRP sheets were U-

wrapped around the beams. Concrete confinement is assumed for the concrete within rectangular ties in the columns. For other locations (e.g., concrete cover, bridge deck and curbs or end abutments), unconfined concrete is assumed.

Retrofitting the bridge with several different CFRP and GFRP schemes creates discontinuities in the thickness, which leads to a modeling difficulty. This can be avoided using an equivalent thickness approach by considering that an increase or a decrease in FRP thicknesses can be compensated by decreasing or increasing the elastic and shear moduli, respectively.

Based in part on the sensitivity study in Part I, the values of material property parameters are shown in Table 4. The bridge FE model (after FRP strengthening) is shown in Fig. 4.2 with typical steel and FRP reinforcement (Figs. 4.2(a)-(c)) and soil interface modeling (Fig. 4.2(d)).

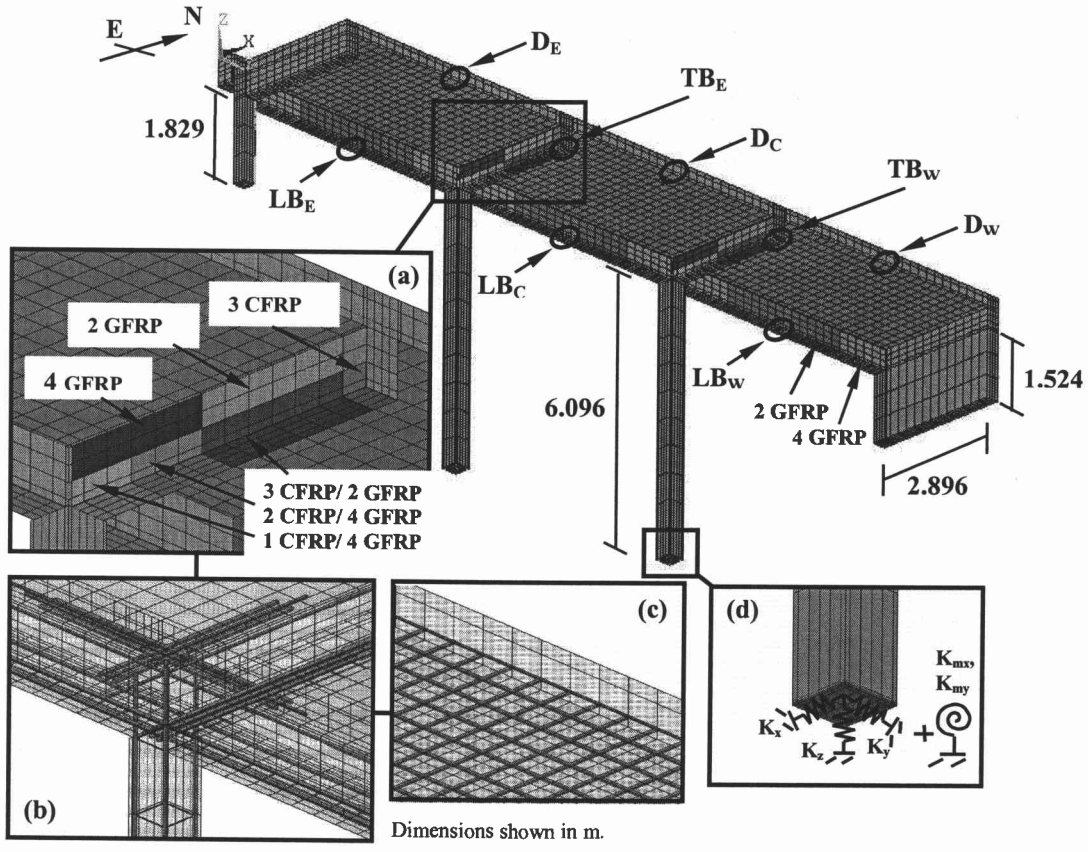

Figure 4.2. Bridge FE Modeling: (a) Typical FRP Reinforcement; (b) Typical Steel Reinforcement in Beams and Columns; (c) Typical Reinforcement in Bridge Deck; (d) Typical Soil-Structure Interface Modeling

Notes: 1. 4 GFRP represents four layers of GFRP laminates, while 1 CFRP/4 GFRP represents a combination of one layer of CFRP laminate and four layers of GFRP laminates, and so on.
2. For the unstrengthened bridge, no FRP reinforcement exists.

The total numbers of elements used in the bridge models before and after FRP strengthening are 15623 and 16791, respectively (SOLID65: 10504; LINK8: 4954; SOLID46 (after FRP strengthening): 1168; SHELL143: 160; and MATRIX27: 5 elements).

Newton-Raphson equilibrium iteration is used to solve for the nonlinear behavior of the bridge models using an incremental process controlled by force and displacement convergence tolerances to obtain accurate predictions. However, the incremental process will stop due to solution divergence once the residual force or displacement exceeds the specified criteria. The system of equations cannot be solved due to the degradation of the structural stiffness matrix when extensive cracking causes an ill-conditioned matrix (Vidosa et al. 1991). Thus, the maximum sustained load in the analysis, corresponding to the last converged load step, is used as the ultimate load prediction (Vidosa et al. 1991, Bhatt and Kader 1998, Balakrishnan and Murray 1988b, and Barzegar and Maddipudi 1997).

Unlike the behavior of the HC bridge under service loading in Part I, the behavior of the bridge here is highly nonlinear and subjected to loads up to failure. More cracking occurs, which requires many iterations in each load step. More attention to adjusting the convergence tolerances is needed. Larger computer resources in terms of disk space and CPU time are required. In this study, the nonlinear analysis of each HC bridge model took approximately 120 hrs to reach the ultimate load on a HP J6000 workstation with 2x 552 MHz HP PA-8600 processors with 2GB of RAM and consumed disk space up to 3 GB.

Force and displacement convergence criteria are 10% and 4%, respectively, for failure analysis of the bridges based on mass-proportional loading, and are 10% and 6%, respectively, for that based on multiples of truck loading. The maximum number of iterations per loading increment is 50 for both analyses.

4.3 FULL-SCALE BEAM STUDY AND DEVELOPMENT OF FAILURE PREDICTING MODELS

Four full-scale reinforced concrete beams (Kachlakev and McCurry 2000) replicating the transverse beams of the HC bridge were fabricated and tested. They include an unstrengthened (control) beam, a flexure-strengthened beam, a shear-strengthened beam, and a flexure/shear-strengthened beam. All beams had the same geometry and steel reinforcement. CFRP sheets were applied to the bottom of the flexure-strengthened beam and GFRP sheets to the sides of the shear-strengthened beam to increase the flexural and shear capacities of the beam, respectively. For the flexure/shear-strengthened beam, a direct combination of these FRP strengthening methods was applied. The control and the flexure/shear-strengthened beams replicate the transverse beams of the HC bridge before and after FRP retrofitting, respectively. Conventional 60 mm strain gauges were placed throughout the beams; i.e., on the steel reinforcing, on the concrete, and on FRP surfaces. Direct current displacement transducers (DCDTs) were installed at the

center bottom fiber of all the beams at midspan. The beams were simply supported and subjected to four-point loading until failure except for the flexure/shear-strengthened beam, for which the applied load had to be terminated at 710 kN (160 kips) due to the limitations of the testing machine (Kachlakev and McCurry 2000).

Three-dimensional FE models were developed to simulate the behavior of the four full-scale experimental beams using ANSYS (1998). Confinement in the concrete due to FRP encasement and multi-axial stresses from concentrated loads were taken into consideration. Modeling methodology presented in the previous section was also implemented in the study of the full-scale beams. Taking advantage of symmetry, only a quarter of the beam was modeled. Fig. 4.3 shows the geometry and steel reinforcement details for all the beams.

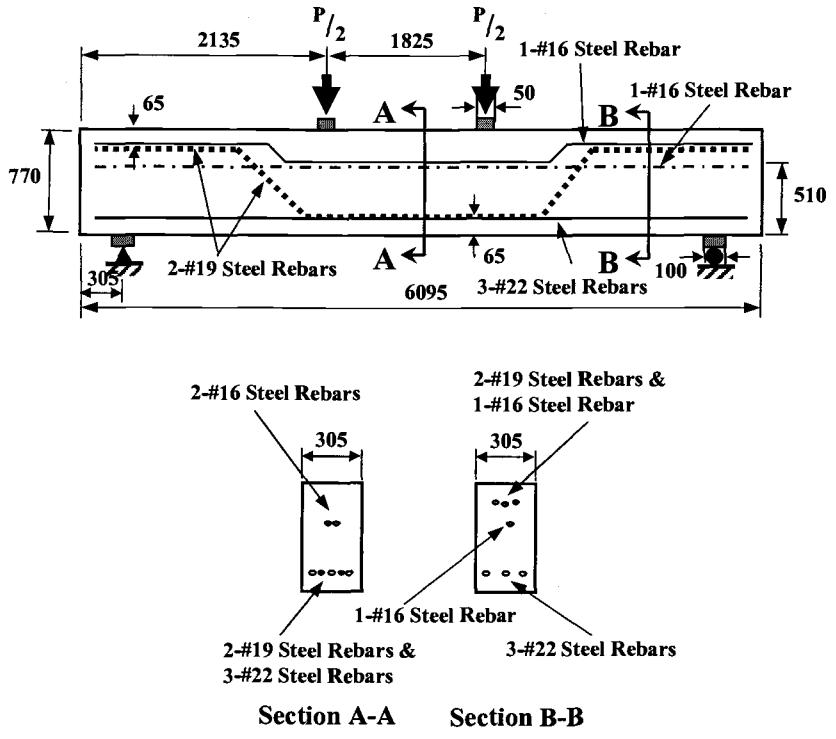
P/2
2135
1825
P/2
1-#16 Steel Rebar
1-#16 Steel Rebar
65
50
A
B
770
510
A
65
B
2-#19 Steel Rebars
305
6095
3-#22 Steel Rebars
100
2-#16 Steel Rebars
2-#19 Steel Rebars &
1-#16 Steel Rebar
305
305
1-#16 Steel Rebar
2-#19 Steel Rebars &
3-#22 Steel Rebars
3-#22 Steel Rebars
Section A-A
Section B-B

(a)

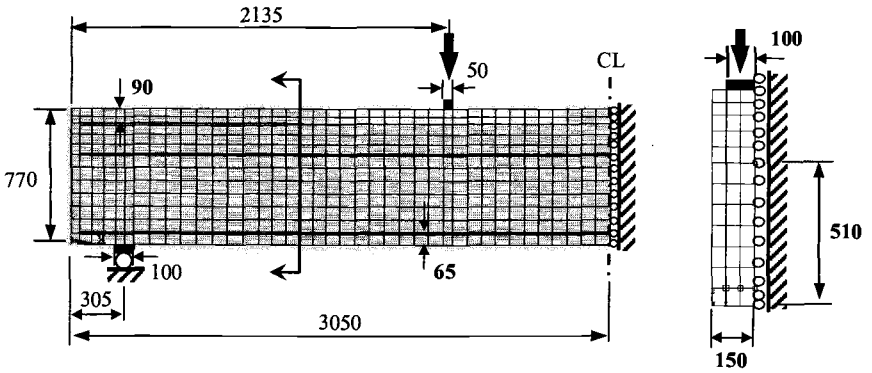
2135
50
CL
90
770
100
65
305
3050
100
510
150

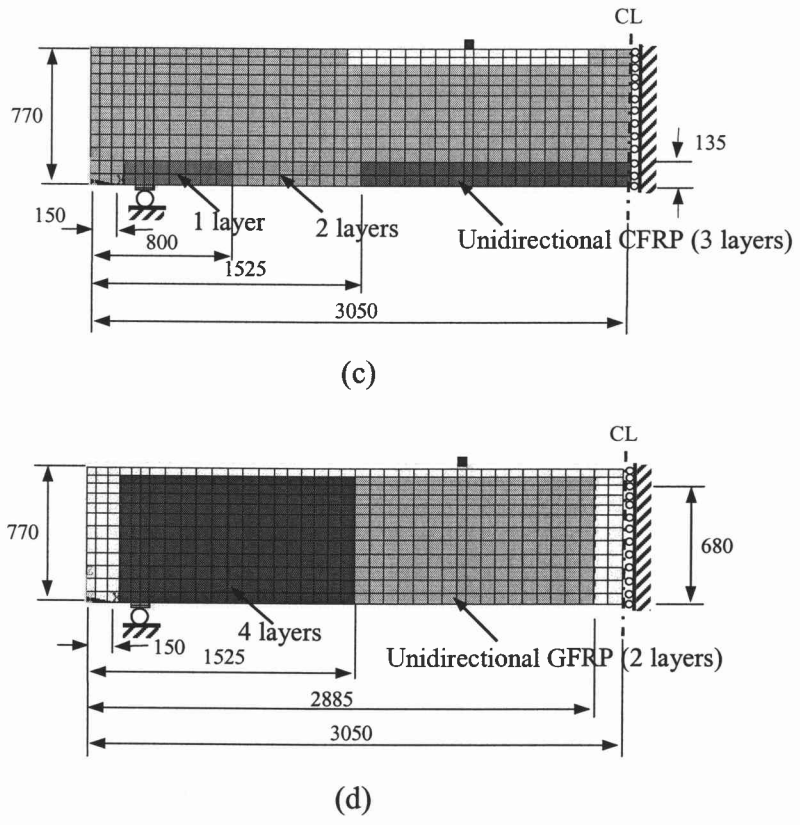

Figure 4.3. Geometry and Steel Reinforcement Details for Experimental Beams (dimensions shown in mm.): (a) Experimental Beam; (b) Unstrengthened Beam Model; (c) Flexure-Strengthened Beam Model; (d) Shear-Strengthened Beam Model

Figs. 4.3(b)-(d) show FE models of the unstrengthened, flexure-strengthened, and shear-strengthened beams, respectively. The FE model for the flexure/shear-strengthened beam is the direct combination of Figs. 4.3(c) and 4.3(d). In this paper, comparisons between FE predictions and experimental results are presented for load vs. tensile strain for the main steel rebar for all beams (Fig.

4.4) and crack patterns for the unstrengthened and flexure/shear-strengthened beams (Fig. 4.5).

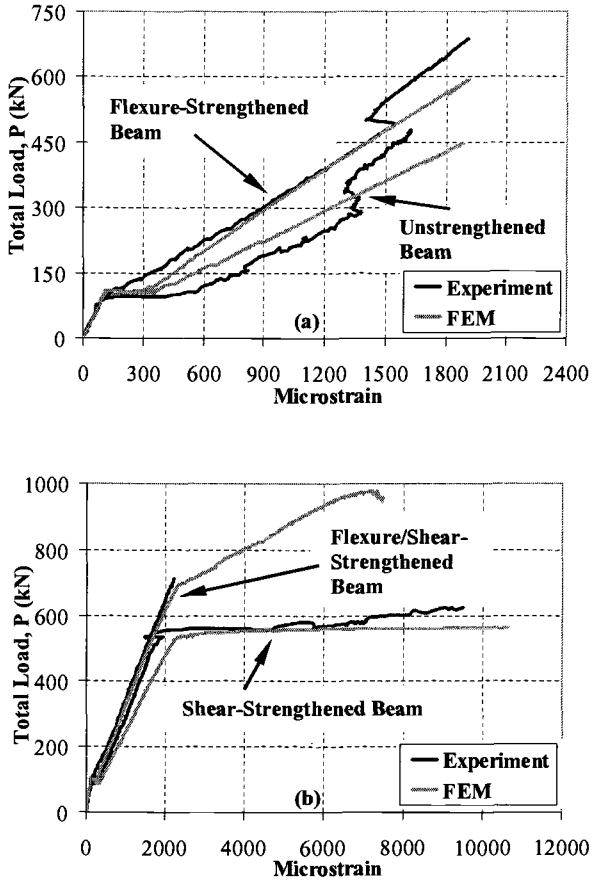

Figure 4.4. Load-Tensile Strain Plots for Main Steel Rebar: (a) Unstrengthened and Flexure-Strengthened Beams; (b) Shear and Flexure/Shear-Strengthened Beams

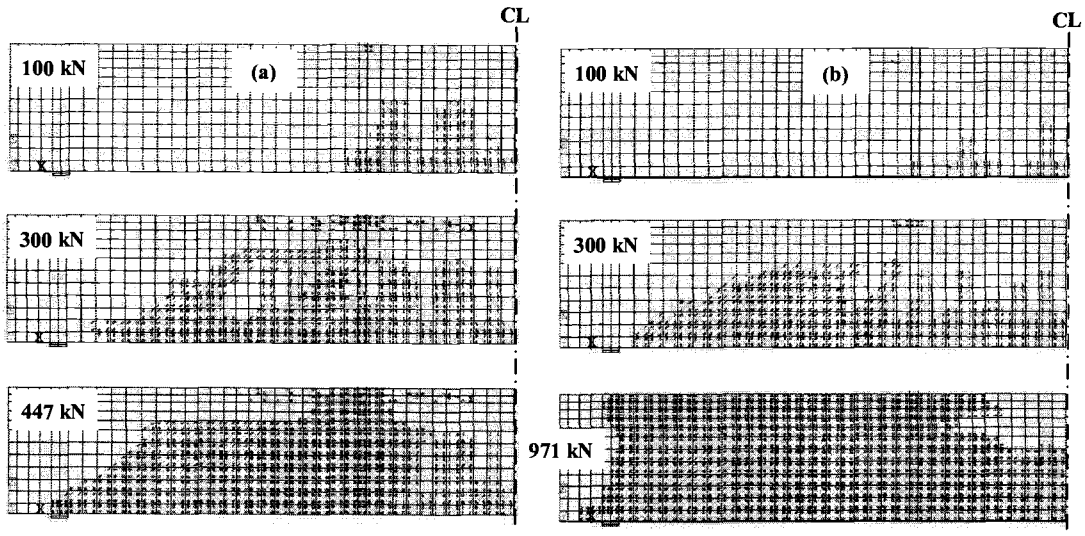

Figure 4.5. Crack Pattern Development: (a) Unstrengthened Beam; (b) Flexure/Shear Strengthened Beam

The FE models show good agreement with data and observations from the beam experiments. For additional comparisons and discussion, see Chansawat et al. (2002a).

Since the FE models can predict the behavior of the actual full-scale beams up to failure, the FE bridge models, including these same beams, are extended to predict overall bridge responses in the nonlinear range. The results and discussion of the bridge responses under scaled gravity and scaled truck loadings to failure are included in the following sections.

4.4 NONLINEAR BEHAVIOR OF THE HC BRIDGE UNDER SCALED GRAVITY LOAD

4.4.1 Analysis Procedure

To determine the actual capacity of bridges, destructive testing has to be performed. However, the HC bridge is a historic structure and is still operational. One practical approach is to use the analytical tool that was developed in the study of the full-scale beams tested to failure and in the service load study of the HC bridge presented in Part I.

Two bridge models are examined in this study; i.e., the unstrengthened and FRP-strengthened HC bridge. The strengthened bridge model is that obtained from the sensitivity study in Part I. The unstrengthened bridge model lacks the FRP elements (SOLID46) on the beams, and there is no concrete confinement for the beams. The models are subjected to downward, mass-proportional (gravity) loading of increasing amplitude up to failure from the virgin state (w/o cracks). Unit weight for each material is defined; i.e., 22.78 kN/m^3 for concrete and 76.82 kN/m^3 for steel. Weight of the FRP sheets is neglected.

Comparisons of structural behaviors are made in terms of load-deflection relationships, crack patterns, and yielding in reinforcing steel. For the load-deflection relationships (Fig. 4.6), in each loading step the total load can be back-calculated from the sum of the vertical reactions at each support. The locations of the deflections of interest are at the center bottom of the east and west transverse

beams (TB_E and TB_W) (TB-transverse beam, E and W-at east and west sides); at the center bottom of the east, center, and west sides of the deck (D_E, D_C, and D_W) (D-bridge deck, E, C, and W-at east, center, and west sides); and at the center bottom of the east, center, and west longitudinal beams at the middle of each span (LB_E, LB_C, and LB_W) (L-longitudinal beam, E, C, and W-at east, center, and west sides). Each location is shown in Fig. 4.2.

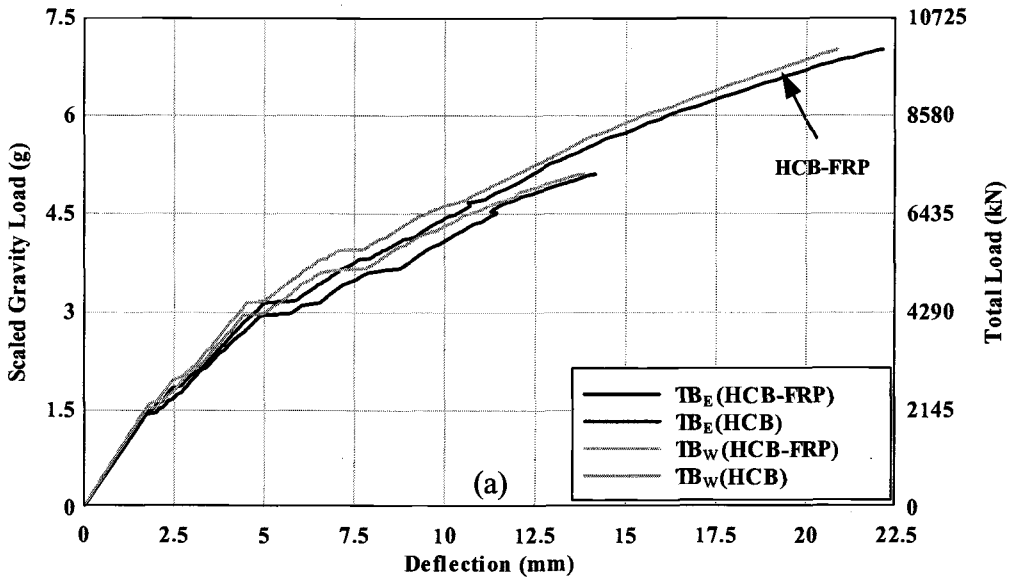

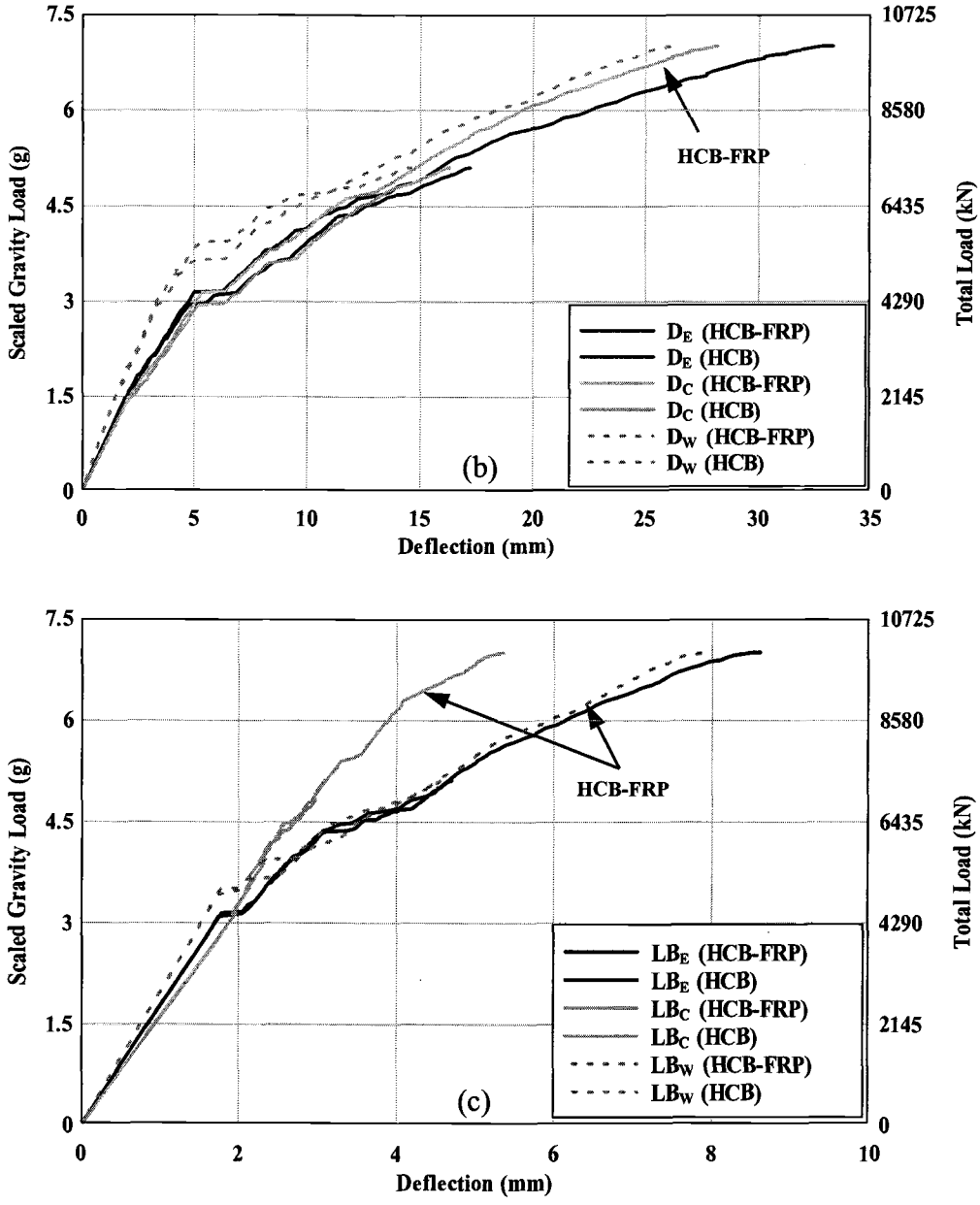

Figure 4.6. Scaled Gravity Load/Total Load-Deflection Relationships: (a) Transverse Beams; (b) Bridge Deck; (c) Longitudinal Beams

To present how cracks propagate from the bottom to the top of the bridge deck, three concrete layers (B-Bottom, M-Middle, and T-Top) from the deck are plotted separately. Fig. 4.7 shows typical initial cracks in the bridge deck. Fig. 4.8 shows crack development in both unstrengthened and strengthened bridge models at higher load levels. The crack patterns for each model are plotted for both transverse beams in Fig. 4.9. The yielding of the reinforcing bars is also shown (Fig. 4.10) to better understand failure mechanisms. The steel shown in the transverse beams are tension bars, which are located on the bottom of the beams, and those shown in the deck are reinforcing bars in the bottom mat.

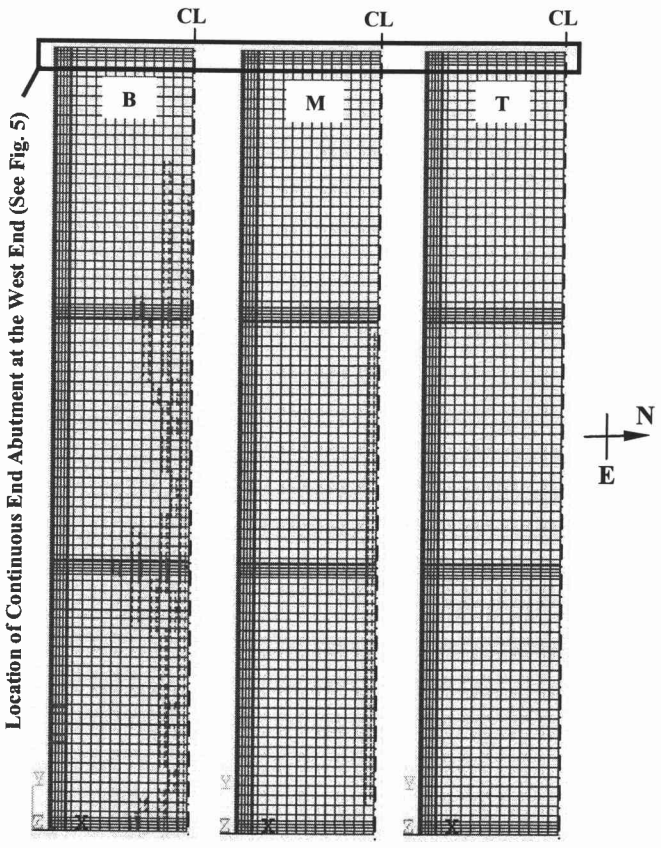

Figure 4.7. Initial Cracks in Bridge Deck

Notes: 1. These plan views are observed from the top of the deck.
2. These cracks are based on a scaled gravity load of 3.5g on the FRP-strengthened bridge.

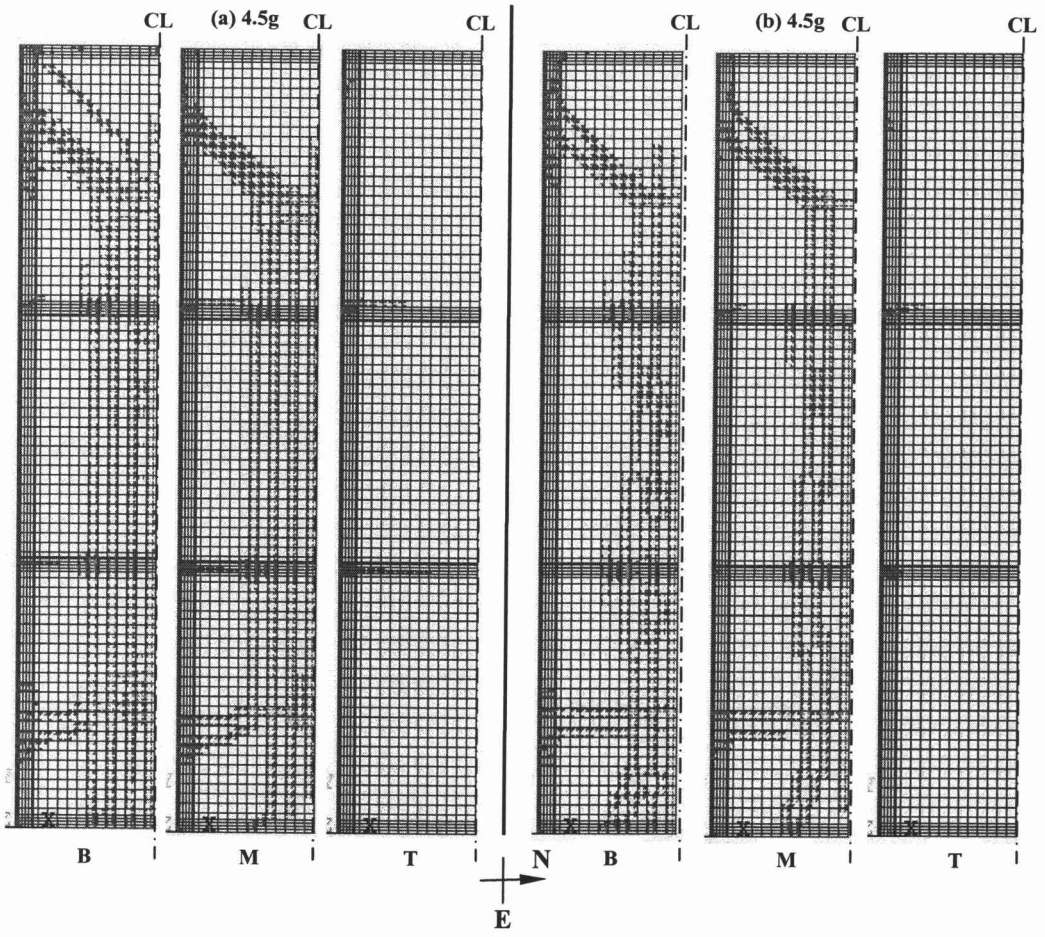

Figure 4.8. Crack Propagation in Bridge Deck (Scaled Gravity Loading): (a) Unstrengthened Bridge; (b) FRP-Strengthened Bridge

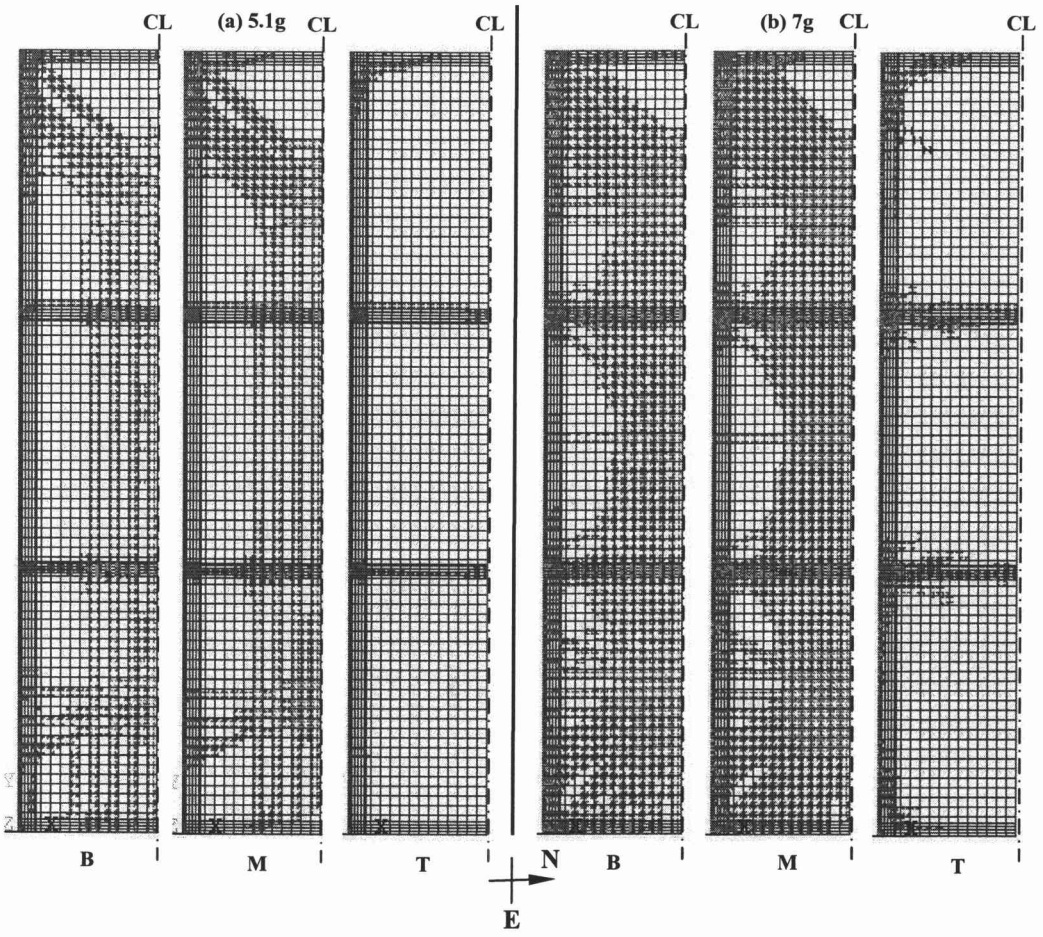

Figure 4.8 (Cont'd). Crack Propagation in Bridge Deck (Scaled Gravity Loading): (a) Unstrengthened Bridge; (b) FRP-Strengthened Bridge

Note: These plan views are observed from the top of the deck.

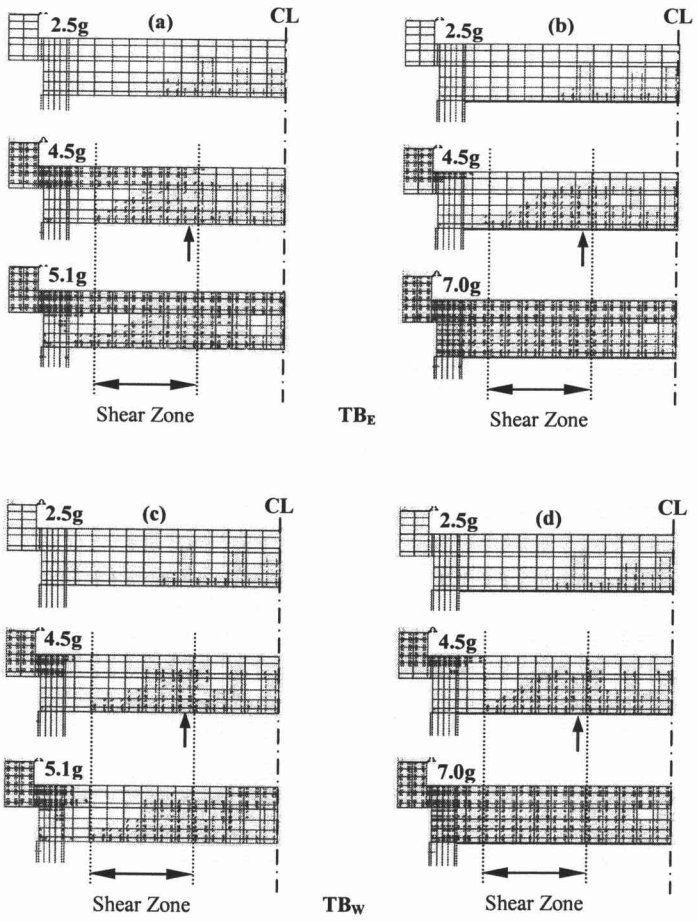

Figure 4.9. Crack Propagation in Transverse Beams (Scaled Gravity Loading): (a) and (c) Unstrengthened Bridge; (b) and (d) FRP-Strengthened Bridge

Note: ↑ indicates the location of the tension steel bars that yield first (also see Fig. 4.10).

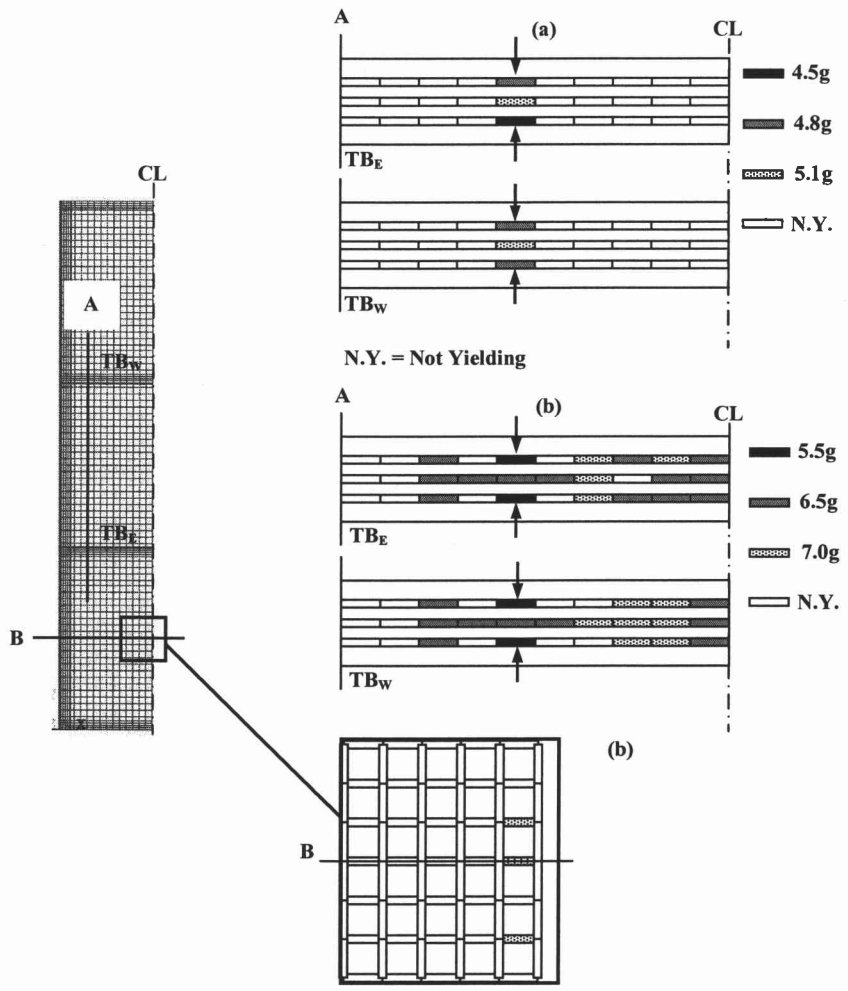

Figure 4.10. Yielding in Reinforcing Steel (Scaled Gravity Loading): (a) Unstrengthened Bridge; (b) FRP-Strengthened Bridge

Note: ↑ indicates the location of the tension steel bars that yield first.

4.4.2 Load-Deflection Relationships

The ultimate scaled gravity loads that can be applied to the unstrengthened and FRP-strengthened bridge models (from the last converged load steps) are 5.1g (1g = 9.81 m/sec^2) and 7g, respectively (support reactions are 7300 kN and 10000 kN, respectively). The mass-proportional loading-based capacity of the bridge is increased by 37% due to FRP strengthening. Like the full-scale beams from the previous study, regardless of the presence of the FRP sheets, both bridge models first crack (both starting in the transverse beams) at about the same loading level; i.e., at 1.455g (2080 kN) and at 1.458g (2083 kN) for the unstrengthened and strengthened bridges, respectively. In Fig. 4.6(a), major cracks simultaneously occurring in the transverse beams can be observed from a sudden increase in deflection at constant scaled gravity load. From the plot, those cracks develop in the unstrengthened transverse beams at a scaled gravity load of 3g, while at about a scaled gravity load of 3.3g in the strengthened beams. Moreover, the strengthened beams deflect less than the unstrengthened beams at the same load level.

From Fig. 4.6(b), D_W shows the highest deck stiffness between the start of loading and about 3.5g. This is because fewer cracks propagate to the west side of the deck, which is influenced by the continuous end abutment. It can be seen in Fig. 4.7 that fewer cracks develop in the bottom layer of the west deck. Moreover, no cracks propagate through the middle layer of the deck. For LB_C, no cracks have

developed, and LB_C shows the highest stiffness compared to the other longitudinal beams (Fig. 4.6(c)).

4.4.3 Crack Patterns

Crack development in both models is shown in Figs. 4.7 to 4.9. Generally, for both models, cracks first start in the transverse beams (not shown here). Then, they longitudinally propagate through the deck starting from the bottom layer (Fig. 4.7). As the loading increases, more cracks develop and penetrate through the upper layers (Figs. 4.7 and 4.8). The cracks on the west end of the deck grow diagonally toward the south-west corner of the deck, instead of growing longitudinally along the deck as on the east end. This is due to the presence of the continuous end abutment at the west end. Cracks also develop in the longitudinal beams, mostly in the end spans (not shown here). Fewer cracks and a narrower band of cracks in the deck can be observed for the strengthened bridge at the same loading level (Fig. 4.8 at a load of 4.5g). The crack patterns at failure for the transverse beams from both models resemble those of the full-scale unstrengthened and flexure/shear-strengthened beams (Figs. 4.9(a) and 4.9(c) vs. Fig. 4.5(a) and Figs. 4.9(b) and 4.9(d) vs. Fig. 4.5(b)). Therefore, it can be expected that a shear failure would occur in the transverse beams of the unstrengthened bridge, as in the

experimental beam (due to the lack of shear reinforcement).

4.4.4 Yielding in Reinforcing Steel

The tension steel bars in the transverse beams for both models start yielding in the shear zone, as indicated in Figs. 4.9 and 4.10. For the strengthened beams, the yielding in the steel bars is delayed due to the contribution of the FRP sheets (Fig. 4.10). That is, one of the bars yields first in the unstrengthened beam (TB_E) at a scaled gravity load of 4.5g (Fig. 4.10(a)), and then more bars yield as the load increases up to a load of 5.1g, at which the structure is considered failed. For the strengthened beams, the bars yield first at a scaled gravity load of 5.5g (Fig. 4.10(b)) and yielding progresses as the load increases. Moreover, yielding for the strengthened beams also develops in the flexure zone (at midspan and vicinity), indicating that the stress can be redistributed to the reinforcing steel in the flexure zone through the FRP sheets. Yielding is also found near the center of the east side of the deck at the ultimate load (Section B) (Fig. 4.10(b)).

It should be noted that at failure the maximum strain is 3310 microstrain in the CFRP, which is lower than the limiting strain of the CFRP shown in Table 4. The maximum strain occurs at the same place where the tension bars start yielding in both beams. Fig. 4.10(a) confirms that the unstrengthened bridge would fail in shear in the transverse beams (most likely in TB_E), as yielding of the tensile steel

bars occurs only within the shear zone. The strengthened bridge is also expected to fail in the transverse beams, but due to flexural failure (the tension bars yield in the flexure zone, as discussed). Flexural failure for the strengthened beam was similarly expected in the full-scale beam test (McCurry 2000).

4.5 NONLINEAR BEHAVIOR OF THE HC BRIDGE UNDER SCALED TRUCK LOADS

4.5.1 Analysis Procedure

The nonlinear response of the bridge to scaled truck loads is examined in this section. The loading configuration and axle weights are based on the full truck load in Part I. The locations of the front and tandem axles of the truck on the bridge deck are shown in Fig. 4.11(a) (Position 4). This truck location is used in the study, as it induces the maximum strain in the east transverse beam (TC in Part I).

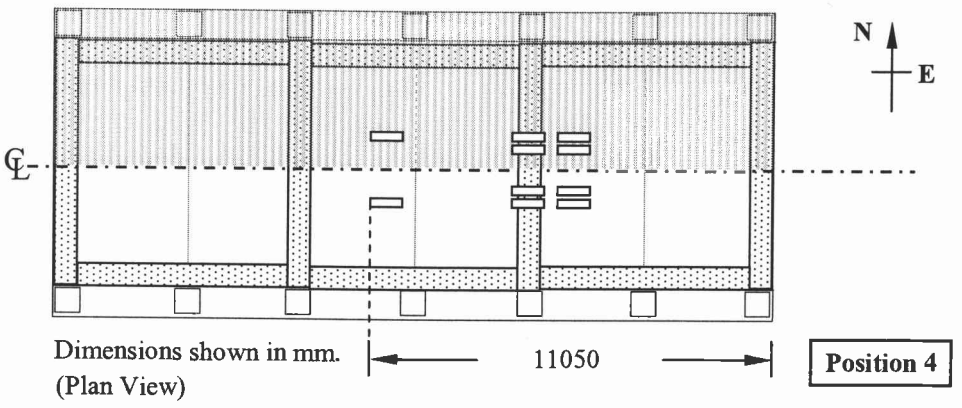

Figure 4.11. Location of Applied Truck Load

The two models (unstrengthened and FRP-strengthened bridge) are again used for comparison purposes. They are gradually loaded to failure from the virgin state with increments of the full truck load. The self-weight of the bridge is included in the loading. Comparisons of structural behaviors between the unstrengthened and FRP-strengthened models are made in terms of load-deflection relationships, crack patterns, and yielding development in reinforcing steel as shown in Figs. 4.12 to 4.15, respectively.

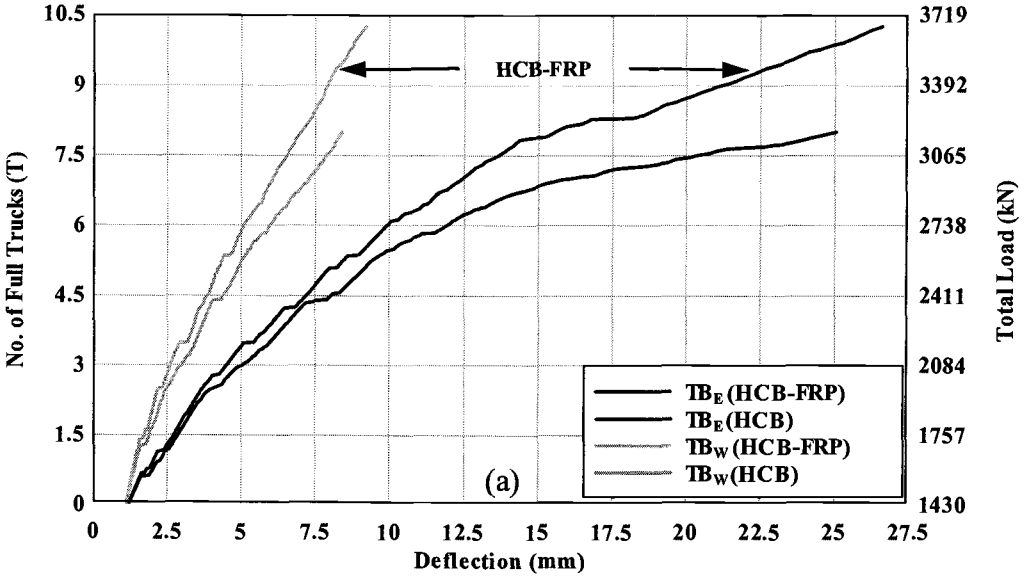
HCB-FRP
(a)
TB_E (HCB-FRP)
TB_E (HCB)
TB_W (HCB-FRP)
TB_W (HCB)
No. of Full Trucks (T)
Total Load (kN)
Deflection (mm)
10.5
9
7.5
6
4.5
3
1.5
0
3719
3392
3065
2738
2411
2084
1757
1430
0
2.5
5
7.5
10
12.5
15
17.5
20
22.5
25
27.5

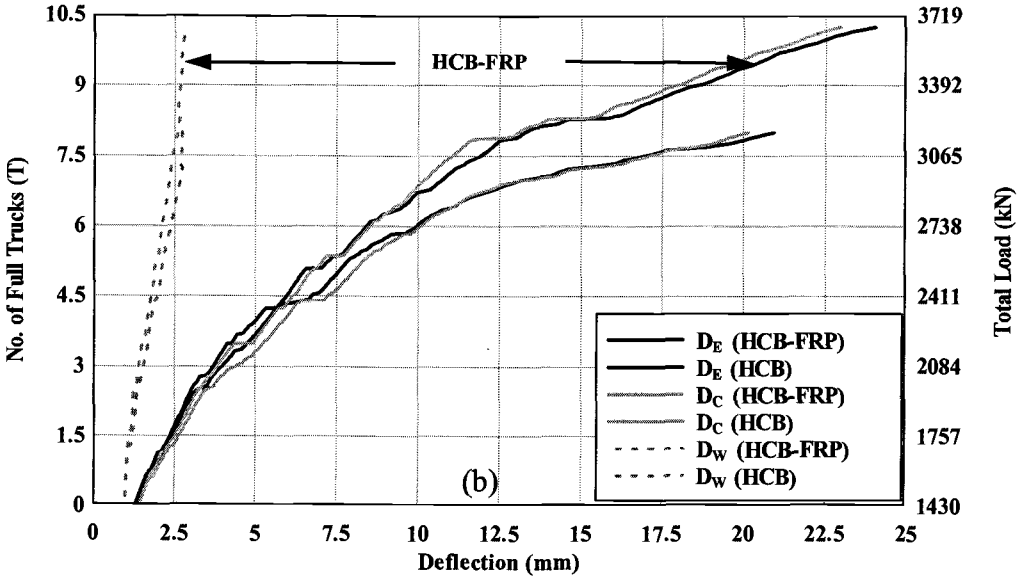
HCB-FRP
(b)
D_E (HCB-FRP)
D_E (HCB)
D_C (HCB-FRP)
D_C (HCB)
D_W (HCB-FRP)
D_W (HCB)
No. of Full Trucks (T)
Total Load (kN)
Deflection (mm)
10.5
9
7.5
6
4.5
3
1.5
0
3719
3392
3065
2738
2411
2084
1757
1430
0
2.5
5
7.5
10
12.5
15
17.5
20
22.5
25

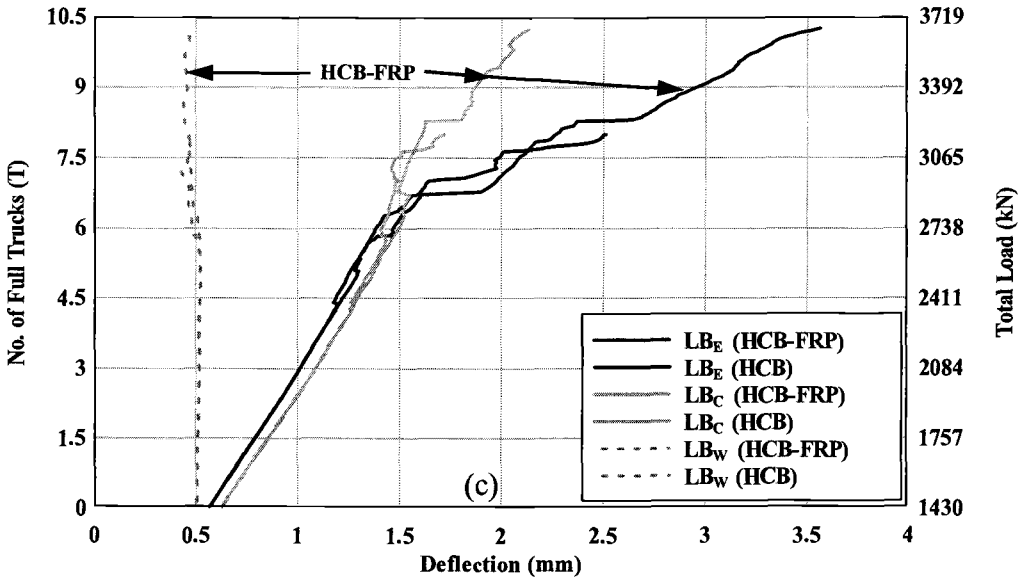

Figure 4.12. Scaled Truck Load/Total Load-Deflection Relationships: (a) Transverse Beams; (b) Bridge Deck; (c) Longitudinal Beams

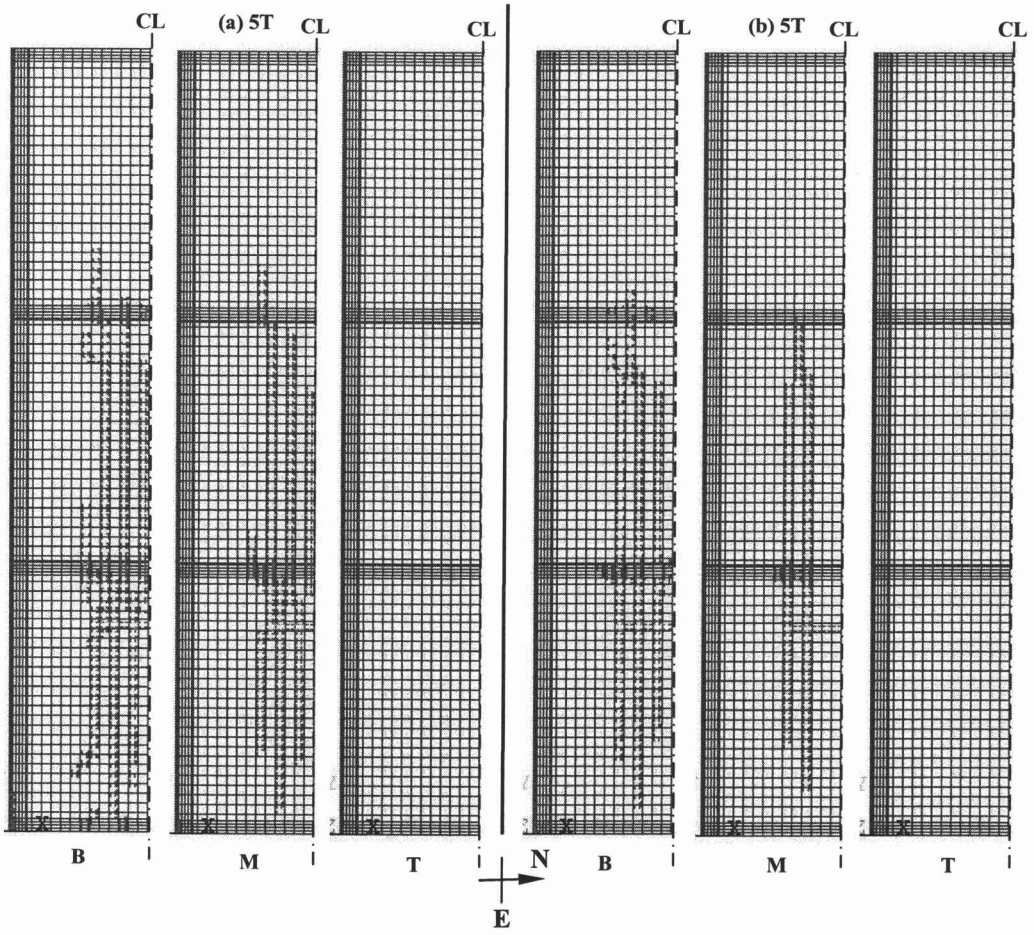

Figure 4.13. Crack Propagation in Bridge Deck (Scaled Truck Loading): (a) Unstrengthened Bridge; (b) FRP-Strengthened Bridge

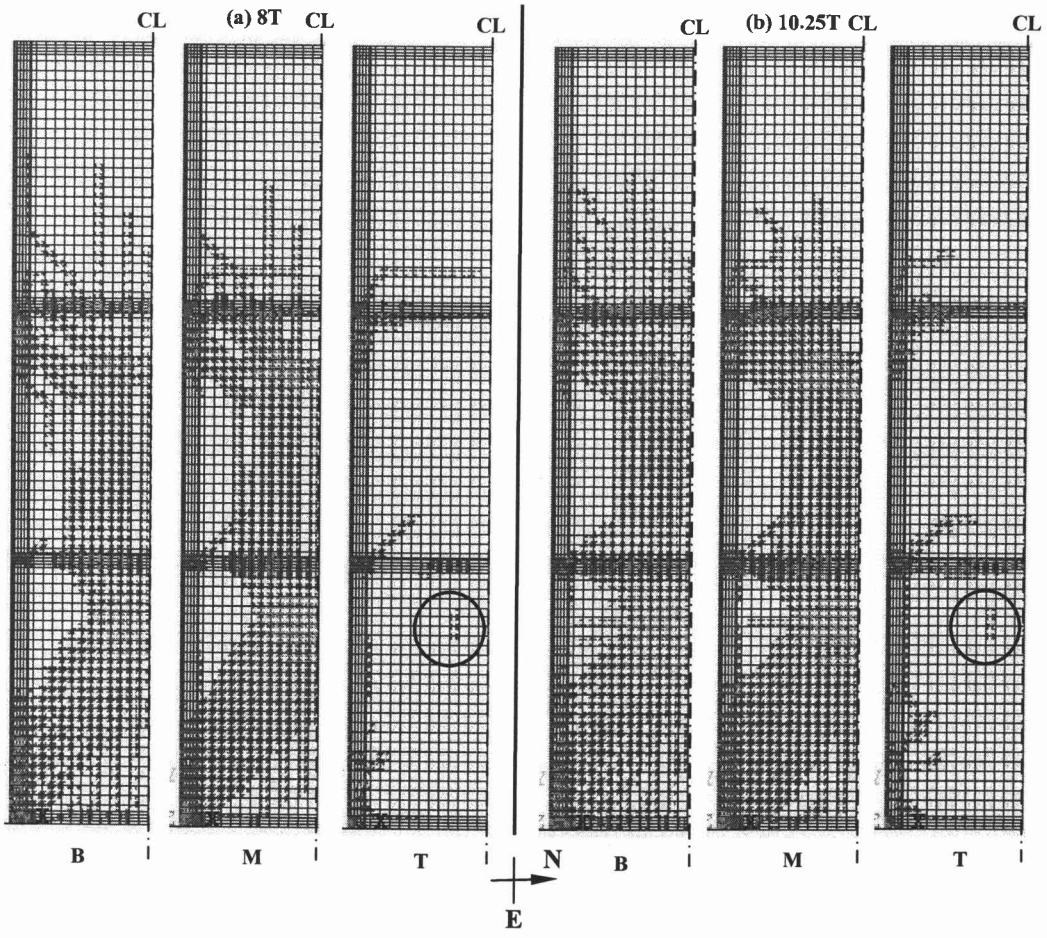

Figure 4.13 (Cont'd). Crack Propagation in Bridge Deck (Scaled Truck Loading): (a) Unstrengthened Bridge; (b) FRP-Strengthened Bridge

Note: These plan views are observed from the top of the deck.

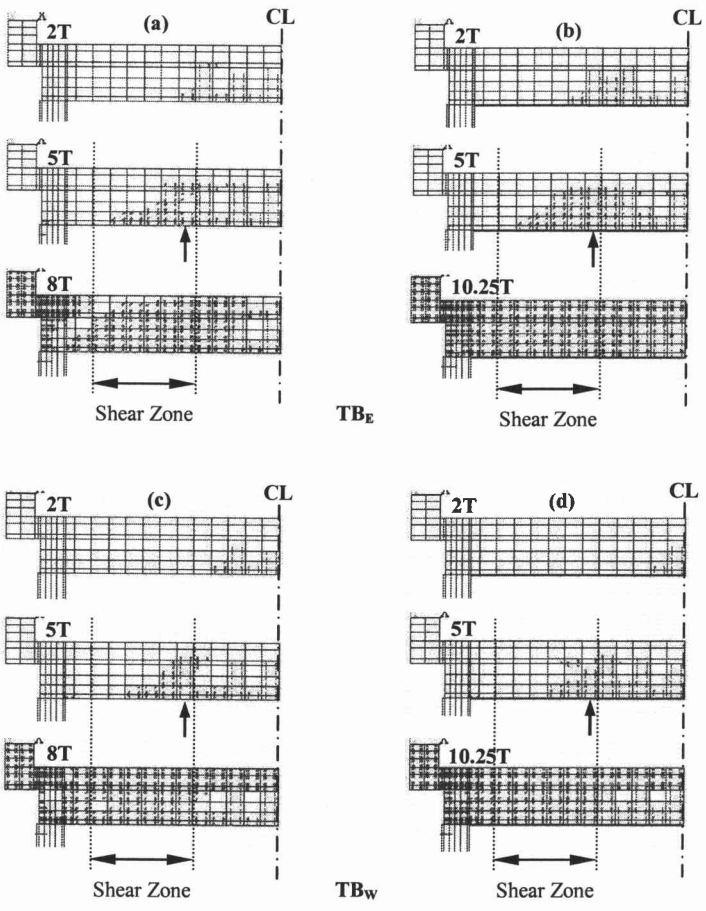

Figure 4.14. Crack Propagation in Transverse Beams (Scaled Truck Loading): (a) and (c) Unstrengthened Bridge; (b) and (d) FRP-Strengthened Bridge

Note: ↑ indicates the location of the tension steel bars that yield first (also see Fig. 4.15).

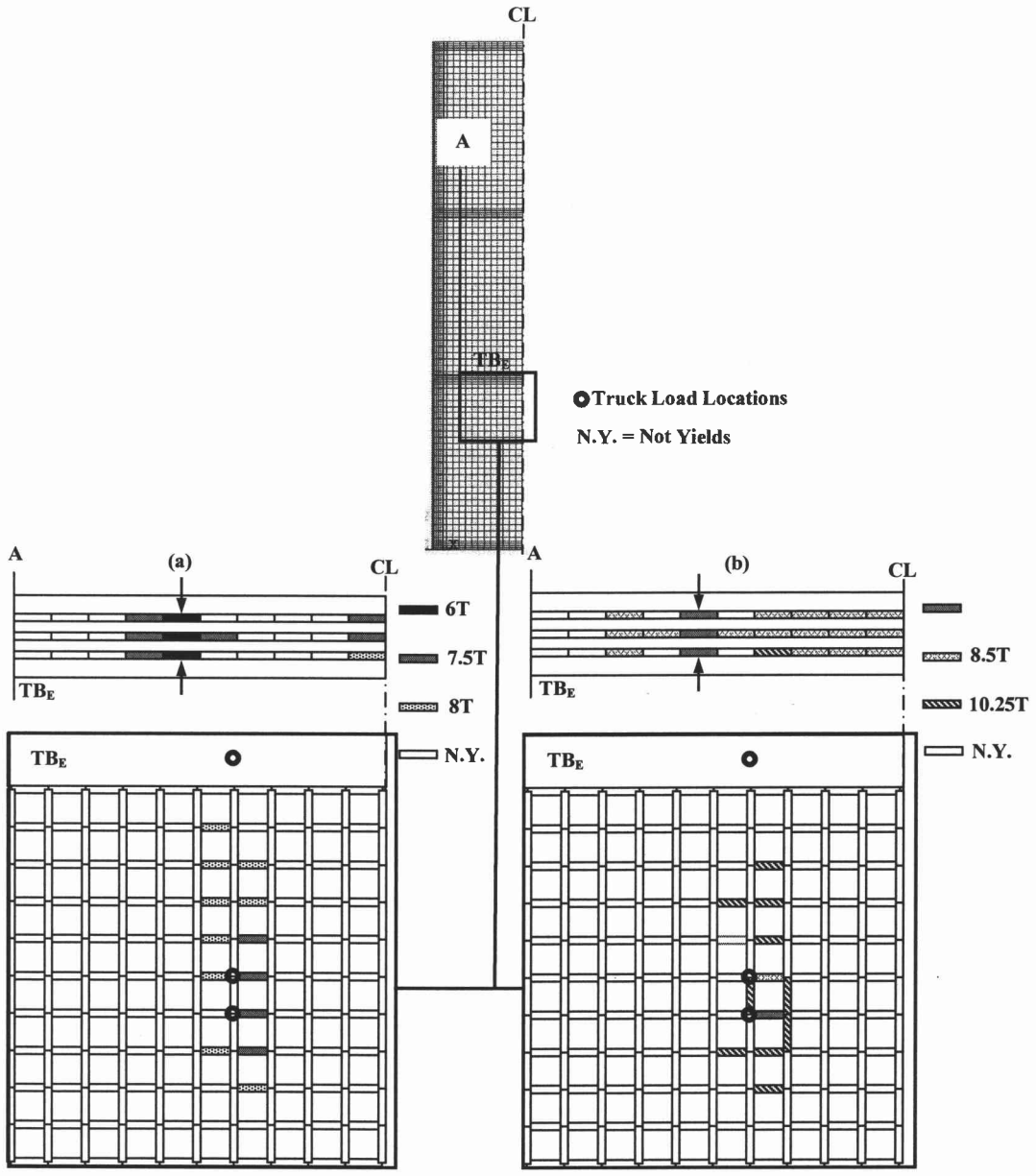

Figure 4.15. Yielding in Reinforcing Steel (Scaled Truck Loading): (a) Unstrengthened Bridge; (b) FRP-Strengthened Bridge

Note: ↑ indicates the location of the tension steel bars that yield first (also see Fig. 15).

4.5.2 Load-Deflection Relationships

The maximum scaled truck loads, including the bridge self-weight, that can be applied to the unstrengthened and FRP-strengthened bridges are 8T (1T = 1 full truck = 218 kN) or 1750 kN and 10.3T (2240 kN), respectively. The truck-carrying capacity is increased by 28% when FRP sheets are installed. Again, regardless of the FRP strengthening, both bridges start cracking in the transverse beams at about the same loading level; i.e., at 0.62T (135 kN) and at 0.63T (139 kN) for the unstrengthened and strengthened bridge, respectively. It can be seen from Fig. 4.12(a) that the deflection of the strengthened beams is less than that of the unstrengthened beams at the same load level. Moreover, for both models, the west transverse beam (TB_W) deflects less than the east one (TB_E). This is because no yielding occurs in the tension steel bars in TB_W, and there is more influence from the tandem axles of the applied truck load placed right above TB_E (Fig. 4.11).

From Fig. 4.12(b), the behaviors of the east side (D_E) and center (D_C) of the deck are similar in each model. However, the deflections of the east side (D_E) and center (D_C) of the deck can be significantly reduced from FRP strengthening. The slope of the load-deflection curve of D_W for both models is steepest, as fewer cracks occur in the west side of the deck (Fig. 4.13), due to the truck load applied on the east side and center of the deck (Fig. 4.11).

4.5.3 Crack Patterns

Crack development in both models under the scaled truck loading is similar to that under the scaled gravity loading. That is, cracks first begin in the transverse beams (not shown here), and then propagate through the deck from the bottom layer (similar to Fig. 4.7). However, the cracks are most dense at the east side and center of the deck where the loads are applied (Fig. 4.13). Furthermore, cracks penetrate through the top layer of the east side of the deck under the loading for both models at ultimate (circled in Fig. 4.13). Like the bridge under the scaled gravity load, fewer cracks develop in the bridge deck (mostly on the east side and center of the bridge deck) for the strengthened bridge (Fig. 4.13 at a load of 5T). A narrower band of cracks can also be observed in the strengthened bridge. The crack patterns of the transverse beams from both bridge models at failure, again, resemble those of the full-scale unstrengthened and flexure/shear-strengthened beams (Figs. 4.14(a) and 4.14(c) vs. Fig. 4.5(a) and Figs. 4.14(b) and 4.14(d) vs. Fig. 4.5(b)). A shear failure is, again, expected in TB_E of the unstrengthened bridge, while a flexural failure is expected in TB_E for the strengthened bridge.

4.5.4 Yielding in Reinforcing Steel

As in the scaled gravity load case, the tension steel yields first in the transverse beams for both models in the shear zone (Fig. 4.14). The yielding of the steel in the strengthened beam is delayed. The tension steel yields first in the unstrengthened beam (TB_E) at a scaled truck load of 6T, while it yields first in the FRP-strengthened beam at a load of 7.5T (Figs. 4.15(a) and (b)). Steel yielding in the flexure zone can be found in the unstrengthened beam, but yielding in the shear zone dominates (Fig. 4.15(a)). For the strengthened beam, the yielding of the steel develops mostly in the flexure zone (Fig. 4.15(b)). There is no yielding in the tension steel bars for TB_W for both models because the truck load is applied far enough from TB_W. Yielding in the reinforcing steel mat of the east side of the deck develops in both models below the loading locations (Fig. 4.15). However, fewer steel bars yield in the strengthened model at the same load level. The failure mechanism for each bridge model under the scaled truck load is the same as that under the mass-proportional loading. That is, the unstrengthened bridge would fail in shear in the east transverse beam (TB_E), while the strengthened bridge would fail in flexure, also in TB_E.

As in the scaled gravity load case, the maximum strain at failure in the CFRP (4300 microstrain) is less than the limiting strain of the CFRP in Table 4. It occurs in both the shear and flexure zones in the transverse beam (TB_E).

4.6 CONCLUSIONS

Failure analyses of the HC bridge were performed using the proposed 3-D FE models. The model was calibrated by conducting a sensitivity study varying uncertain parameters and comparing the results with field data under service loads. In this study, the bridge under failure loads shows improvements gained from FRP strengthening. That is, the capacities of the HC bridge after FRP strengthening, based on mass-proportional loading and a scaled truck load, are increased by 37% and 28%, respectively. Yielding of both the tension steel in the transverse beams and steel reinforcement in the bridge deck is delayed in the FRP-strengthened bridge. Also, crack propagation is delayed, and fewer cracks are observed for the strengthened bridge. The strengthened bridge model deflects less under the same loading level. The failure mode of the bridge is shifted from shear failure in the transverse beams to flexural failure through the FRP strengthening.

ACKNOWLEDGMENTS

This project was supported by the Oregon Department of Transportation (ODOT), Salem, OR, and the Department of Civil, Construction, and Environmental Engineering, Oregon State University, Corvallis, OR.

REFERENCES

ACI Committee 318. (2002). *Building Code Requirements for Structural Concrete (ACI 318-02) and Commentary (ACI 318R-02).* ACI, Farmington Hills, MI.

ANSYS User's Manual, Vol. I-IV; Revision 5.5. (1998). Swanson Analysis System, Inc., Houston, PA.

Balakrishnan, S., and Murray, D.W. (1988). "Concrete Constitutive Model for NLFE Analysis of Structures." *J. Struct. Engrg.*, ASCE, 114(7), 1449-1466.

Balakrishnan, S., Elwi, A.E., and Murray, D.W. (1988). "Effect of Modeling on NLFE Analysis of Concrete Structures" *J. Struct. Engrg.*, ASCE, 114(7), 1467-1487.

Bangash, M.Y.H. (1989). Concrete and Concrete Structures: Numerical Modeling *and Applications*. Elsevier Science Publishers, LTD., Essex, England.

Barnard, P.R. (1964). "Researches into the Complete Stress-Strain Curve for Concrete," *Magazine of Concrete Research*, 16(49), 203-210.

Barzegar, F., and Maddipudi, S. (1997). "Three-Dimensional Modeling of Concrete Structures. II: Reinforced Concrete." *J. Struct. Engrg.*, ASCE, 123(10), 1347-1356.

Bhatt, P., and Kader, M.A. (1998). "Prediction of Shear Strength of Reinforced Concrete Beams by Nonlinear Finite Element Analysis." *Computers and Struct.*, 68, 139-155.

Chansawat, K., Potisuk, T., Miller, T.H., Yim, S.C.S., and Kachlakev, D.I. (2002a). "FE Models of GFRP and CFRP Strengthening of Reinforced Concrete Beams." Submitted to *ACI Struct. J.*

Chansawat, K., Yim, S.C.S., and Miller, T.H. (2002b). "NLFE Analysis of an FRP-Strengthened Reinforced Concrete Bridge. I: Modeling and Experimental Calibration." Submitted to *J. of Bridge Engrg.*, ASCE.

Isenberg, J. (1993). *Finite Element Analysis of Reinforced Concrete Structures II.* ASCE, New York, NY.

Kachlakev, D.I., and McCurry, D.Jr. (2000). "Testing of Full-Size Reinforced Concrete Beams Strengthened with FRP Composites: Experimental Results and Design Methods Verification." *SPR387, United States Department of Transportation Federal Highway Administration and the Oregon Department of Transportation*, Selem, OR.

Kemp, A.R. (1998). "The Achievement of Ductility in Reinforced Concrete Beams." *Magazine of Concrete Research*, 50(2), 123-132.

Kent, D.C., and Park, R. (1971). "Flexural Members with Confined Concrete." *J. Struct. Div.*, ASCE, 97(7), 1969-1990.

Park, R., Priestley, M.J.N., and Gill, W.D. (1982). "Ductility of Square-Confined Concrete Columns." *J. Struct. Div.*, ASCE, 108(4), 929-950.

Popovics, S. (1973). "A Numerical Approach to the Complete Stress-Strain Curve of Concrete." *Cement and Concrete Research*, 3, 583-599.

Stevens, N.J., Uzumeri, S.M., Collins, M.P., and Will, T.G. (1991). "Constitutive Model for Reinforced Concrete Finite Element Analysis," *ACI Struct. J.*, 88(1), 49-59.

Thimmhardy, E.G., Marsh, C., Chen, H., and Tessema, M. (1995). "Nonlinear Analysis of Steel and Concrete Bridge Components." *Computers & Structures*, 56(2/3), 439-459.

Vidosa, F.G., Kotsovos, M.D., and Pavlovic', M.N. (1991). "Nonlinear Finite-Element Analysis of Concrete Structures: Performance of a Fully Three-Dimensional Brittle Model." *Computers & Structures*, 40(5), 1287-1306.

Wang, P.T., Shah, S.P., and Naaman, A.E. (1978). "Stress-Strain Curves of Normal and Lightweight Concrete in Compression." *J. of ACI*, 75(11), 603-611.

NOTATION

CL = centerline of the beams;

D_E, D_C, D_W = east, center, and west sides of bridge deck;

E_0 = initial modulus of elasticity of concrete in beams;

E_1 = slope of descending branch of FRP-confined concrete;

E_{11}, E_{22}, E_{33} = moduli of elasticity of FRP in fiber direction and in the axes perpendicular to the fiber direction;

F_z, F = unit vertical and horizontal forces;

f_c = compressive stress in confined concrete in columns;

f_c' = uniaxial compressive strength of concrete;

f_r = ultimate tensile strength (modulus of rupture) of concrete;

f_y = yield strength in reinforcing steel;

f_{yt} = yield strength of steel ties;

G_{12}, G_{13}, G_{23} = shear moduli of FRP in the 1-2, 1-3, and 2-3 planes. 1-2 and 1-3 planes are the planes perpendicular to the fiber direction;

g = acceleration due to gravity;

h'' = width of the concrete core measured to outside of the peripheral tie;

K = modification factor of confined concrete strength;

K_z, K_x, K_y = vertical and horizontal (x and y directions) spring stiffnesses;

K_{mx}, K_{my} = rotational spring stiffnesses about x and y axes;

LB_E, LB_C, LB_W = east, center, west of longitudinal beams;

M = unit moment about x or y axis;

s_t = center-to-center spacing of ties;

Z_m = modification factor of confined concrete strength in descending branch;

β = shear transfer coefficient;

ε = compressive strain in concrete;

ε_c = compressive strain in confined concrete in columns;

ε_{FRP} = limiting strain in FRP;

ε_y = yield strain in reinforcing steel;

ε_0 = compressive strain at ultimate confined compressive stress in concrete in columns;

ϵ'_0 = compressive strain at ultimate unconfined and confined compressive stress in concrete in beams;

ρ_s = ratio of volume of rectangular steel ties to volume of concrete core measured to outside of the peripheral tie;

σ = compressive stress in concrete;

ν = Poisson's ratio;

$\nu_{12}, \nu_{13}, \nu_{23}$ = Poisson's ratios in the 1-2, 1-3, and 2-3 planes. 1-2 and 1-3 planes are the planes perpendicular to the fiber direction.

CHAPTER 5: NONLINEAR DYNAMIC ANALYSIS OF AN FRP-STRENGTHENED RC BRIDGE TO ASSESS SEISMIC RISK

by Kasidit Chansawat, Thomas H. Miller, Member, ASCE,
and Solomon C.S. Yim, Member, ASCE

ABSTRACT

The Horsetail Creek (HC) bridge was retrofitted using fiber-reinforced polymers (FRP) to increase flexural and shear capacities for traffic loads. However, seismic retrofits have not yet been considered for this bridge. A three-dimensional finite element (FE) model is developed to investigate the HC bridge's seismic risk. A nonlinear time-history analysis is performed using ground motions appropriate to the Pacific Northwest site. The HC bridge model is subjected to EQ acceleration-time histories appropriate for the site. The EQ time histories are scaled so that the response spectrum, within natural periods of interest, matches the 1996 AASHTO design response spectrum. The analytical results show the most likely failure mechanism for the bridge. Column confinement is recommended to increase ductility and reduce potential for substructure collapse in future seismic events.

5.1 INTRODUCTION

5.1.1 Overview

Most of the bridges in Oregon were designed with little or no consideration for seismic loads. Design prior to 1958 did not account for seismic loading. The Horsetail Creek (HC) bridge is an example of an Oregon bridge that was not designed to withstand earthquake (EQ) excitations. The bridge was built in 1914 and retrofitted in 1998 to correct the structural deficiencies caused by increases in traffic load requirements, corrosion problems, and an outdated code-based design. The fiber-reinforced polymer (FRP) rehabilitation involved unidirectional carbon-FRP and glass-FRP sheets laminated to the bridge to increase flexural and shear capacities for traffic loads, respectively. However, the bridge has not been seismically strengthened.

5.1.2 Earthquakes in Oregon

The seismic environment in Oregon is dominated by the relative movement of the Juan de Fuca Plate (subducting plate) under the North American Plate (overriding plate) along the Cascadia Subduction Zone. Three types of earthquake sources exist in Oregon: crustal earthquakes (less than 32 km below the surface from faults within the overriding North American Plate), intraplate earthquakes (32

to 64 km in depth in the subducting Juan de Fuca Plate), and interface earthquakes (plate interlocking and energy release along the Cascadia Subduction Zone). Fig. 5.1 shows these three earthquake sources in Oregon, and the overall plate tectonic conditions.

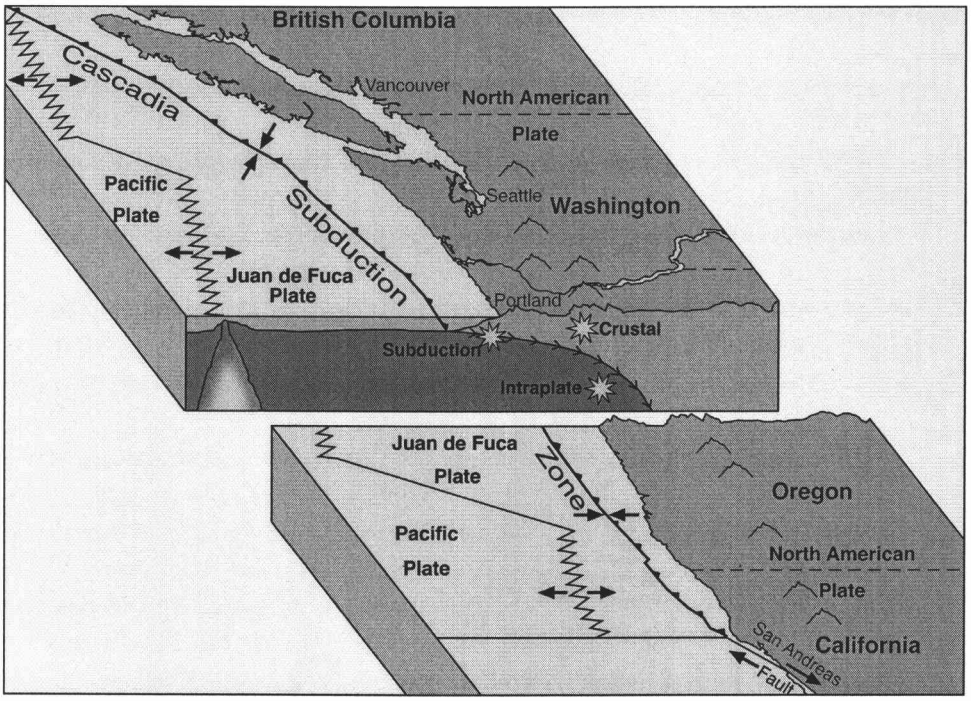

Figure 5.1. Cascadia Subduction Zone (USGS 2000)

Subduction zone earthquakes can be of very large magnitude and long duration of shaking and affect a large area, as large portions of the plate boundary (over 1000

km long) may be involved. Intervals between the earthquakes are difficult to determine due to uncertainties about the number and ages of the earthquakes. Current estimates for the return period for great Cascadia earthquakes may be between 300 and 500 years (Adams 1990). Based on historic and geologic evidence, the last large subduction zone earthquake occurred most recently about A.D. 1700 (Atwater et al. 1991). Therefore, a major subduction zone earthquake could occur at any time and could affect as many as 70% of the state's 6500 bridges (Groff et al. 1999).

In this study, three-dimensional finite element (FE) bridge models are developed to investigate the HC bridge's seismic risk. Nonlinear time-history dynamic analyses are performed in ANSYS using ground motions appropriate to the Pacific Northwest site. Four representative earthquakes are chosen based on types of EQ sources, EQ characteristics, and for comparison purposes: 1979 El Centro EQ (Crustal EQ); 1986 North Palm Springs (Crustal EQ with a broad spectrum); 1965 Puget Sound (Olympia Hwy. Test Lab) EQ (Intraplate EQ); and 1985 Valparaiso (Vina del Mar.) EQ (Subduction Zone EQ). Two simultaneous orthogonal components of horizontal ground accelerations are applied at the supports of the bridge with uniform support motion. The EQ acceleration-time histories used are scaled so that their mean response spectrum, within natural periods of interest, matches the 1996 AASHTO design response spectrum (AASHTO 1996). The results obtained from the analyses of the bridge subjected to these modified EQ excitations are compared in terms of displacement-time

histories, crack propagation, and yielding development in the reinforcing steel. Discussions and recommendations are made based on the analytical results.

5.2 FINITE ELEMENT MODELING AND ANALYSIS APPROACH

5.2.1 FE Bridge Models and Simplification

Three-dimensional FE models are developed based on the optimal FE bridge model obtained from the sensitivity study in Chapter 3, as it best represents the actual bridge conditions. In this study, the advantage of symmetry cannot, however, be taken, as the dynamic loading is not symmetrical. Full bridge models are developed instead of the longitudinal half model. From the nonlinear static analyses in Chapter 4, it is evident that a large amount of disk space and CPU time are needed. It would require even larger computer resources for a nonlinear time-history dynamic analysis. Therefore, due to limited disk space and to efficiently analyze bridge responses under seismic loading, simplification of the full bridge model is required.

Simplification should be made in such a way that the total number of elements is reduced, but accuracy in predicting dynamic response is still maintained. Due to the fact that the HC bridge has not been seismically strengthened, it is expected that (if the bridge were to fail) the failure of the bridge under EQ excitations would occur at the columns. As a result, a coarser mesh for

the bridge deck and beams can be used, while the refined mesh is maintained for the columns. Moreover, "smeared" rebars are used in the bridge deck, as reinforcement is uniformly distributed. Other than in the bridge deck, discrete rebars are still implemented in the model. It is important to ascertain that the proposed model can accurately simulate the service limit state response characteristics of the structures before it is used to predict nonlinear dynamic bridge response. Verification of the simplified models under static loading is, therefore, made. It is found that the differences between the displacement results obtained from the optimal FE bridge model (from Chapter 3) and those from the simplified model are only between 1% and 5%, which is acceptable. Fig. 5.2 shows the simplified bridge models before and after FRP strengthening, and Table 5.1 shows the comparisons of the total number of elements used for the optimal and simplified bridge FE models.

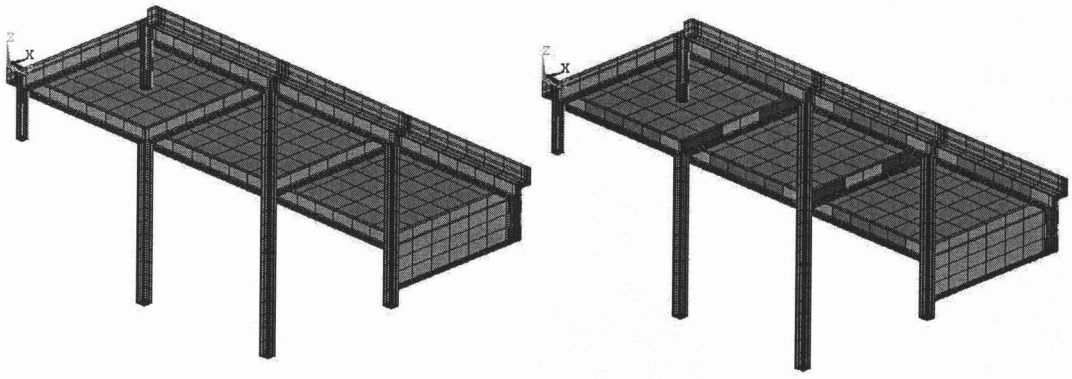

(a) (b)

Figure 5.2. Simplified Bridge Model: (a) Before FRP Strengthening; (b) After FRP Strengthening

Table 5.1. Comparison of the Total Number of Elements

Element type	NO. OF ELEMENTS					
	HCB[1]			HCB-FRP[2]		
	Optimal[3]	Simplified	% Red.[4]	Optimal[3]	Simplified	% Red.[4]
SOLID65	21008	6848	67	21008	6848	67
LINK8	9908	2488	75	9908	2488	75
SHELL143	320	248	23	320	248	23
MATRIX27	10	9	10	10	9	10
SOLID46	-	-	-	2336	512	78
Total	31246	9593	69	33582	10105	70

1. HC bridge before FRP strengthening.
2. HC bridge after FRP strengthening.
3. The optimal bridge model from Chapter 3 with the number of elements used if the full model were developed.
4. The percentage of reduction.

5.2.2 Analysis Approach

A transient dynamic analysis, sometimes called time-history analysis, is performed to determine the dynamic behavior of the HC bridge system under EQ excitations. The equation of motion in time-history analysis is as follows:

$$[M]\cdot\{\ddot{u}\}+[C]\cdot\{\dot{u}\}+[K]\cdot\{u\}=\{F(t)\} \qquad [5.1]$$

where: [M] = mass matrix

[C] = damping matrix

[K] = stiffness matrix

$\{\ddot{u}\}$ = nodal relative acceleration vector

$\{\dot{u}\}$ = nodal relative velocity vector

{u} = nodal relative displacement vector

$\{F(t)\}$ = load vector = $-[M]\ddot{g}(t)$

$\ddot{g}(t)$ = ground acceleration

The Newmark method of numerical integration, which is an implicit time-integration algorithm, is employed to solve eq. [5.1] in ANSYS. In this method, the equations of motion (eq. [5.1]) at any given time are thought of as a set of "static" equilibrium equations and then solved at discrete time points. The consistent mass matrix formulation, using the actual distributed mass matrix, is employed to yield better results.

In major earthquakes, most RC bridges are likely to crack to some degree. The damage may be even worse for the HC bridge, as it was not designed for

seismic loads and has not been seismically strengthened. As the bridge cracks, the structural stiffness matrix degrades, causing the structure to behave nonlinearly. In addition, material nonlinearities defined for concrete and steel elements also cause nonlinear behavior when the bridge is subjected to sufficient loads. The mode superposition method of forced vibration analysis, in which results from decoupled analyses of the separate modes are superimposed, is not a correct approach to handle this nonlinear behavior of the bridge, as the mode shapes are not fixed but are changing with changes in stiffness (Clough and Penzien 1993). The so-called full method in ANSYS that uses full system matrices, where all displacements and stresses are calculated in a single step, is implemented instead.

Rayleigh damping, which implies that the system damping matrix is proportional to the mass and stiffness matrices using two constants: Alpha-α (mass) and Beta-β (stiffness), is used instead of modal damping ratios (ξ) used in the mode superposition method. The Rayleigh damping matrix is given by:

$$[C] = \alpha[M] + \beta[K] \qquad [5.2]$$

The constants α and β are related to modal damping ratio and natural circular frequency as follows (Clough and Penzien 1993):

$$\xi_n = \frac{\alpha}{2\omega_n} + \frac{\beta\omega_n}{2} \qquad [5.3]$$

where ω_n = natural circular frequency for mode n

ξ_n = modal damping ratio for mode n

The α and β values can simultaneously be solved for if the modal damping ratios ξ_m and ξ_n associated with two specific natural circular frequencies for modes m and n; i.e., ω_m and ω_n, are known. This leads to:

$$\begin{Bmatrix}\alpha\\ \beta\end{Bmatrix} = \frac{2\omega_m\omega_n}{\omega_n^2-\omega_m^2}\begin{bmatrix}\omega_n & -\omega_m\\ -\frac{1}{\omega_n} & \frac{1}{\omega_m}\end{bmatrix}\begin{Bmatrix}\xi_m\\ \xi_n\end{Bmatrix} \qquad [5.4]$$

When the modal damping ratios for modes m and n are the same, eq. [5.4] becomes:

$$\begin{Bmatrix}\alpha\\ \beta\end{Bmatrix} = \frac{2\xi}{\omega_n+\omega_m}\begin{Bmatrix}\omega_m\omega_n\\ 1\end{Bmatrix} \qquad [5.5]$$

It is recommended that ω_m and ω_n be selected as the most dominant frequencies within the range of natural circular frequencies which most contribute to the dynamic response. In other words, these two natural frequencies should be selected from the modes that most significantly contribute to the dynamic response (Clough and Penzien 1993 and Tedesco et al. 1999).

Consequently, an undamped free-vibration analysis, modal analysis in ANSYS, is performed to obtain natural circular frequencies of the bridge models used in eq. [5.5]. Additionally, with the modal analysis, other dynamic characteristics of the HC bridge can be assessed; i.e., mode shapes and mass participation in each global direction. Although they are derived from a linear system, they provide a better understanding of how the bridge would behave, what types of motion would dominate the bridge response, and what type of failure mechanism would occur under earthquake excitations. The modal analysis,

together with results in terms of the dynamic characteristics of the HC bridge, will be presented in the next section.

In the transient analysis, Newton-Raphson equilibrium iteration is used to solve nonlinear problems.

5.2.3 Dynamic Characteristics of the HC Bridge

The vibration characteristics in terms of natural circular frequencies and mode shapes of the HC bridge can be obtained from the eigenvalue equation given by:

$$[K].\{\phi_i\} = \omega_i^2.[M].\{\phi_i\} \qquad [5.6]$$

where: $\{\phi_i\}$ = mode shape vector (eigenvector) of mode i

w_i = natural circular frequency of mode i

Mass participation can be calculated from the distribution of the effective modal mass for the different mode shapes as follows (Hodhod 1997):

$$\%EM_{jm} = \frac{\left(\sum_i M_{im}\phi_{imj}\right)^2}{\sum_i M_{im}\phi_{imj}^2} \times \frac{100}{\sum_i M_{im}} \qquad [5.7]$$

where: m = X, Y, Z global directions

i = structural node number

j = mode number

M_{im} = translational mass associated with the i^{th} node in the global m direction

ϕ_{imj} = translational component at the i^{th} node in the global m direction for the j^{th} mode shape

The effective modal mass ($\%EM_{jm}$) measures the percentage of the total mass that is excited for the j^{th} mode shape in the m^{th} global direction. It describes the portion of the total mass responding to the earthquake in each mode (Clough and Penzien 1993).

In this study, the first 40 modes of the HC bridge before and after FRP strengthening are extracted, which are sufficient for three reasons:

1. The included modes cover the frequency range from 0 – 10 Hz which is the effective frequency range for most earthquakes (Issa et al. 2000, Wahab and Roeck 1999, and Hodhod 1997). The earthquakes used in the study also have high Fourier amplitudes within this frequency range, as can be seen later in the Fourier spectrum plots.
2. The included modes cover the two dominant modes that most significantly contribute to the dynamic response.
3. The included modes cover more than 90% of the cumulative effective modal mass in all three global directions. They are used to select a range of the natural periods of interest used in the EQ modification in this study.

However, only the dynamic characteristics of the first 20 modes (in terms of the natural frequency, natural period, and effective mass in all three global directions) of the HC bridge before and after FRP strengthening are shown in Tables 5.2 and

5.3. Moreover, the first 10 mode shapes of the HC bridge after FRP strengthening are also shown in Figs. 5.3 and 5.4. It should be noted that due to the similar mode shapes for the unstrengthened and FRP-strengthened HC bridge models, only the mode shapes from the FRP-strengthened bridge are shown.

Table 5.2. Dynamic Characteristics of the HC Bridge before FRP Strengthening

Mode	Freq. (Hz)	Period (sec)	Mass Participation*					
			$\%EM_x$	$\%Cum_x$	$\%EM_y$	$\%Cum_y$	$\%EM_z$	$\%Cum_z$
1	6.435	0.1554	69.16	69.16	-	0.00	-	0.00
2	8.228	0.1215	-	69.16	96.58	96.58	0.28	0.28
3	16.52	0.0605	-	69.16	0.03	96.61	61.95	62.23
4	18.91	0.0529	-	69.16	0.79	97.40	0.47	62.71
5	23.10	0.0433	-	69.16	0.78	98.19	8.39	71.09
6	27.60	0.0362	0.54	69.70	-	98.19	-	71.09
7	29.33	0.0341	1.93	71.63	-	98.19	-	71.09
8	30.36	0.0329	16.02	87.65	-	98.19	-	71.09
9	30.69	0.0326	-	87.65	0.01	98.19	3.88	74.98
10	30.99	0.0323	-	87.65	0.05	98.24	6.77	81.74
11	31.41	0.0318	0.84	88.49	-	98.24	-	81.74
12	32.08	0.0312	-	88.49	0.05	98.29	0.23	81.97
13	32.40	0.0309	0.42	88.91	-	98.29	-	81.97
14	33.26	0.0301	-	88.91	0.71	99.00	0.02	81.99
15	33.56	0.0298	1.70	90.62	-	99.00	-	81.99
16	33.92	0.0295	-	90.62	0.04	99.04	0.62	82.61
17	33.96	0.0294	2.21	92.83	-	99.04	-	82.61
18	37.02	0.0270	0.07	92.90	-	99.04	-	82.61
19	37.58	0.0266	-	92.90	0.03	99.06	7.98	90.59
20	39.77	0.0251	-	92.90	0.29	99.36	1.00	91.59

* Shows percentages of effective ($\%EM_x$, $\%EM_y$, and $\%EM_z$) and cumulative ($\%Cum_x$, $\%Cum_y$, and $\%Cum_z$) modal mass in X, Y, and Z global directions, respectively.

Table 5.3. Dynamic Characteristics of the HC Bridge after FRP Strengthening

Mode	Freq. (Hz)	Period (sec)	Mass Participation*					
			$\%EM_x$	$\%Cum_x$	$\%EM_y$	$\%Cum_y$	$\%EM_z$	$\%Cum_z$
1	6.437	0.1554	69.16	69.16	-	0.00	-	0.00
2	8.231	0.1215	-	69.16	96.58	96.58	0.28	0.28
3	16.58	0.0603	-	69.16	0.03	96.61	62.17	62.45
4	18.95	0.0528	-	69.16	0.79	97.40	0.51	62.95
5	23.12	0.0433	-	69.16	0.79	98.19	8.42	71.38
6	27.60	0.0362	0.54	69.70	-	98.19	-	71.38
7	29.35	0.0341	1.94	71.64	-	98.19	-	71.38
8	30.38	0.0329	16.06	87.71	-	98.19	-	71.38
9	30.73	0.0325	-	87.71	0.01	98.20	3.67	75.04
10	31.03	0.0322	-	87.71	0.05	98.24	6.74	81.78
11	31.42	0.0318	0.84	88.54	-	98.24	-	81.78
12	32.09	0.0312	-	88.54	0.05	98.29	0.22	82.01
13	32.43	0.0308	0.43	88.97	-	98.29	-	82.01
14	33.28	0.0301	-	88.97	0.71	99.00	0.02	82.03
15	33.58	0.0298	1.64	90.61	-	99.00	-	82.03
16	33.93	0.0295	-	90.61	0.04	99.04	0.61	82.64
17	33.97	0.0294	2.22	92.83	-	99.04	-	82.64
18	37.04	0.0270	0.07	92.90	-	99.04	-	82.64
19	37.66	0.0266	-	92.90	0.03	99.07	7.95	90.59
20	39.86	0.0251	-	92.90	0.29	99.36	0.99	91.58

* Shows percentages of effective ($\%EM_x$, $\%EM_y$, and $\%EM_z$) and cumulative ($\%Cum_x$, $\%Cum_y$, and $\%Cum_z$) modal mass in X, Y, and Z global directions, respectively.

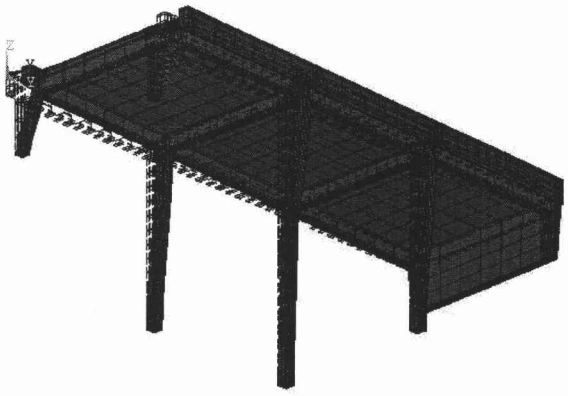

1st Mode Shape

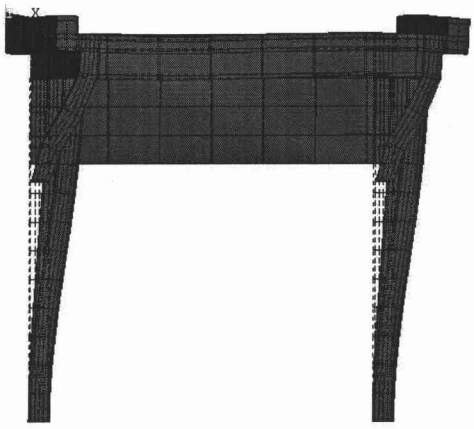

1st Mode Shape (Front View)

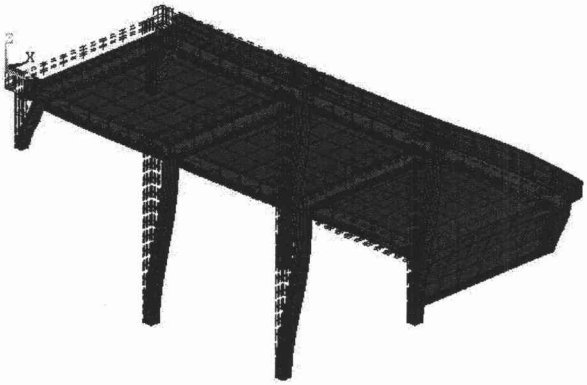

2nd Mode Shape

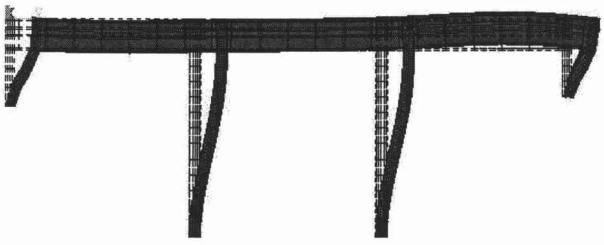

2nd Mode Shape (Side View)

Figure 5.3. First and Second Mode Shapes of the HC Bridge

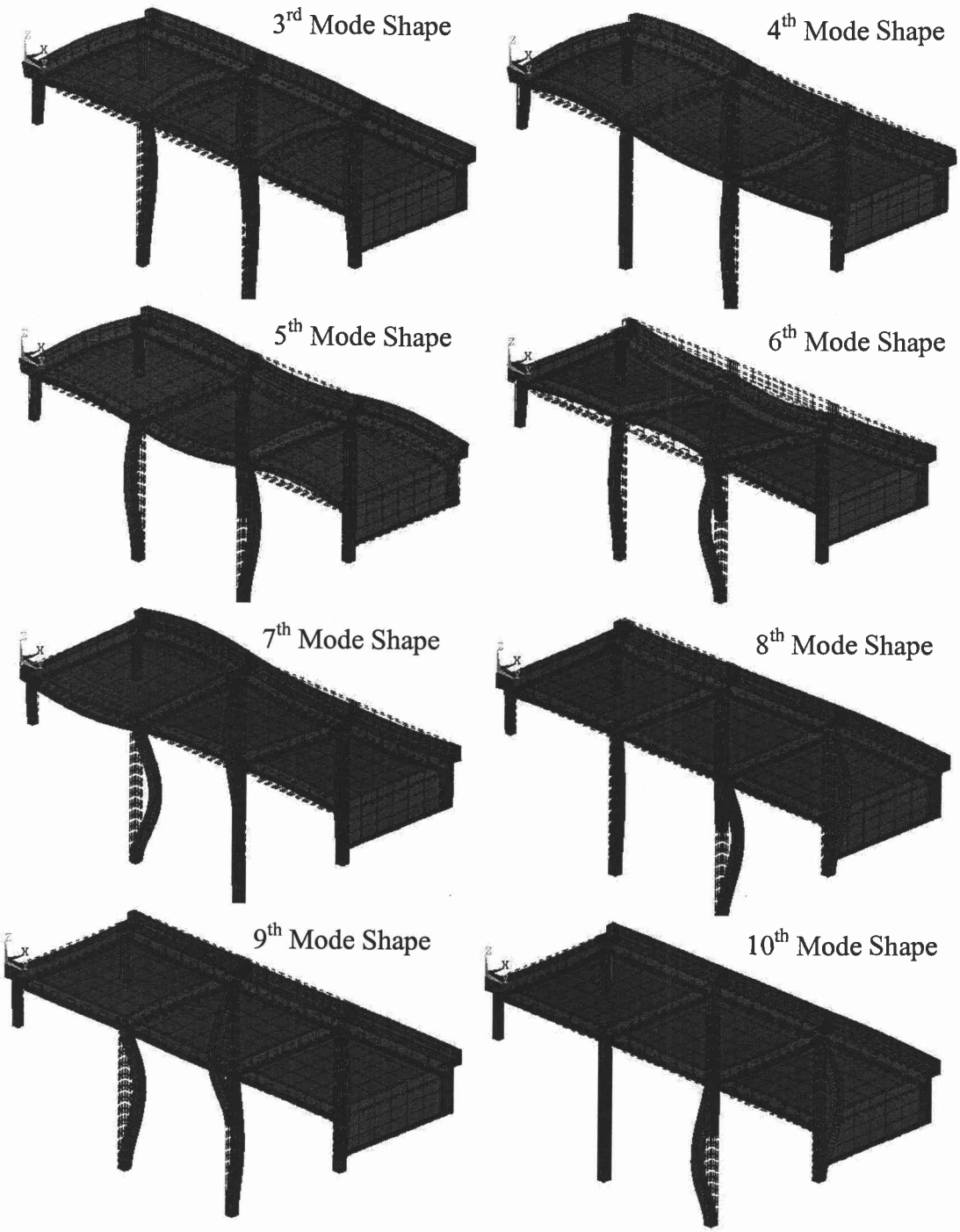

Figure 5.4. Other Mode Shapes of the HC Bridge

From Tables 5.2 and 5.3, it can be seen that strengthening the bridge with FRP laminates increases the structural stiffness, which, in turn, increases the natural frequencies, however, not significantly. This is also pointed out in Issa et al. (2000). It can also be seen that the natural frequency of the first two modes falls in the effective frequency range of 0 – 10 Hz.

For the effective modal mass of different modes in each global direction, larger mass distribution percentages usually indicate important modes in the corresponding dynamic response analysis. It is obvious from Tables 5.2 and 5.3 that the first and second modes have the largest effective modal mass in the X and Y global directions where the horizontal components of earthquake excitations are applied.

There are six principal types of motion in bridge structures: (1) rigid-body longitudinal translation; (2) rigid-body lateral translation; (3) rigid-body in-plane rotation of the bridge deck; (4) vertical flexure; (5) lateral flexure; and (6) torsional distortion of the bridge deck (Wakefield et al. 1991). Fig. 5.3 shows that the first two modes have a rigid body motion. That is, the first mode is a rigid-body lateral translation, while the second mode is a rigid-body longitudinal translation with very little bending in the bridge deck. From Fig. 5.4, the third, fourth, and fifth modes are, basically, vertical flexure accompanied by a little bending in some columns. The sixth and seventh modes mainly show a torsional distortion of the bridge deck. The other modes show bending in the columns.

The natural frequencies of the first two modes are in the effective range of 0 – 10 Hz, and the largest effective modal mass percentages in the directions of the applied ground motions are from the first two modes. Also, the first two modes of free vibration of the HC bridge are dominated by rigid-body motion with no substantial flexural or torsional motion. These first two modes are most likely to be those that most significantly contribute to the dynamic response. These dominant frequencies from the first two modes are used to calculate the α and β proportional damping required in a nonlinear transient analysis using eq. [5.5]. It is assumed that the damping ratios for both modes are the same and equal to 5%. This modal damping ratio for RC structures is recommend in Hodhod (1997), Tedesco et al. (1999), Chopra (2000), and Booth (1994). The α and β proportional damping values used in the study are given in Table 5.4.

Table 5.4. α and β Proportional Damping

Model	Mode	Natural freq. (Hz)	Natural circular freq. (rad/sec)	Proportional Damping	
				α	β
HC bridge	1	6.435	40.44	2.269	1.0854E-03
before FRP strengthening	2	8.228	51.70		
HC bridge	1	6.437	40.45	2.270	1.0851E-03
after FRP strengthening	2	8.231	51.72		

5.3 CHARACTERISTICS OF EARTHQUAKE EXCITATIONS AND MODIFICATION

5.3.1 Earthquakes for the Pacific Northwest Site

The suite of time histories representing earthquakes in the Pacific Northwest used in this investigation was obtained from "Suites of Earthquake Ground Motions for Analysis of Steel Moment Frame Structures" in Woodward-Clyde (1997). The motions were developed to be used for the SAC project for analyses of structures located in Los Angeles, Seattle, and Boston. Only the horizontal acceleration-time histories are available. One of the EQ suites (i.e., Seattle earthquakes) was selected to represent earthquakes in Oregon. Like Oregon, the seismic hazard in Seattle is influenced by the same three categories of seismic sources for the Cascadia Subduction Zone. The suite of time histories is based on ground motions having a 10% probability of exceedance in 50 years (a 475-year return period) obtained from deaggregation of probabilistic seismic hazard analyses. It covers approximate ranges of magnitudes and source-to-site distances between 6-8 and 15-80 km, respectively (Woodward-Clyde 1997). It is noted that all of the horizontal time histories provided in this study have been rotated into strike-normal and strike-parallel components. The suite of time-history ground motions for design in the Pacific Northwest (from the SAC project) is shown in Table 5.5.

Table 5.5. Suite of Pacific Northwest Ground Motions

SAC Name	Event Description	Date	Comp.[1]	Seismic Sources[2]	M[3]	Dist. (km)	No. of Points	Time Step (sec)	Duration (sec)	PGA[4] (cm/sec^2)
SE01	El Centro, CA, Array 6, Huston Rd.	10/15/1979	fn	CE	6.5	1.2	3912	0.020	78.24	170.55
SE02	El Centro, CA, Array 6, Huston Rd.	10/15/1979	fp	CE	6.5	1.2	3912	0.020	78.24	132.70
SE03	Morgan Hill, CA, Gilroy 3	4/24/1984	fn	CE	6.2	15	3000	0.020	60.00	378.82
SE04	Morgan Hill, CA, Gilroy 3	4/24/1984	fp	CE	6.2	15	3000	0.020	60.00	649.80
SE05	Western WA, Olympia Hwy. Test Lab.	4/13/1949	fn	IE	6.5	56	4002	0.020	80.04	376.18
SE06	Western WA, Olympia Hwy. Test Lab.	4/13/1949	fp	IE	6.5	56	4002	0.020	80.04	345.11
SE07	Western WA, Seattle Army Base	4/13/1949	fn	IE	6.5	80	3336	0.020	66.72	289.19
SE08	Western WA, Seattle Army Base	4/13/1949	fp	IE	6.5	80	3336	0.020	66.72	381.26
SE09	North Palm Springs, CA	7/8/1986	fn	CE	6.0	6.7	3000	0.020	60.00	576.45
SE10	North Palm Springs, CA	7/8/1986	fp	CE	6.0	6.7	3000	0.020	60.00	558.10
SE11	Puget Sound, WA, Olympia Hwy. Test Lab.	4/29/1965	fn	IE	7.1	80	4092	0.020	81.84	737.82
SE12	Puget Sound, WA, Olympia Hwy. Test Lab.	4/29/1965	fp	IE	7.1	80	4092	0.020	81.84	584.52
SE13	Puget Sound, WA, Fed. Ofc. Bldg.	4/29/1965	fn	IE	7.1	61	3708	0.020	74.16	362.31
SE14	Puget Sound, WA, Fed. Ofc. Bldg.	4/29/1965	fp	IE	7.1	61	3708	0.020	74.16	297.30
SE15	Western WA, Tacoma	4/29/1965	fn	IE	7.1	60	3000	0.020	60.00	284.72
SE16	Western WA, Tacoma	4/29/1965	fp	IE	7.1	60	3000	0.020	60.00	563.47
SE17	Valparaiso Central, Chile, Llolleo	3/3/1985	fn	SZE	8.0	42	4002	0.025	100.05	684.27
SE18	Valparaiso Central, Chile, Llolleo	3/3/1985	fp	SZE	8.0	42	4002	0.025	100.05	657.89
SE19	Valparaiso Central, Chile, Vina del Mar.	3/3/1985	fn	SZE	8.0	42	4002	0.025	100.05	531.05
SE20	Valparaiso Central, Chile, Vina del Mar.	3/3/1985	fp	SZE	8.0	42	4002	0.025	100.05	376.88

1. EQ horizontal components: fn – strike-normal; fp – strike-parallel.
2. Three categories of seismic sources: CE – Crustal earthquake; IE – Intraplate earthquake; SZE – Subduction Zone earthquake.
3. Magnitude

5.3.2 Earthquake Modification

In this study, the EQ acceleration-time histories from the previous section are modified so that the mean response spectrum, within natural periods of interest, matches the 1996 AASHTO design response spectrum for the HC bridge site. However, before the modification is performed, the time histories from the SAC suite have to be back-scaled to the original data. This is because they have been altered so that the mean response spectrum matches the 1997 NEHRP design spectrum (Building 1997), for the design and construction of building structures, not for bridges. After the back-scaling, scaling to the design response spectrum based on AASHTO (1996) is made. The provisions apply to bridges of conventional steel and concrete girder and box girder construction with spans not longer than 150 m. To construct the design response spectrum, the elastic seismic response coefficient for multimodal analysis is calculated as follows (AASHTO 1996):

$$C_{sm} = \frac{1.2AS}{T_m^{2/3}} \qquad [5.8]$$

where: C_{sm} = elastic seismic response coefficient for mode m

A = acceleration coefficient

S = site coefficient

T_m = period of the m^{th} mode of vibration

The value of C_{sm} need not exceed 2.5A. When T_m exceeds 4.0 sec, the value of C_{sm} for that mode is determined as follows:

$$C_{sm} = \frac{3AS}{T_m^{4/3}} \qquad [5.9]$$

The parameters needed to develop the design response spectrum for the HC bridge site are tabulated in Table 5.6.

Table 5.6. Design Response Spectrum Parameters

Parameter	Input
Soil type	I
Site coefficient	1
Acceleration coefficient	0.16*

* From the national earthquake ground motion map, a probabilistic map of PGA on rock, which was developed by the U.S. Geological Survey (USGS) in 1988. The map provides contours of PGA for a probability of exceedance of 10% in 50 years (AASHTO 1996)

Selection of the natural periods of interest for the bridge structure is determined based on the percentage of cumulative effective modal mass in all three global directions. It is shown in Tables 5.2 and 5.3 that a range of natural periods between 0.0266 and 0.1554 sec (from the first to the 19th modes) includes more than 90% of the total effective modal mass for both models in all three directions.

The mean response spectrum value for each component of the original ground motions within this range of natural periods is calculated, and the scaling factor to match the 1996 AASHTO design response spectrum is determined. The original EQ acceleration time history is, then, modified using this factor. This approach is applied to all the EQ acceleration time histories listed in Table 5.5. Four of the 10 earthquakes are selected and used in the study. The EQ selection is based on the following criteria:

1. The earthquakes are from the three types of EQ sources.
2. Peak ground accelerations occur early in the records to save disk space and CPU time when an analysis is performed.
3. EQ characteristics are critical for the bridge structure; i.e., in particular, an earthquakes having a broad spectrum.
4. They are well-known and commonly used.

All of the modified earthquakes are compared based on these criteria, and four of them are selected as follows: the 1979 El Centro EQ (Crustal EQ); 1986 North Palm Springs EQ (Crustal EQ with a broad spectrum); 1965 Puget Sound (Olympia Hwy. Test Lab) EQ (Intraplate EQ); and 1985 Valparaiso (Vina del Mar.) EQ (Subduction Zone EQ). The response spectra at 5% damping, modified EQ time histories, and Fourier spectra for the earthquakes used in the study are shown in Figs. 5.5 to 5.12. The other earthquakes considered are shown in Appendix C.

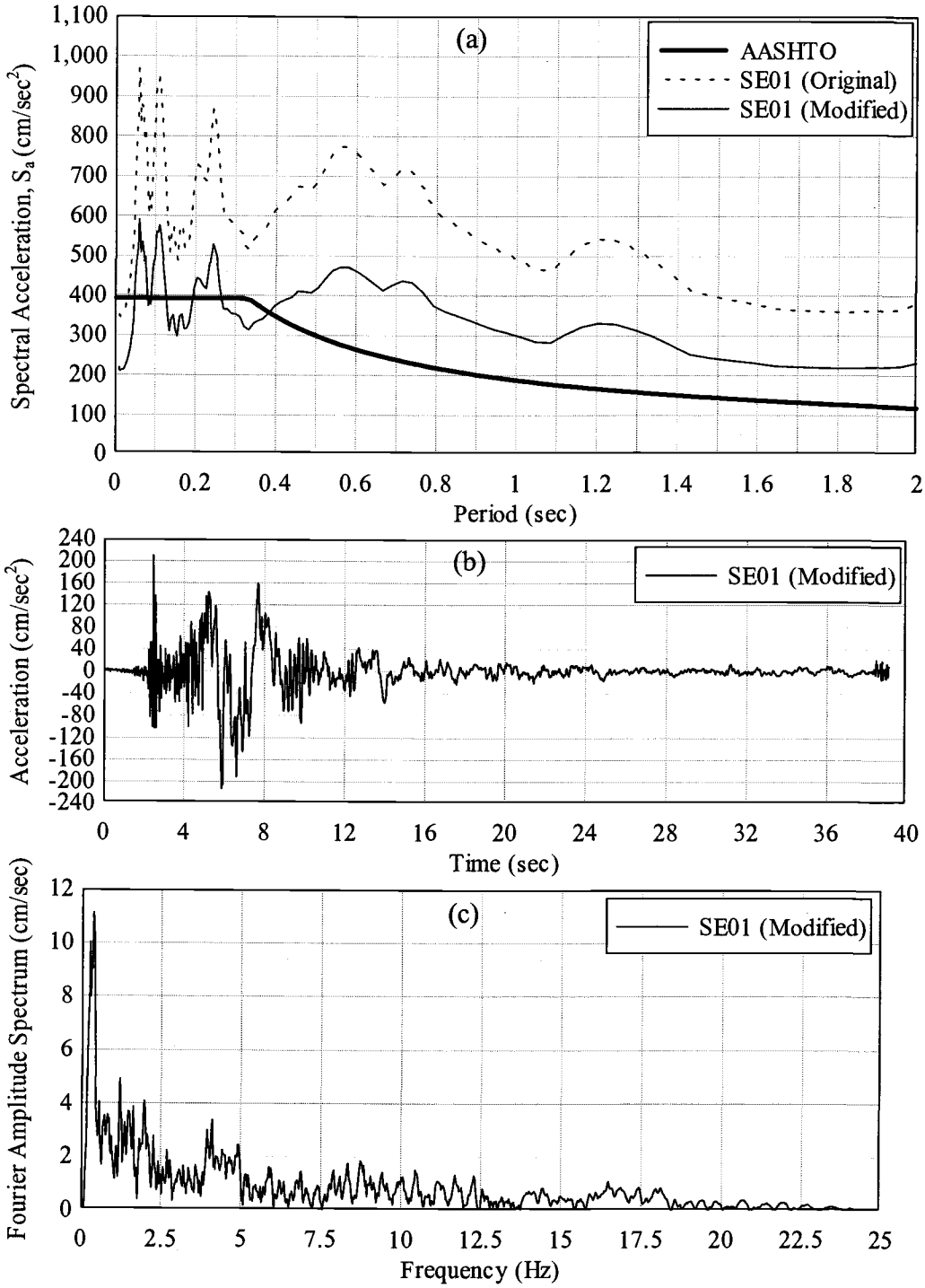

Figure 5.5. 1979 El Centro EQ (Strike-Normal): (a) Response Spectra; (b) Modified Time History; (c) Fourier Spectrum

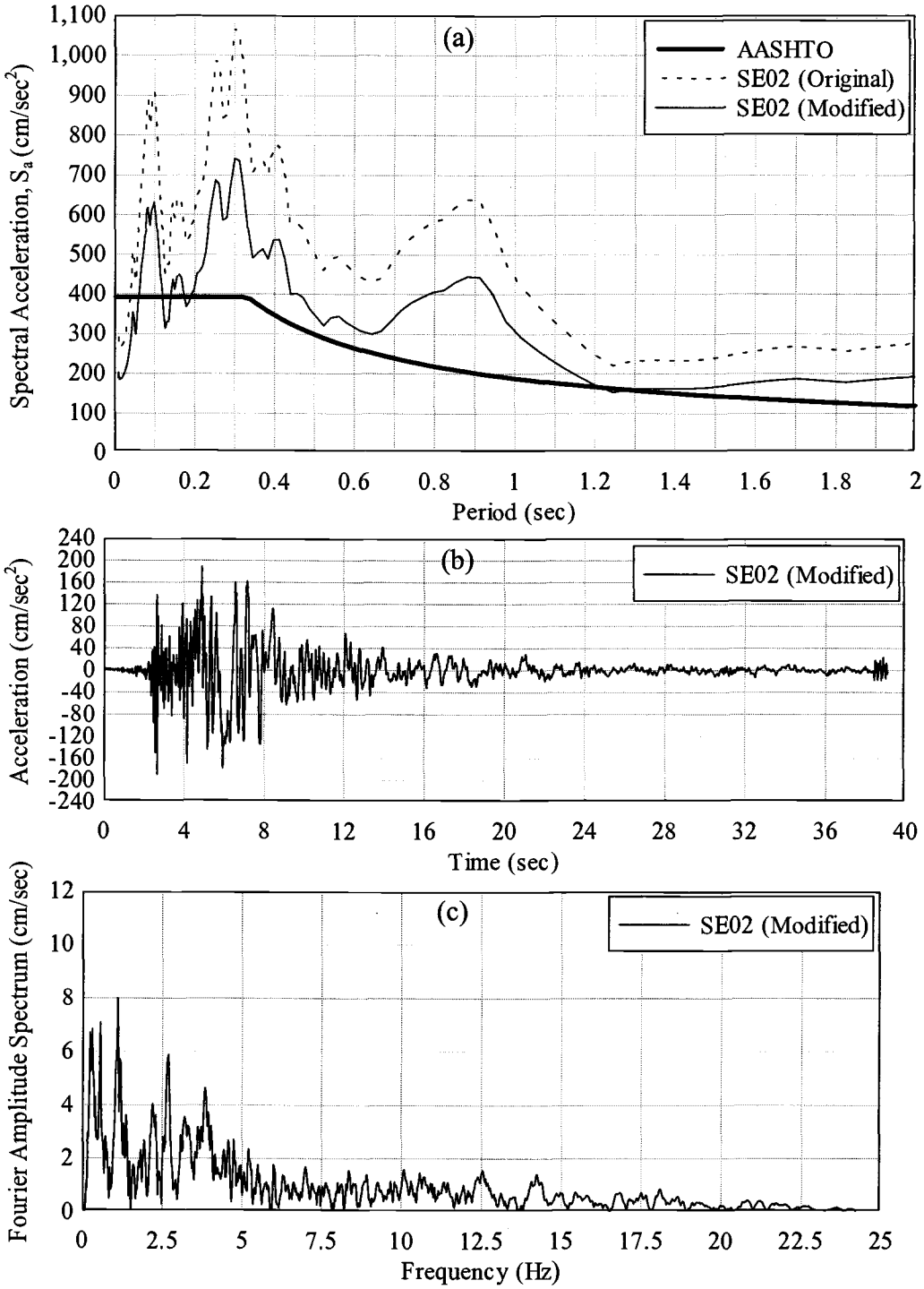

Figure 5.6. 1979 El Centro EQ (Strike-Parallel): (a) Response Spectra; (b) Modified Time History; (c) Fourier Spectrum

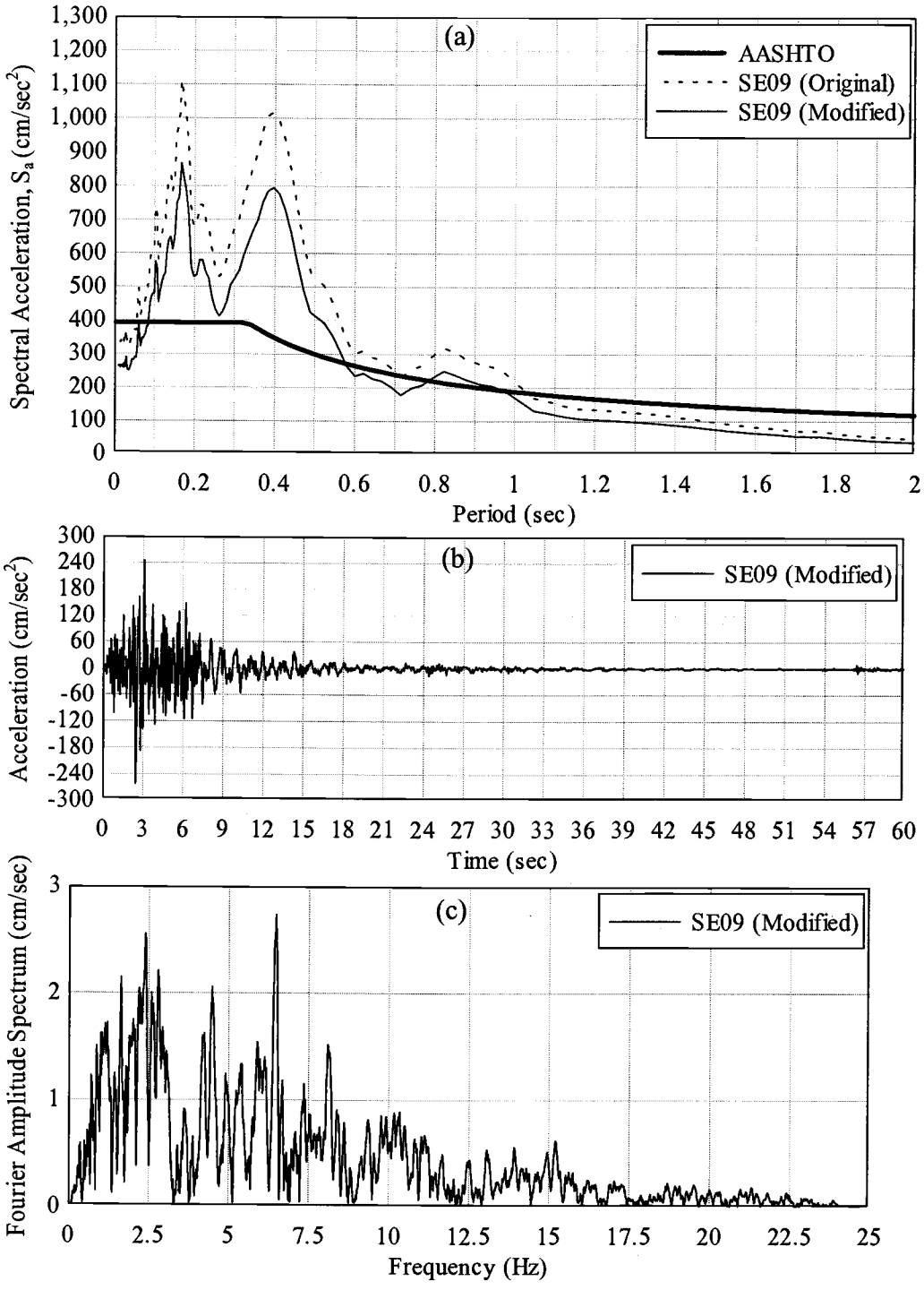

Figure 5.7. 1986 North Palm Springs EQ (Strike-Normal): (a) Response Spectra; (b) Modified Time History; (c) Fourier Spectrum

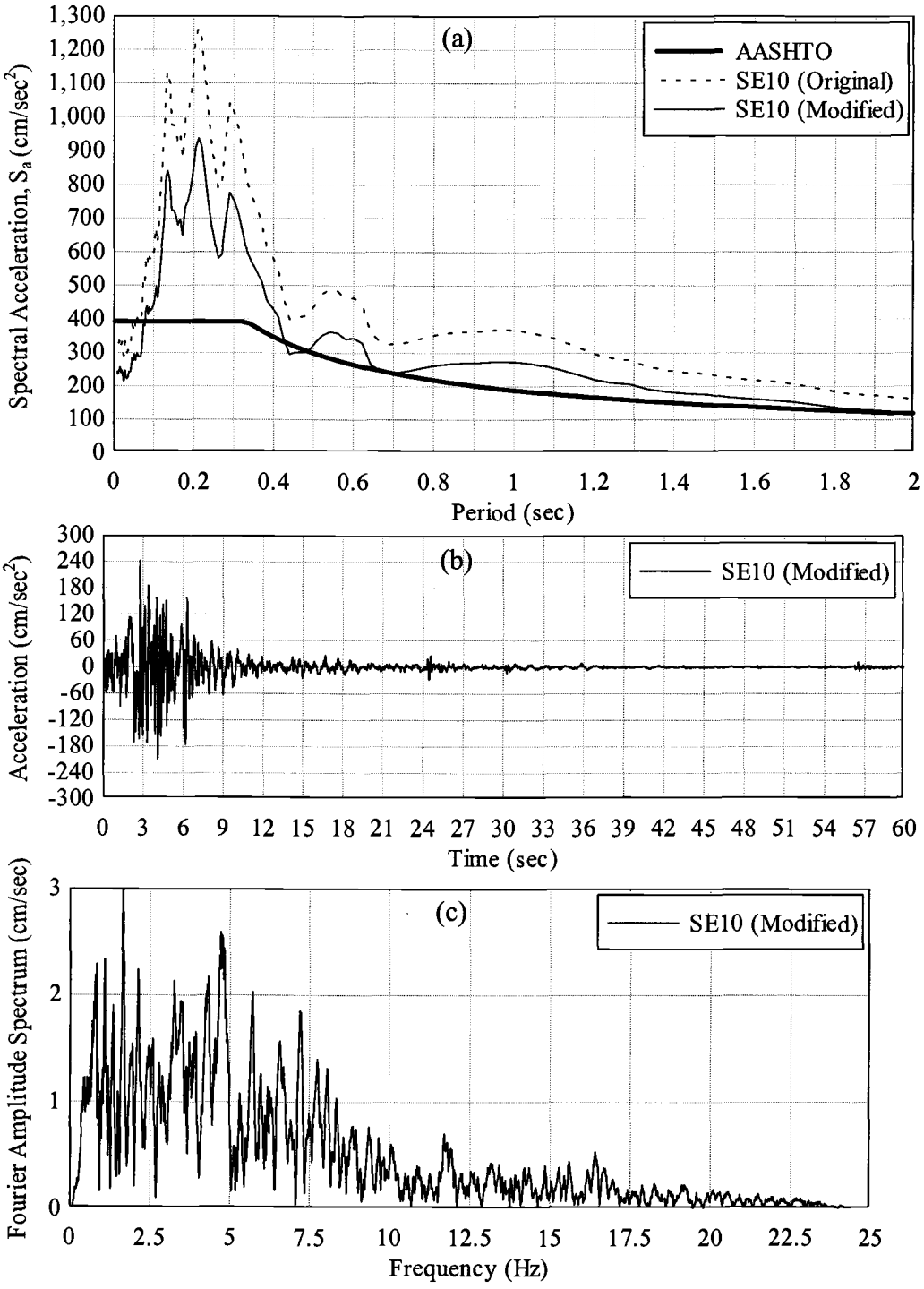

Figure 5.8. 1986 North Palm Springs EQ (Strike-Parallel): (a) Response Spectra; (b) Modified Time History; (c) Fourier Spectrum

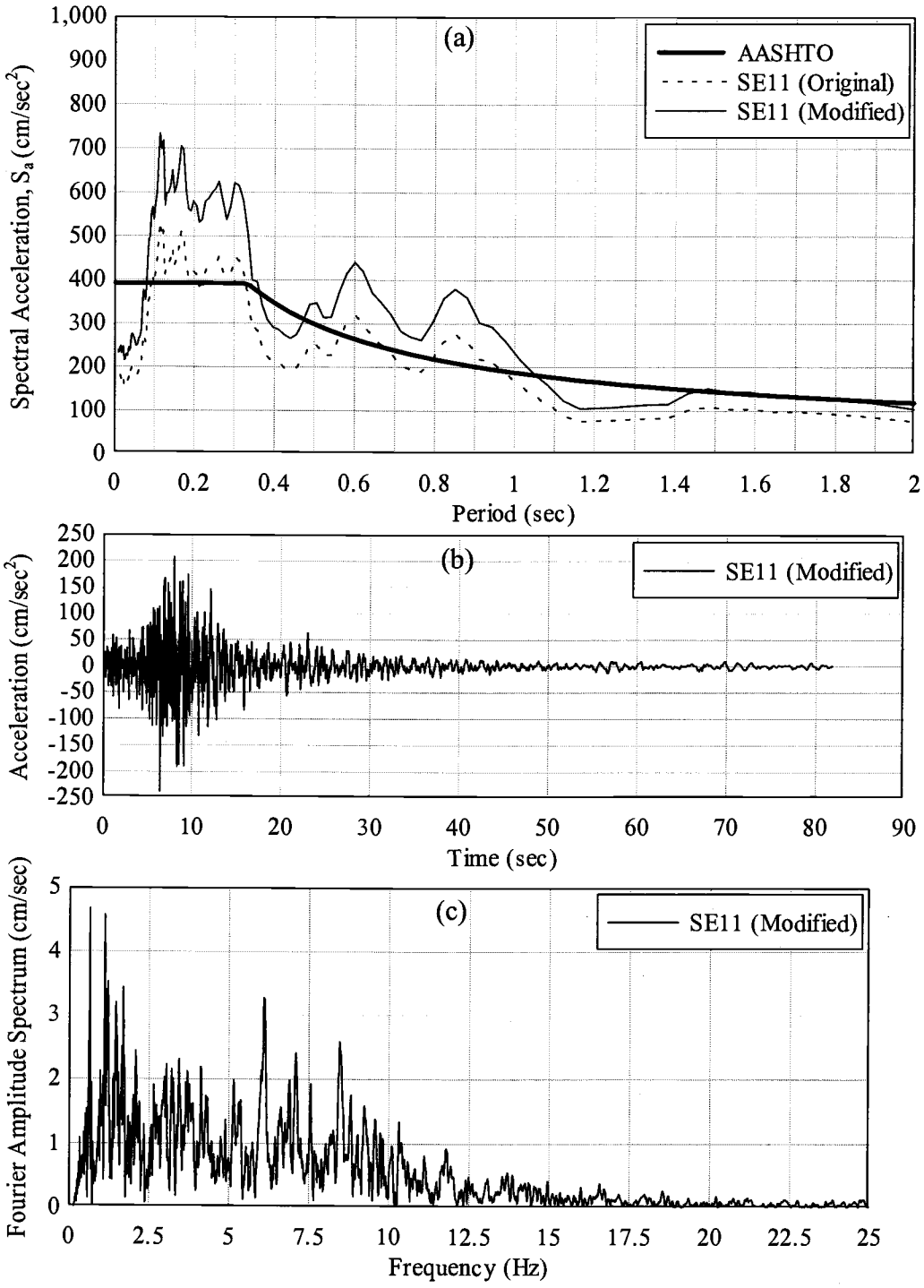

Figure 5.9. 1965 Puget Sound EQ (Strike-Normal): (a) Response Spectra; (b) Modified Time History; (c) Fourier Spectrum

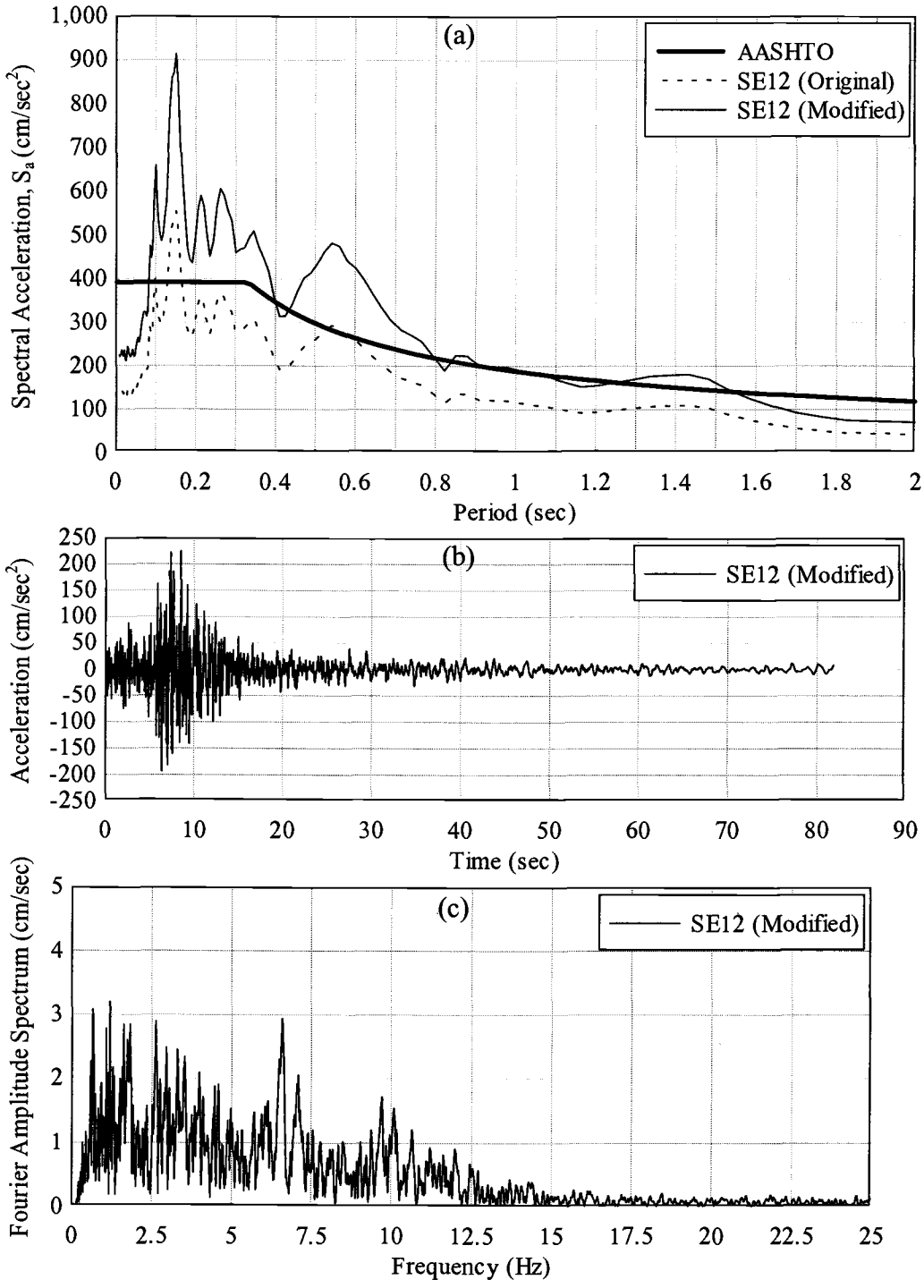

Figure 5.10. 1965 Puget Sound EQ (Strike-Parallel): (a) Response Spectra; (b) Modified Time History; (c) Fourier Spectrum

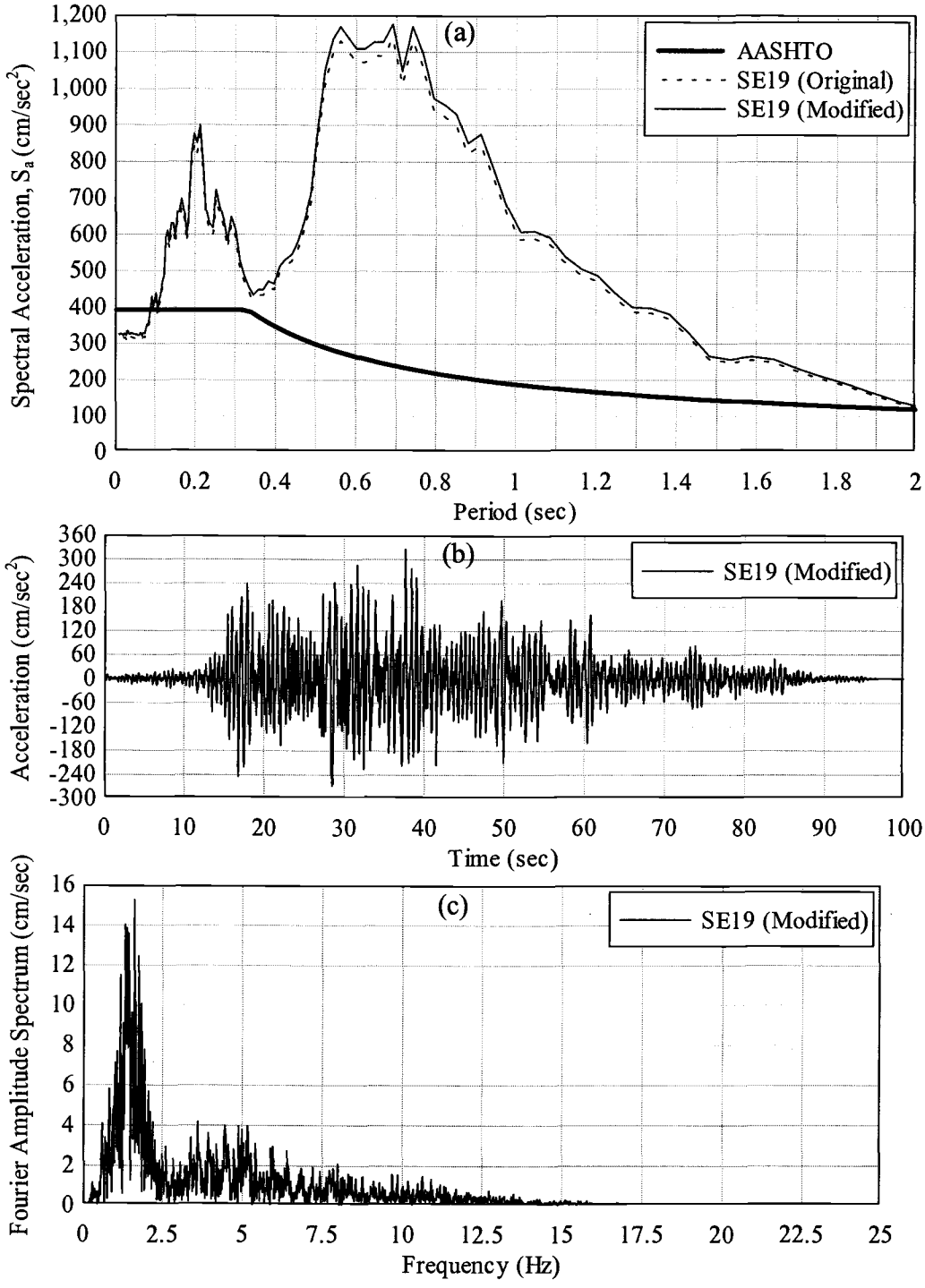

Figure 5.11. 1985 Valparaiso EQ (Strike-Normal): (a) Response Spectra; (b) Modified Time History; (c) Fourier Spectrum

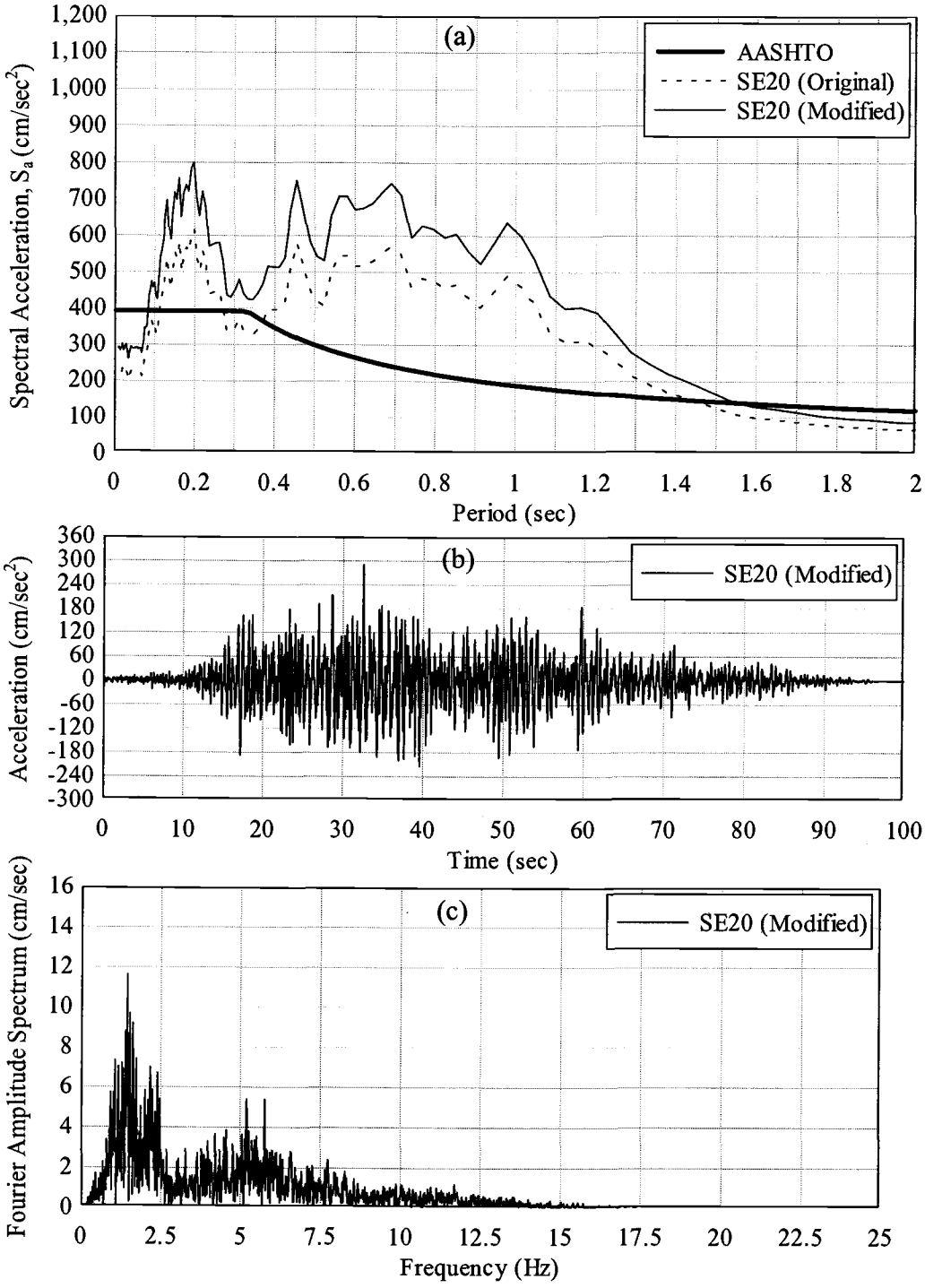

Figure 5.12. 1985 Valparaiso EQ (Strike-Parallel): (a) Response Spectra; (b) Modified Time History; (c) Fourier Spectrum

5.4 ANALYTICAL RESULTS AND DISCUSSION

In preliminary analyses of the HC bridge before and after FRP strengthening, it is found that regardless of the presence of FRP laminates, the dynamic response of the models is basically the same for seismic loads. The FRP strengthening was primarily designed for vertical load capacity enhancement. Moreover, as previously presented, the dominant motions of the HC bridge during earthquakes are rigid-body lateral and longitudinal translations in the bridge deck. The bridge motion, then, involves flexure in the columns, not in the beams. As a result, the FRP laminates installed on the beams do not significantly affect the dynamic response of the bridge. For this study, only the HC bridge after FRP strengthening is, therefore, investigated.

To achieve solution convergence in the nonlinear dynamic analysis, seismic loads must gradually be applied with proper adjustment on force and displacement convergence tolerances. The minimum integration time step used in the transient dynamic analysis is 1/50 of the time interval of the recorded EQ data. Force and displacement convergence criteria are 15% and 5%, respectively. The maximum number of iterations per loading increment is 75. The bridge structure is assumed to fail when the solution diverges, and the residual force or displacement exceeds the specified criteria. This is due to an ill-conditioned stiffness matrix as explained in Chapter 3. Additionally, for the dynamic study, the use of the point where the solution starts to diverge to indicate failure of the bridge under EQ excitations can

be found in Wakefield et al. (1991). Besides the solution divergence, there is also physical evidence showing the failure of the bridge; i.e., extensive cracking and yielding in reinforcing steel. This will be examined later in detail.

The four earthquake records selected in the previous section are employed in the study. For each earthquake, the stronger horizontal component of the ground motions based on PGA is directed along the critical axis of the structure; i.e., in the transverse direction (X-axis). Comparisons of analytical results obtained from the FRP-strengthened HC bridge in terms of displacement-time histories, crack propagation, and yielding development in reinforcing steel are made.

5.4.1 Displacement-Time Histories

For the displacement-time histories, only horizontal displacements in the x (transverse) and y (longitudinal) directions are plotted, as the vertical displacements are too small to be considered significant from the applied EQ excitation. Displacement-time histories of the bridge response to the input ground motion at several points on the bridge are collected. Fig. 5.13 shows the locations of these points, which are at the center and top of all columns and at the two abutment corners.

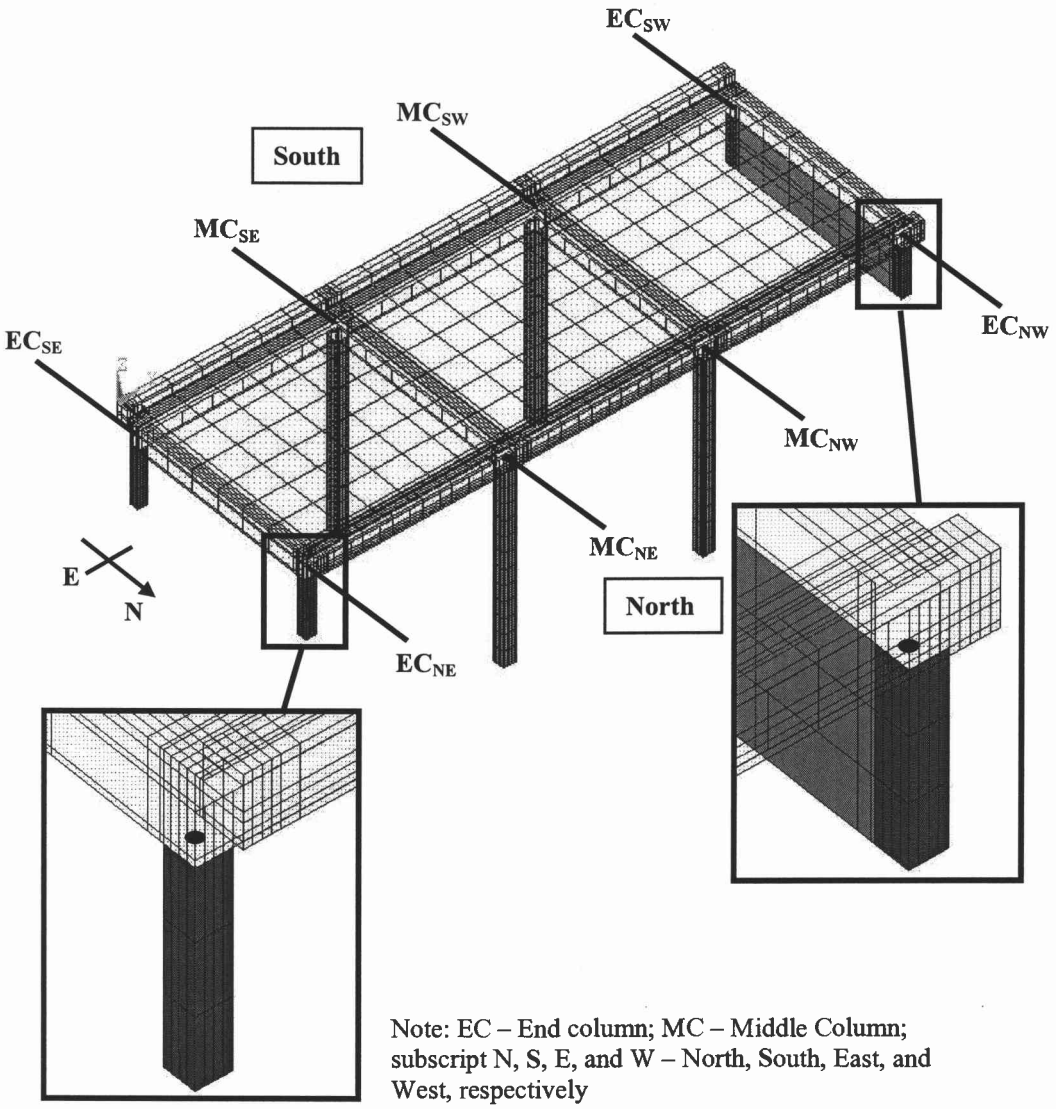

Figure 5.13. Monitored Locations for Displacement-Time Histories

As discussed previously, the bridge motions are dominated by rigid-body motions in the transverse and longitudinal directions, so the difference in

displacements between columns that are on the same transverse plane (e.g. EC_{SE} and EC_{NE} or MC_{SE} and MC_{NE}) is insignificant. Only the displacement-time histories from EC_{SE}, MC_{SE}, MC_{SW}, and EC_{SW} are, then, selected to represent the bridge motions under seismic loads. Displacement-time histories for the selected locations under the 1979 El Centro EQ (Crustal EQ); 1986 North Palm Springs EQ (Crustal EQ with a broad spectrum); 1965 Puget Sound (Olympia Hwy. Test Lab) EQ (Intraplate EQ); and 1985 Valparaiso (Vina del Mar.) EQ (Subduction Zone EQ) are plotted and shown in Figs. 5.14 to 5.17, respectively.

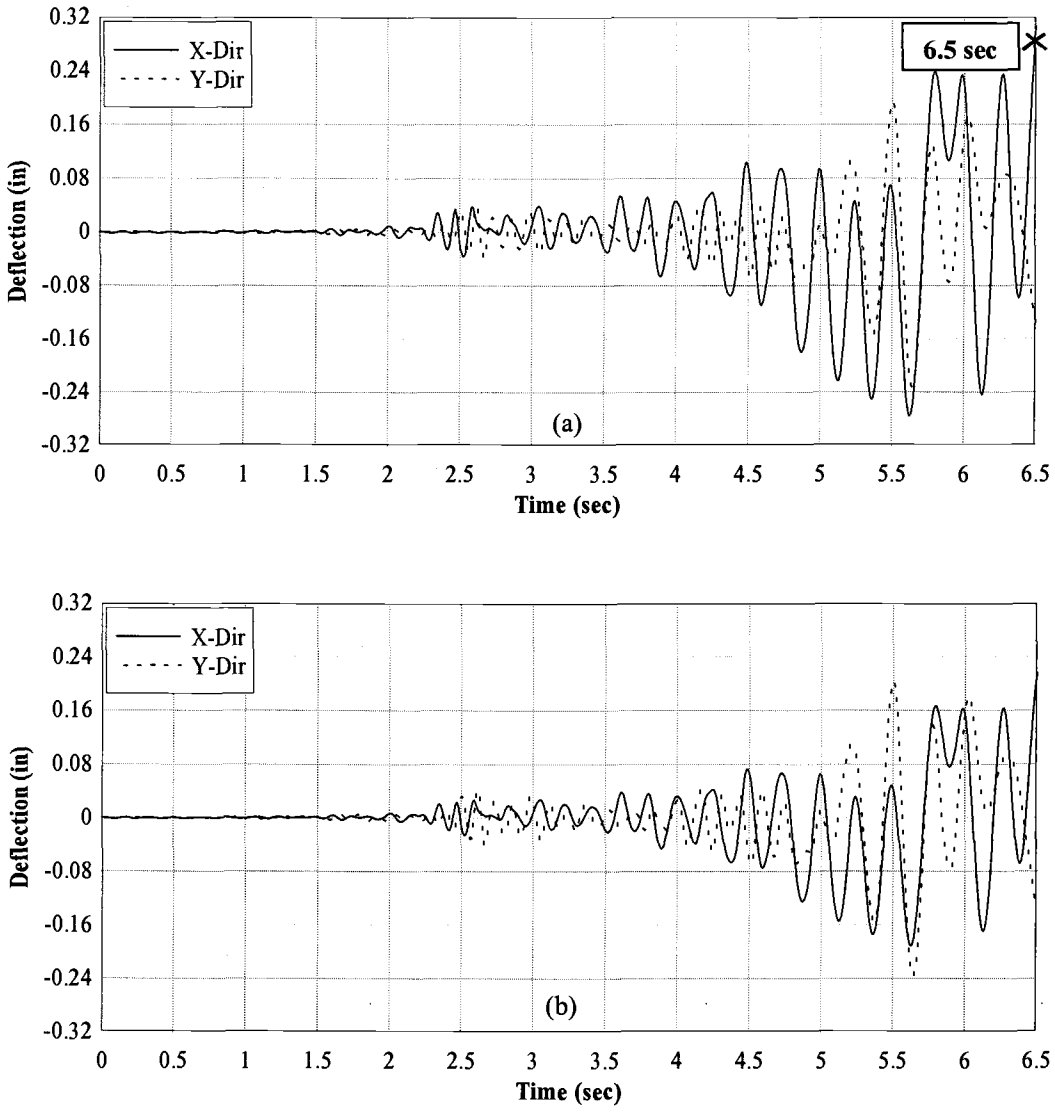

Figure 5.14. Deflection-Time History under 1979 El Centro EQ (Crustal EQ): (a) EC_{SE}; (b) MC_{SE}; (c) MC_{SW}; (d) EC_{SW}

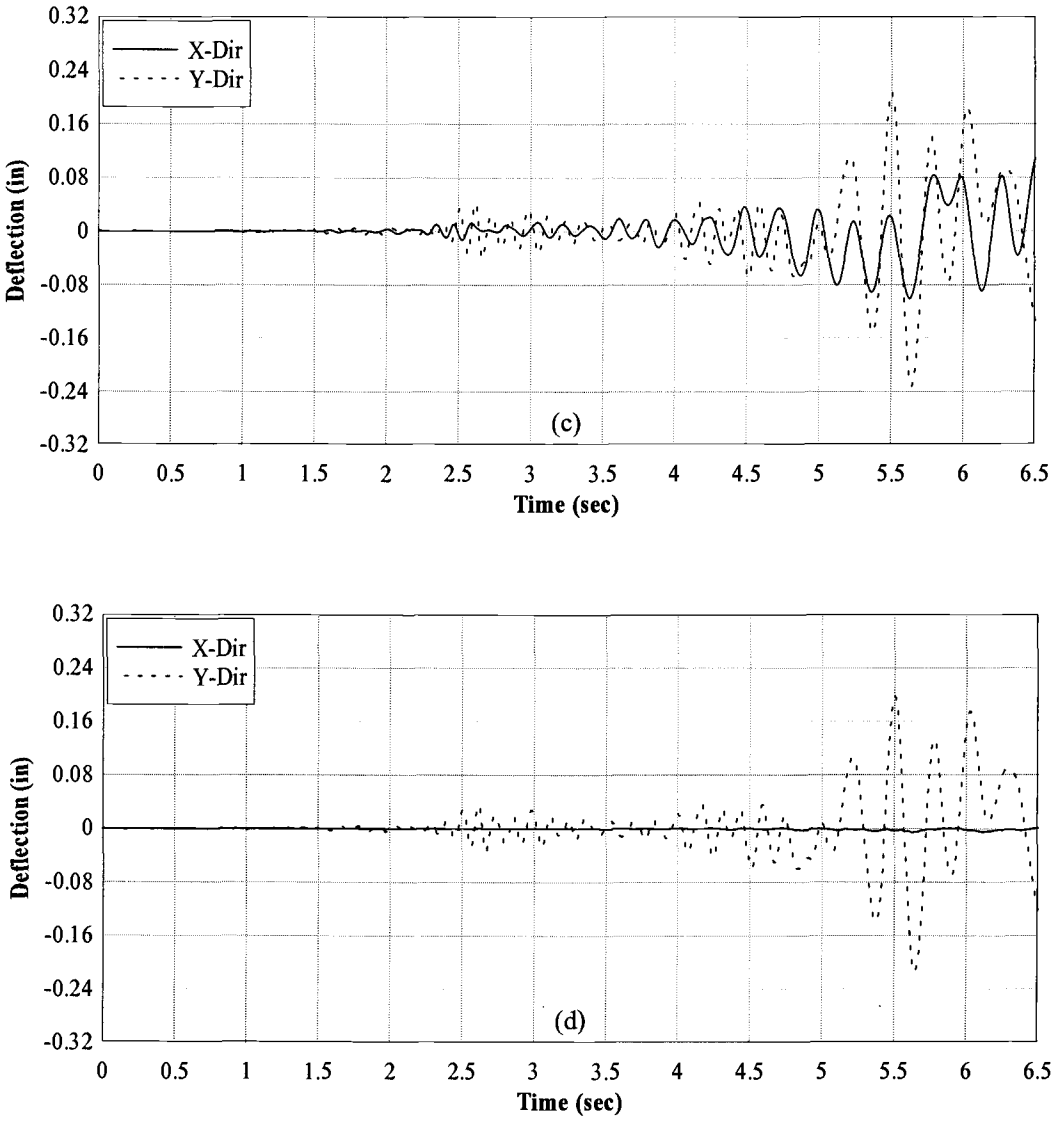

Figure 5.14 (Cont'd). Deflection-Time History under 1979 El Centro EQ (Crustal EQ): (a) EC_{SE}; (b) MC_{SE}; (c) MC_{SW}; (d) EC_{SW}

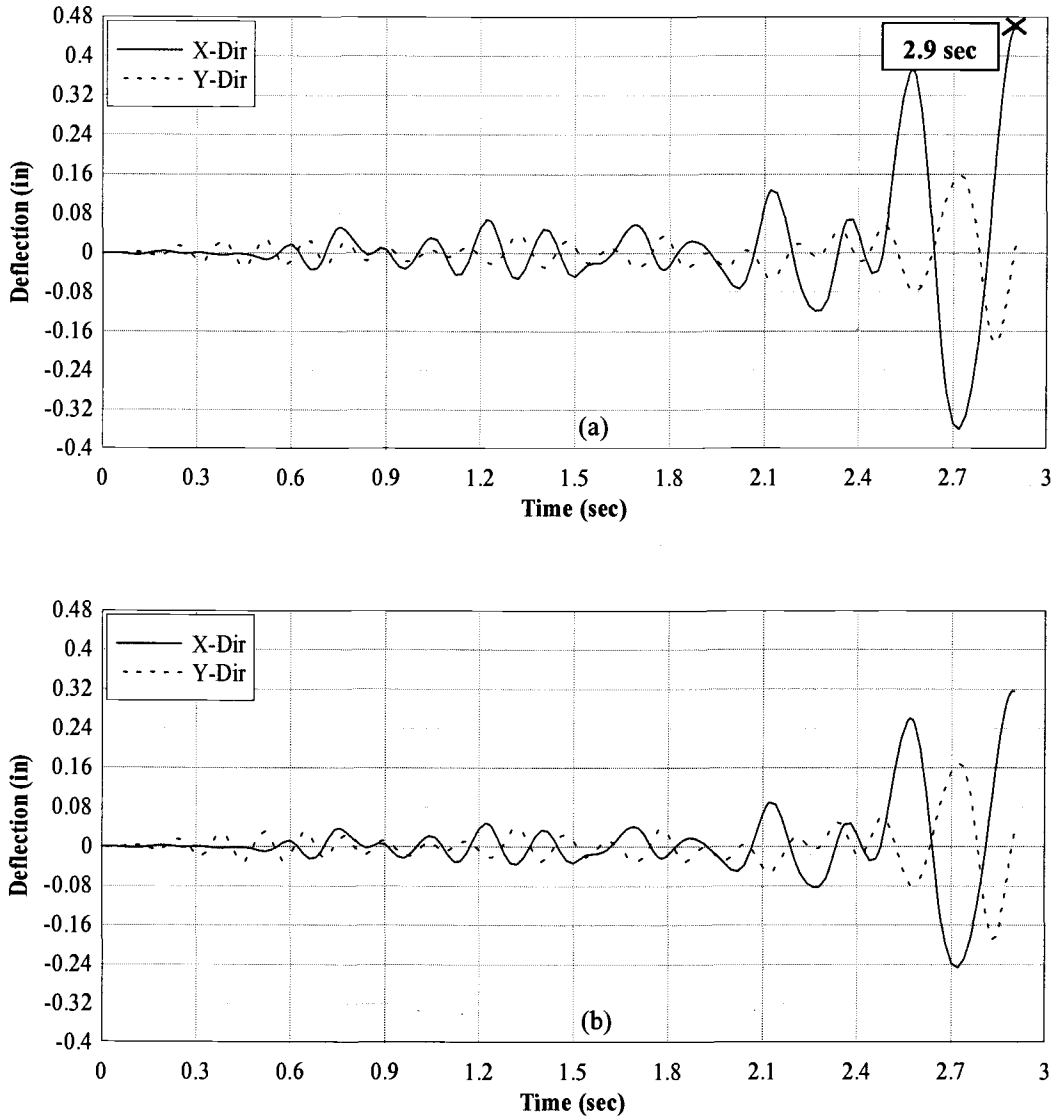

Figure 5.15. Deflection-Time History under 1986 North Palm Springs EQ (Crustal EQ with a Broad Spectrum): (a) EC_{SE}; (b) MC_{SE}; (c) MC_{SW}; (d) EC_{SW}

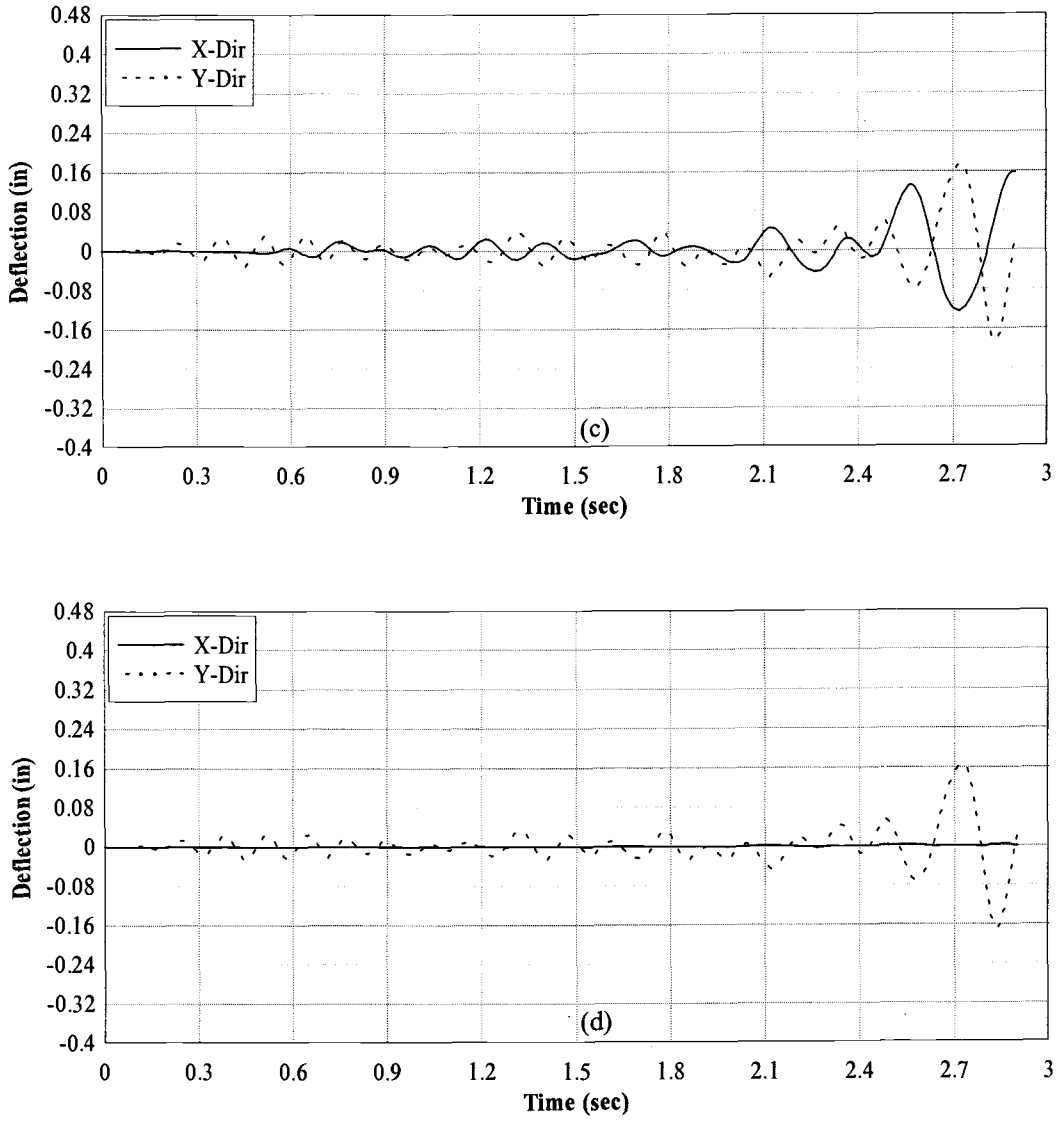

Figure 5.15 (Cont'd). Deflection-Time History under 1986 North Palm Springs EQ (Crustal EQ with a Broad Spectrum): (a) EC_{SE}; (b) MC_{SE}; (c) MC_{SW}; (d) EC_{SW}

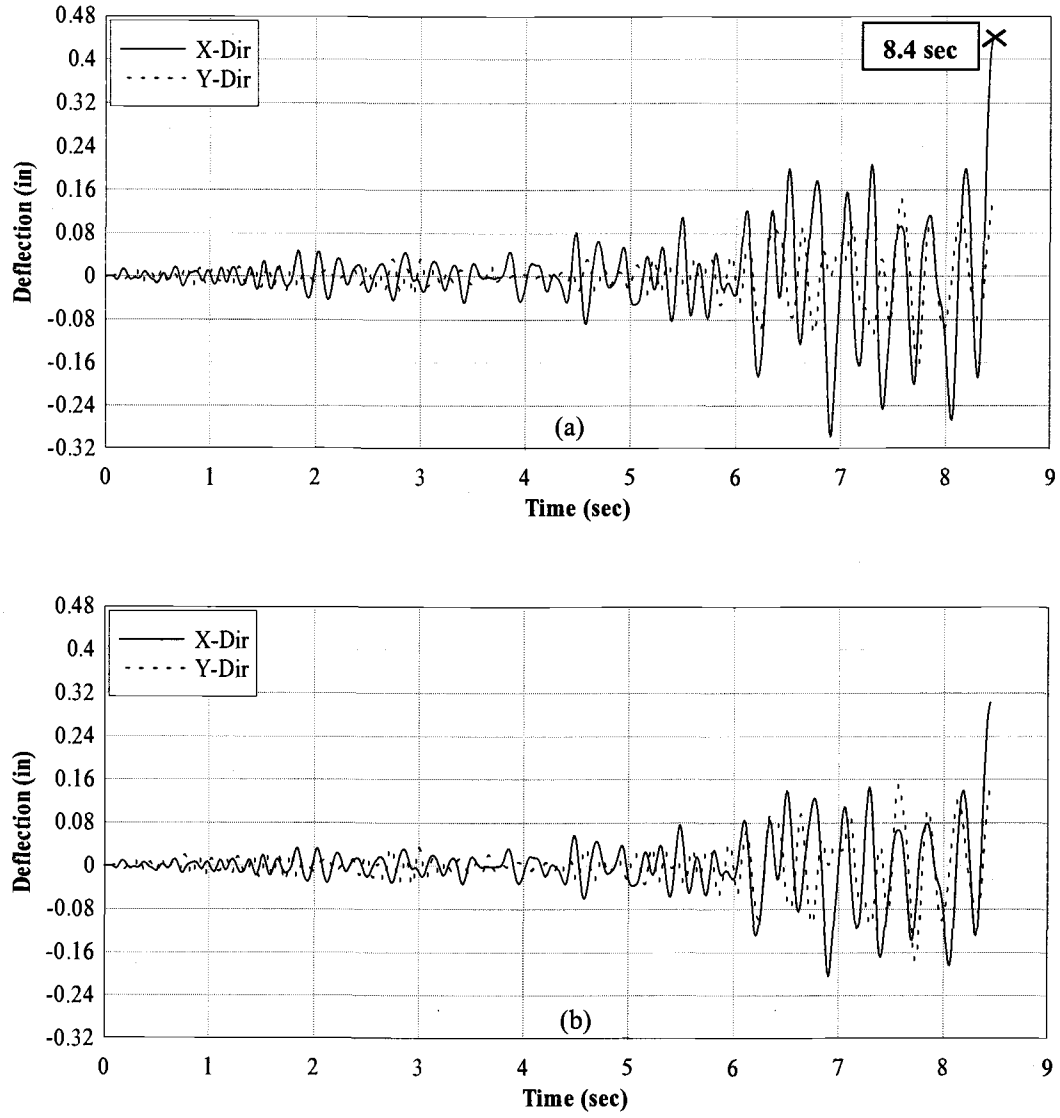

Figure 5.16. Deflection-Time History under 1965 Puget Sound EQ (Intraplate EQ): (a) EC_{SE}; (b) MC_{SE}; (c) MC_{SW}; (d) EC_{SW}

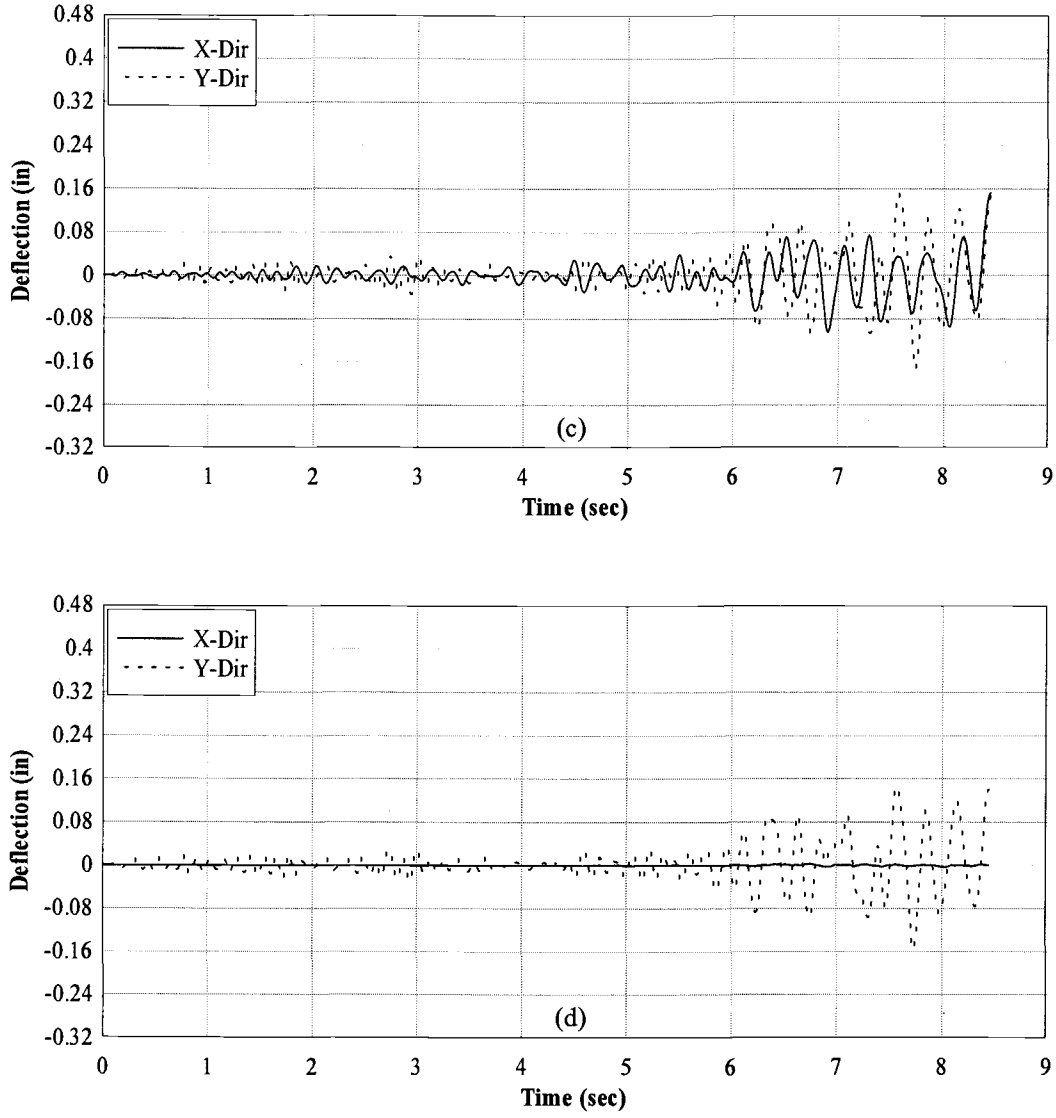

Figure 5.16 (Cont'd). Deflection-Time History under 1965 Puget Sound EQ (Intraplate EQ): (a) EC_{SE}; (b) MC_{SE}; (c) MC_{SW}; (d) EC_{SW}

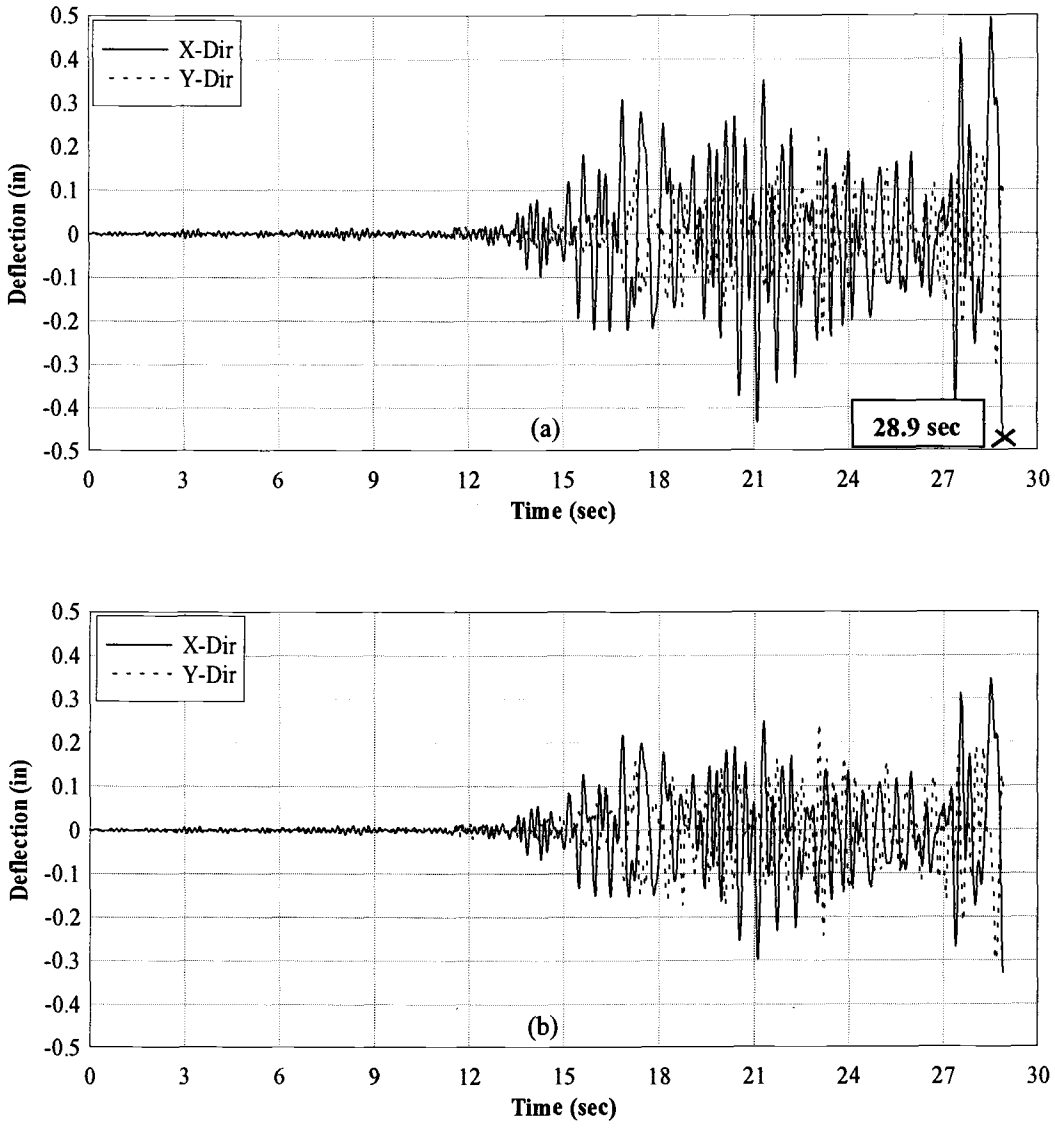

Figure 5.17. Deflection-Time History under 1985 Valparaiso EQ (Subduction Zone EQ): (a) EC_{SE}; (b) MC_{SE}; (c) MC_{SW}; (d) EC_{SW}

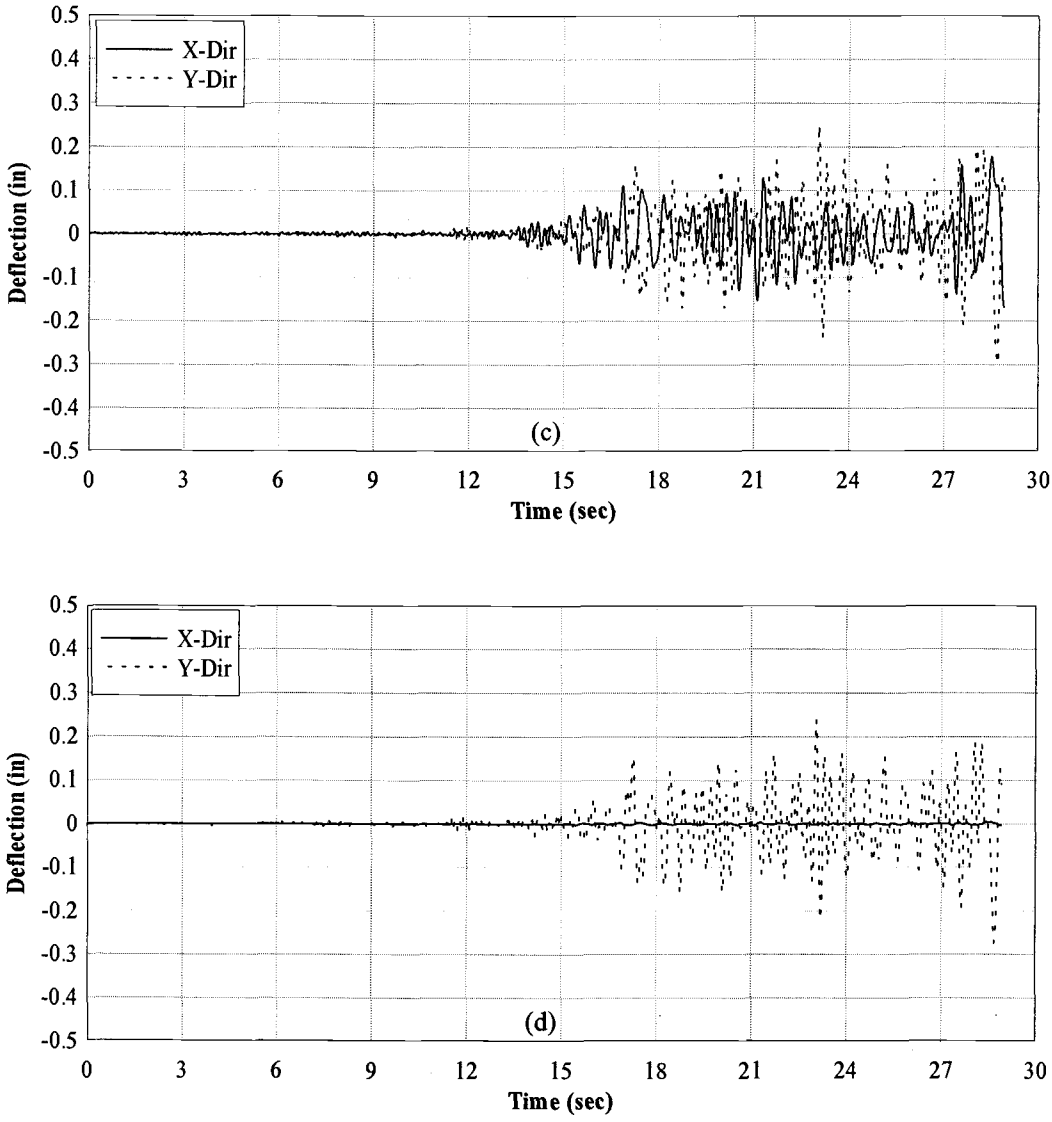

Figure 5.17 (Cont'd). Deflection-Time History under 1985 Valparaiso EQ (Subduction Zone EQ): (a) EC_{SE}; (b) MC_{SE}; (c) MC_{SW}; (d) EC_{SW}

It can be seen from Figs. 5.14 to 5.17 that the maximum displacements under the 1979 El Centro; 1986 North Palm Springs; 1965 Puget Sound; and 1985 Valparaiso earthquakes occur at 6.5 sec, 2.9 sec, 8.4 sec, and 28.9 sec, respectively, at which points, the solutions diverge, and the bridge is considered to fail, as discussed previously. They are obtained from location EC_{SE} in transverse direction (X-Dir). The maximum displacements are reached shortly after the maximum ground accelerations applied along the transverse axis (X-axis) occur; i.e., 212.6 cm/sec^2 at 5.9 sec, 262.9 cm/sec^2 at 2.5 sec, 237.6 cm/sec^2 at 6.4 sec, and 267.1 cm/sec^2 at 28.5 sec for the 1979 El Centro; 1986 North Palm Springs; 1965 Puget Sound; and 1985 Valparaiso earthquakes, respectively. It should be noted that the actual maximum ground acceleration for the 1985 Valparaiso EQ is 325.3 cm/sec^2 at 37.6 sec, but the solution ceases to converge before the actual maximum is reached. At failure, extensive cracks develop throughout the east end columns (EC_{SE} and EC_{NE}), as observed in Fig. 5.19(c). Moreover, longitudinal steel bars and some ties in the columns yield, as indicated by solid bars in Fig. 5.20 (shown later).

The bridge's response to all of the earthquakes is approximately dominated by frequencies in the 4-5 Hz range. The natural frequencies of the first two modes of vibration of the bridge (6.44 Hz and 8.23 Hz) are closest to this range. Consequently, the assumption that the first two modes dominate the bridge response to the earthquake excitations is believed to be reasonable.

For the response to each earthquake, it is shown that the displacement-time histories in the longitudinal direction (Y-Dir) are almost the same for all the locations, as there is no bending in the bridge deck during the rigid body-based bridge motion. The magnitude of the displacements in the transverse direction (X-Dir) decreases, as the distance increases from the east end. This is because the lateral stiffness in the east end of the bridge is less than that in the west end, where there is a continuous end abutment. As a result, during an earthquake, the displacements in the east end are relatively larger than those in the west end.

The bridge under the 1986 North Palm Springs EQ fails earliest because the earthquake has high Fourier amplitudes within the dominant natural frequencies of the bridge (Figs 5.7 and 5.8). The bridge also cracks almost right at the beginning of the earthquake (Table 5.7 shown later). This will be explained in detail later. The bridge under the 1985 Valparaiso EQ fails latest due to the fact that the magnitude of the accelerations during the first 15 seconds of the earthquake is small (Figs 5.11 and 5.12).

5.4.2 Development of Cracks in Concrete and Yielding in Reinforcing Steel

The cracking and yielding behaviors of the bridge under all the earthquake motions are examined, and it is found that the responses of the bridge to those earthquakes are similar. That is, the bridge starts cracking in the east end columns (either EC_{SE} or EC_{NE}). Following that, cracks in the west end columns (EC_{SW} or EC_{NW}) are found. Typical first cracking in EC_{SE} and EC_{NE} is shown in Fig. 5.18.

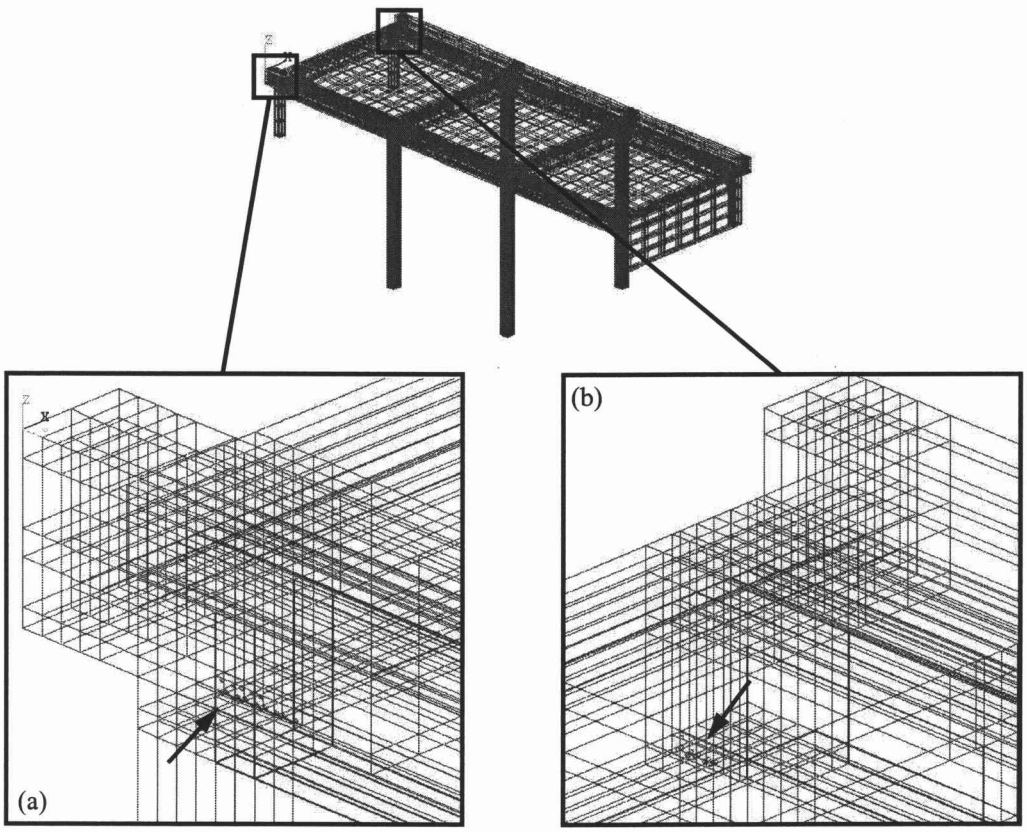

Figure 5.18. Typical First Cracking: (a) EC_{SE}; (b) EC_{NE}

A few seconds after cracks develop in the end columns, the middle columns (MC_{SE}, MC_{NE}, MC_{SW}, and MC_{NW}) start cracking. The cracks can occur either at the top (T) or the bottom (B) of the middle columns, as indicated in Table 5.17 (shown later). Next, more cracks develop in all the columns, especially in the east end columns. Figs 5.19(a) to (c) show typical cracks developing in the columns.

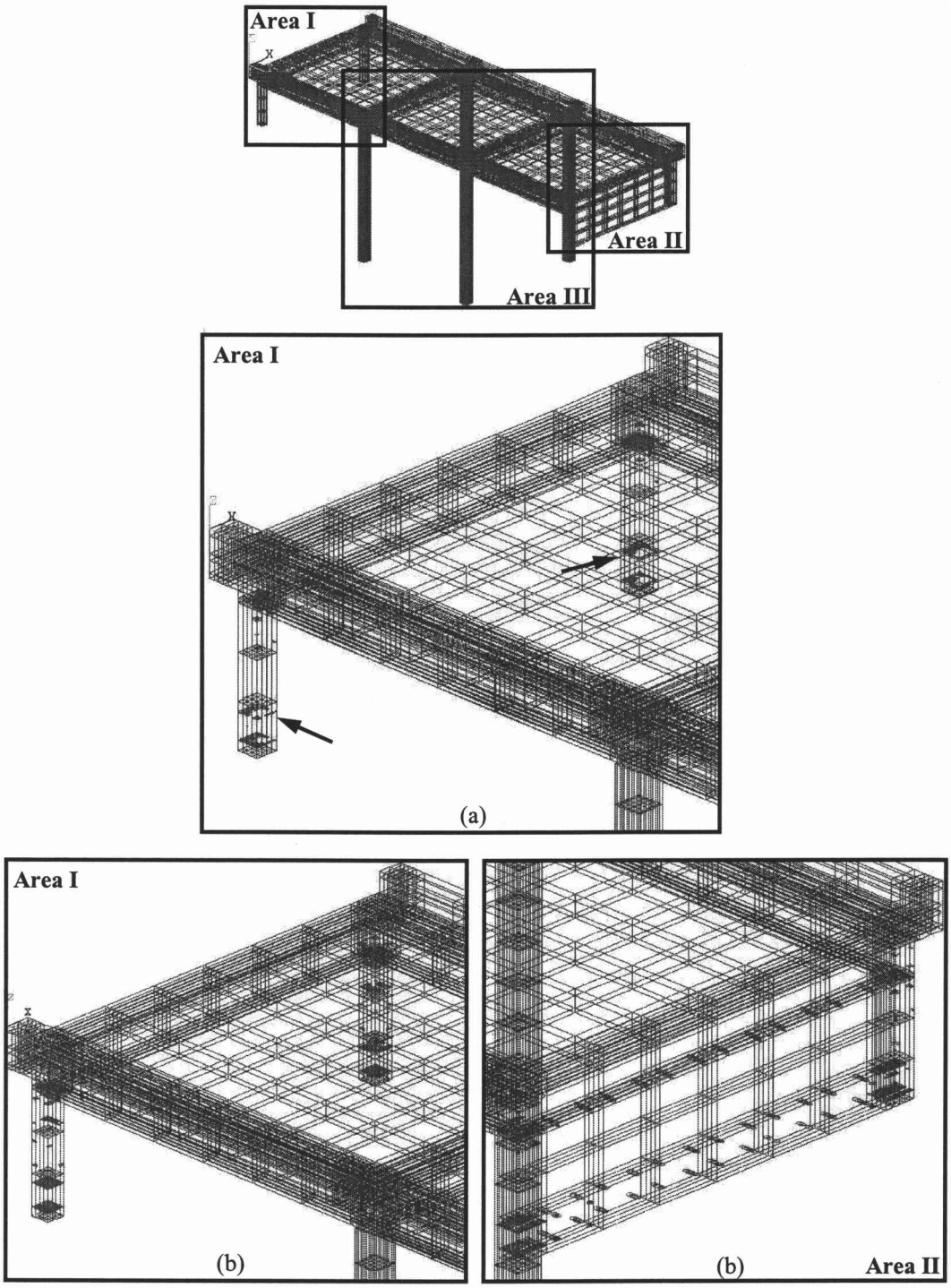

Figure 5.19. Typical Cracks: (a) Cracking Level 1; (b) Cracking Level 2; (c) At Failure

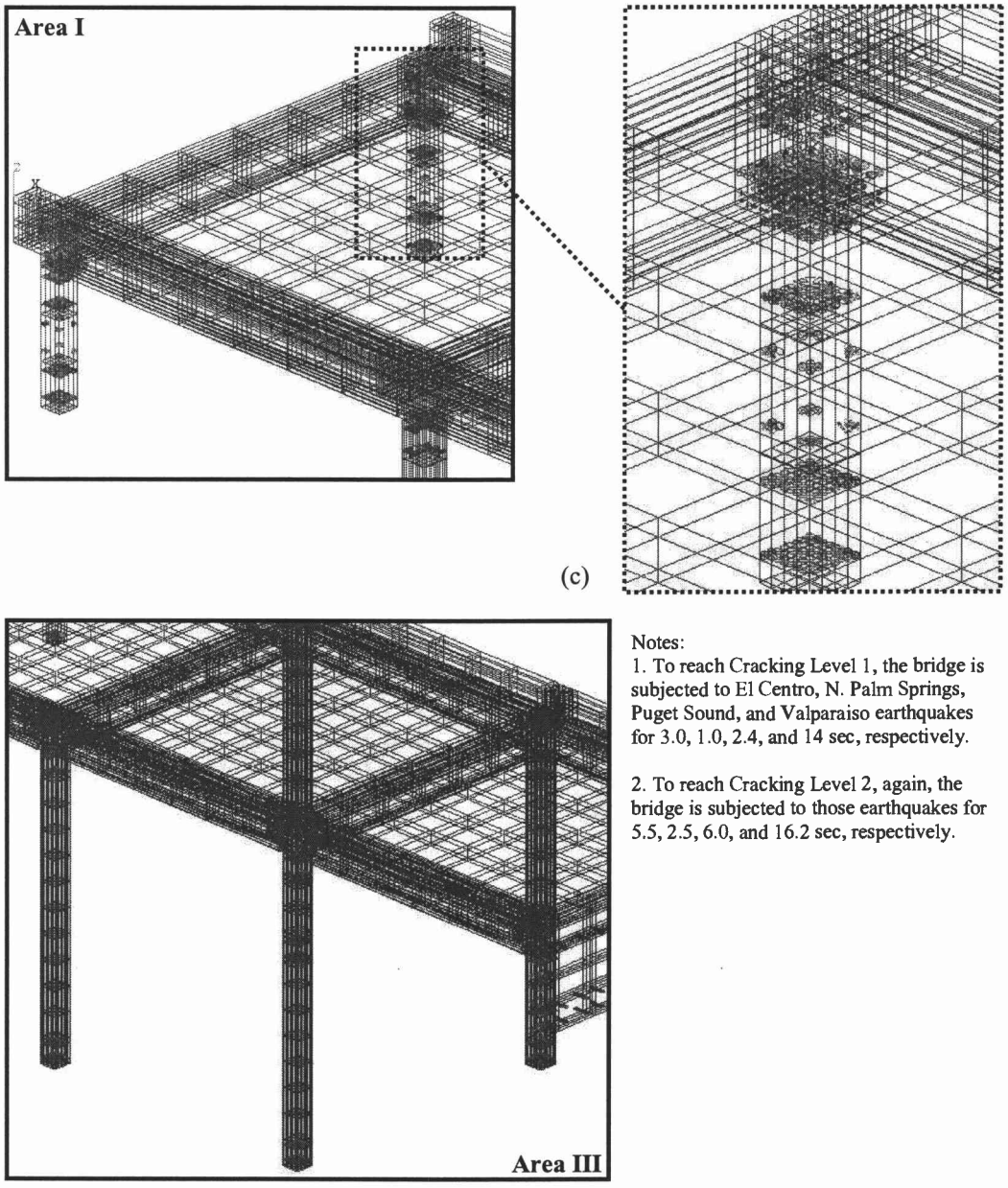

Figure 5.19 (Cont'd). Typical Cracks: (a) Cracking Level 1; (b) Cracking Level 2; (c) At Failure

As shown in Fig. 5.19(c), dense cracks develop at the top of the east end columns (EC_{SE} and EC_{NE}), as they displace the most. No cracks can be found in the bridge deck during the earthquakes. This is because the bridge response is dominated by rigid-body motion, as discussed earlier.

Table 5.7 shows times, at which each column starts cracking and reinforcing steel starts yielding under all the ground motions.

Table 5.7. Time of First Cracking in Concrete and First Yielding in Steel

Earthquake	TIME OF FIRST CRACKING IN CONCRETE (SEC)								Time of first yielding in reinforcing steel (sec)	Time at Failure (sec)
	Location									
	EC_{SE}	EC_{NE}	EC_{SW}	EC_{NW}	MC_{SE}	MC_{NE}	MC_{SW}	MC_{NW}		
1979 El Centro	2.33	2.41	2.55	2.55	5.33 T&B	4.83 T	5.33 B	5.33 T	4.85	6.5
1986 N. Palm Springs	0.58	0.46	0.32	0.32	2.54 T&B	2.54 T&B	2.54 B	2.54 B	2.52	2.9
1965 Puget Sound	1.22	0.50	0.84	1.34	6.20 B	6.20 T&B	7.56 B	6.20 B	6.20	8.4
1985 Valparaiso	11.60	12.63	12.10	12.10	16.83 T&B	16.83 B	16.83 B	18.13 B	16.80	28.9

Note: T – Top and B – Bottom

The east end columns (EC_{SE} and EC_{NE}) crack first under all the earthquakes except the 1986 North Palm Springs EQ where the west end columns (EC_{SW} and EC_{NW}) crack first. The time for first cracking is shortest for the bridge under the 1986 North Palm Springs EQ, which has a broad spectrum covering the dominant modes of the bridge response. The time is longest for the bridge under the 1985

Valparaiso EQ, as the accelerations are small for the first 10 seconds of the ground motion. It is interesting that first cracking in the middle columns occurs at almost the same time as first yielding in the reinforcing steel that is in the east end columns (EC_{SE} and EC_{NE}). This may be because once the reinforcing steel yields in the columns, the load is redistributed to the middle column, causing cracking.

Fig. 5.20 shows locations of typical yielding in reinforcing steel at failure.

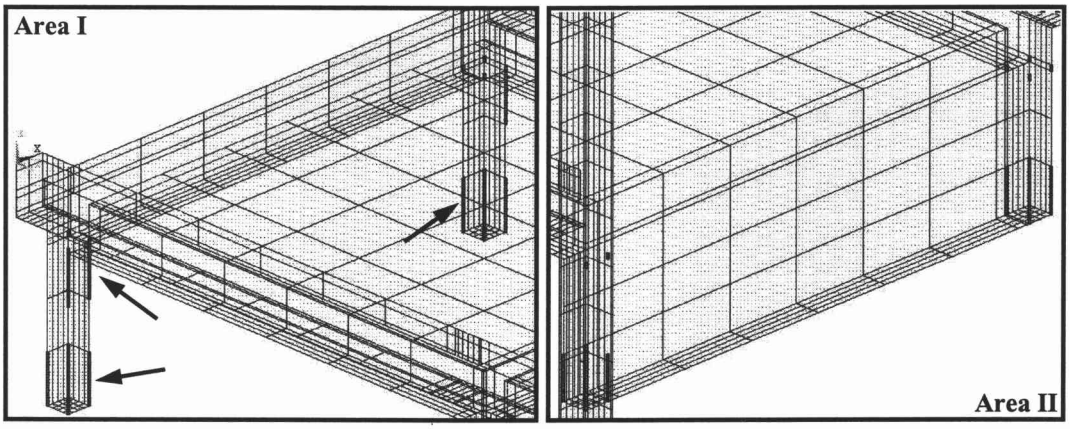

Figure 5.20. Typical Yielding in Reinforcing Steel at Failure

It can be seen that all longitudinal bars yield at both the top and bottom of the east end columns, corresponding to the extensive cracks occurring in these columns at failure (Fig. 5.19(c)).

5.5 CONCLUSIONS

Using three-dimensional finite element models, results obtained from nonlinear dynamic analyses of the Horsetail Creek bridge subjected to earthquake excitations are used to investigate behavior and to assess the bridge's seismic risk. In this study, earthquake acceleration-time histories appropriate to the Pacific Northwest site are modified so that their response spectrum, within a range of natural periods of interest, matches the 1996 AASHTO design response spectrum. The earthquakes are selected based on types of earthquake sources and characteristics. They are the 1979 El Centro EQ (Crustal EQ); 1986 North Palm Springs EQ (Crustal EQ with a broad spectrum); 1965 Puget Sound (Olympia Hwy. Test Lab) EQ (Intraplate EQ); and 1985 Valparaiso (Vina del Mar.) EQ (Subduction Zone EQ). Dynamic response to these earthquakes in terms of displacement-time histories, development of cracking in concrete and yielding in reinforcing steel are examined.

The results show that the bridge response is dominated by rigid-body motion of the deck in the first and second modes of vibration; i.e., transverse and longitudinal translations, respectively. The motion causes a number of cracks in the columns, but no cracks in the superstructure during the earthquakes. The bridge is considered to fail when the nonlinear solutions start to diverge, which is at 6.5 sec, 2.9 sec, 8.4 sec, and 28.9 sec for the 1979 El Centro; 1986 North Palm Springs; 1965 Puget Sound; and 1985 Valparaiso earthquakes, respectively. The maximum

displacements obtained for the east end columns in the transverse direction (X-Dir) under all the seismic inputs are reached at those points of time of failure. They occur shortly after the time of maximum ground acceleration.

The bridge responses in terms of cracking in concrete and yielding in reinforcing steel for all the seismic motions are similar. That is, cracking first starts in the east end columns, and then progresses to the west end columns. After more cracks develop in those columns for a few seconds, the middle columns start cracking. At failure, extensive cracks can be observed in the east end columns, corresponding to the yielding in longitudinal steel bars and ties in the columns. Cracks occur soonest in the bridge under the 1986 North Palm Springs EQ and the bridge reaches failure earliest, compared to the other earthquakes, due to the broad spectrum covering most dominant modes of the bridge response. On the other hand, the bridge under the 1985 Valparaiso EQ fails latest due to the small magnitudes of the ground accelerations during the first 15 seconds of the record.

It can be concluded from the investigation that the bridge would fail under the applied earthquakes due to substructure collapse (column failure) at the east end columns of the bridge from extensive cracking and yielding in the longitudinal steel bars. This is because the bridge structure was not designed to resist lateral forces induced by an earthquake. The design does not contain adequate reinforcement for column confinement and vertical bar splices and anchorage. Substructure seismic retrofits are recommended for the Horsetail Creek bridge to increase ductility. These can involve external wrapping with FRP sheets or straps or steel casing filled

with grout. The proposed seismic retrofits will reduce the potential for substructure collapse in future seismic events.

REFERENCES

AASHTO Subcommittee on Bridges and Structures. (1996). *Standard Specifications for Highway Bridges*. 16th ed., Including up to 1999 Interim Revisions. American Association of State and Highway Transportation Officials, Washington D.C.

Adams, J. (1990). "Paleoseismicity of the Cascadia Subduction Zone Evidence from Turbidites off the Oregon-Washington Margin." *Tectonics*, 9, 569-583.

Atwater, B.F., Stuiver, M., and Yamaguchi, D.K. (1991). "Radiocarbon Test of Earthquake Magnitude at the Cascadia Subduction Zone." *Nature*, 353(6340), 156-158.

Booth, E.D. (1994). *Concrete Structures in Earthquake Regions: Design and Analysis*." Longman Scientific & Technical, Essex, England.

Building Seismic Safety Council. (1997). *NEHRP Recommended Provisions for Seismic Regulations for New Buildings and other Structures.*, Washington D.C.

Chopra, A.K. (2000). *Dynamics of Structures: Theory and Applications to Earthquake Engineering*. 2nd ed., Prentice Hall, Upper Saddle River, NJ.

Clough, R.W., and Penzien, J. (1993). *Dynamics of Structures*. 2nd ed., McGraw-Hill, Inc., New York, New York.

Groff, R., Shike, C., and Hirota, M. (1999). "Assessing Oregon's Seismic Risk." ODOT paper for US-Japan Bridge Engineering Workshop, Salem, OR.

Hodhod, O.A. (1997). "Seismic Performance of a Fiber-Reinforced Plastic Cable-Stayed Bridge." *Structural Engineering and Mechanics*, 5(4), 399-414.

Issa, M.A., Yousif, A.A., and Issa, M.A. (2000). "Effect of Construction Loads and Vibrations on New Concrete Bridge Decks." *J. of Bridge Engineering*, ASCE, 5(3), 249-258.

Tedesco, J.W., Stallings, J.M., and El-Mihilmy, M. (1999). "Finite Element Method Analysis of a Concrete Bridge Repaired with Fiber Reinforced Laminates." *Computers and Structures*, 72, 379-407.

USGS. (2000). "Glossary of Earthquake Terms." <http://earthquake.usgs.gov>.

Wahab, M.M.A., and Roeck, G.D. (1999). "Effect of Excitation Type on Dynamic System Parameters of a Reinforced Concrete Bridge." *Structural Engineering and Mechanics*, 7(4), 387-400.

Wakefield, R.R., Nazmy, A.S., and Billington, D.P. (1991). "Analysis of Seismic Failure of Skew RC Bridge." *J. of Structural Engineering*, ASCE, 117(3), 972-986.

Woodward-Clyde Federal Services. (1997) "Develop Suites of Time Histories." *Draft report for SAC Project Task: 5.4.1.*, Pasadena, CA.

CHAPTER 6: CONCLUSIONS AND RECOMMENDATIONS

The conclusions from the study can be divided into two main parts; i.e., conclusions made for FE models of the full-scale beams and those for the HC bridge. They are discussed as follows.

6.1 CONCLUSIONS FOR FE MODELS OF THE FULL-SCALE BEAMS

1. The FE models can simulate the overall behavior of the full-scale beams. They also simulate the local behavior in terms of load-strain relationships at the selected locations. For the load-tensile strain plots for the main steel rebar at midspan, the FE analyses correlate very well with the experiments in both the linear and nonlinear ranges. The load-tensile strain plots for the FRP composites show reasonable agreement between the FE analyses and the experimental results. Also, for the comparisons of the load-compressive strain relationship at the center of the top face of the beams at midspan, good agreement can also be observed.
2. The trends in the load-deflection plots at midspan obtained from the FE predictions and the experimental data correlate well. However, the FE models are slightly stiffer than the actual beams in both the linear and

nonlinear ranges. This may be due to existing microcracks in the actual beams that are not included in the FE models, the assumption of perfect bond between the concrete and steel rebars made in the FE models, and additional constraints provided in the FE models themselves.

3. Crack patterns obtained from the FE models at the peak loads resemble very well those at failure of the experimental beams.
4. The ultimate loads from the FE models are lower than those from the experiments by 6% - 18%. These differences can be attributed to strain hardening in the steel, which is not included in the models, and toughening mechanisms at the crack faces in the actual beams.
5. Modeling methodology developed in this study can be used as a guideline for further FE studies in reinforced concrete strengthened by FRP laminates.

6.2 CONCLUSIONS FOR FE MODELS OF THE HC BRIDGE

The conclusions for the study of the HC bridge can be subdivided into three phases as follows:

6.2.1 Service Limit State

Based on the sensitivity study of uncertain bridge parameters, investigating influences of some aspects of bridge geometry, levels of existing damage in the bridge, strength of in-situ concrete, and soil foundation stiffness, the following conclusions can be drawn:

1. Existing damage of the bridge must be taken into consideration in order to obtain a realistic bridge model that can best simulate the responses under service loads. To include the existing damage, the bridge model is pre-cracked with an initial load before the service truck load is applied.
2. The results from the study of the influence of concrete strength and on-site pulse-velocity measurements suggest that the actual concrete strength is much higher than the value recommended by AASHTO. That is, the in-situ concrete strength of the bridge is most likely to be around 27.6 MPa (4000 psi) rather than the conservative 17.3 MPa (2500 psi) suggested by AASHTO for bridge evaluations (AASHTO 1989 and 1994).
3. Soil-structure interface modeling is necessary as a fine-tuning tool to predict bridge response and represent realistic boundary conditions of the bridge. Translational and rotational spring elements are used to represent the bridge footings on soil foundation. Varying soil stiffness primarily affects the strains on the longitudinal beams.

4. Strains predicted by the optimal FE bridge model obtained from the sensitivity study correlate very well with the field data.
5. From the field test and FE simulations, it is shown that when the single axle of the full truck is positioned at 11.05 and 15.35 m. from the east end of the bridge deck (Positions 4 and 6), maximum strains occur in the monitored transverse and longitudinal beams, respectively. However, the strain on the east end of the longitudinal beam reaches maximum when the load is placed at 12.34 m. (Position 5). This is because the loads from both the single and tandem axles strongly influence the beams when positioned at those locations.

6.2.2 Inelastic Behavior and Ultimate Load States

1. Strengthening the HC bridge with FRP laminates increases load carrying capacity based on scaled gravity load and scaled truck load by 37% and 28%, respectively.
2. Yielding of both the tension steel in the transverse beams and steel reinforcement in the bridge deck is delayed for the FRP-strengthened bridge.
3. Crack propagation is delayed, and fewer cracks are observed for the bridge strengthened with FRP laminates.

4. The failure mechanism of the bridge is altered from shear failure in the transverse beams to flexure failure with the FRP strengthening.

6.2.3 Dynamic Response

1. The response under earthquakes, which are appropriate to the bridge's site, is dominated by rigid-body motion of the deck in the first and second modes of vibration; i.e., transverse and longitudinal translations, respectively. This causes a number of cracks in the columns, but no cracks in the bridge deck and beams during the earthquakes.
2. It is found that dynamic responses of the unstrengthened and FRP-strengthened bridges are the same, as the FRP strengthening was primarily designed to increase flexure and shear capacities for traffic-loads. Lateral stiffness is not enhanced. Additionally, the dominant bridge motion is a rigid-body translation of the deck involving flexure in the columns, not the beams where the FRP sheets were installed.
3. In this study, the bridge fails at 6.5 sec, 2.9 sec, 8.4 sec, and 28.9 sec under the 1979 El Centro, 1986 North Palm Springs, 1965 Puget Sound, and 1985 Valparaiso earthquakes, respectively. The maximum displacements are reached at these points of time of failure and occur shortly after the absolute maximum ground acceleration of the earthquakes.

4. The bridge responses in terms of cracking in concrete and yielding in reinforcing steel under all the earthquakes are similar. That is, cracks start first in the corner columns, and, then, develop in the middle columns. At failure, extensive cracking can be observed in the east end columns, corresponding to the yielding in longitudinal steel bars and ties in these columns.
5. It can be concluded that the bridge would fail under the earthquakes due to substructure collapse (column failure) at the east end columns of the bridge, as the bridge was not designed to withstand lateral forces induced by an earthquake. Substructure seismic retrofits are recommended for the Horsetail Creek bridge using FRP sheets or straps wrapped around the columns or steel casing filled with grout. The proposed seismic retrofits will increase ductility of the bridge and reduce potential for substructure collapse in future seismic events.

6.3 RECOMMENDATIONS

Nonlinear FE analysis is required to examine structural behavior of reinforced concrete beams and bridges with FRP strengthening in the inelastic regime to failure. As the load increases, more cracks develop, and the structures behave more nonlinearly. An iterative analysis procedure needs to be performed to

obtain a converged solution. This results in a large requirement for computer resources in terms of CPU time and disk space. The recommendations are made based on this study so that nonlinear FE analysis of the reinforced concrete structures with FRP laminates can be performed more efficiently and accurately. They mainly focus on the FE modeling methodology and analysis approach as follows:

1. Simplification should be made in modeling both full-scale beams and bridges to reduce the amount of the computer resources required. This can be done by taking an advantage of symmetry (if possible); "lumping" rebars in locations associated with the FE mesh; considering the use of "smeared" rebars when reinforcement is uniformly distributed; using a consistent overall thickness of FRP composites to avoid discontinuities; and assigning a coarser mesh to parts of the structures which do not significantly contribute to structural response.
2. For simplification of the truck load configurations, the load from each set of tires for both single and tandem axles can be lumped to the center of each set. Furthermore, the lumped load at locations where it does not coincide with a node in the FE mesh needs to be linearly distributed to the nearest nodes in order to analyze a variety of truck locations on the bridge deck.
3. Once the structure cracks, loads must be gradually applied to the models to avoid numerical instability. Sufficiently small load step sizes are required, particularly at changes in behavior of the reinforced concrete structures; i.e.,

major cracking of concrete, yielding in steel, and approaching failure of the structures. Tolerances in convergence criteria should be carefully defined. With load adjustment, tolerances for both force and displacement criteria may need to be relaxed to avoid a diverged solution. After the load range that produces a diverged solution is revealed from a previous trial run, either tolerance or load adjustments or both have to be made to prevail over the divergence problem at that loading level.

4. Complete stress-strain curves of concrete need to accurately predict structural behavior up to failure.
5. Concrete confinement induced by FRP encasement, localized effects from applied concentrated loads, and steel ties in the columns should be included in the models to better represent the actual behavior of the structures.
6. Soil-structure interface modeling should be considered in modeling bridges. This can be achieved by replacing the bridge footings with translational and rotational spring elements to simulate realistic foundation behavior.
7. For older bridges, existing damage should be included by introducing some cracks to the bridge models in the pre-loading step to more closely represent the actual bridge conditions.

REFERENCES

AASHTO Subcommittee on Bridges and Structures. (1989). *Guide Specifications for Strength Evaluation of Existing Steel and Concrete Bridges*. American Association of State and Highway Transportation Officials, Washington D.C.

AASHTO Subcommittee on Bridges and Structures. (1994). *Manual for Condition Evaluation of Bridge*. American Association of State and Highway Transportation Officials, Washington D.C.

BIBLIOGRAPHY

AASHTO Subcommittee on Bridges and Structures. (1989). *Guide Specifications for Strength Evaluation of Existing Steel and Concrete Bridges*. American Association of State and Highway Transportation Officials, Washington D.C.

AASHTO Subcommittee on Bridges and Structures. (1994). *Manual for Condition Evaluation of Bridge*. American Association of State and Highway Transportation Officials, Washington D.C.

AASHTO Subcommittee on Bridges and Structures. (1996). *Standard Specifications for Highway Bridges*. 16th ed., Including up to 1999 Interim Revisions. American Association of State and Highway Transportation Officials, Washington D.C.

ACI Committee 318. (2002). *Building Code Requirements for Structural Concrete (ACI 318-02) and Commentary (ACI 318R-02)*. ACI, Farmington Hills, MI.

ACI 440, American Concrete Institute. (2002). *Guide for the Design and Construction of Externally Bonded FRP Systems for Strengthening Concrete Structures*. American Concrete Institute, Farmington Hills, Michigan.

Adams, J. (1990). "Paleoseismicity of the Cascadia Subduction Zone Evidence from Turbidites off the Oregon-Washington Margin." *Tectonics*, 9, 569-583.

Atwater, B.F., Stuiver, M., and Yamaguchi, D.K. (1991). "Radiocarbon Test of Earthquake Magnitude at the Cascadia Subduction Zone." *Nature*, 353(6340), 156-158.

American Society for Testing and Materials (ASTM) Subcommittee C09.70. (1994). *Standard Test Method for Static Modulus of Elasticity and Poisson's Ratio of Concrete in Compression*, Designation C 469-94, ASTM, West Conshohocken, Pennsylvania.

ANSYS User's Manual, Vol. I-IV; Revision 5.5. (1998). Swanson Analysis System, Inc., Houston, PA.

Balakrishnan, S., and Murray, D.W. (1988). "Concrete Constitutive Model for NLFE Analysis of Structures." *J. Struct. Engrg.*, ASCE, 114(7), 1449-1466.

Balakrishnan, S., Elwi, A.E., and Murray, D.W. (1988). "Effect of Modeling on NLFE Analysis of Concrete Structures" *J. Struct. Engrg.*, ASCE, 114(7), 1467-1487.

Bangash, M.Y.H. (1989). *Concrete and Concrete Structures: Numerical Modeling and Applications*. Elsevier Science Publishers, LTD., Essex, England.

Barnard, P.R. (1964). "Researches into the Complete Stress-Strain Curve for Concrete." *Magazine of Concrete Research*, 16(49), 203-210.

Barzegar, F., and Maddipudi, S. (1997). "Three-Dimensional Modeling of Concrete Structures. II: Reinforced Concrete." *J. Struct. Engrg.*, ASCE, 123(10), 1347-1356.

Bazant, Z. P. (1984). "Mechanics of Fracture and Progressive Cracking in Concrete Structures." *Fracture Mechanics of Concrete*, edited by Sih, G. C. and Tommase, A. D., Martinus Nijhoff, Dordrecht.

Bhatt, P., and Kader, M.A. (1998). "Prediction of Shear Strength of Reinforced Concrete Beams by Nonlinear Finite Element Analysis." *Computers and Struct.*, 68, 139-155.

Booth, E.D. (1994). *Concrete Structures in Earthquake Regions: Design and Analysis.*" Longman Scientific & Technical, Essex, England.

Building Seismic Safety Council. (1997). *NEHRP Recommended Provisions for Seismic Regulations for New Buildings and other Structures.*, Washington D.C.

Chansawat, K., Kachlakev, D.I., Miller, T.H., and Yim, S.C.S. (2001). "FEA of the Horsetail Creek Bridge Strengthened with FRP Laminates." 46th International SAMPE Symposium, 46(2), 1772-1783.

Chansawat, K., Kachlakev, D.I., Miller, T.H., and Yim, S.C.S. (2001). "FE Modeling and Experimental Verification of an FRP Strengthened Bridge." SEM Annual Conference on Experimental and Applied Mechanics, 624-627.

Chansawat, K., Potisuk, T., Miller, T.H., Yim, S.C.S., and Kachlakev, D.I. (2002). "FE Models of GFRP and CFRP Strengthening of Reinforced Concrete Beams." Submitted to *ACI Struct. J.*

Chansawat, K., Yim, S.C.S., and Miller, T.H. (2002). "NLFE Analysis of an FRP-Strengthened Reinforced Concrete Bridge. I: Modeling and Experimental Calibration." Submitted to *J. of Bridge Engrg.*, ASCE.

Chansawat, K., Miller, T.H., and Yim, S.C.S. (2002). "NLFE Analysis of an FRP-Strengthened Reinforced Concrete Bridge. II: Performance Evaluation." Submitted to *J. of Bridge Engrg.*, ASCE.

Chopra, A.K. (2000). *Dynamics of Structures: Theory and Applications to Earthquake Engineering.* 2nd ed., Prentice Hall, Upper Saddle River, NJ.

CH2M Hill Consulting Engineers in conjunction with TAMS Consultants. (1997). "Evaluation and Resolution of Under Capacity State Bridges: Bridge #04543, Horsetail Creek Bridge." CH2M HILL, Inc., Corvallis, OR.

Clough, R.W., and Penzien, J. (1993). *Dynamics of Structures*. 2nd ed., McGraw-Hill, Inc., New York, New York.

Daniel, I.M., and Ishai, O. (1994). *Engineering Mechanics of Composite Materials*. Oxford University Press, NY.

Darby, J.J. (1999). "Role of Bonded Fibre-Reinforced Composites in Strengthening of Structures," *Strengthening of Reinforced Concrete Structures Using Externally-Bonded FRP Composites in Structural and Civil Engineering*, edited by L.L. Hollaway and M.B. Leeming, Woodhead Publishing, Cambridge, England.

Desayi, P. and Krishnan, S. (1964). "Equation for the Stress-Strain Curve of Concrete." *Journal of the American Concrete Inst.*, 61, 345-350.

Groff, R., Shike, C., and Hirota, M. (1999). "Assessing Oregon's Seismic Risk." ODOT paper for US-Japan Bridge Engineering Workshop, Salem, OR.

Hambly, H.C. (1991). *Bridge Deck Behavior*. 2nd ed. Clays Ltd, St Ives plc, England.

Head, P.R. (1992). "Design Methods and Bridge Forms for the Cost Effective Use of Advanced Composites in Bridges." *Advanced Composite Materials in Bridges and Structures*, 15-30.

Hodhod, O.A. (1997). "Seismic Performance of a Fiber-Reinforced Plastic Cable-Stayed Bridge." *Structural Engineering and Mechanics*, 5(4), 399-414.

Isenberg, J. (1993). *Finite Element Analysis of Reinforced Concrete Structures II.* ASCE, New York, NY.

Issa, M.A., Yousif, A.A., and Issa, M.A. (2000). "Effect of Construction Loads and Vibrations on New Concrete Bridge Decks." *J. of Bridge Engineering*, ASCE, 5(3), 249-258.

Jumikis, A.R. (1983). *Rock Mechanics*. Gulf Publishing Co., Houston, TX.

Kachlakev, D.I. (1998). "Strengthening Bridges Using Composite Materials." *SHWA-OR-RD-98-08, United States Department of Transportation Federal Highway Administration and the Oregon Department of Transportation*, Salem, OR.

Kachlakev, D.I., and McCurry, D.Jr. (2000). "Testing of Full-Size Reinforced Concrete Beams Strengthened with FRP Composites: Experimental Results and Design Methods Verification." *SPR387, United States Department of Transportation Federal Highway Administration and the Oregon Department of Transportation*, Salem, OR.

Kachlakev, D.I., Miller, T.H., Yim, S.C.S., Chansawat, K., and Potisuk, T. (2001). "Finite Element Modeling of Concrete Structures Strengthened with FRP Laminate." *SPR316, United States Department of Transportation Federal Highway Administration and the Oregon Department of Transportation*, Salem, OR.

Kemp, A.R. (1998). "The Achievement of Ductility in Reinforced Concrete Beams." *Magazine of Concrete Research*, 50(2), 123-132.

Kent, D.C., and Park, R. (1971). "Flexural Members with Confined Concrete." *Journal Struct. Div.*, ASCE, 97(7), 1969-1990.

Malek, A. M., Saadatmanesh, H., and Ehsani M. R. (1998). "Prediction of Failure Load of R/C Beams Strengthened with FRP Plate Due to Stress Concentration at the Plate End." *ACI Structural Journal*, 95(1), 142-152.

Malhotra, V.M., and Carino, N.J. (1991). *CRC Handbook on Nondestructive Testing of Concrete*. CRC Press Inc., Boca Raton, FL.

Mander, J.B., Priestley, M.J.N., and Park, R. (1988). "Theoretical Stress-Strain Model for Confined Concrete." *J. Struct. Engrg.*, ASCE, 114(8), 1804-1826.

McCurry, D., Jr. (2000). "Strengthening of Reinforced Concrete Beam Using FRP Composite Fabrics: Full-Scale Experimental Studies and Design Concept Verification." *MS Thesis*, Oregon State University, Corvallis, OR.

Nilson, A. H. (1968). "Nonlinear Analysis of Reinforced Concrete by the Finite Element Method." *Journal of the American Concrete Inst.*, 65(9), 757-766.

Oregon Department of Transportation (ODOT) Field Test Data. (1999). Private Correspondence, Salem, Oregon.

Oregon Department of Transportation (ODOT) Field Test Data. (2000). Private Correspondence, Salem, Oregon.

Oregon Department of Transportation (ODOT) Field Test Data. (2001). Private Correspondence, Salem, Oregon.

Park, R., Priestley, M.J.N., and Gill, W.D. (1982). "Ductility of Square-Confined Concrete Columns." *J. Struct. Div.*, ASCE, 108(4), 929-950.

Phillips, W.M. (1987). *Geologic Map of the Vancouver Quadrangle, Washington and Oregon*. Washington State Department of Natural Resources, Olympia, WA.

Popovics, S. (1973). "A Numerical Approach to the Complete Stress-Strain Curve of Concrete." *Cement and Concrete Research*, 3, 583-599.

Potisuk, T., Kachlakev, D.I., Miller, T.H., and Yim, S.C.S. (2001). "Effects of Shear Strengthening with GFRP on Reinforced Concrete Beams." 46th International SAMPE Symposium, 46(2), 1759-1771.

Potisuk, T., Kachlakev, D.I., Miller, T.H., and Yim, S.C.S. (2001). "Experimental Verification of FE Models of FRP Strengthened RC Beams." SEM Annual Conference on Experimental and Applied Mechanics, 620-623.

Poulos, H.G., and Davis, E.H. (1973). *Elastic Solutions for Soil and Rock Mechanics.* John Wiley & Sons, Inc., NY.

Ross, C. A., Jerome D. M., Tedesco J. W., and Hughes M. L. (1999). "Strengthening of Reinforced Concrete Beams with Externally Bonded Composite Laminates." *ACI Structural Journal*, 96(2), 212-220.

Samaan, M., Mirmiran, A., and Shahawy, M. (1998). "Model of Concrete Confined by Fiber Composites." *Journal Struct. Engrg.*, ASCE, 124(9), 1025-1031.

Stevens, N.J., Uzumeri, S.M., Collins, M.P., and Will, T.G. (1991). "Constitutive Model for Reinforced Concrete Finite Element Analysis," *ACI Struct. J.,* 88(1), 49-59.

Suidan, M. and Schnobrich, W. C. (1973). "Finite Element Analysis of Reinforced Concrete." *Journal of the Structural Division*, ASCE, ST10, 2109-2122.

Tedesco, J. W., Stallings J. M., El-Mihilmy, M., and McCauley, M. (1996). "Rehabilitation of Concrete Bridges Using FRP Laminates." 4th Materials Conference, "Materials for the New Millennium," editor K. Chong, American Society of Civil Engineers, Washington, D. C.

Tedesco, J.W., Stallings, J.M., and El-Mihilmy, M. (1999). "Finite Element Method Analysis of a Concrete Bridge Repaired with Fiber Reinforced Laminates." *Computers and Structures*, 72, 379-407.

Teng, J.G., Chen, J.F., Smith, S.T., and Lam, L. (2001). *FRP Strengthened RC Structures.* John Wiley & Sons, Ltd, West Sussex, England.

Thimmhardy, E.G., Marsh, C., Chen, H., and Tessema, M. (1995). "Nonlinear Analysis of Steel and Concrete Bridge Components." *Computers & Structures*, 56(2/3), 439-459.

USGS. (1993). *Multnomah Falls Quadrangle Oregon-Washington 7.5 Minute Series (Topographic) Scale 1:24000.* USGS, Denver, CO.

USGS. (2000). "Glossary of Earthquake Terms." <http://earthquake.usgs.gov>.

Wahab, M.M.A., and Roeck, G.D. (1999). "Effect of Excitation Type on Dynamic System Parameters of a Reinforced Concrete Bridge." *Structural Engineering and Mechanics*, 7(4), 387-400.

Wakefield, R.R., Nazmy, A.S., and Billington, D.P. (1991). "Analysis of Seismic Failure of Skew RC Bridge." *J. of Structural Engineering*, ASCE, 117(3), 972-986.

Wang, P.T., Shah, S.P., and Naaman, A.E. (1978). "Stress-Strain Curves of Normal and Lightweight Concrete in Compression." *J. of ACI*, 75(11), 603-611.

Walker, G.W., and MacLeod, N.S. (1991). *Geologic Map of Oregon: Scale 1:500000.* U.S. Geological Survey, Denver, CO.

Whiteman, R.V., and Richart, F.E. (1967). "Design Procedures for Dynamically Loaded Foundations." *J. of the Soil Mech. and Foundations Div.*, ASCE, 93(6), 169-193.

William, K. J. and Warnke, E. P. (1975). "Constitutive Model for the Triaxial Behavior of Concrete." *Proceedings, International Association for Bridge and Structural Engineering*, Vol. 19, ISMES, Bergamo, Italy, 174-190.

Woodward-Clyde Federal Services. (1997) "Develop Suites of Time Histories." *Draft report for SAC Project Task: 5.4.1.*, Pasadena, CA.

Vidosa, F.G., Kotsovos, M.D., and Pavlović, M.N. (1991). "Nonlinear Finite-Element Analysis of Concrete Structures: Performance of a Fully Three-Dimensional Brittle Model." *Computers & Structures*, 40(5), 1287-1306.

APPENDICES

APPENDIX A: MATERIALS ASSOCIATED WITH CHAPTER 1

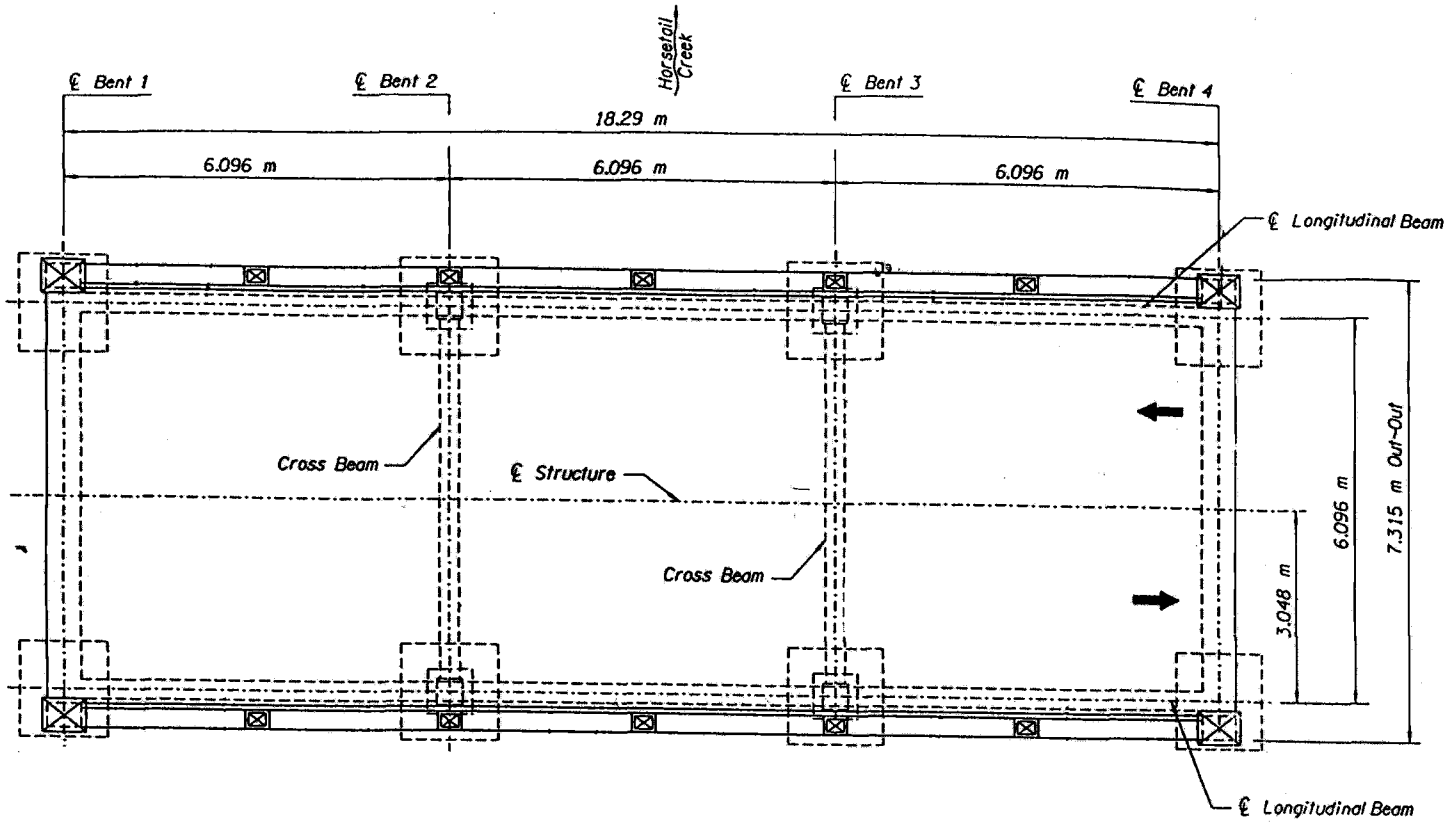

Figure A.1. Horsetail Creek Bridge Plan (Not to scale)

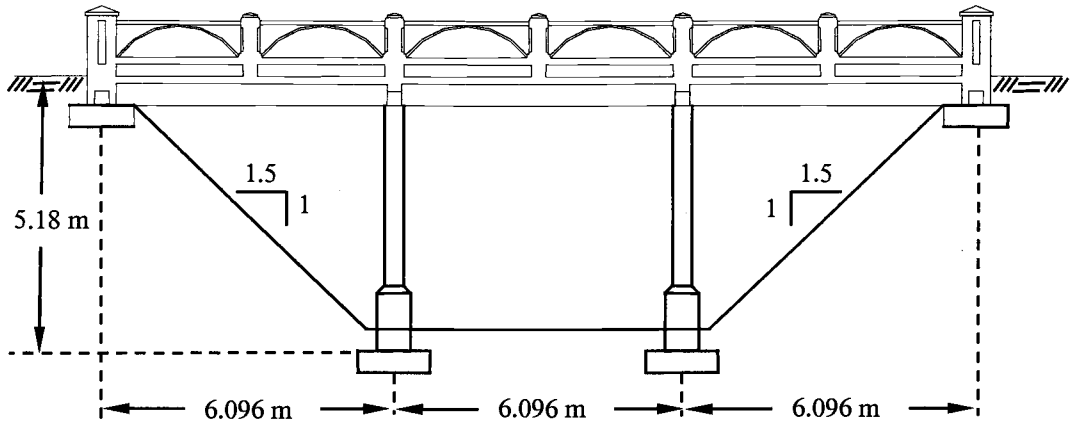

Figure A.2. Horsetail Creek Bridge Elevation (Not to scale)

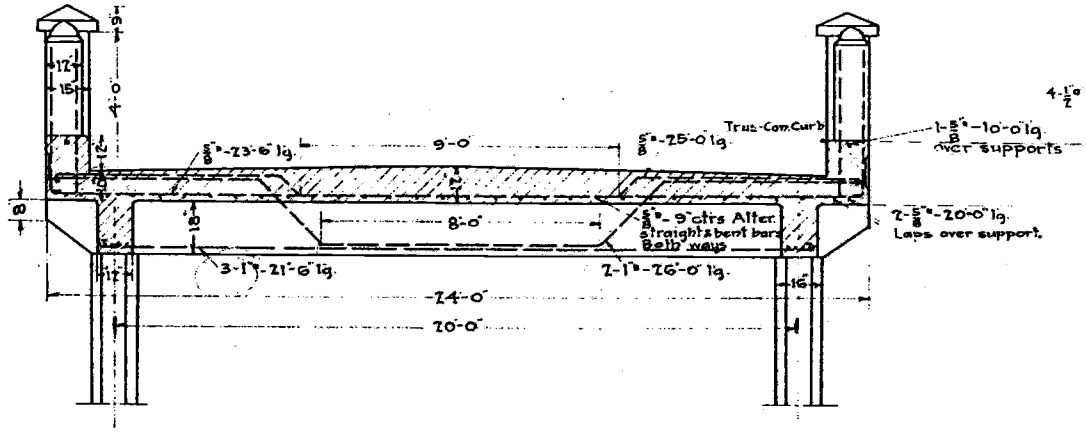

Figure A.3. Typical Steel Reinforcement Details in Transverse Beams

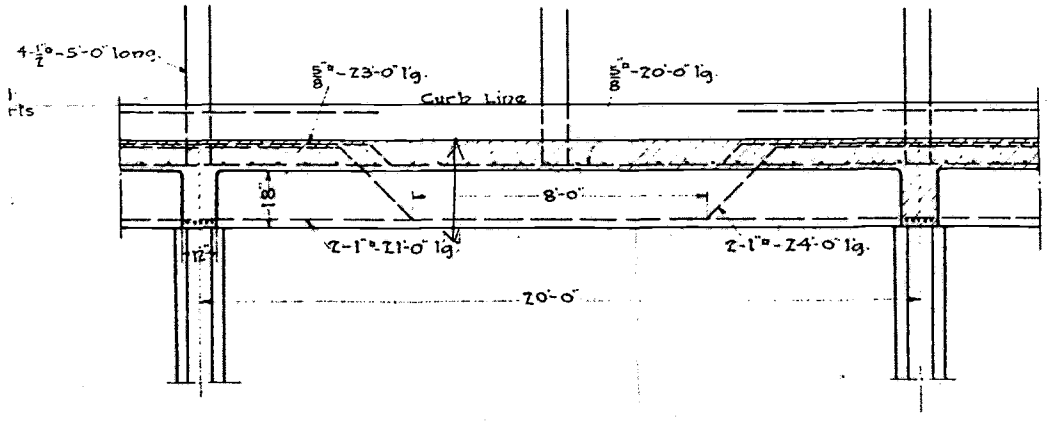

Figure A.4. Typical Steel Reinforcement Details in Longitudinal Beams

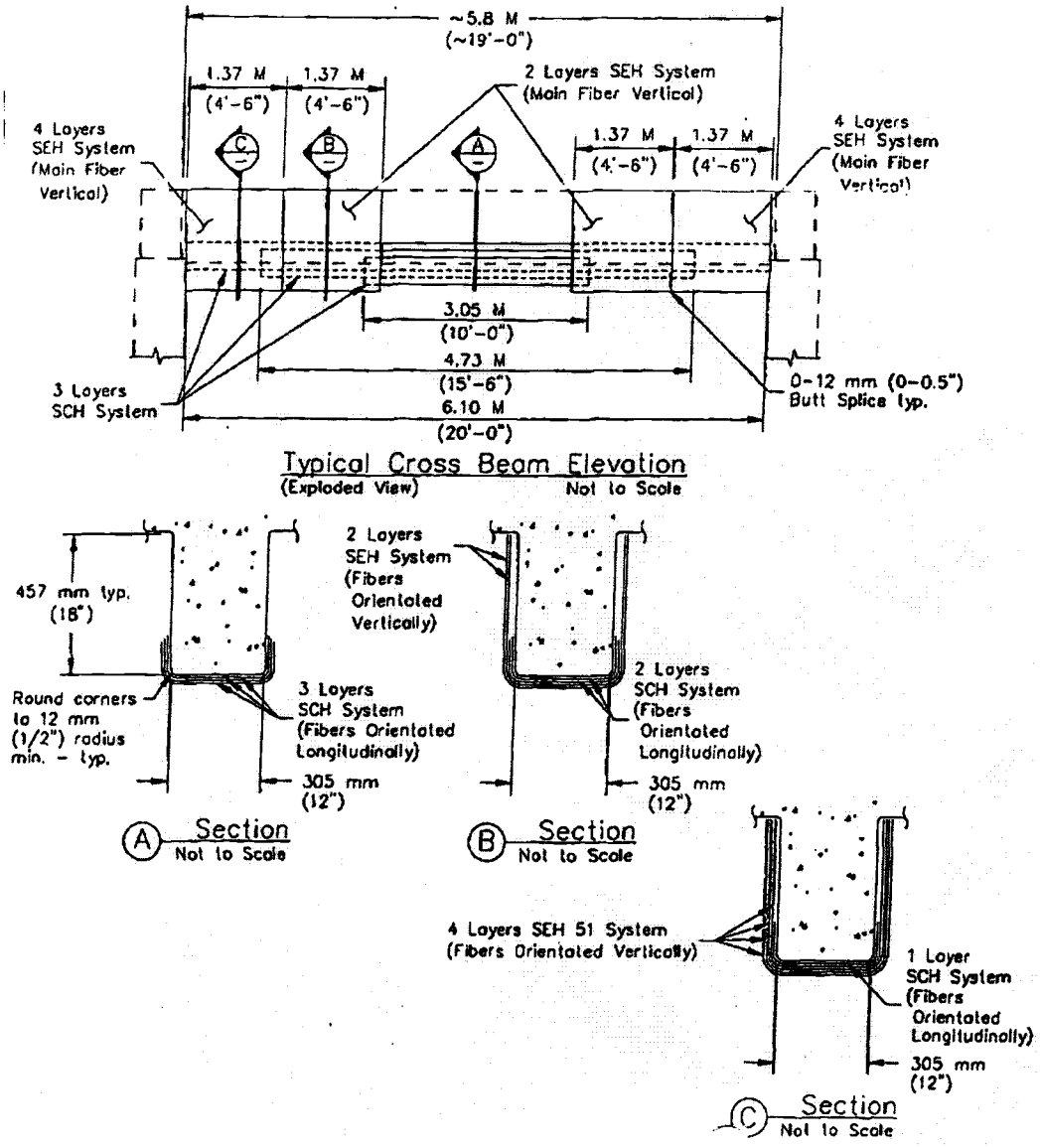

Figure A.5. Typical FRP Reinforcement Details in Transverse Beams

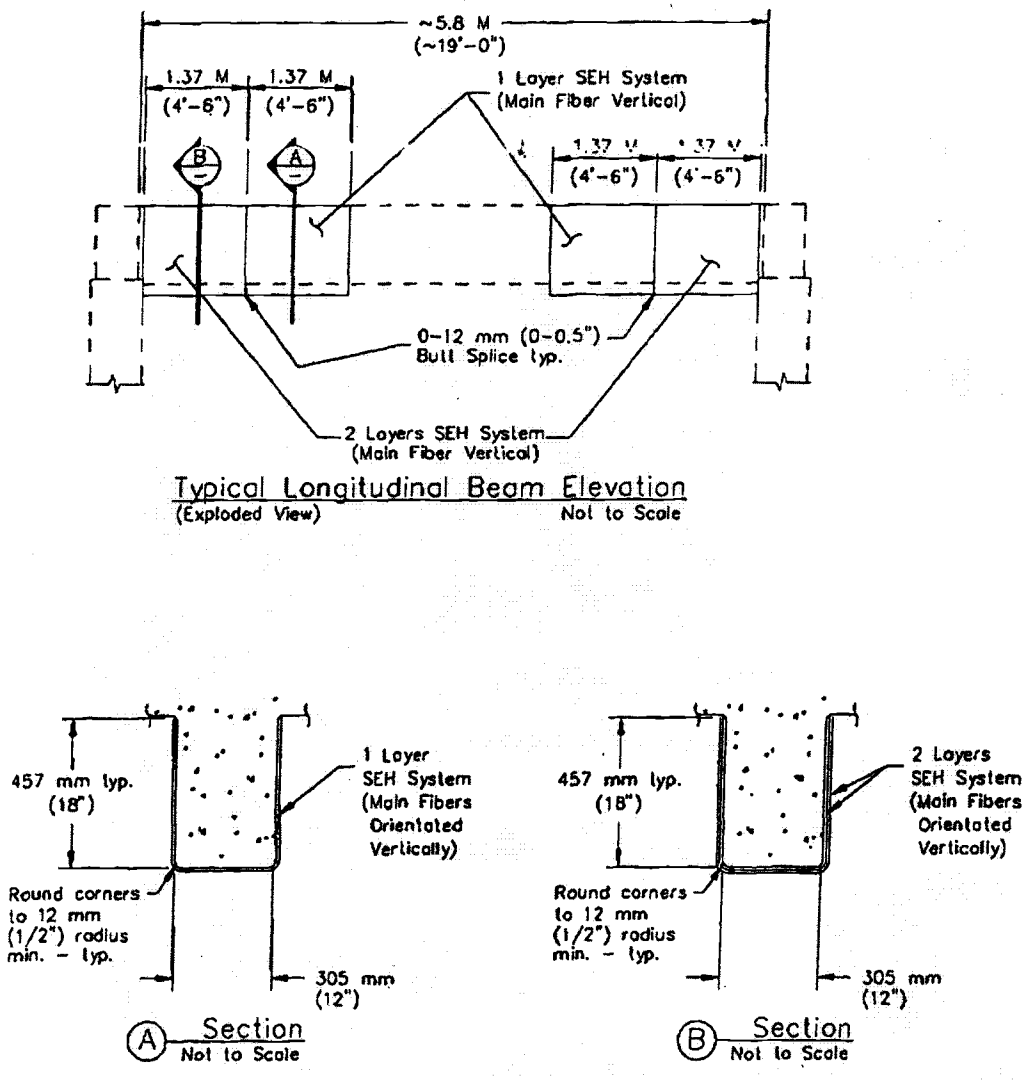

Figure A.6. Typical FRP Reinforcement Details in Longitudinal Beams

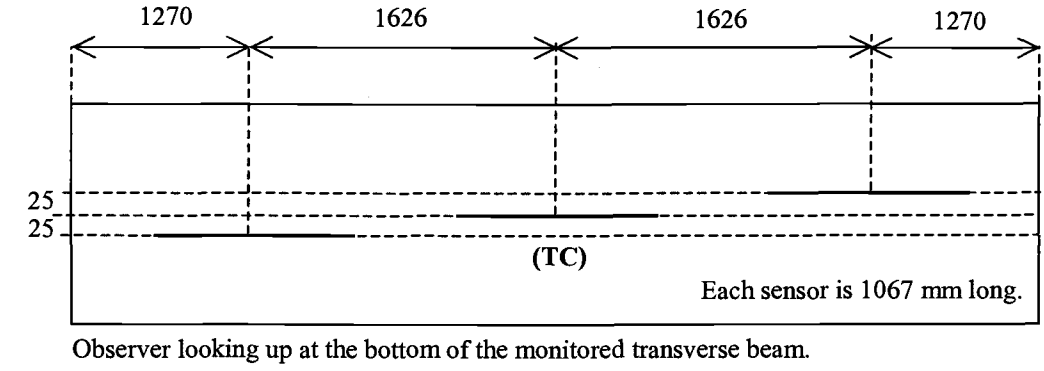

(a)

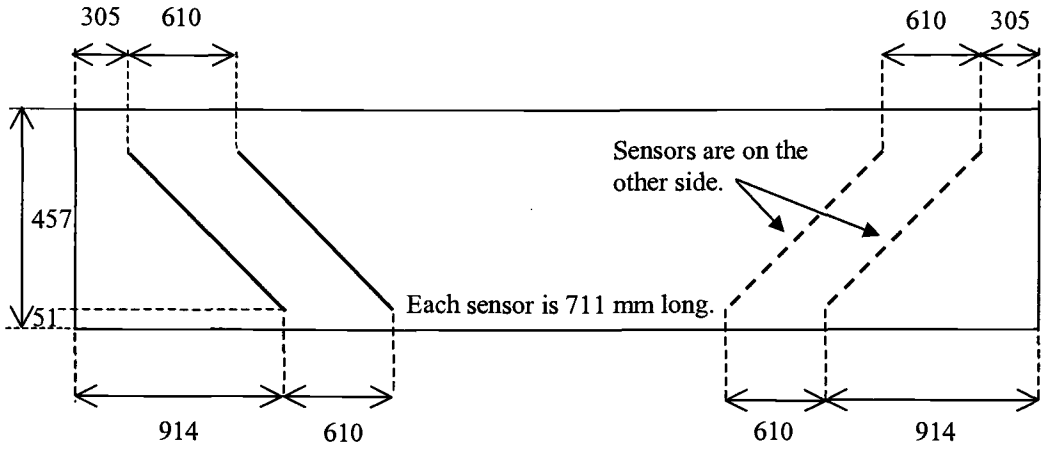

(b)

Figure A.7. Locations of Fiber Optic Sensors on Transverse Beam (Dimensions shown in mm): (a) Bottom; (b) Sides

Note: The monitored transverse beam is on the east side of the bridge (refer to Fig. 3.3).

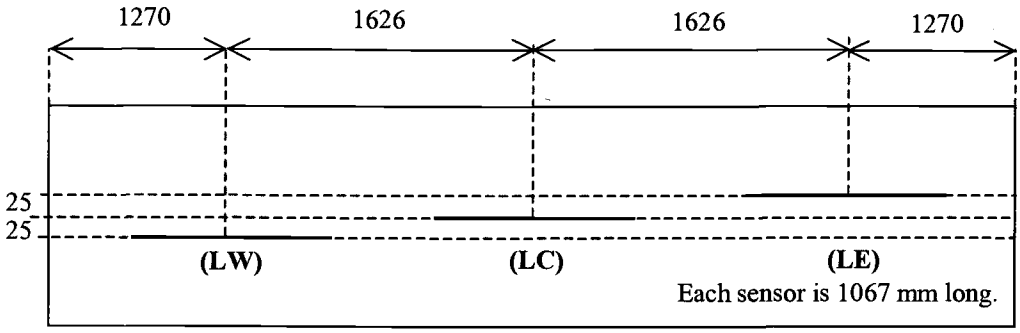

Observer looking up at the bottom of the monitored longitudinal beam.

(a)

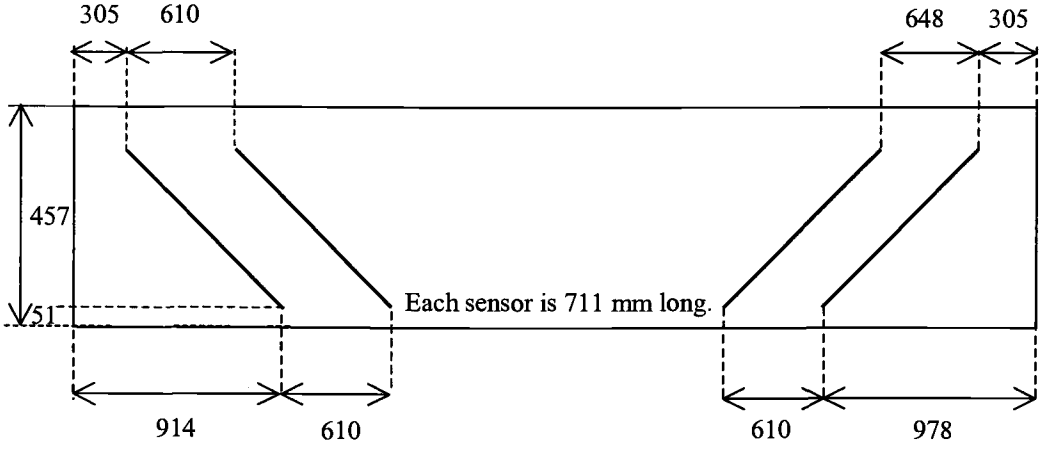

(b)

Figure A.8. Locations of Fiber Optic Sensors on Longitudinal Beam (Dimensions shown in mm): (a) Bottom; (b) Sides

Note: The monitored longitudinal beam is on the south side of the bridge (refer to Fig. 3.3).

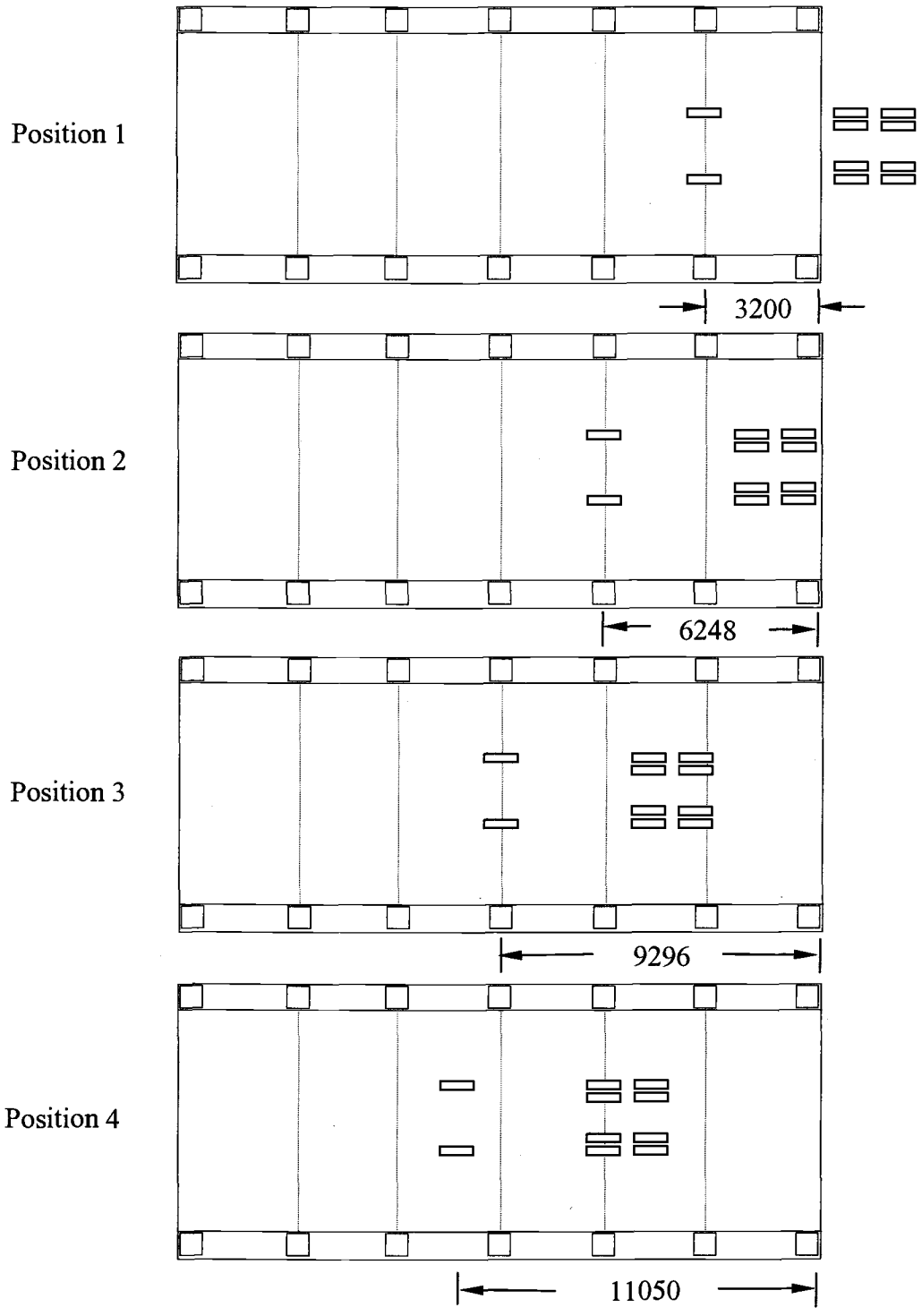

Figure A.9. Locations of Truck

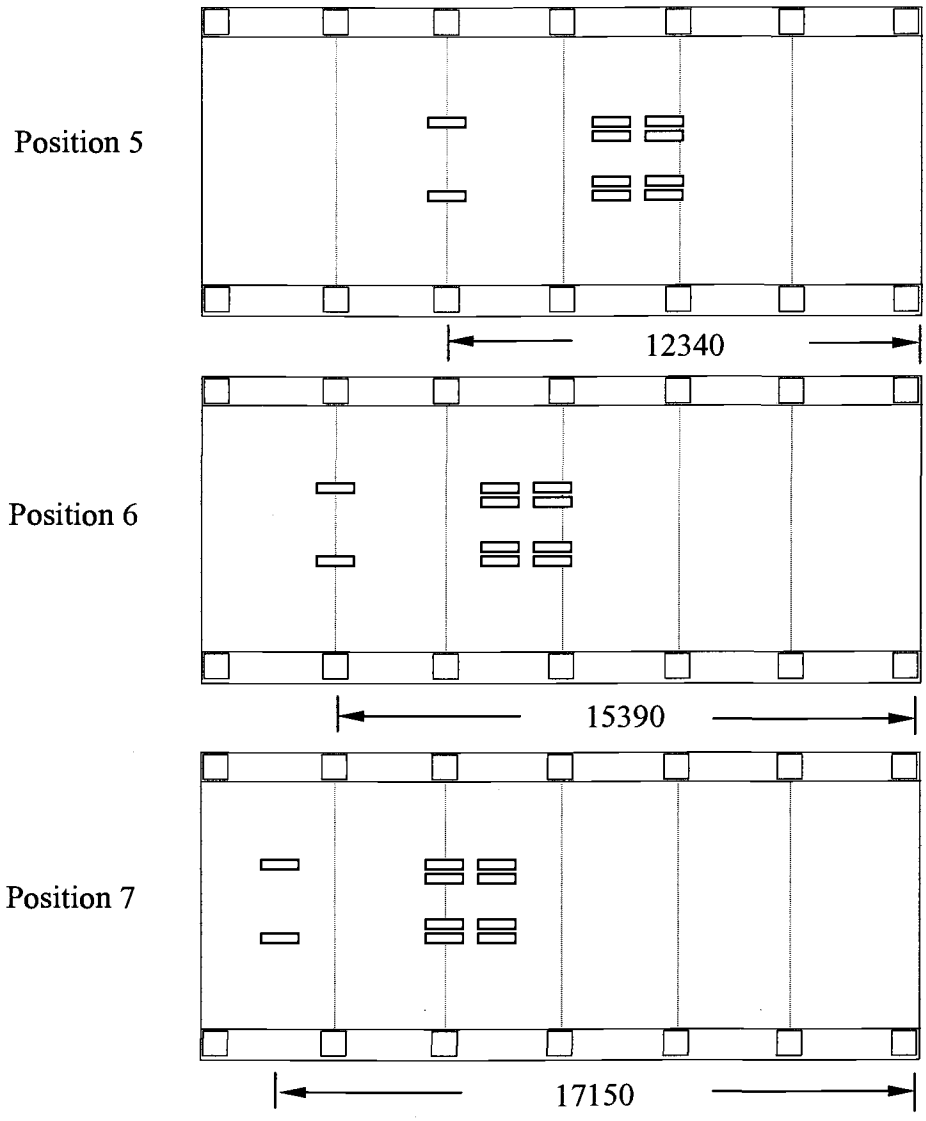

Figure A.9 (Cont'd). Locations of Truck

Note: The distance of the front axle of the truck from the end of the bridge is shown for each position (in mm).

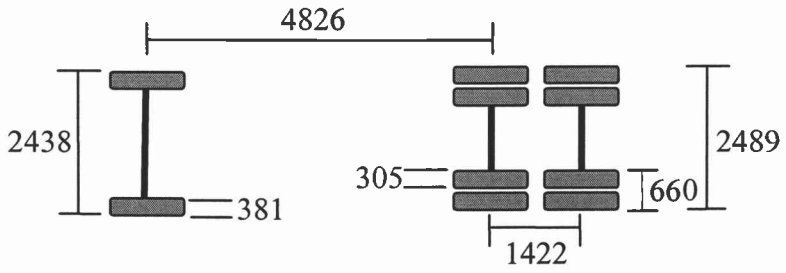

Figure A.10. Truck Configuration (Dimensions shown in mm)

Table A. Axle Weights

Position	Truckload (kN)	
	Empty	Full
Front	56.94	69.40
Center	33.36	75.17
Back	31.14	73.84

APPENDIX B: MATERIALS ASSOCIATED WITH CHAPTER 3

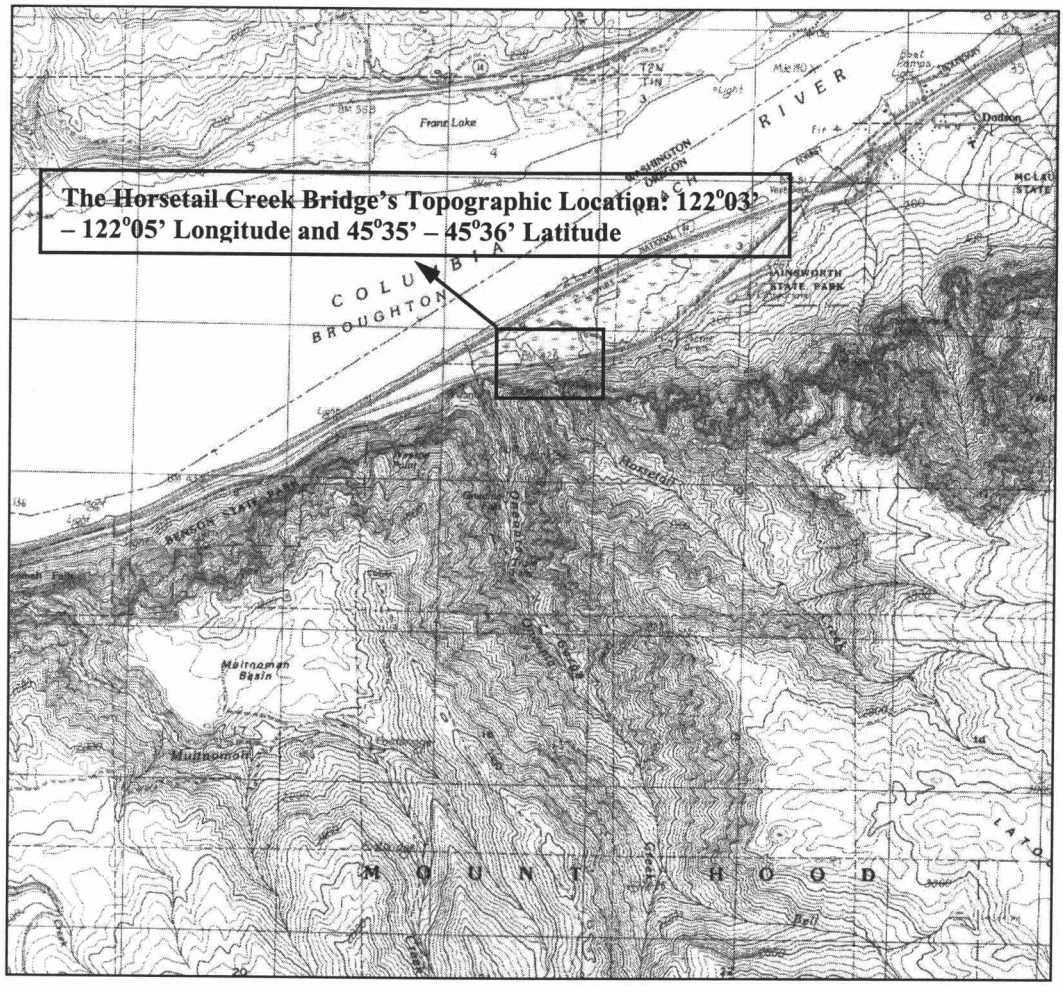

Figure B.1. Topographic Location of the Horsetail Creek Bridge (USGS 1993)

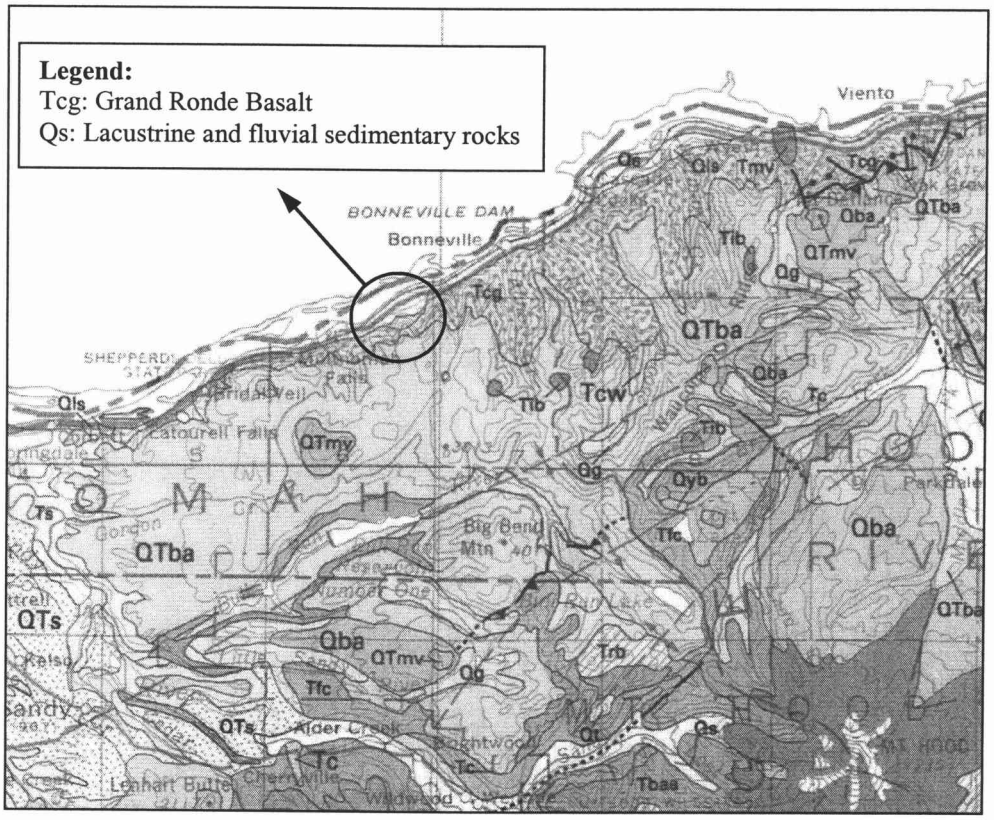

Figure B.2. Geological Properties of Soil Foundation at the Bridge Site (Walker and MacLeod 1991)

FE Strain Calculation

The relatively long gauge length of the sensor (1067 mm (42 in.)) on the monitored beams of the HC bridge made comparisons challenging where the strains varied considerably over those lengths. Due to the length of the fiber optic sensors, it would not be appropriate to use the result from only one node from the FE model

to represent the strain value. The strains from several nodes need to be examined to obtain a strain comparable to the field data. The strain calculation is based on a weighted average that depends on the "tributary" length for each node. For instance, consider a fiber optic sensor attached on a part of an FE model with length L, as follows:

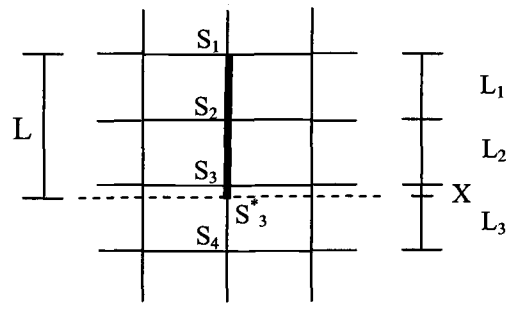

Figure B.3. Fiber Optic Sensor (Plan view)

$$S_{avg} = \frac{\frac{S_1 L_1}{2} + \frac{S_2}{2}(L_1 + L_2) + \frac{S_3}{2}(L_2 + X) + \frac{S_3^* X}{2}}{L} \qquad (B.1)$$

where

S_{avg} = Average strain used to compare with the field strain data

S_1, S_2, S_3, and S_4 = ANSYS nodal strains

L_1, L_2, and L_3 = Length of each element

L = Length of the fiber optic sensor

S^*_3 = Interpolated strain between S_3 and S_4 which is

$$S_4 = S_3 + X\left(\frac{S_4 - S_3}{L_3}\right) \tag{B.2}$$

Truck Load Simplification

To be able to analyze a variety of truck locations on the bridge deck, on which the FE mesh is fixed, the load from each set of dual tires for the tandem axles is lumped and assumed to occur at the center of each set of the dual tires, as shown in Figure B.4.

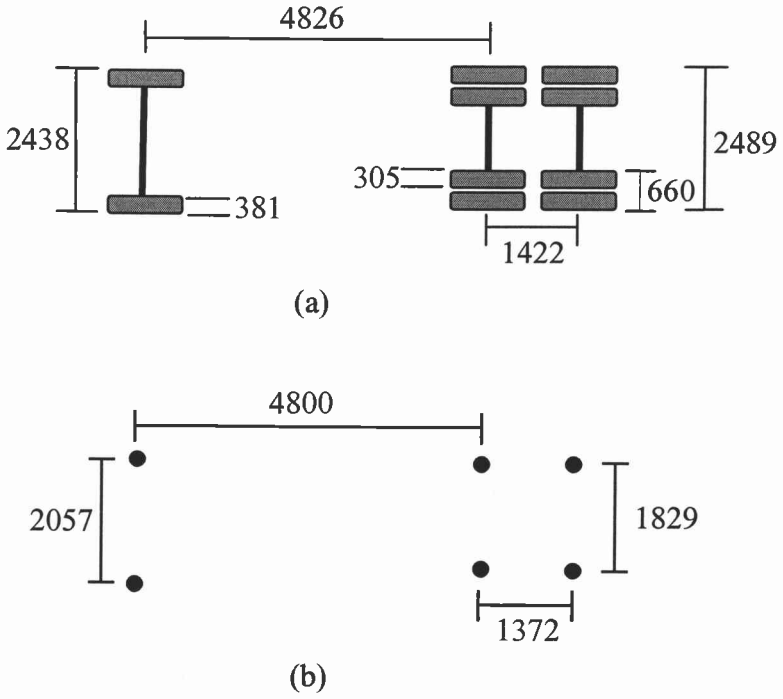

Figure B.4. Truck Load Simplification: (a) Truck Configuration; (b) Simplified Truck Configuration

Moreover, the lumped load at locations where it does not coincide with a node in the FE mesh needs to be linearly distributed to the nearest nodes. An example of this distribution is shown in Figure B.5. With this approach, truck loads can then be applied on the bridge deck, regardless of the locations of the FE mesh/nodes.

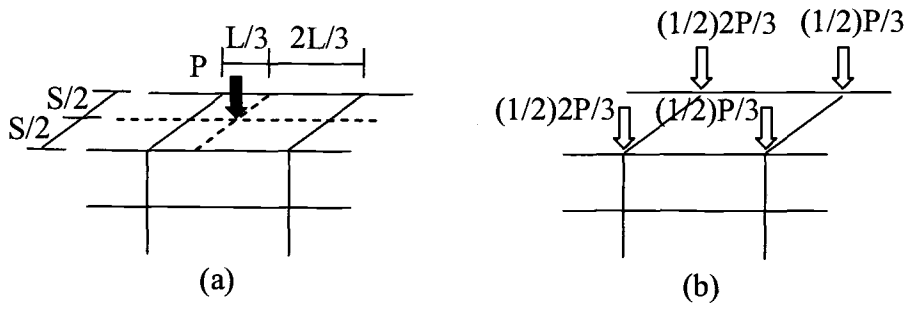

Figure B.5. Linear Truck Load Distribution: (a) Lumped Load; (b) Distributed Lumped Load

APPENDIX C: MATERIALS ASSOCIATED WITH CHAPTER 5

Four earthquake time histories from Table 5.5 are selected (based on the criteria discussed in Chapter 5). For reference, several other earthquakes are shown here in terms of the response spectra at 5% damping, modified EQ time histories, and Fourier spectrum as follows:

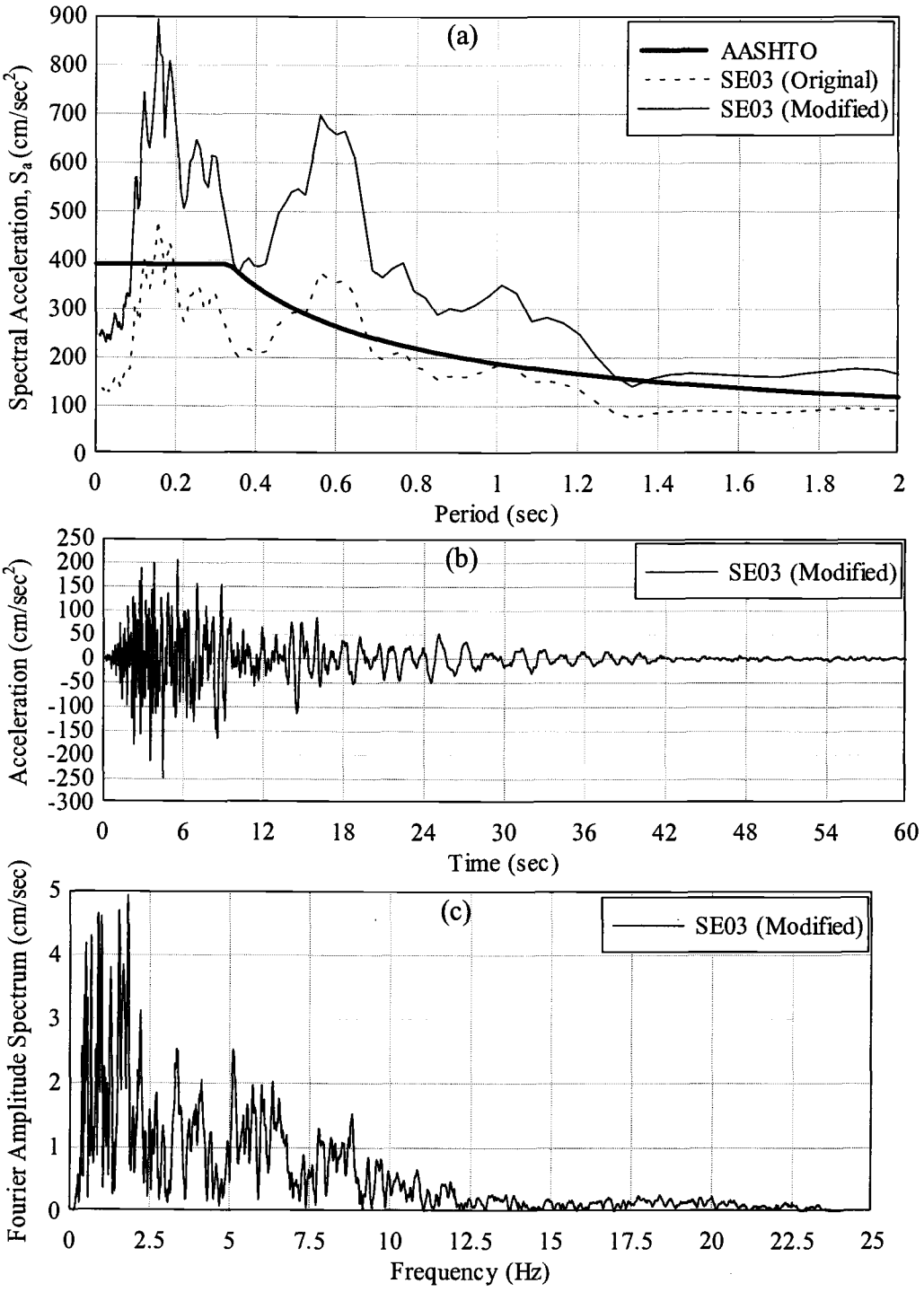

Figure C.1. 1984 Morgan Hill EQ (Strike-Normal): (a) Response Spectra; (b) Modified Time History; (c) Fourier Spectrum

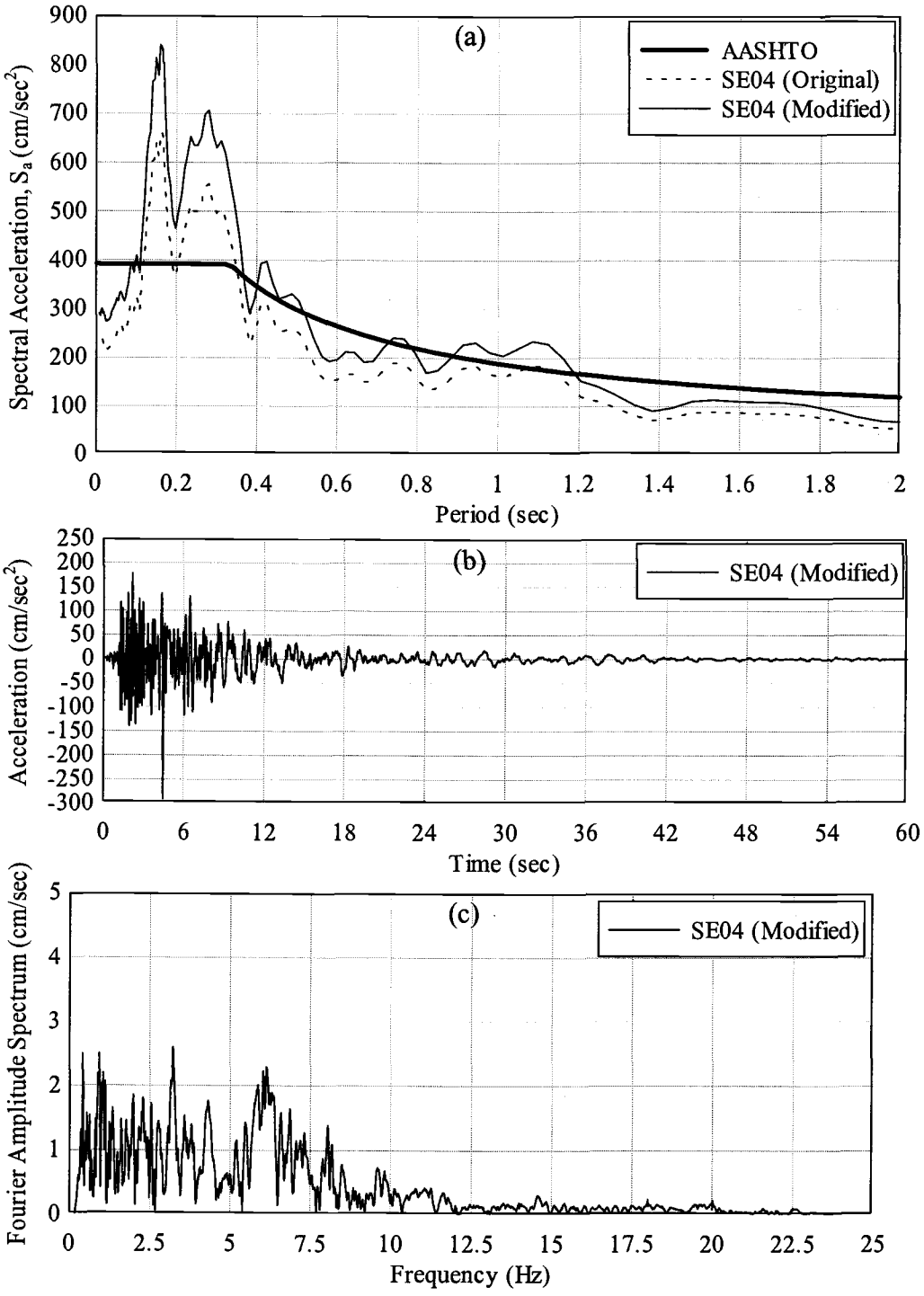

Figure C.2. 1984 Morgan Hill EQ (Strike-Parallel): (a) Response Spectra; (b) Modified Time History; (c) Fourier Spectrum

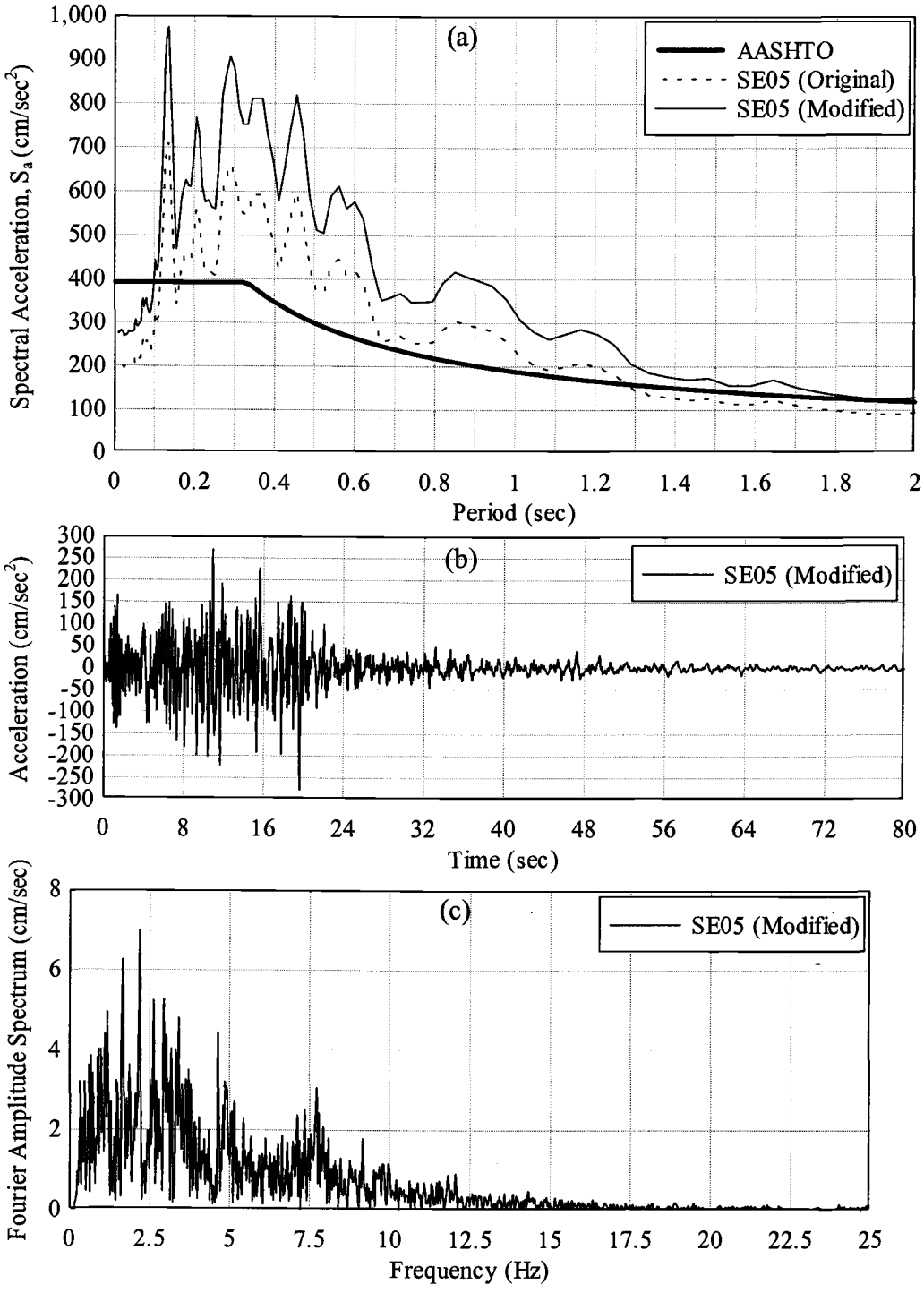

Figure C.3. 1949 Western WA (Olympia Hwy. Test Lab) EQ (Strike-Normal): (a) Response Spectra; (b) Modified Time History; (c) Fourier Spectrum

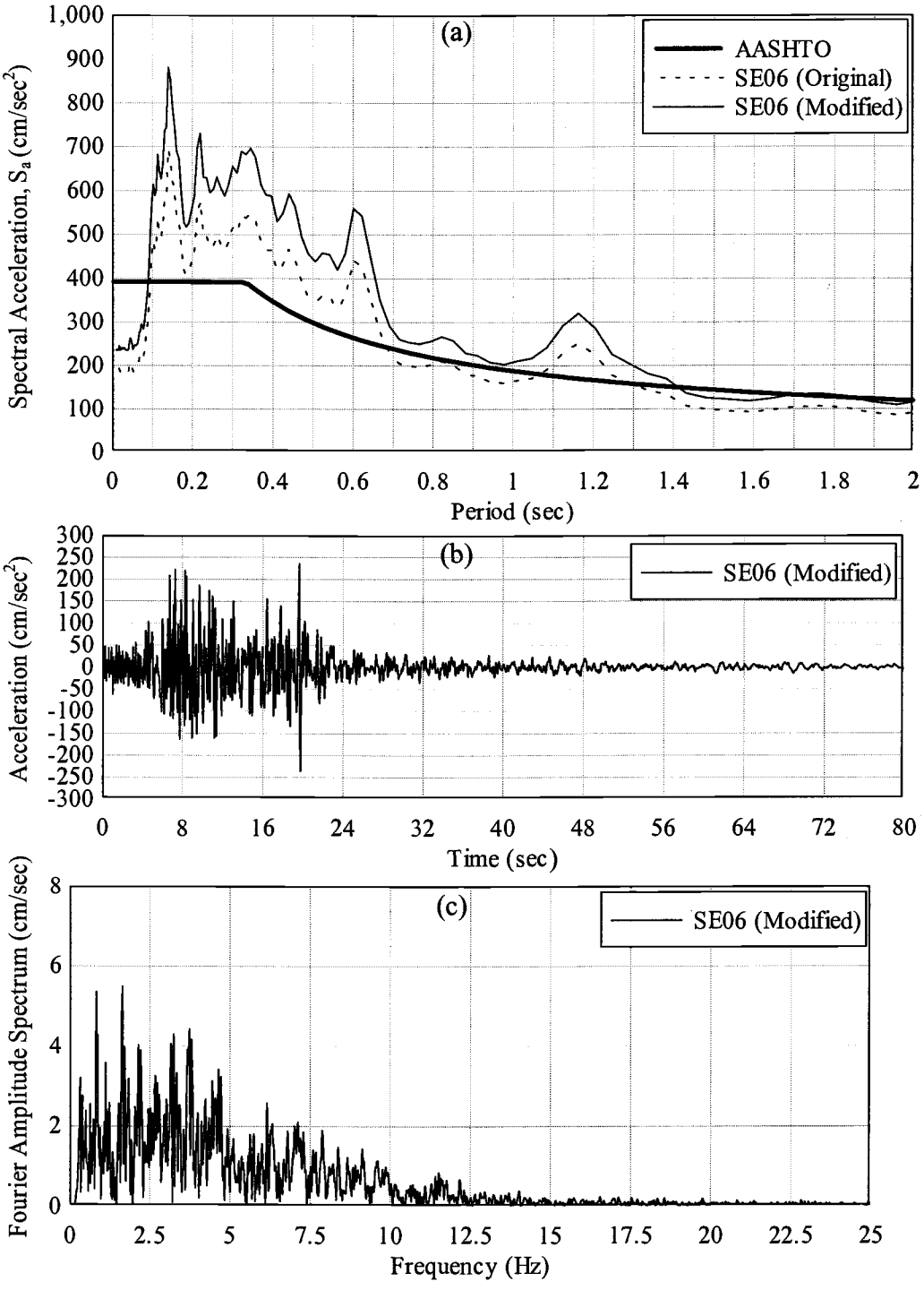

Figure C.4. 1949 Western WA (Olympia Hwy. Test Lab) EQ (Strike-Parallel): (a) Response Spectra; (b) Modified Time History; (c) Fourier Spectrum

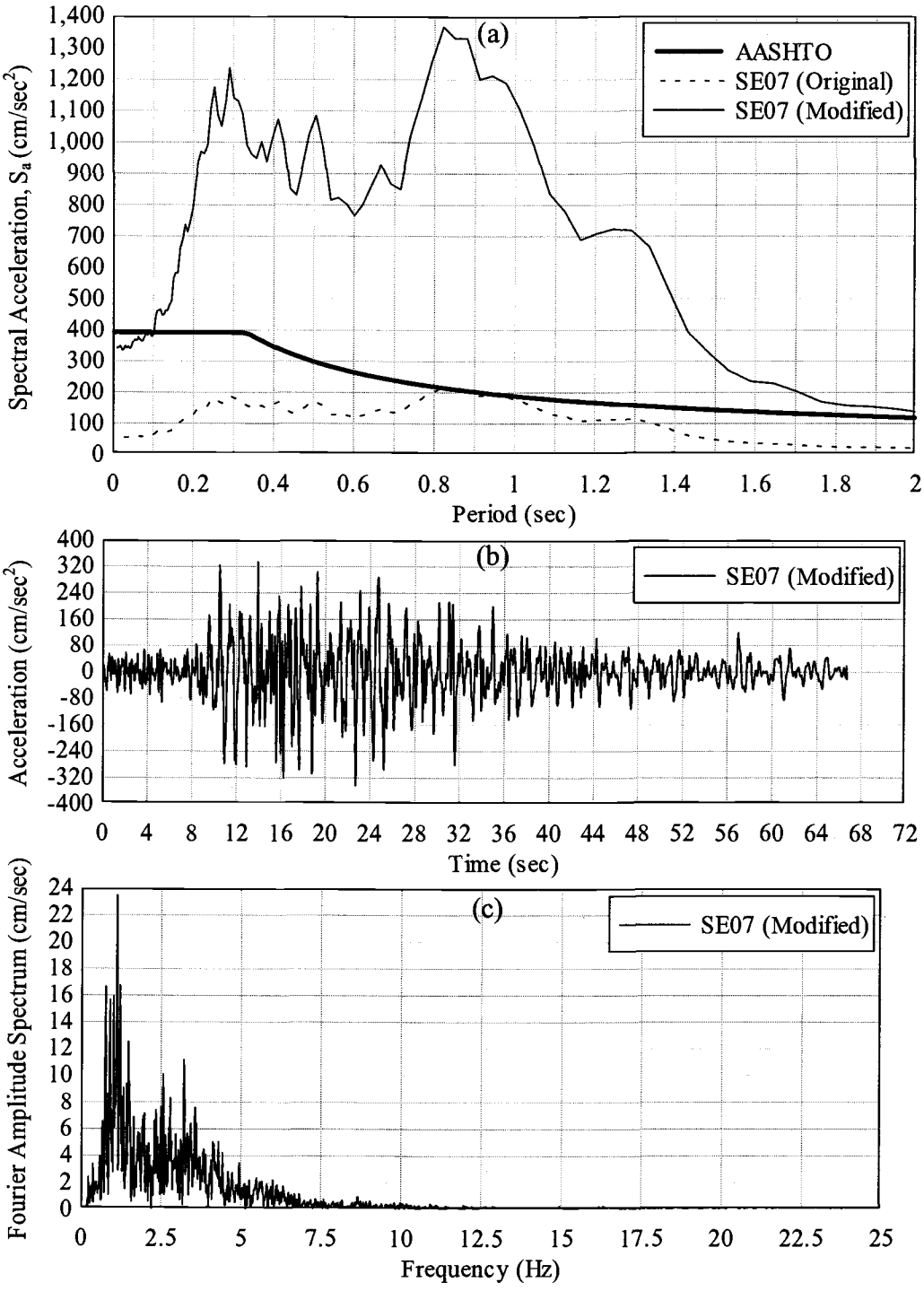

Figure C.5. 1949 Western WA (Seattle Army Base) EQ (Strike-Normal): (a) Response Spectra; (b) Modified Time History; (c) Fourier Spectrum

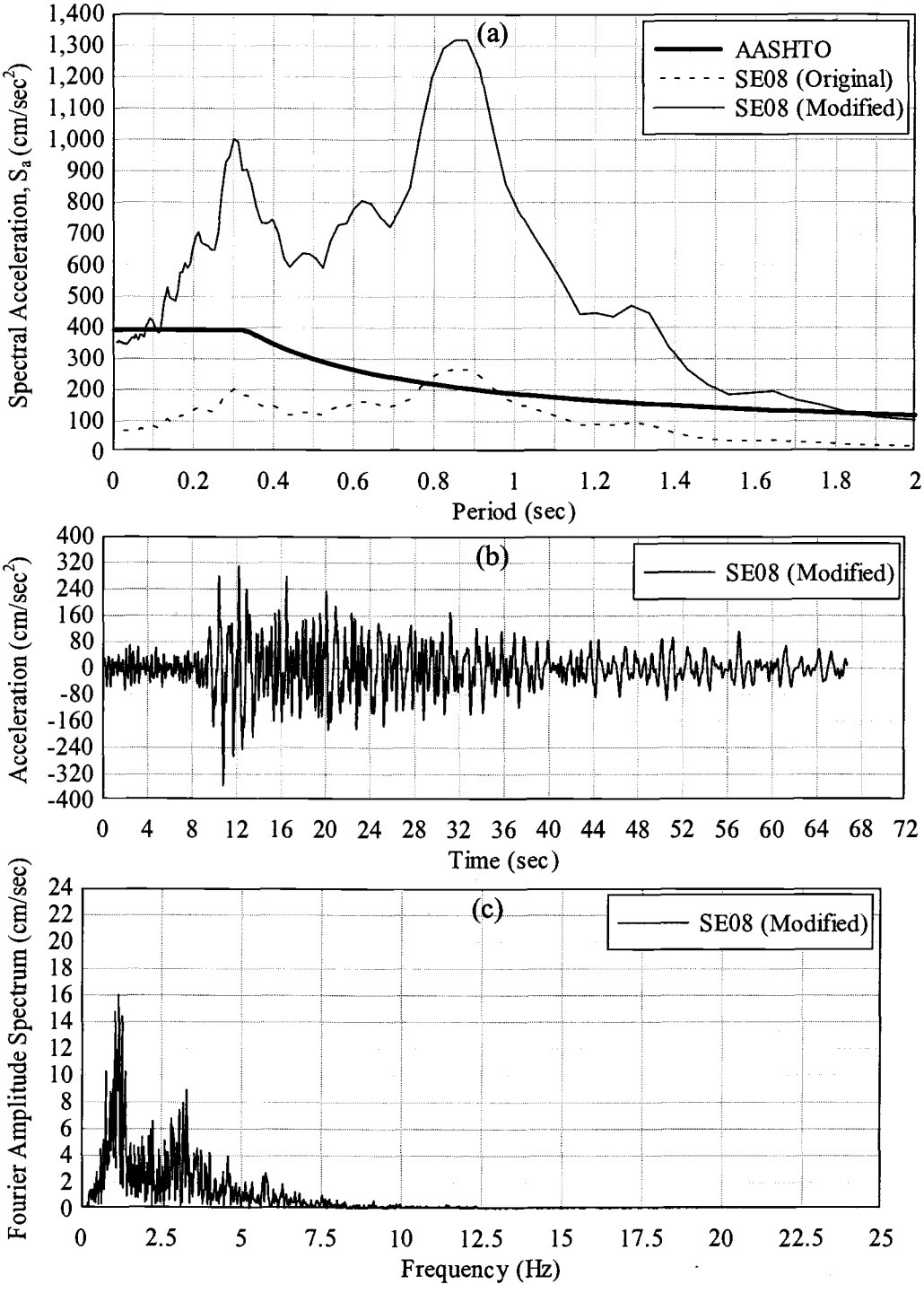

Figure C.6. 1949 Western WA (Seattle Army Base) EQ (Strike-Parallel): (a) Response Spectra; (b) Modified Time History; (c) Fourier Spectrum

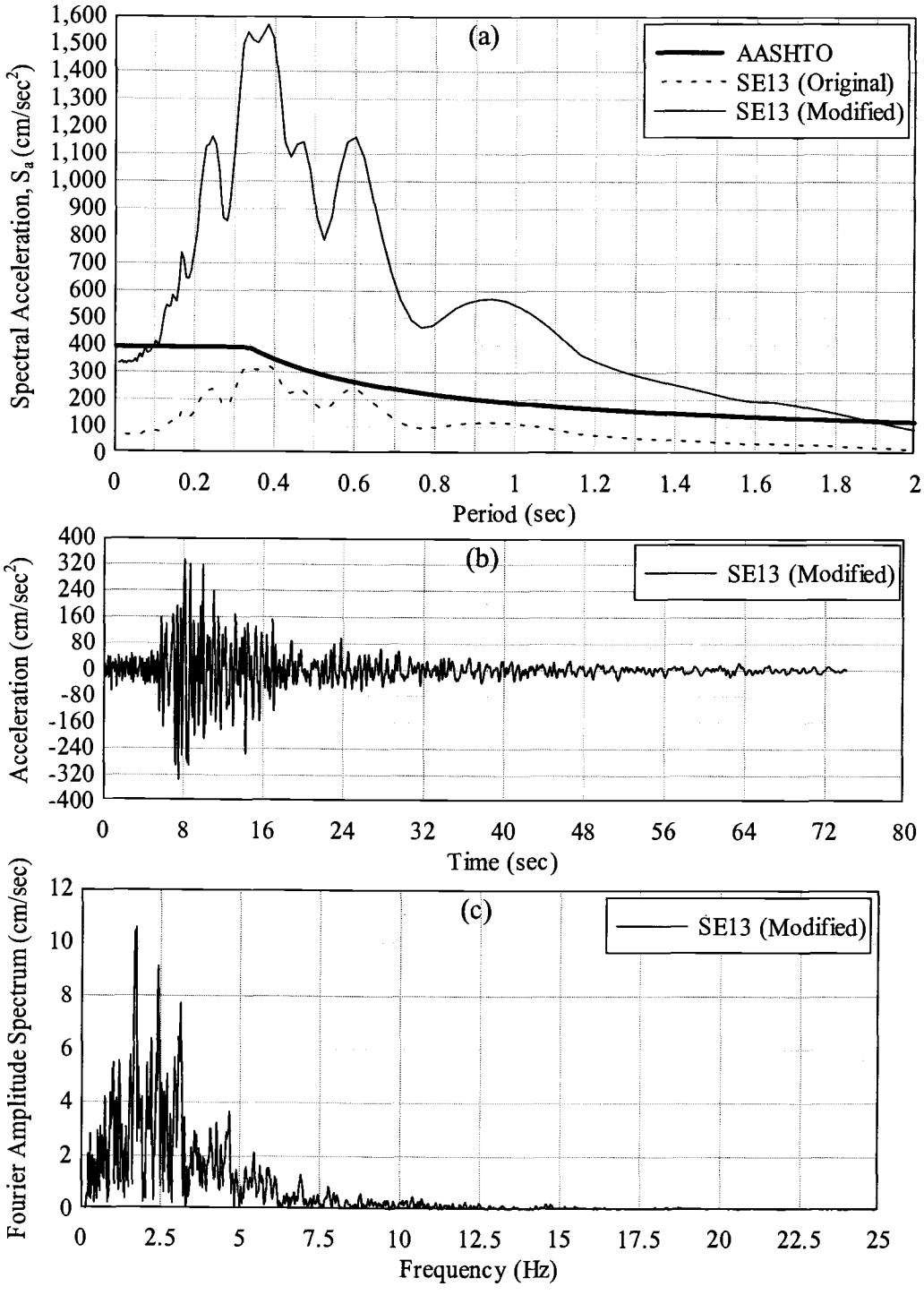

Figure C.7. 1965 Puget Sound EQ (Strike-Normal): (a) Response Spectra; (b) Modified Time History; (c) Fourier Spectrum

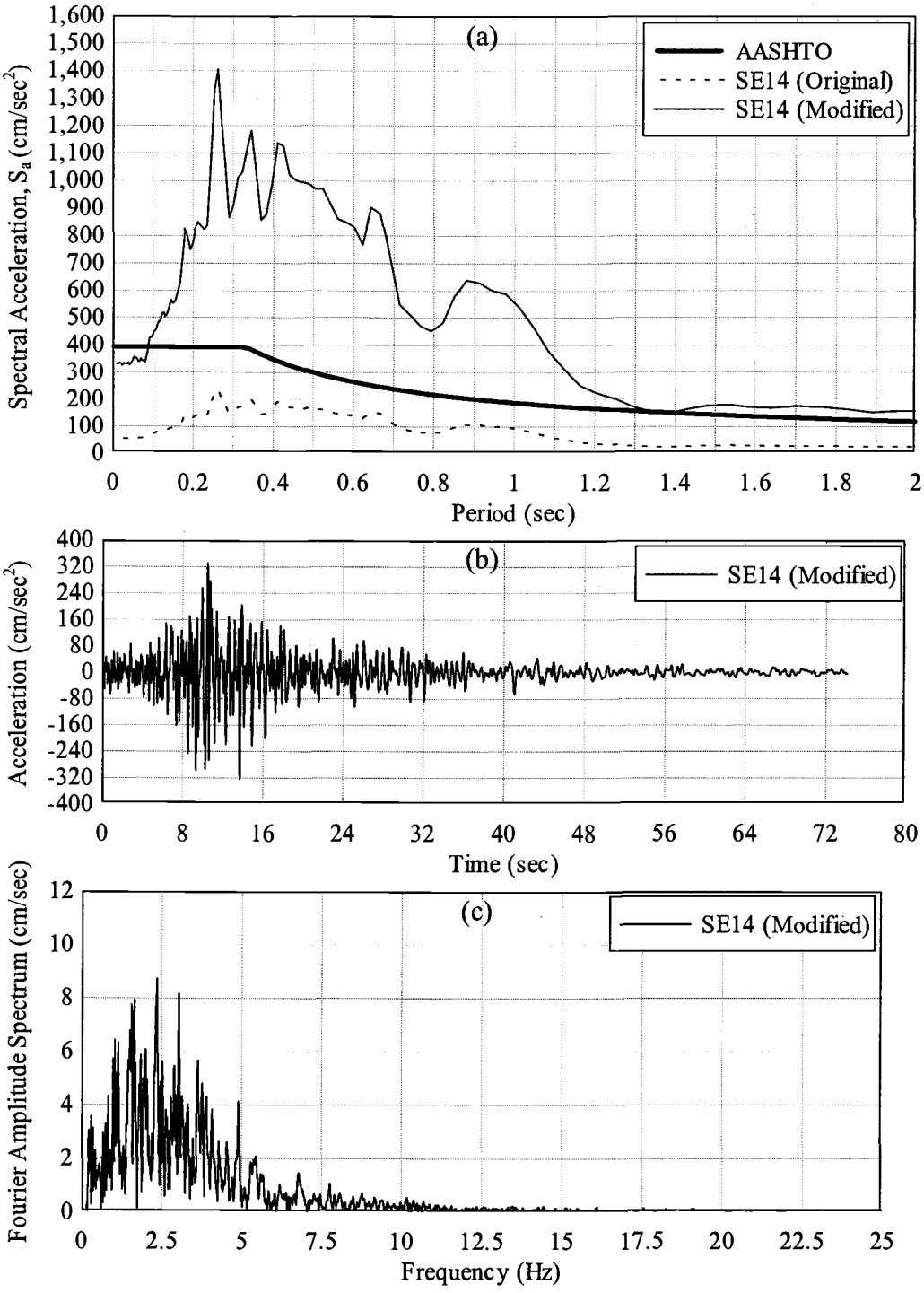

Figure C.8. 1965 Puget Sound EQ (Strike-Parallel): (a) Response Spectra; (b) Modified Time History; (c) Fourier Spectrum

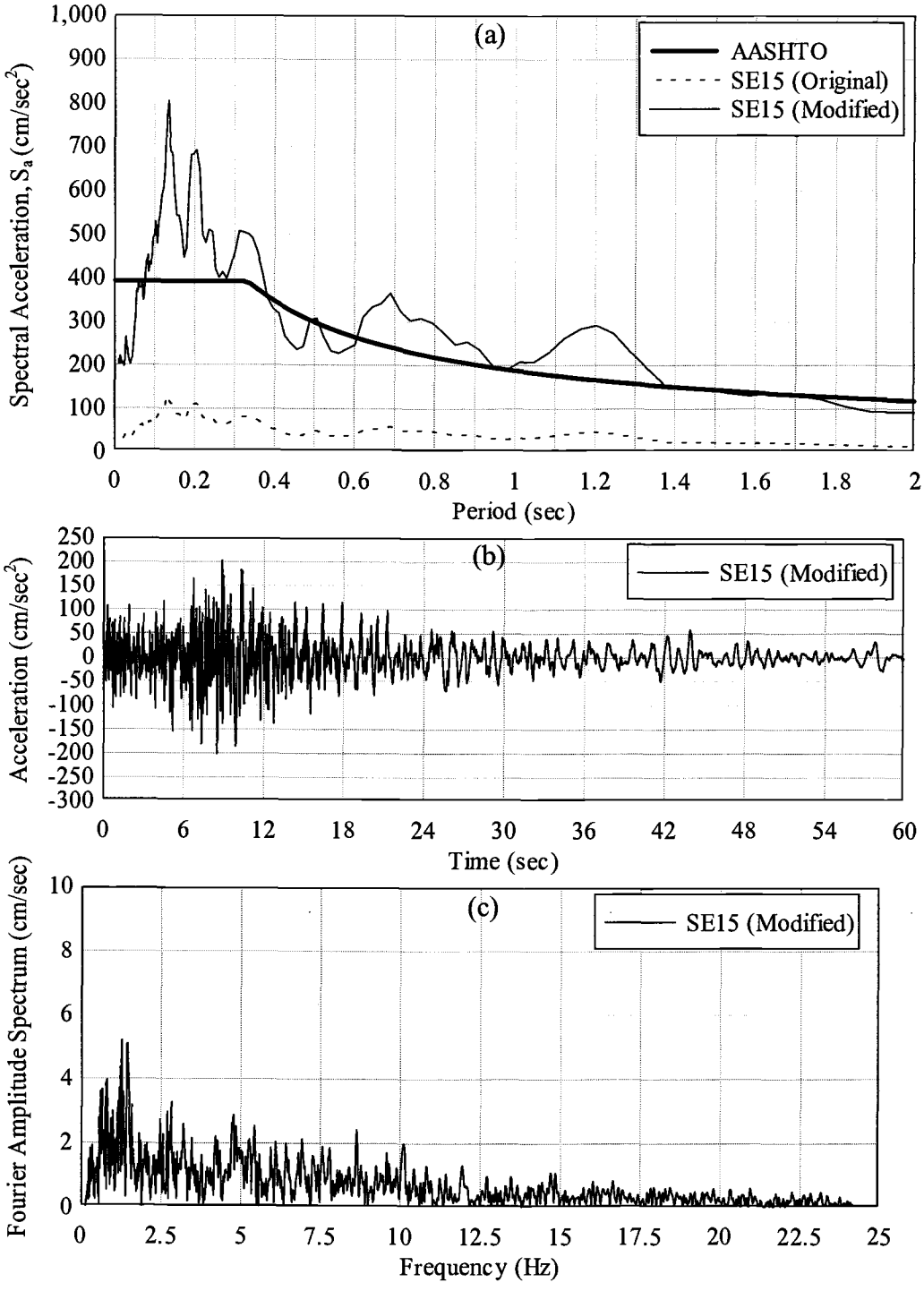

Figure C.9. 1965 Western WA EQ (Strike-Normal): (a) Response Spectra; (b) Modified Time History; (c) Fourier Spectrum

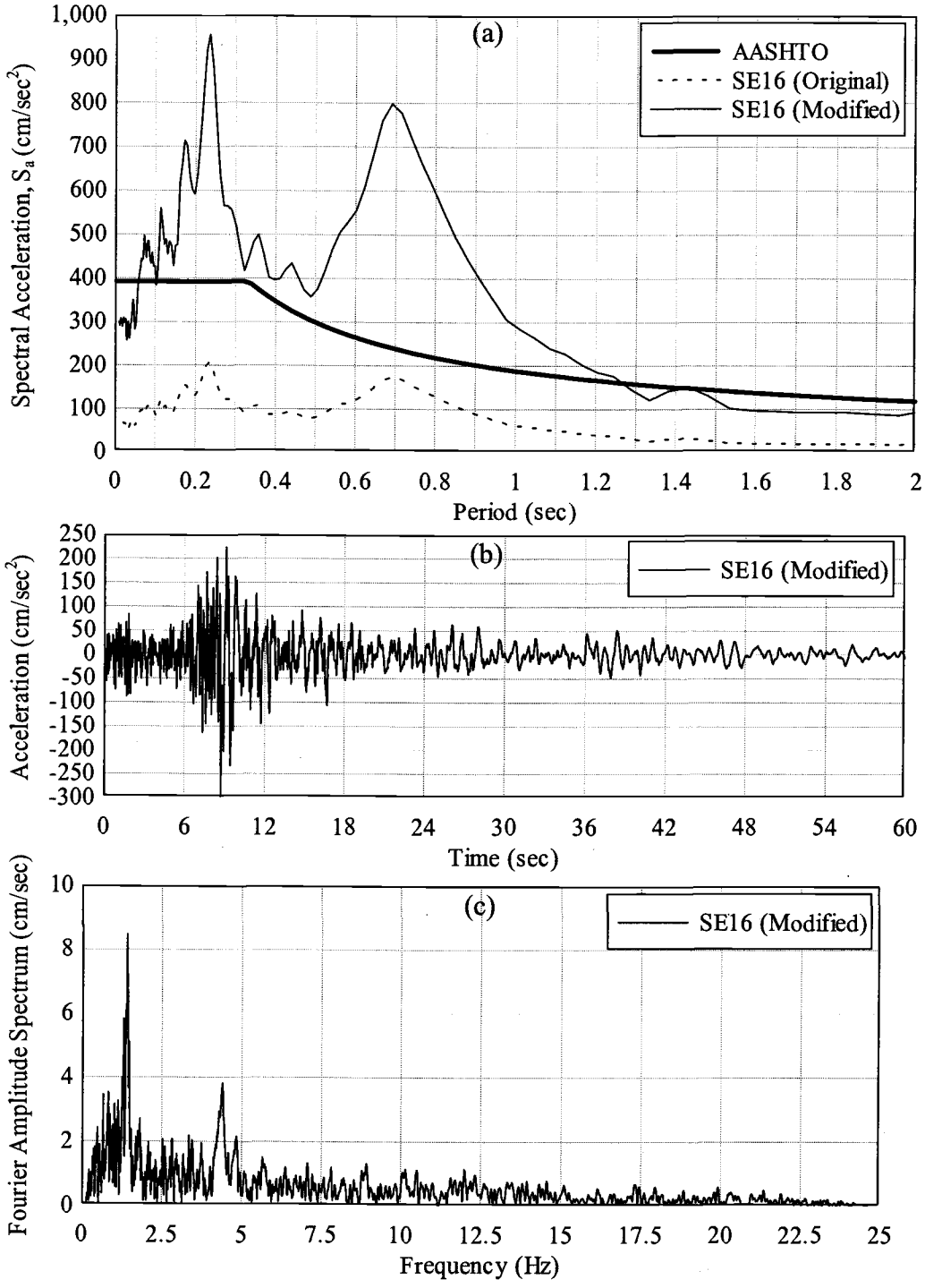

Figure C.10. 1965 Western WA EQ (Strike-Parallel): (a) Response Spectra; (b) Modified Time History; (c) Fourier Spectrum

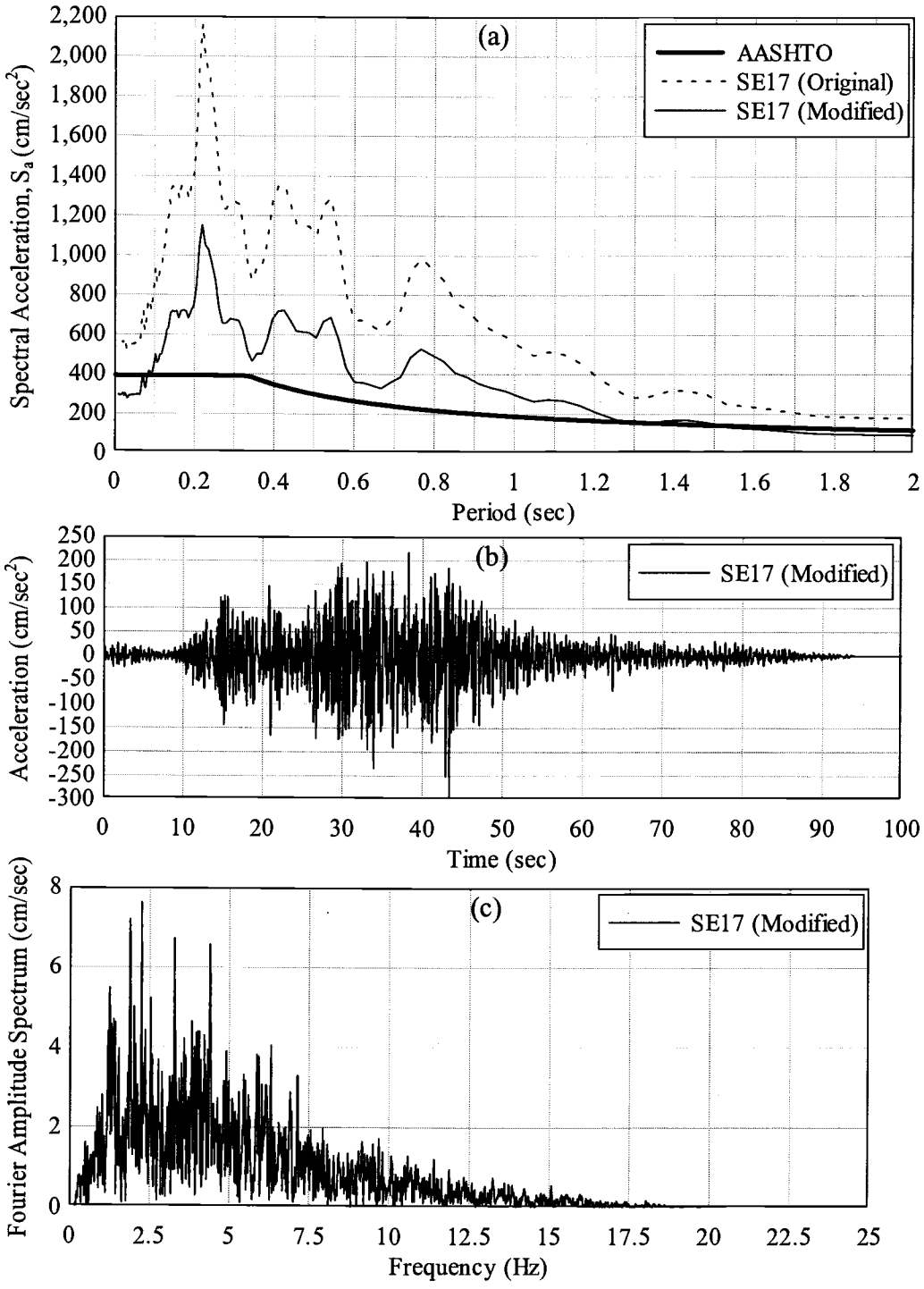

Figure C.11. 1985 Valparaiso EQ (Strike-Normal): (a) Response Spectra; (b) Modified Time History; (c) Fourier Spectrum

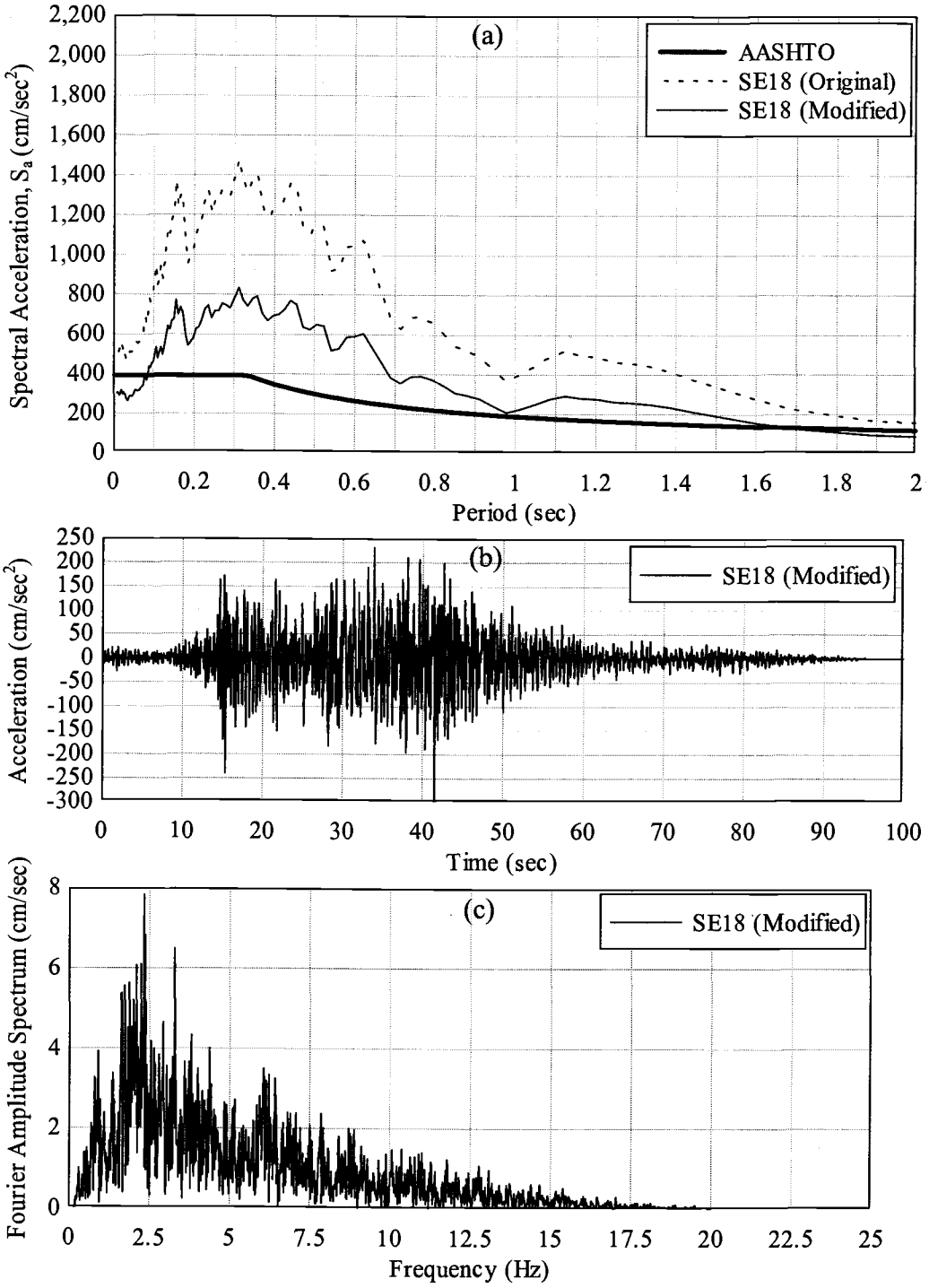

Figure C.12. 1985 Valparaiso EQ (Strike-Parallel): (a) Response Spectra; (b) Modified Time History; (c) Fourier Spectrum